Targeting Synthetic Advances in Extended Phenanthrene and Phenanthroline Systems

Robert Conway-Kenny B.A. (Mod.)

A thesis submitted to the University of Dublin for the degree of Doctor of Philosophy

November 2017

Declaration

I declare that this thesis has not been submitted as an exercise for a degree at this or any other university and it is entirely my own work.

I agree to deposit this thesis in the University's open access institutional repository or allow the library to do so on my behalf, subject to Irish Copyright Legislation and Trinity College Library conditions of use and acknowledgement.

_____

Robert Conway-Kenny B.A. (Mod.)

"Phencyclone is not easy to prepare."

C. F. H Allen, R. Y. Ning, *Can. J. Chem.,* 1964, **42**, 2151-2152

Summary

Chapter 1

This chapter gives a general introduction to a number of unfused and fused polyphenylene and polycyclic aromatic hydrocarbon (PAH) systems. Synthetic access to these systems is described *via* Knoevenagel reactions, Diels-Alder [4+2] cycloaddition reactions, and inverse Diels-Alder reactions. Heteroatom substitution of these systems is described, with particular focus on the inclusion of nitrogen atoms.

The chapter then details the use of this novel dehydration method towards the generation of "PhenBlue" at temperatures of 130 °C, and its use in Diels-Alder cycloaddition reactions with alkene dienophiles. Significant synthetic difficulties are worked through, coupled with a thorough discussion of each decision. The generation of four novel ligand systems, two containing 1,4-quinone moieties, is achieved. All ligands are structurally characterised with multinuclear NMR and HRMS studies, with single crystal X-ray diffraction data obtained for all systems. The X-ray data reveals large twists from the expected planarity of these ligands. Photophysical and electrochemical investigations of the four partially-fused PAH-type ligands are detailed. A concise account of a significant volume of other work is also given, towards three identified "gateway" ligands that did not yield successful results.

Chapter 2

This chapter begins with a small introduction covering transition metal complexes bearing partially- or fully-fused PAH-type ligands. A brief account of some practical applications of these systems is detailed, including photoinitiated electron collection (PEC), and photocatalytic proton reduction. Work of the metal complexation of the two quinone-containing ligands to $[Ru(bpy)_2Cl_2]$ and $[Ru(phen)_2Cl_2]$ was undertaken. Three systems are structurally characterised *via* multinuclear NMR, and HRMS studies, with NMR studies revealing a loss of symmetry of the non-fused phenyl rings due to a proposed "ring locking", or "ring slowing". The photophysical and electrochemical properties are detailed and discussed. Metal complexation of the non-quinone ligands to $[Ru(bpy)_2Cl_2]$ and $[((ppy)_2IrCl)_2]$ was also undertaken. The Ru(II) and Ir(III) complexes bearing the pyridazine ring-containing ligand achieved turnover numbers (TONs) of 35 and 160 (over 18 hours) respectively. Future work towards the surface immobilisation of the quinone-containing

systems is described, as well as synthetic strategies towards the development of partially fused systems for DNA intercalation studies.

Chapter 3

This chapter begins with an introduction to the research area of the nitrogen-substituted graphene nanoribbons (N-GNRs). Due to the current small size of this research area, a detailed literature review is completed, finishing on two theoretical studies of pyridazine ring system substitution. The synthesis of the first pyridazine substituted GNR precursor is documented. Structural characterisation *via* multinuclear NMR, and HRMS studies are also documented. The thermal stability of the precursor was analysed *via* Thermogravimetric Analysis (TGA), revealing good thermal stability to 350 °C. Scanning Tunneling Microscopy (STM) studies carried out on Au(111) are also included, revealing the successful polymerisation of the precursor at normal polymerisation temperatures. STM studies also reveal a decomposition step of the polymer before the successful cyclodehydrogenation step towards GNR construction. This is postulated as a thermal decomposition of the pyridazine ring structure. Future work detailing alternate syntheses and cyclodehydrogenation routes are given.

Chapter 4

This chapter begins with a detailed introduction of Donor-Acceptor-Donor (D-A-D) compounds in the literature used towards a number of active research areas. A simplified explanation of the benefits of these systems *versus* that of Donor-Acceptor (D-A) is given. Significant detail is given to structural moieties common as donor or acceptor components in these systems, with explanations of their uses and results also given. The use of pyridazine ring systems, and phenanthrene ring systems are detailed at the end of the introduction, highlighted the lack of phenanthrene-pyridazine hybrid systems in the literature. Four target phenanthrene-pyridazine systems are introduced as the first systems of their kind. Detailed attempted synthetic preparations are given, coupled with a detailed discussion on synthetic issues encountered. Three structures are characterised by multinuclear NMR and HRMS studies. Detailed photophysical and electrochemical investigations of the single acceptor, and D-A-D pyrene-containing systems are detailed, revealing intramolecular charge transfer (ICT) transitions occurring in the D-A-D compound. The thermal stability of both compounds were studied *via* TGA measurements to assess their suitability for inclusion in devices. Detailed future work is given towards the rapid diversification of a compound library derived of a phenanthrene-pyridazine core system.

Chapter 5

This chapter details the experimental work carried out within this volume of work. NMR, HRMS, and IR is included in this section for each compound or complex.

Annex

The annex contains crystal X-ray diffraction refinement tables.

Acknowledgements

I would like to sincerely thank my supervisor, Prof. Sylvia Draper, for allowing me to complete my PhD in synthetic organic and inorganic chemistry. The wide variety of research attempted (and reattempted, and reattempted, …)$_n$ allowed me the great opportunity to carry out research beyond what I could have hoped to achieve. I must also thank Prof. Sarath Perera for his helpful suggestions across his numerous stays within the group. I thank all of the technical team who have helped me during my time in TCD, including but not limited to, Drs. Martin Feeney, Gary Hessman, Manuel Ruether, and Brendan Twamley. I give a special thank you to Dr. John O'Brien for his massive kindness is running NMR samples at any hour of the day to meet surprise deadlines, or in races against the dreaded "I think its falling out of solution". I also thank Teresa McDonnell, Patsy Greene, Peter Brien, Peggy Brehon, Dorothy Delahunty, Mark Keegan, Maura Boland, and Fred Cowzer. I especially thank Dr. John O'Donoghue and Tom Conroy for their help with my outreach activities during my PhD. On the administrative side, I thank Dr. Noelle Scully, Dr. Sinead Boyce, AnneMarie Farrell, Jennifer McHugh, and Tess Lalor.

I thank all of the Draper group members, past and present, for their help and encouragement. To Niamh, Lankani, Gearoid, Colm, Nitheen, Yue, Bryan, Junsi, Eugene, Colin, Justo, Martha, Claire, and Nidhi …. Go raibh cead míle maith agaibh, gracias, 谢谢, शुक्रिया, istuti, Thank You! A special thousand thank you's to Gearoid for assisting with the maintenance of a caffeine addiction for four years, and for being a great friend! And to Bryan, for proving that it really (no really … the joke is four years old!) is all fun and games till one uses copper cyanide, then it's hilarious! And a huge thank you to both Junsi and Yue for their Herculean efforts to help me throughout the PhD, but especially in the last few months. 多谢!, 多谢!, 多谢!

I thank Dr. Peter Staunton for good discussions, and Prof. Craig Chigwedere for even better ones. Finally, to my family, all of you have helped in your own way to the completion of this report, thank you Mum and Dad, Jack, Rhona, Jane, Hannah, Lucy, Molly and Teddy. A special thanks to Cleo for brightening tough times.

Beyond that, there are too many people to thank individually. I just ask that if I have forgotten to thank you personally, that you please just blame the chemicals! 😊

Abbreviations

1D	one-dimensional
2D	two-dimensional
Å	angstrom
Ar	aryl
a.u.	arbitrary units
B	generic base
bpy	2,2'-bipridine
Bu	butyl
C	Celsius
cm	centimetre
COSY	correlation spectroscopy
CVD	chemical vapour deposition
d	doublet
dd	doublet of doublets
DEPT	distortionless enhancement by polarisation transfer
DFT	density functional theory
DLC	discotic liquid crystal
DMF	dimethylformamide
DMPD	1,4-dimethylpiperazine-2,3-dione
DMSO	dimethylsulfoxide
e	electron
EPR	electron paramagnetic resonance
em	emission
ESI-MS	electrospray ionisation mass spectrometry
FET	field effect transistor

FTIR	Fourier transform infrared spectroscopy
g	gram
GNR	graphene nanoribbon
HBC	hexa-peri-hexabenzocoronene
HMBC	heteronuclear multiple-bond correlation
HMQC	heteronuclear multiple-quantum correlation
HOMO	highest occupied molecular orbital
HPLC	high-performance liquid chromatography
hr	hour
Hz	hertz
i	current
i	iso
IR	infrared
J	coupling constant
K	Kelvin
kJ	kilojoule
L	ligand
LUMO	lowest unoccupied molecular orbital
m	multiplet
M	molarity
min	minute
mol	mole
m.p.	melting point
m.u.	mass units
m/z	mass to charge ratio
MALDI-TOF MS	matrix-assisted laser desorption/ionisation – time of flight mass
max	maximum
Me	methyl

mg	milligram
MHz	megahertz
mL	millilitre
mmol	millimole
mol	mole
MS	mass spectrometry
mV	millivolt
N-1⁄2	HSB half-cyclised nitrogen-heterosuperbenzene
N-HSB	nitrogen-heterosuperbenzene
nm	nanometre
NMR	nuclear magnetic resonance
ns	nanoseconds
Nu	nucleophile
OFET	organic field-effect transistor
OLED	organic light emitting diode
OPV	organic photovoltaic
ORR	oxygen reduction reaction
PAH	polycyclic aromatic hydrocarbon
PEMFC	proton exchange membrane fuel cell
Ph	phenyl
POM	polarising optical microscopy
ppm	parts per million
PVD	photovoltaic device
RT	room temperature
s	singlet
SCE	saturated calomel electrode
STM	scanning tunnelling microscopy
sec	second

solv.	solvent
t	triplet
t or tert	tertiary
THF	tetrahydrofuran
TLC	thin layer chromatography
TMS	tetramethylsilane
TOCSY	total correlation spectroscopy
UHV	ultra-high vacuum
UV/Vis	ultraviolet-visible
V	volt
vs.	versus
XPS	X-ray photoelectron spectroscopy
°	degrees
δ	chemical shift
Δ	heat
ε	molar absorption coefficient
λ	wavelength
μs	microsecond
τ	half life
%	percentage

Table of Contents

Glossary of Structures – Part 1 (L)

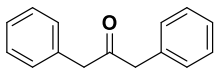

L1

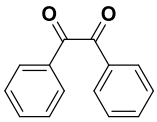

L2

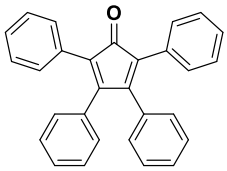

L3

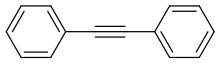

L4

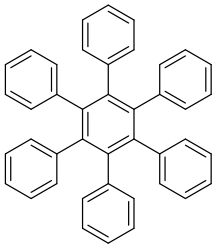

L5

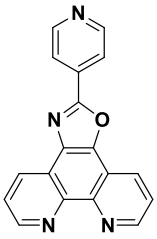

L6

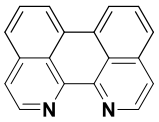

L7

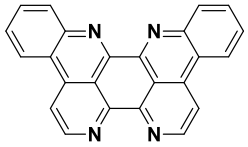

L8

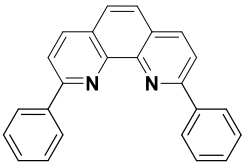

L9

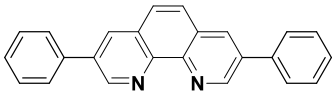

L10

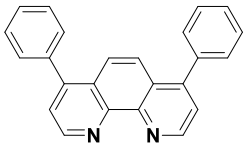

L11

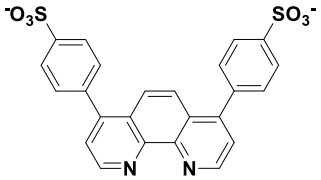

L12

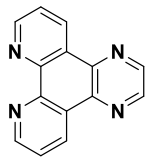

L13

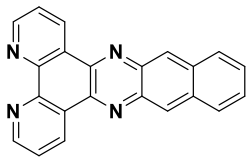

L14

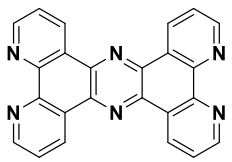

L15

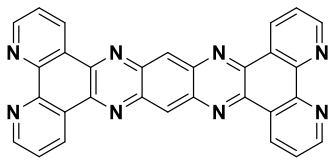

L16

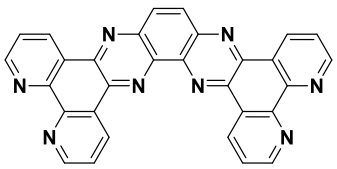

L17

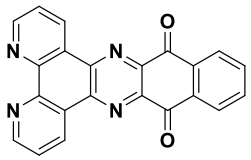

L18

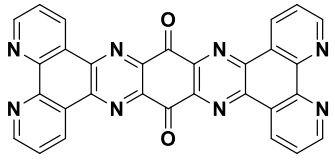

L19

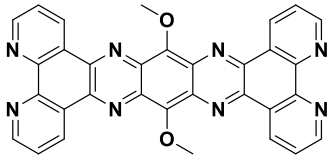

L20

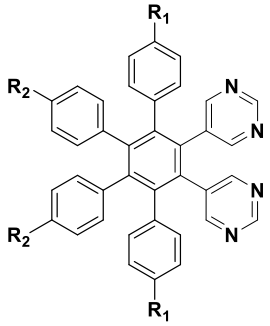

R_1 = t-butyl, R_2 = t-butyl; L21
R_1 = t-butyl, R_2 = OMe; L22

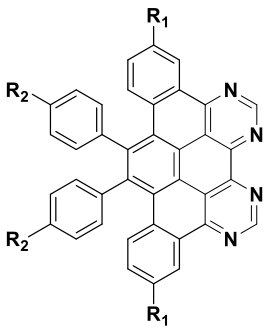

R_1 = t-butyl, R_2 = Br; L23
R_1 = t-butyl, R_2 = t-butyl; L24

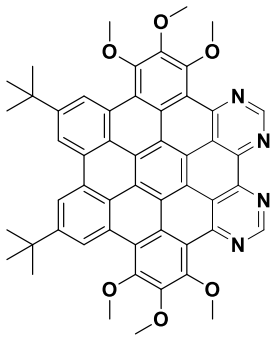

L25

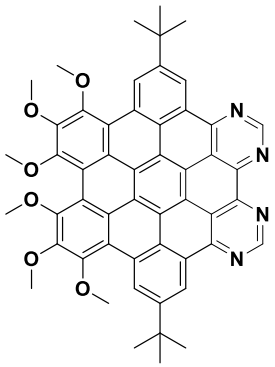

L26

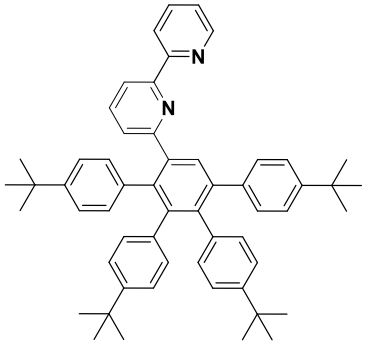

L27

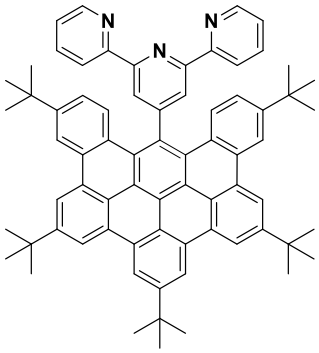

L28

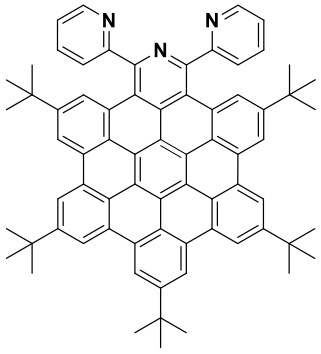

L29

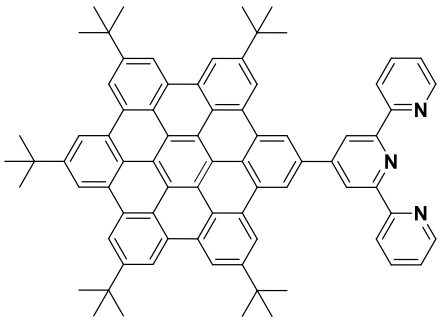

L30

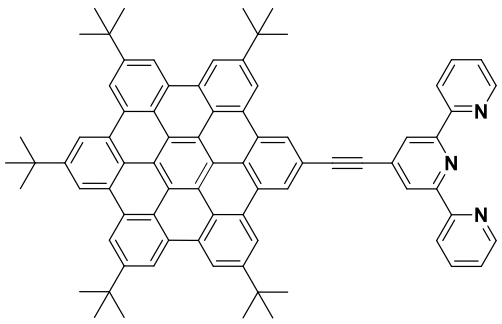

L31

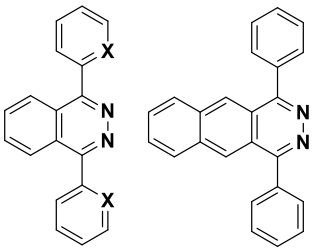

X = C; L32
X = N; L33

L34

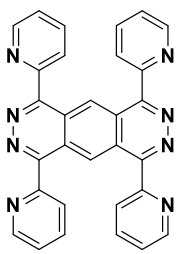

L-35

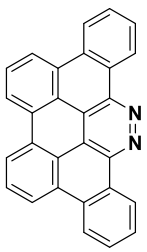

L-36

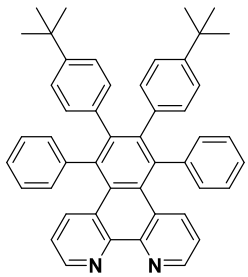

L37

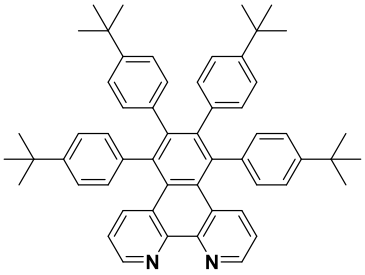

L38

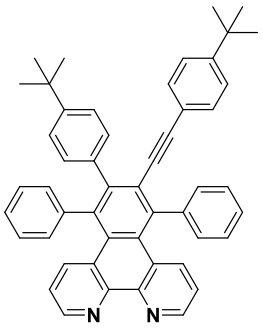

L39

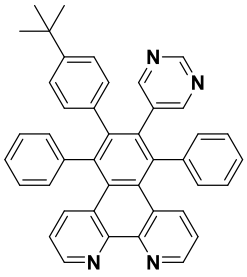

L40

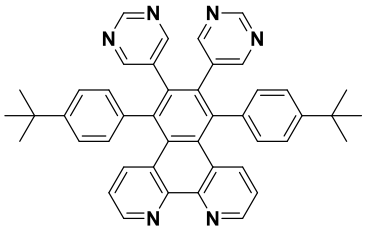

L41

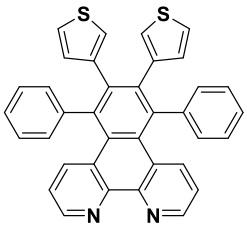

L42

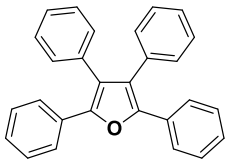

L43

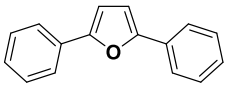

L44

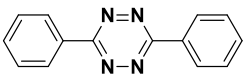

L45

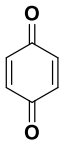

L46

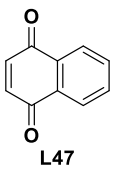

L47

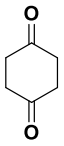

L48

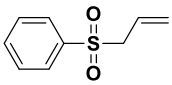

L49

L50

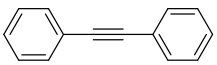

L51

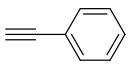

L52

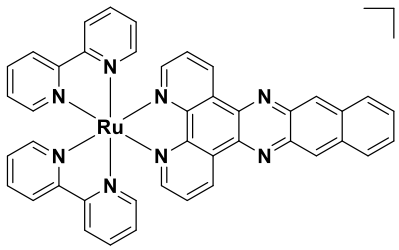

L53

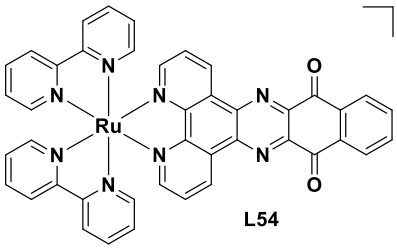

L54

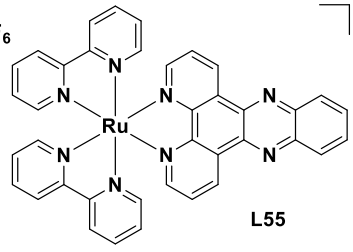

L55

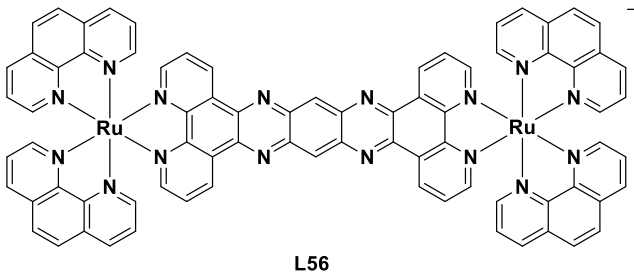

L56

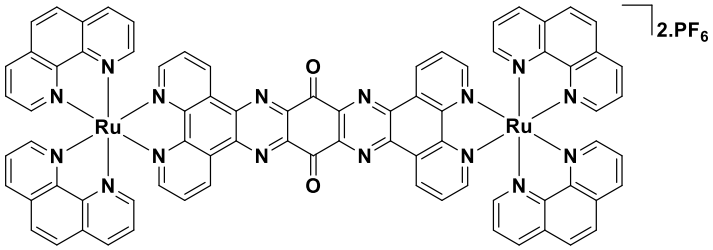

L57

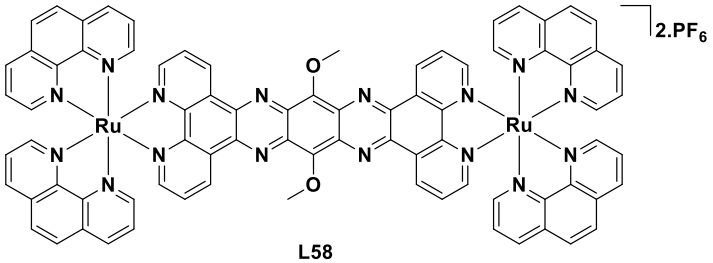

L58

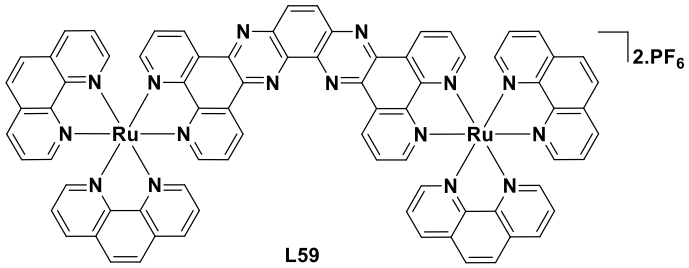

L59

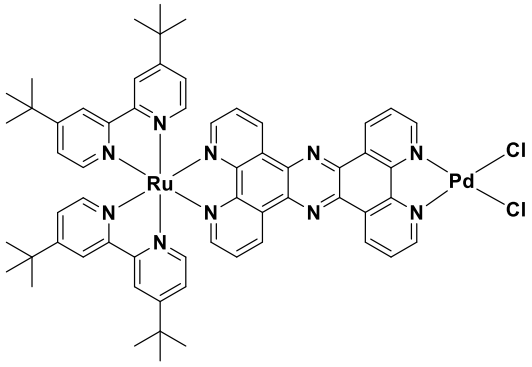

L60

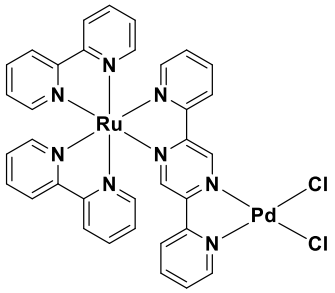

L61

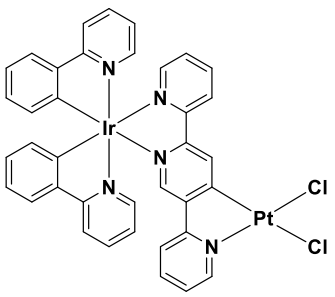

L62

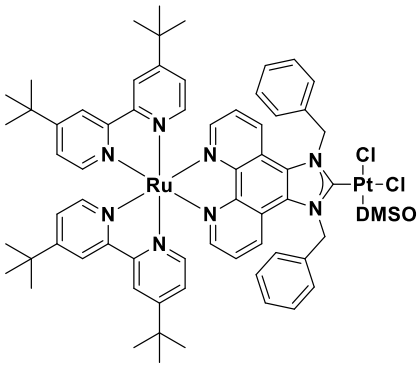

L63

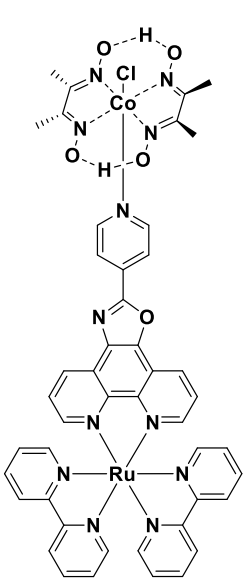

L64

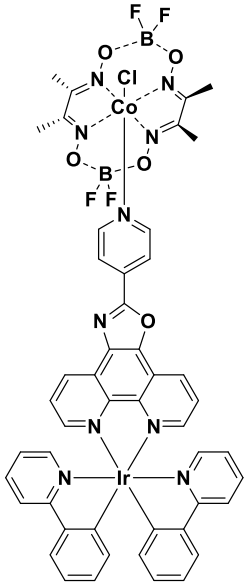

L65

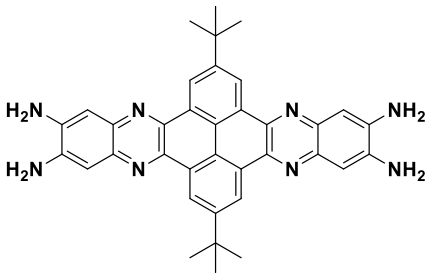

L66

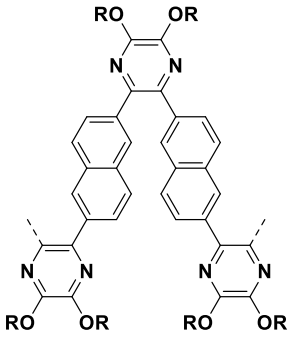

L67

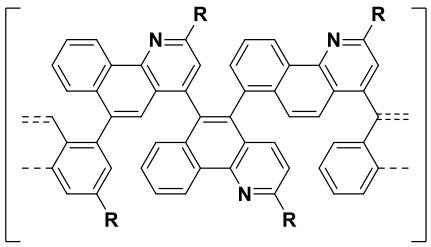

L68

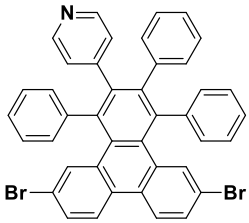

L69

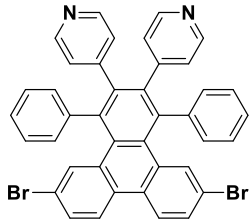

L70

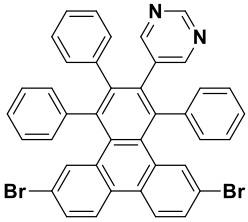

L71

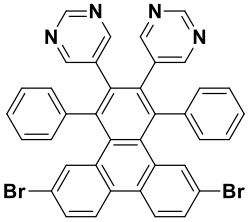

L72

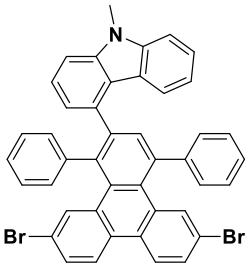

L73

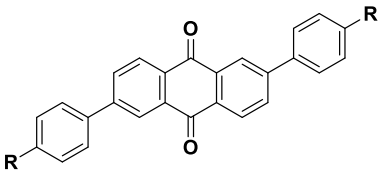

L74

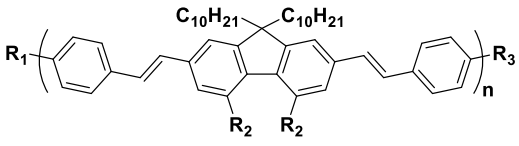

L75

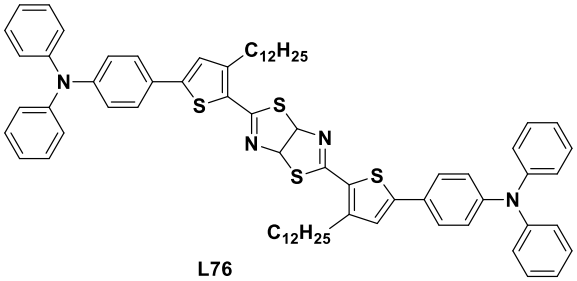

L76

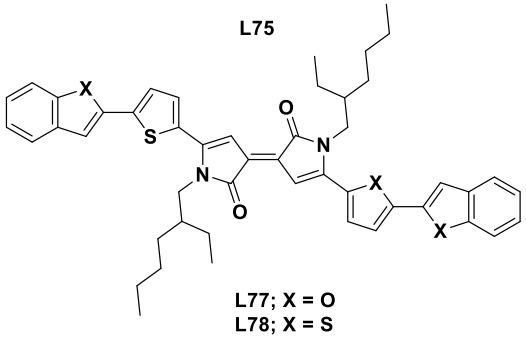

L77; X = O
L78; X = S

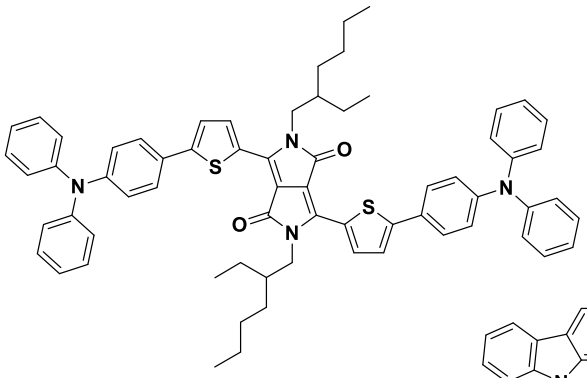

L79

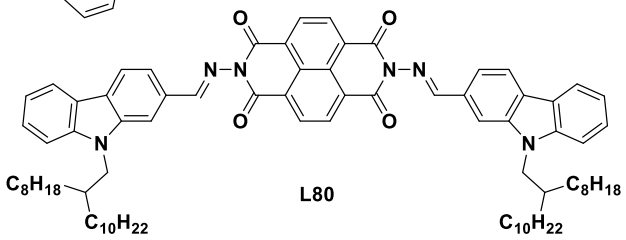

L80

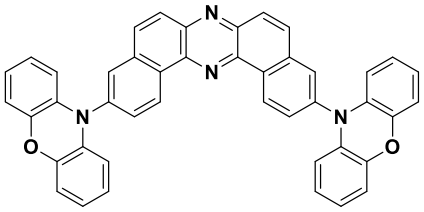

L81

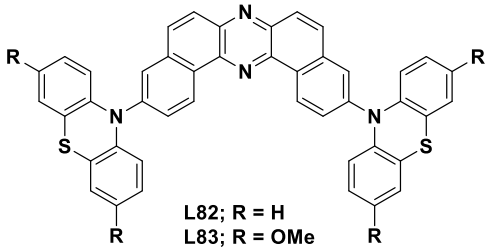

L82; R = H
L83; R = OMe

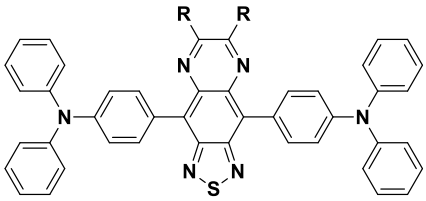

L84; R = H
L85; R = Ph

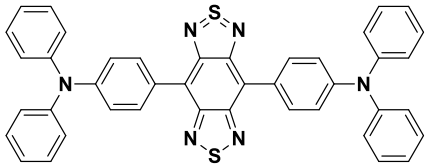

L86

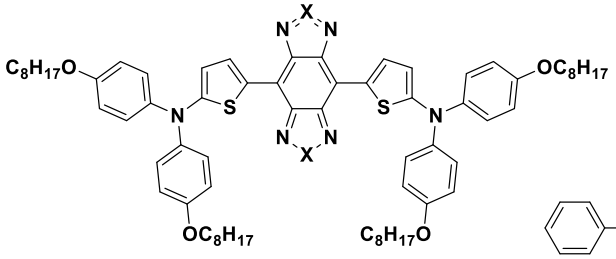

L87; X = S
L88; X = Se

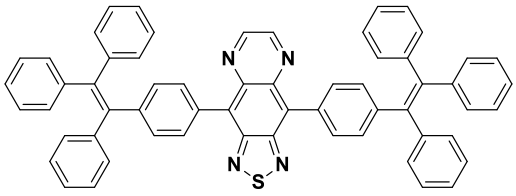

L89

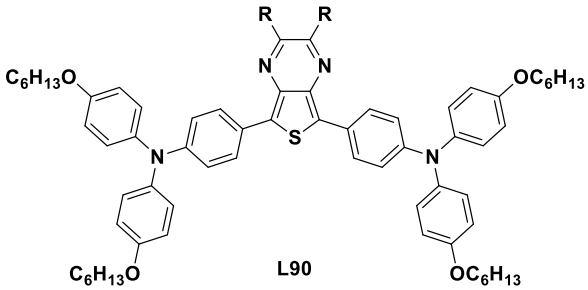

L90

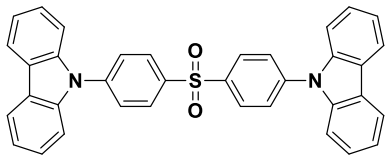

L91

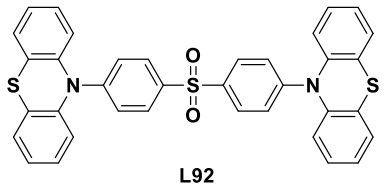

L92

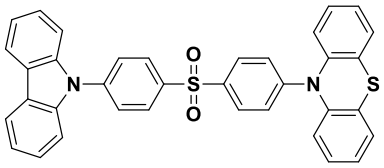

L93

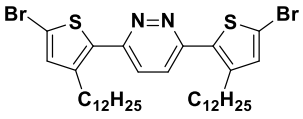

L94

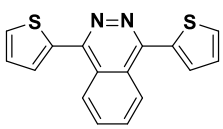

L95

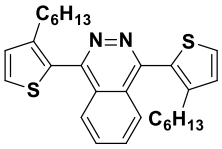

L96

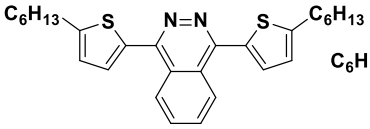

L97

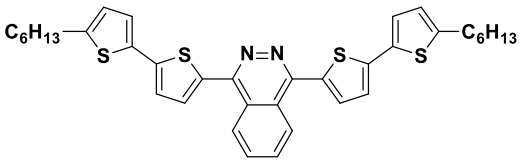

L98

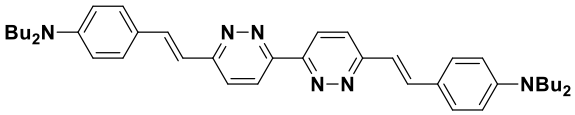

L99

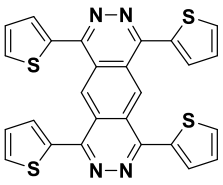

L100

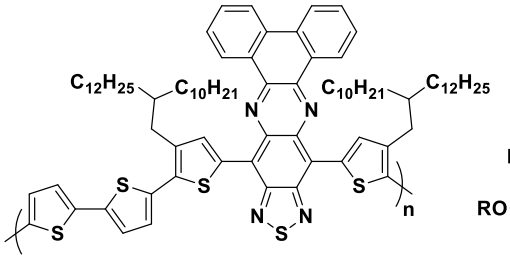

L101

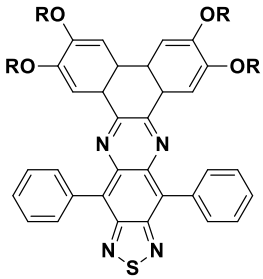

L102; R = —$(CH_2)_9CH_3$
L103; R = 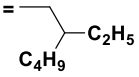

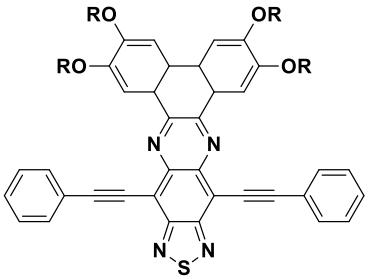

L104; R = —$(CH_2)_9CH_3$
L105; R = 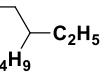

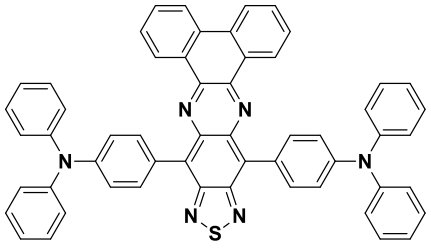

L106

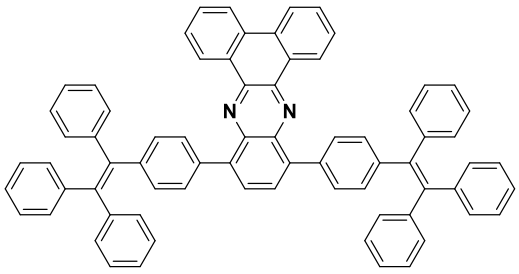

L107

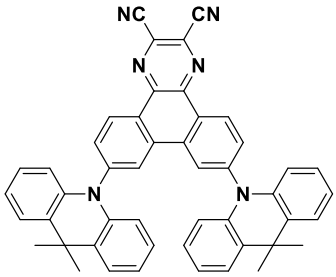

L108

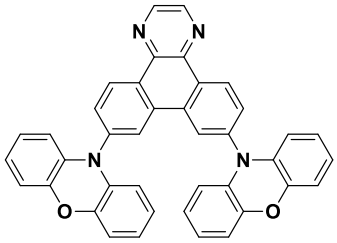

L109

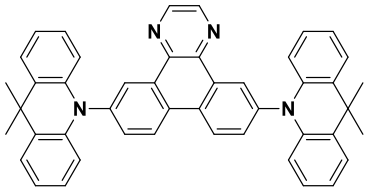

L110

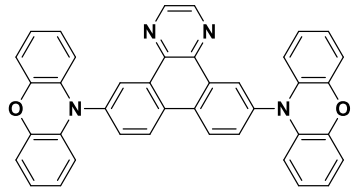

L111

Glossary of Structures – Part 2

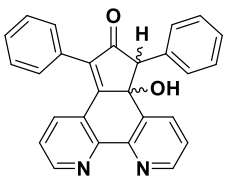

1

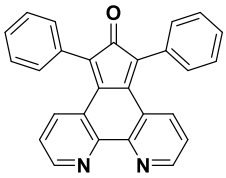

2

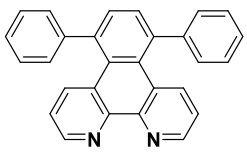

3

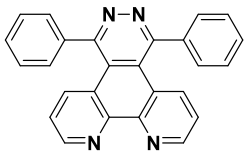

4

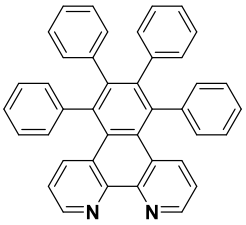

5

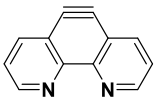

6

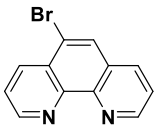

7

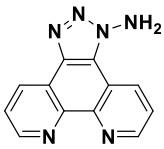

8

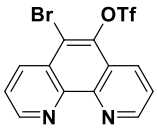

9

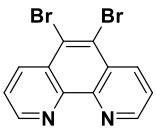

10

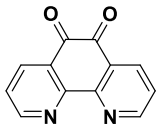

11

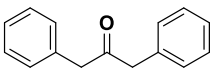

12

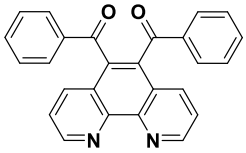

13

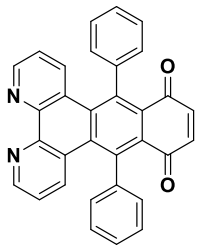

14

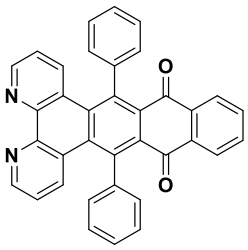

15

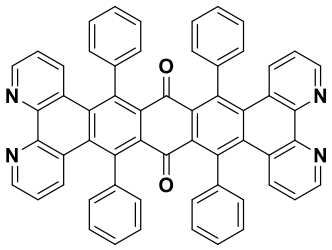

16

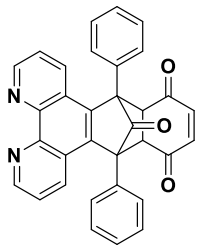

17

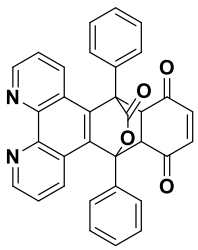

18

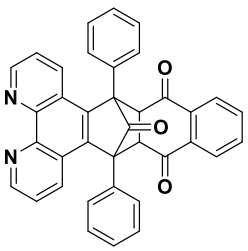

19

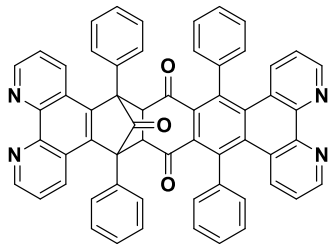

20

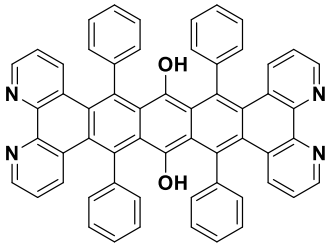

21

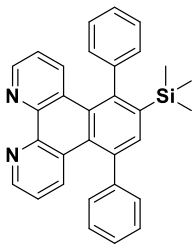

23

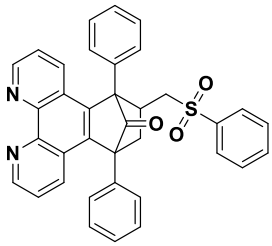

24

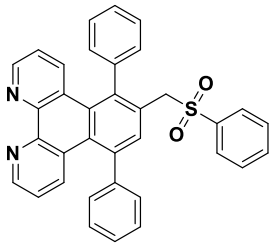

25

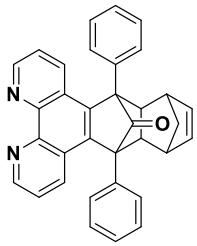

26

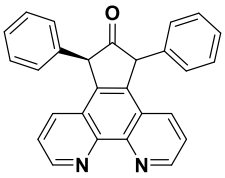

27

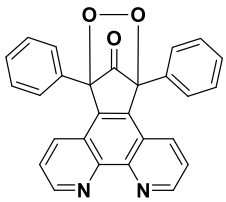

28

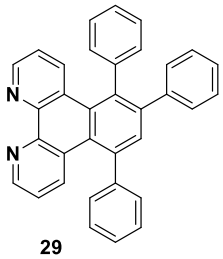

29

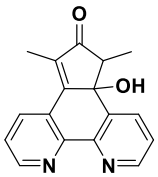

30

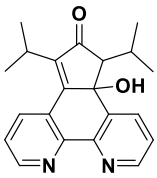

31

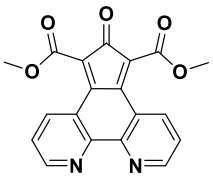

32

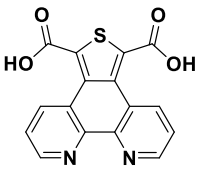

33

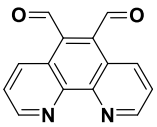

34

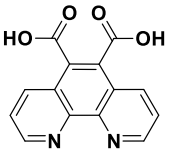

35

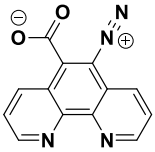

36

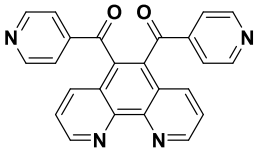

37

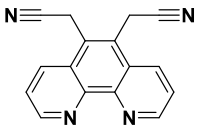

38

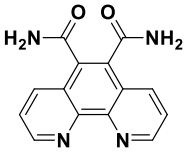

39

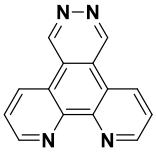

40

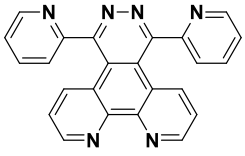

41

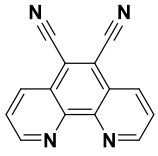

42

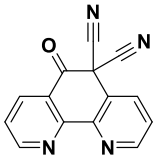

43

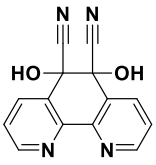

44

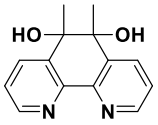

45

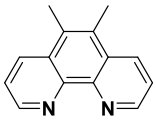

46

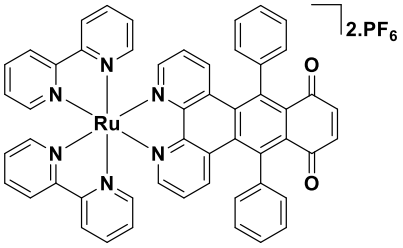

47

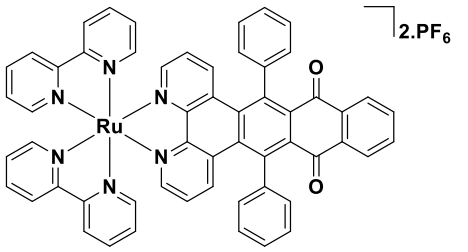

48

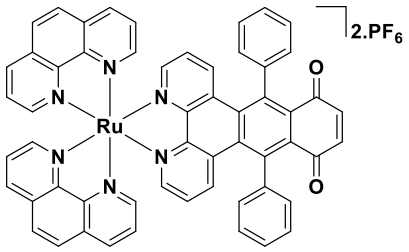

49

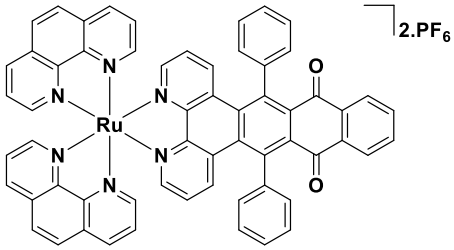

50

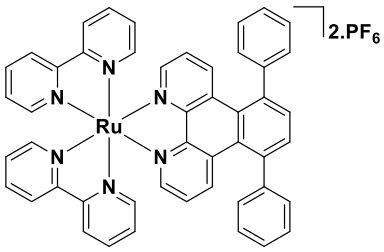

51

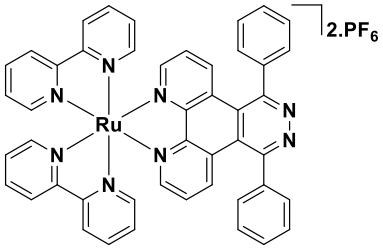

52

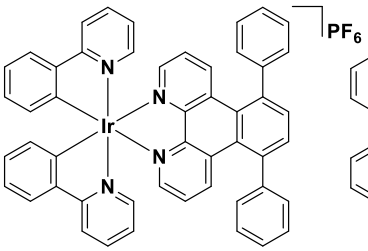

53

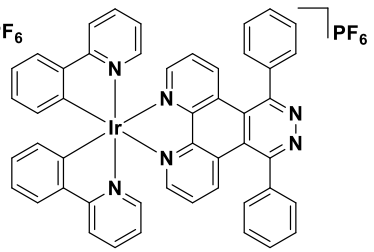

54

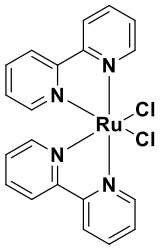

55

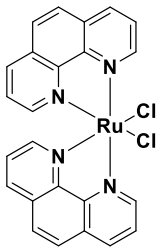

56

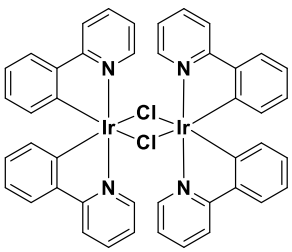

57

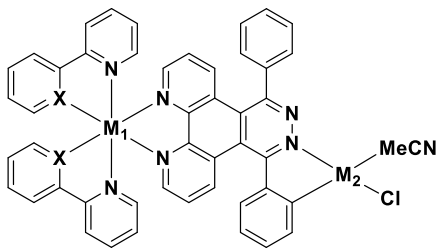

58; M_1 = Ru(II), M_2 = Pt(II), X = N
59; M_1 = Ir(III), M_2 = Pt(II) X = C

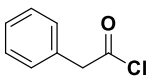

60

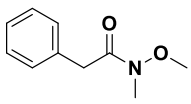

61

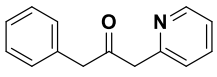

62

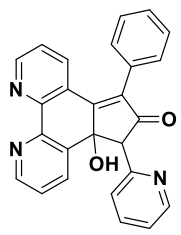

63

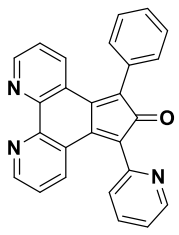

64

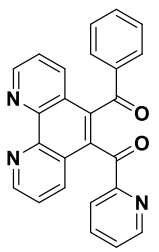

65

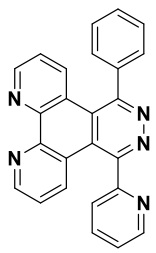

66

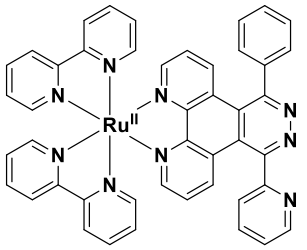

67

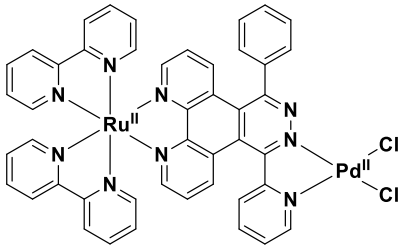

68

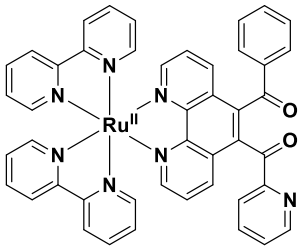

69

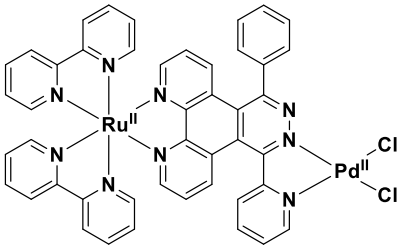

70

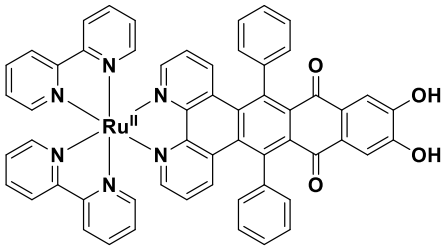

71

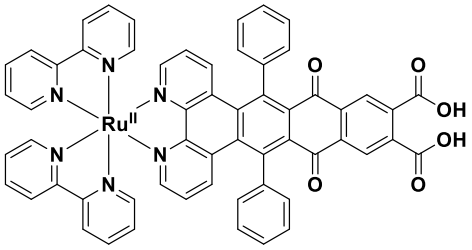

72

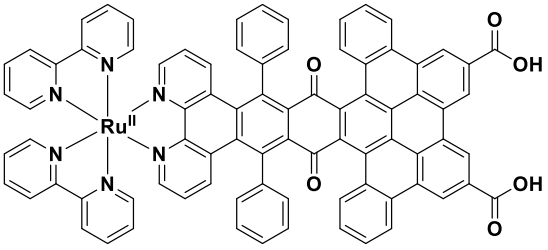

73

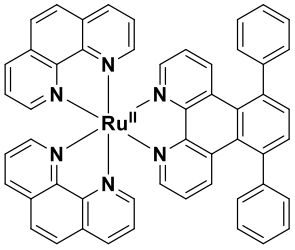

74

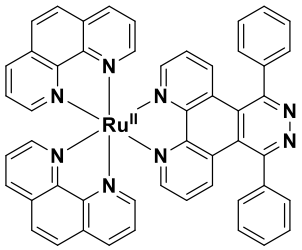

75

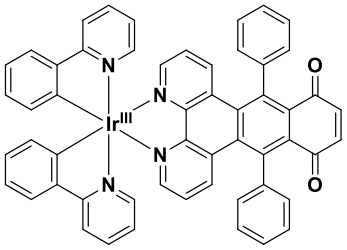

76

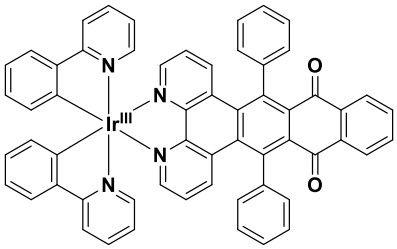

77

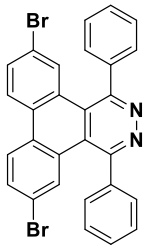

78

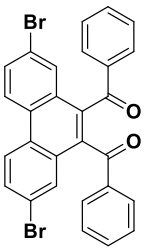

79

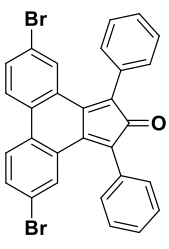

80

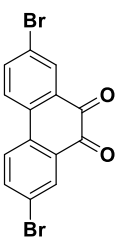

81

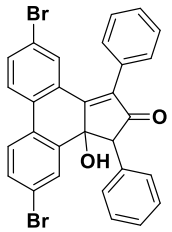

82

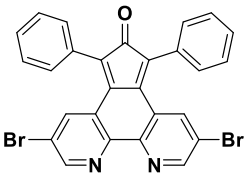

83

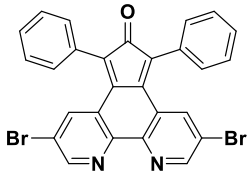

84

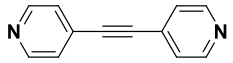

85

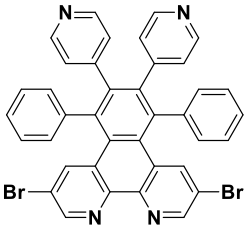

86

87

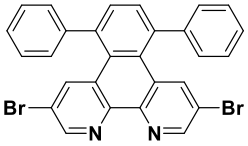

88

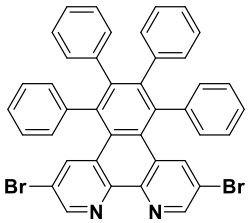

89

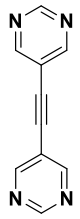

90

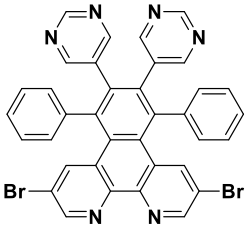

91

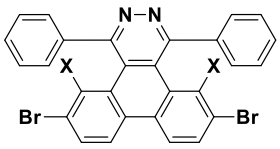

92

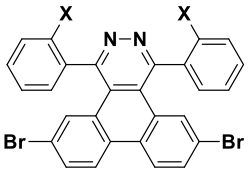

93

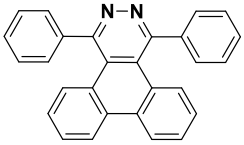

94

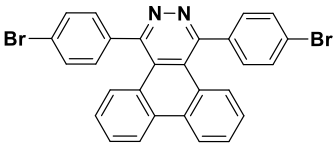

95

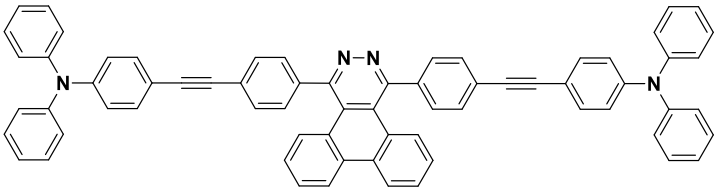

96

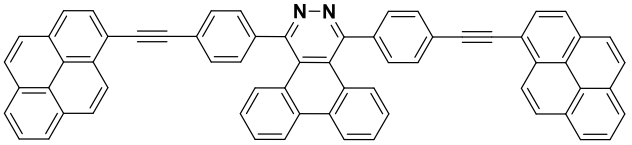

97

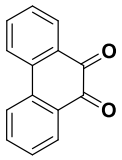

98

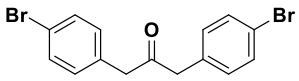

99

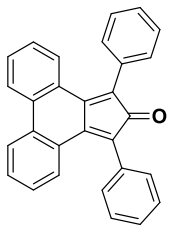

100

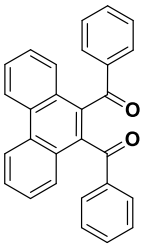

101

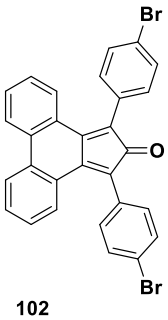

102

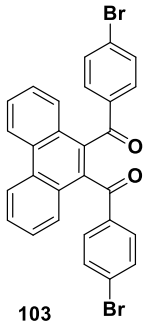

103

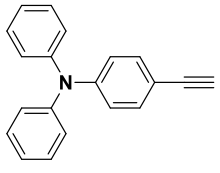

105

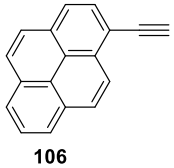

106

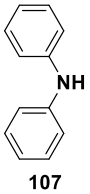

107

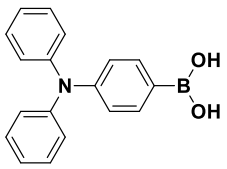

108

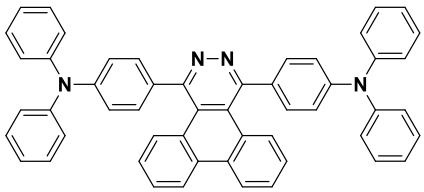

109

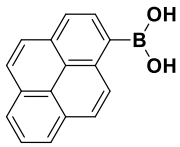

111

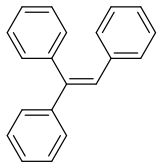

112

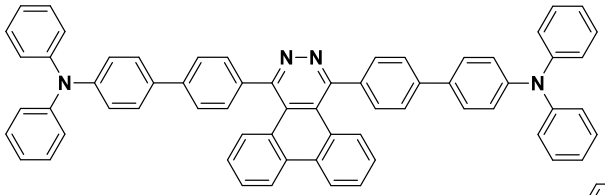

110

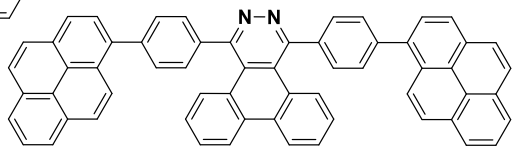

113

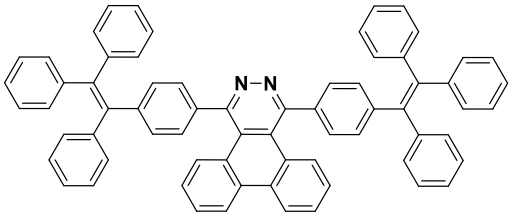

114

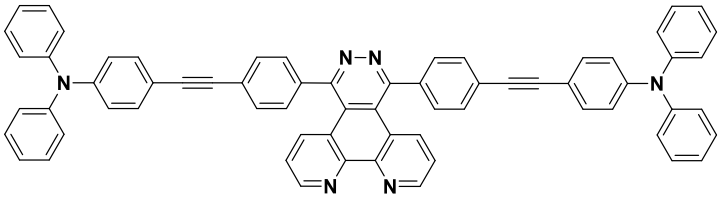

115

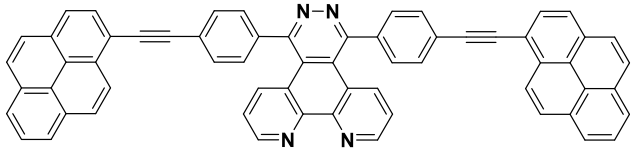

116

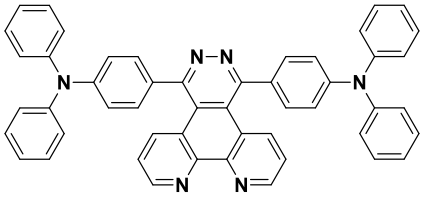

117

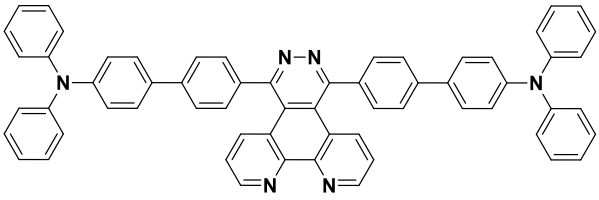

118

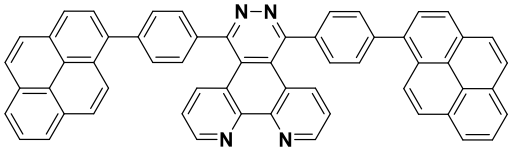

119

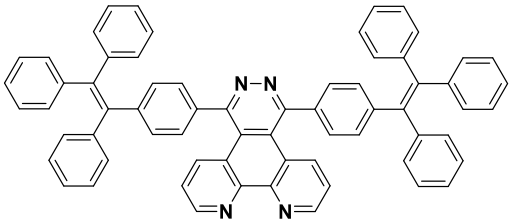

120

General Thesis Introduction

Introduction

Polycyclic aromatic hydrocarbons (PAHs) are multi-ring aromatic systems that are found in coal and tar deposits,[1] and in interstellar media.[2] They are ubiquitous in organic chemistry, and are currently undergoing a significant renewed research interest for their use in the area of organic materials science.[3,4] When considered at their simplest form, constructed of only carbon and hydrogen, PAHs may be thought of as molecular fragments of graphene, with many of these fragments discussed in basic chemical education – anthracene, phenanthrene, coronene and pyrene.

Larger PAH systems can be doped with heteroatoms, whereas smaller systems can be substituted with the same. On addition of the two most popular heteroatoms, nitrogen[5] and oxygen[6], the optoelectronics properties of the PAH can be dramatically altered. Nitrogen has long been considered as the premier addition to PAH systems, as it offers the possibility of generating single- or multi-nuclear metal complexes bearing those PAH compounds as ligands. These complexes typically readily access desired charge transfer states, due to the low lying LUMO orbital of the highly conjugated ring structure of the PAH ligand.[7]

Not limited to use as ligands, the incorporation of nitrogen into larger PAH systems generates a band gap within a PAH sheet, a property absent in the all-carbon systems.[8] The formation of a band gap offers their use as novel conductors and semiconductors, with considerable research interest on-going towards their eventual replacement of current silicon and germanium semiconductors.[9] This is driven primarily by their improved cost, toxicity, and their ease of design.

However, despite all of their beneficial properties, novel PAH molecules (both all-carbon, and nitrogen substituted) are relatively rare in current literature. This is undoubtedly due to their poor solubility,[10] and a shortage of synthetic access to readily modifiable core ring systems. Addressing this problem is the core focus of this thesis, connecting all of the four chapters, despite their individual primarily applications.

There are very few "standard" synthetic strategies currently utilised in the generation of novel PAH compounds. Despite its use in nearly all modern PAH publications, there has been very little attention given to modifying the core ring system of the PAH precursor in the Knoevenagel reaction. As most authors have mainly focused on using functionalised alkynyl co-reagents,[11–14] a fantastic opportunity exists to investigate the functionalisation of the cyclopentadienone product, and to address the shortage of novel core PAH ring systems. In particular, an opportunity has been identified to generate novel PAH ligands utilising the core ring system of 1,10-

phenanthroline. While many authors have used bis-phenanthroline compounds to generate bridging ligands, these systems have almost exclusively relied on pyrazine as a central ring.[15–17] Pyrazine within a PAH core is unsuitable for a number of reasons. The primary reason being that pyrazine retards the growth of the PAH due to the position of it's nitrogen atoms. Small, partially-fused systems, were identified as useful ligand systems for aqueous photocatalytic proton reduction.[18] Larger systems, incorporating the same phenanthroline ring system suitable for metal complexation, and further incorporating a quinone moiety in the core PAH ring system were also identified. These systems could offer a close comparison to the current literature-based pyrazine systems, with further options to form a larger PAH ring system not offered by those same pyrazine compounds. These novel structural motifs would offer new and exciting systems for artificial photosynthesis in the form of photoinduced electron collection coupled photovoltaic processes.[19] In the synthetic design stage, a significant volume of new synthetic preparations were devised to further the generation of novel PAH core ring systems. Nearly all of these attempts will be attempted towards considerable advances in the library of accessible PAH-type ligands.

With a number of new PAH-type compounds capable of metal complexation, the opportunity now existed to investigate their properties as ligands. As Ru(II) and Ir(III) are the most common photoactive metals currently used in the literature,[20,21] these metals would offer the closest comparison to current literature-based compounds. As previously mentioned, smaller PAH ligand-bearing complexes are used for photocatalytic proton reduction, and photoinitiated electron collection. However, they may also find use in molecular biology, through their use as DNA intercalators. Typically, these systems would be fully-fused and planar, as it was believed that this was a necessary spatial, and steric, requirement for successful intercalation.[22] However, recent work has shown that partially fused systems can intercalate DNA through a threading mechanism (*via* their freely rotating phenyl rings), and may offer much slower dissociation kinetics compared to current planar intercalators.[23] This work is just the beginning of a completely novel approach to DNA intercalation, and may offer significant advances in current therapies.

A substantial research area has emerged in the area of generating novel PAH systems for their use as molecular nanoribbons.[24] These ribbons can be considered as 1D ribbons of graphene, with their width directly affecting their optoelectronic properties, due to quantum confinement within the ribbon.[25] Despite nitrogen doping being achieved by authors through incorporation of pyridine, pyrimidine, pyrazine, and phenanthridine, there has been no successful incorporation

of the pyridazine ring. Computational studies suggest that pyridazine will be unique among the other nitrogen-containing rings, and will generate nanoribbons of a metallic-type conductance.[26] This would therefore be an ideal candidate to explore for the replacement of copper in electronic circuits. Due to the benefits of synthetic control in the "bottom-up" strategy, a novel pyridazine-containing feedstock was identified. Successful on-surface polymerisation will be undertaken on Au(111). This surface is often used as the first reactive metal surface of choice *versus* Ag(111) and Cu(111) as it the least reactive of the series. During the synthetic design process, a feedstock incorporating a novel phenanthroline ring system was identified – computational work will determine the optoelectronic properties before attempts to synthesis the compound will be undertaken.

One of the most exciting areas of current PAH research is TADF. Thermally assisted delayed fluorescence (TADF) offers the potentially to rapidly change the entire market of organic luminescent devices. The spatial isolation of the HOMO and LUMO states of a donor-acceptor, or donor-acceptor-donor compound has the effect to profoundly diminish the S_1 and T_1 energy gap of the excited compound.[27] This effect allows efficient intersystem crossing first from the S_1 to the T_1 states, before an equally efficient reverse intersystem crossing back to the S_1 state. The process can therefore access the four exciton spin pairs, equalling the internal quantum efficiency of current transition metal complexes, which rely on the heavy atom effect to access the triplet state.[28,29] However, while current metal-based organic light emitting diodes (OLEDs) therefore emit broad phosphorescence, TADF organic-based compounds emit sharp fluorescence bands, generating increased resolution in devices. Once again however, the use of PAH compounds in TADF studies has focused on a very small library of donor and acceptor components. An appreciable synthetic challenge was encountered, with synthetic strategies designed towards the generation of a novel PAH-type acceptor component – the first to feature an electron withdrawing pyridazine ring, and a phenanthrene ring systems. Coupled with an ethynyl-pyrene donor component, TADF behaviour could be investigated by solvatochromic and degassing studies, with further studies determining the effect of the pyrene-pyrene excimer. A meaningful volume of potential TADF components now accessible through this novel PAH acceptor component was also identified, and will be actively researched in the near future.

All of the chapters actively seek out synthetic challenges, and "gaps" in the literature, where PAH-type compounds can offer solutions to both old and new problems in a diverse field of applications. There has been a resurgence in partially- and fully-fused systems in optoelectronics due their perceived technical benefits *versus* transition metal complexes, while at the same time

overcoming the simultaneous geopolitical issues surrounding the mining of those same materials.[30] This thesis hopes to offer a small but meaningful contribution to this growing field.

References

1 S. A. Wise, D. L. Poster, S. D. Leigh, C. A. Rimmer, S. Mössner, P. Schubert, L. C. Sander and M. M. Schantz, *Anal. Bioanal. Chem.*, 2010, **398**, 717–728.

2 Gredel, R., Carpentier, Y., Rouillé, G., Steglich, M., Huisken, F. and Henning, Th., *A&A*, 2011, **530**, A26.

3 S. Rózsa, B. Pierre-Antoine, N. László and H. Muriel, *ChemPhysChem*, 2017, **18**, 2618–2630.

4 Y. Li, R. G. Clevenger, L. Jin, K. V Kilway and Z. Peng, *J. Phys. Chem. C*, 2016, **120**, 841–852.

5 C.-F. Liu, C. Cheng, Y. Jiang, W.-Y. Lai and W. Huang, *New J. Chem.*, 2017, **41**, 13619–13624.

6 S. Daphné, D. Nicola and B. Davide, *Angew. Chemie Int. Ed.*, 2016, **55**, 5947–5951.

7 S. M. Draper, D. J. Gregg, E. R. Schofield, W. R. Browne, M. Duati, J. G. Vos and P. Passaniti, *J. Am. Chem. Soc.*, 2004, **126**, 8694–8701.

8 M.-L. Yang, N. Zhang, K.-Q. Lu and Y.-J. Xu, *Langmuir*, 2017, **33**, 3161–3169.

9 M. Dvorak, W. Oswald and Z. Wu, *Sci. Rep.*, 2013, **3**, 2289.

10 M. Okazaki, Y. Takeda, P. Data, P. Pander, H. Higginbotham, A. P. Monkman and S. Minakata, *Chem. Sci.*, 2017, **8**, 2677–2686.

11 S. M. Draper, D. J. Gregg and R. Madathil, *J. Am. Chem. Soc.*, 2002, **124**, 3486–3487.

12 C. Bronner, S. Stremlau, M. Gille, F. Braußе, A. Haase, S. Hecht and P. Tegeder, *Angew. Chemie Int. Ed.*, 2013, **52**, 4422–4425.

13 Y. Zhang, Y. Zhang, G. Li, J. Lu, X. Lin, S. Du, R. Berger, X. Feng, K. Müllen and H.-J. Gao, *Appl. Phys. Lett.*, 2014, **105**, 23101.

14 T. H. Vo, M. Shekhirev, D. A. Kunkel, F. Orange, M. J.-F. Guinel, A. Enders and A.

Sinitskii, *Chem. Commun.*, 2014, **50**, 4172–4174.

15 J. M. Aslan, M. Yousufuddin, D. J. Boston and F. M. MacDonnell, *Inorg. Chim. Acta*, 2017, **454**, 216–221.

16 S. Singh, N. R. de Tacconi, N. R. G. Diaz, R. O. Lezna, J. Muñoz Zuñiga, K. Abayan and F. M. MacDonnell, *Inorg. Chem.*, 2011, **50**, 9318–9328.

17 Y. Chen, W. Lei, G. Jiang, Q. Zhou, Y. Hou, C. Li, B. Zhang and X. Wang, *Dalt. Trans.*, 2013, **42**, 5924–5931.

18 S. Kaufhold, D. Imanbaew, C. Riehn and S. Rau, *Sustain. Energy Fuels*, 2017, **1**, 2066–2070.

19 S. P. Foxon, C. Green, M. G. Walker, A. Wragg, H. Adams, J. A. Weinstein, S. C. Parker, A. J. H. M. Meijer and J. A. Thomas, *Inorg. Chem.*, 2012, **51**, 463–471.

20 A. Fihri, V. Artero, M. Razavet, C. Baffert, W. Leibl and M. Fontecave, *Angew. Chemie Int. Ed.*, 2008, **47**, 564–567.

21 A. Fihri, V. Artero, A. Pereira and M. Fontecave, *Dalt. Trans.*, 2008, **0**, 5567–5569.

22 H. Song, J. T. Kaiser and J. K. Barton, *Nat. Chem.*, 2012, **4**, 615.

23 M. Li, P. Lincoln and J. Andersson, *J. Phys. Chem. B*, 2011, **115**, 7923–7931.

24 J. Cai, P. Ruffieux, R. Jaafar, M. Bieri, T. Braun, S. Blankenburg, M. Muoth, A. P. Seitsonen, M. Saleh, X. Feng, K. Müllen and R. Fasel, *Nature*, 2010, **466**, 470.

25 S. M. Loh, Y.-H. Huang, K.-M. Lin, W. S. Su, B. R. Wu and T. C. Leung, *Phys. Rev. B*, 2014, **90**, 35450.

26 H. Zhang, J. Zhao and Q. Cai, *Phys. Chem. Chem. Phys.*, 2016, **18**, 5040–5047.

27 G. Méhes, H. Nomura, Q. Zhang, T. Nakagawa and C. Adachi, *Angew. Chemie Int. Ed.*, 2012, **51**, 11311–11315.

28 J. Zhang, F. Zhao, X. Zhu, W.-K. Wong, D. Ma and W.-Y. Wong, *J. Mater. Chem.*, 2012, **22**, 16448–16457.

29 J. Lee, H.-F. Chen, T. Batagoda, C. Coburn, P. I. Djurovich, M. E. Thompson and S. R. Forrest, *Nat Mater*, 2016, **15**, 92–98.

30 C. Sealy, *Mater. Today*, 2008, **11**, 65–68.

Chapter 1

Extended 1,10-Phenanthroline PAH-type Systems as Novel Ligand Architectures

Part 1 of 2

1.1.2 General Introduction

There is a lack of partially-fused PAH-type ligands in the literature which offers an opportunity to rapidly expand this field in an exploration of ligands and complexes of this type through novel synthetic preparations. A goal of this study is to then determine if those partially-fused systems may be used in the place of fully-fused ligand systems, without loss of photostability, or other desirable photophysical properties. Fundamental studies carried out by Draper *et al.* with fused nitrogen-heterosuperbenzenes[1] (NHSB) molecules formed the foundation of this work, and as such, only nitrogen-substituted PAH molecules capable of bidentate ligand functionality were designed and synthesised for this work. As the field of PAH-type ligands lacks significant numbers of partially-fused structures compared to fully-fused systems, discussion of both will be necessary. This chapter will deal exclusively with ligand structures, with the following chapter dealing with transition metal centres of the same ligands. As such, this introduction will feature ligand structures of a similar kind to the proposed compounds synthesised in this chapter, and will detail their syntheses. The next chapter will detail the optoelectronic properties of those complexes synthesised, and those in the literature. For that reason, the following may be considered as only half of this work's introduction.

1.1.1 Synthetic Methods

Compounds generated as part of this chapter are almost exclusively generated through a tandem Knoevenagel condensation reaction, and [4+2] Diels Alder cycloaddition reaction. Both reactions are foundation reactions in the generation of polyphenylene and polycyclic aromatic hydrocarbon (PAH) systems in the literature. Both reactions are now briefly discussed, through use the simplified synthesis of hexaphenylbenzene **L5**.

1.1.1.1 Knoevenagel Condensation

Described by Emil Knoevenagel in the late 19th century, the Knoevenagel condensation reaction is a modified Aldol condensation resulting in C-C bond formation. Through use of a basic catalyst, an initial deprotonation of a weak C-H bond leads to the nucleophilic attack to another carbonyl compound, often followed by a spontaneous dehydration, generating the desired unsaturated C-C bond. Scheme 1.1 demonstrates the formation of 2,3,4,5-tetraphenylcyclopenta-2,4-dien-1-one, tetracyclone **L3**, from 1,3-diphenylpropan-2-one **L1**, and benzil **L2**.

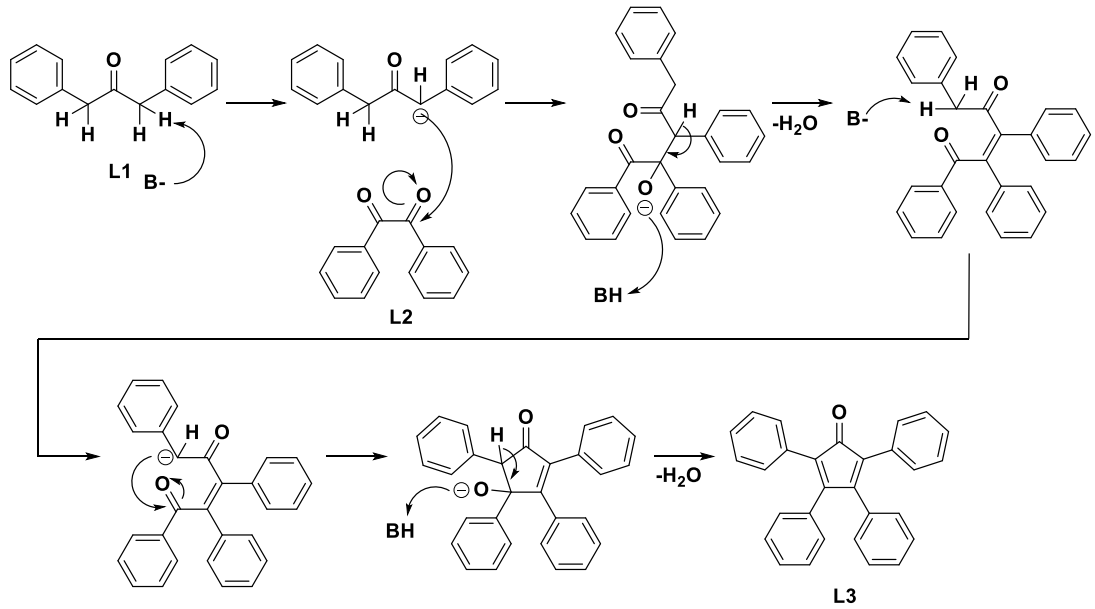

Scheme 1. 1 Simplified synthetic scheme showing the double Knoevenagel condensation reactions towards the synthesis of **L3**. B = base.

1.1.1.2 Diels Alder [4+2] Cycloaddition

The Diels Alder reaction is a [4+2] pericyclic cycloaddition between a conjugated diene molecule, and a dienophile molecule. The electrocyclic reaction is typically carried out with a four-electron diene, and a two-electron dienophile, with the driving force of the reaction being the formation of two new C-C bonds. The newly generated cyclic structure may be aromatic, or partially unsaturated. Hetero-Diels Alder reactions are also possible, where either the diene or dienophile is substituted with the respective heteroatom.[2]

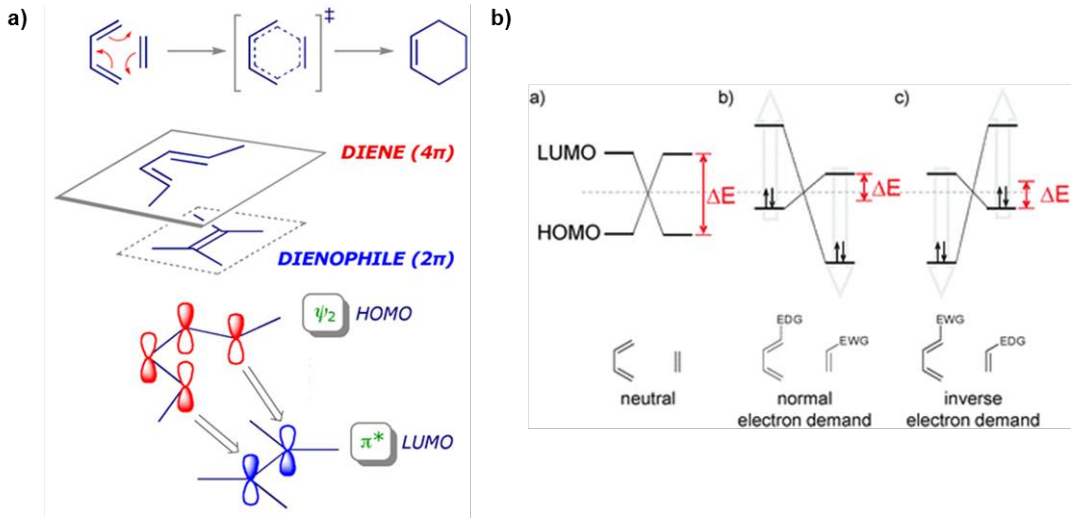

Figure 1. 1 (a) Schematic showing orbital interactions between the diene and dienophile, through generating of a cyclic transition state. The suprafacial nature of the reaction is also shown. (b) Schematic showing the Neutral, Normal, and Inverse Diels Alder reactions. The differences in ΔE are shown, along with simplified HOMO-LUMO arrangements typical in both forms of the reaction.[3]

Three forms of the Diels Alder reaction are possible; Neutral, Normal Demand, and Inverse Demand. The normal demand Diels Alder, features reaction between an electron deficient diene, and an electron rich dienophile. The inverse demand Diels Alder, features reaction between an electron rich diene, and an electron deficient dienophile. Synthetic control over the electron density of the reactive species is enabled through careful substitution of electron withdrawing or donating groups. The neutral Diels Alder reaction does not typically feature electron donating or withdrawing groups. Figure 1.1 shows simplified visual representations of the three forms of Diels Alder reactions. For the purposes of this chapter, only normal demand Diels Alder reactions will be considered.

As mentioned earlier, the construction of polyphenylene or PAH compounds are often *via* a tandem Knoevenagel-Diels Alder reaction, and further to the synthesis of **L3** in Scheme 1.2, the Diels Alder step towards **L5** is through a neutral Diels Alder reaction with diphenylacetylene **L4** as the reaction dienophile.

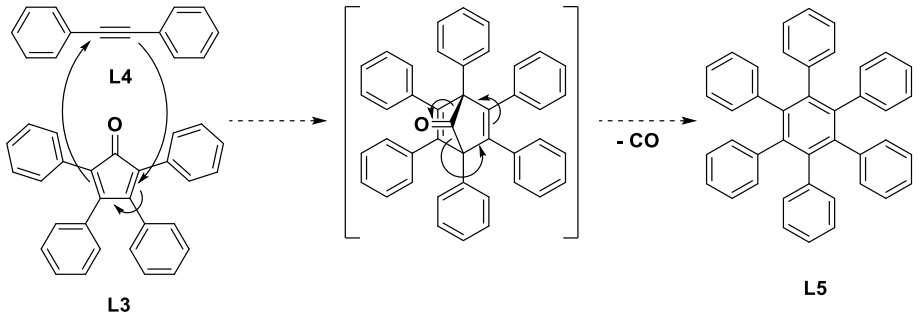

Scheme 1. 2 Simplified synthetic scheme showing the neutral Diels Alder reaction towards the synthesis of **L5**.

1.1.3 1,10-Phenanthroline-type Ligand Structures

The simplest method of generating PAH-type ligand structures, both fully- and partially-fused, is through synthetic modification of a core 1,10-phenanthroline ring system. Chart 1.1 shows ligands comprising a 1,10-phenanthroline core unit.

L6, is an extended phenanthroline system constituting a fused oxazole ring. Here, the compound features a fused phenanthroline system, with an unfused pyridine ring capable of secondary metal complexation. First synthesised by Mayer *et al.*,[4] **L6** was originally synthesised *via* an "on-the-complex" method with a Ru(II)-coordinated 1,10-phenanthroline-5,6-dione ligand, and isonicotinaldehyde. A decade later, Li *et al.* synthesised the free ligand without metal complexation.[5] Both syntheses undoubtedly follow an initial generation of a 2-acylamino-ketone, before undergoing an acid catalysed Robinson–Gabriel synthesis, to form the desired oxazole ring. **L7**, is a fully-fused PAH type molecule. It is synthesised through a potassium assisted cyclodehydrogenation of 1,1'-biisoquinoline.[6] This form of cyclodehydrogenation is commonly used in systems with nitrogen substitution, as the potassium metal cannot coordinate to the iminic nitrogens of the newly generated ring system. **L8**, also known as eilatin, was first isolated from a marine tunicate by Rudi *et al.*,[7] but has since been synthesised *via* a multi-step route.[8]

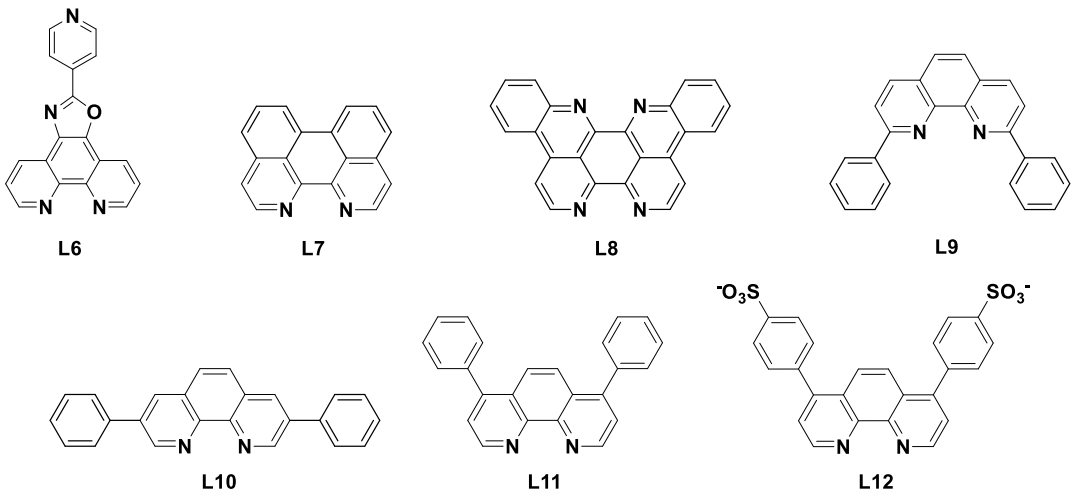

Chart 1. 1 Ligands derived from extended or substituted 1,10-phenanthroline.

L9, **L10**, and **L11** in Chart 1.1 are isomers differing in the positions of their phenyl substituents. 2,9-diphenyl-1,10-phenanthroline **L9** shows phenyl substitution at the 2- and 9 positions,[9] 3,8-diphenyl-1,10-phenanthroline **L10** at the 3- and 8- positions,[10] and 4,7-diphenyl-1,10-phenanthroline **L11** at the 4- and 7-positions.[11] Selective synthetic access to these positions follow common literature procedures and will not be discussed further. Notably however is **L11**, as it is utilised as a ligand far more often than its counterparts. The ligand **L12** features two sulfonates on the free phenyls, which upon metal complexation facilitate water soluble applications.[12]

1.1.4 Ligand Structures *via* Schiff Base Condensation Reactions

1.1.4.1 1,10-Phenanthroline-Pyrazine Ligand Structures

Some of the most common fully-fused PAH-type ligands are those of the 1,10-phenanthroline-pyrazine hybrids. In nearly all cases, use of 1,10-phenanthroline-5,6-dione facilitates an acid or base catalysed Schiff base condensation reaction with a respective ortho di-amine.

Chart 1.2 shows representations of this type of ligand. The smallest is **L13**. It formed by reaction of ethane-1,2-diamine with 1,10-phenanthroline-5,6-dione.[13] Addition of a further two benzene ring forms **L14**.[14] **L15**,[15] features a second phenanthroline ring system, generating the popular bridging ligand, tpphz. **L16**,[16] may be considered a "dimer" of **L13**. Breaking the linear structure of the other ligands, **L17**,[17] features the phenanthroline ring systems at a 120° angle to the core benzene ring. These ligands are synthesised by following

the Schiff base reaction mechanism. The primary uses for these compounds are either DNA intercalation studies,[18] or photoinitiated electron collection.[19]

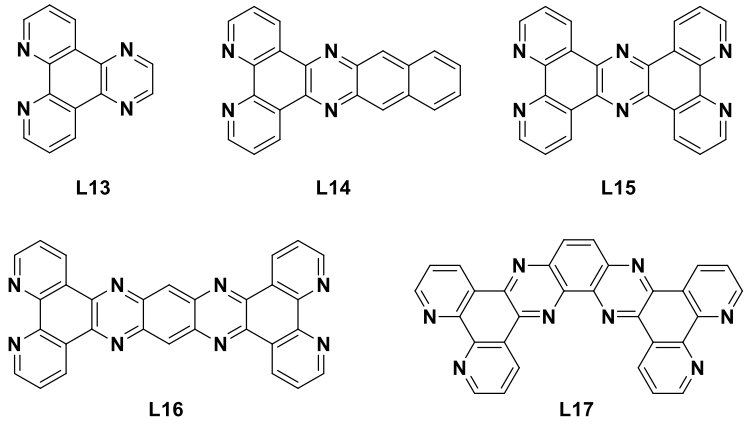

Chart 1. 2 1,10-phenanthroline-pyrazine hybrid ligands.

1.1.4.2 1,10-Phenanthroline-Pyrazine-Quinone Ligand Structures

The incorporation of quinone moieties into the PAH structure of phenanthroline-pyrazine hybrids significantly changes their photophysical and electrochemical properties.

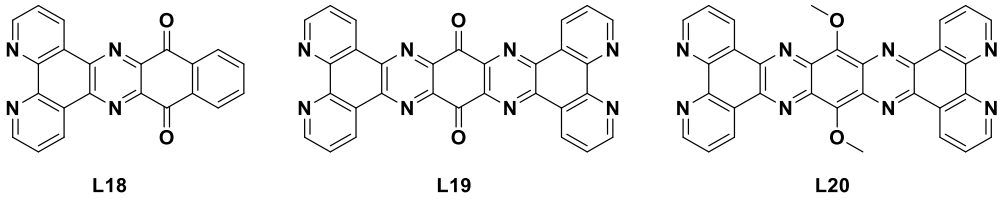

Chart 1. 3 1,10-phenanthroline-pyrazine hybrid ligands incorporating quinone or "trapped quinone" moieties.

Chart 1.3 visualises the most common "naphthalene-quinone" hybrid structures. The simplest system is **L18**. **L19** features a single quinone moiety within the bis-phenanthroline ligand structure. Reaction at the quinone moiety is also possible, through generation of either the semi-quinone or hydroquinone structures. The di-methoxy structure **L20** requires a tandem demethoxylation and oxidation reaction to regenerate the quinone structure.

L18 is synthesised in a similar method to the phenanthroline-pyrazine hybrids discussed earlier, through the Schiff base reaction of 1,10-phenanthroline-5,6-dione and the ortho di-amine product 2,3-diaminonaphthalene-1,4-dione.[20] **L19** follows a similar preparation,

between two equivalents of a coordinated 1,10-phenanthroline-5,6-dione ligand and the tetra-amine benzene-1,2,4,5-tetraamine.[21] The synthesis of **L20** is achieved once again through the use of 1,10-phenanthroline-5,6-dione, *via* a multi-step reaction with N,N'-(4,5-diamino-3,6-dimethoxy-1,2-phenylene)bis(4-methylbenzenesulfonamide).[22]

It is noted that there appears to be no partially-fused phenanthroline-pyrazine ligands, or phenanthroline-pyrazine-quinone ligand structures in the literature.

1.1.5 Ligand Structures *via* Diels-Alder Cycloaddition Reactions

1.1.5.1 Nitrogen-Heterosuperbenzenes (NHSBs)

Chart 1.4 shows the range of compounds known as the Nitrogen-Heterosuperbenzenes, synthesised by Draper *et al.*[1] They are synthesised *via* a Diels-Alder [4+2] cycloaddition reaction, with the two pyrimidine rings forming the acetylene-type dienophile. Substitution of the larger polyphenylene or PAH system is made by modifying the cyclopentadienone system.

Chart 1.4 shows NHSB molecules with differing degrees of aromaticity. Many variants of exist in the literature, with Chart 1.4 demonstrating only some of the more common moieties. **L21** bears tetra-tert-butyl substitution at the para-positions of free phenyl rings, and was one of the first of these systems to be successfully synthesised.[1] **L-22** replaces two of the tert-butyl groups with methoxy moieties.[23] Synthesis of all structures presented are initially achieved through high temperature Diels-Alder reactions using benzophenone melts in electrically heated sand baths, similar to the synthetic preparation of the all-carbon analogues.

The partially-fused systems are successfully generated through either by undertaking the cyclodehydrogenation step under deliberately controlled conditions *via* the method of Delaney *et al.* using Br_2 in toluene,[24] or through the incomplete bond fusion by conventional cyclodehydrogenation methods including $FeCl_3$.[25] **L23**, was synthesised using Br_2 in toluene, while **L24**, was synthesised using $FeCl_3$ as the Lewis acid catalyst and oxidant. The fully-fused bromo or tert-butyl systems are typically synthetically generated *via* the $FeCl_3$ method discussed earlier. Tris-substituted methoxy ring systems can also be fully fused through the $FeCl_3$ method, with two systems **L25** and **L26**, generated by Wijesinghe *et al.*[26]

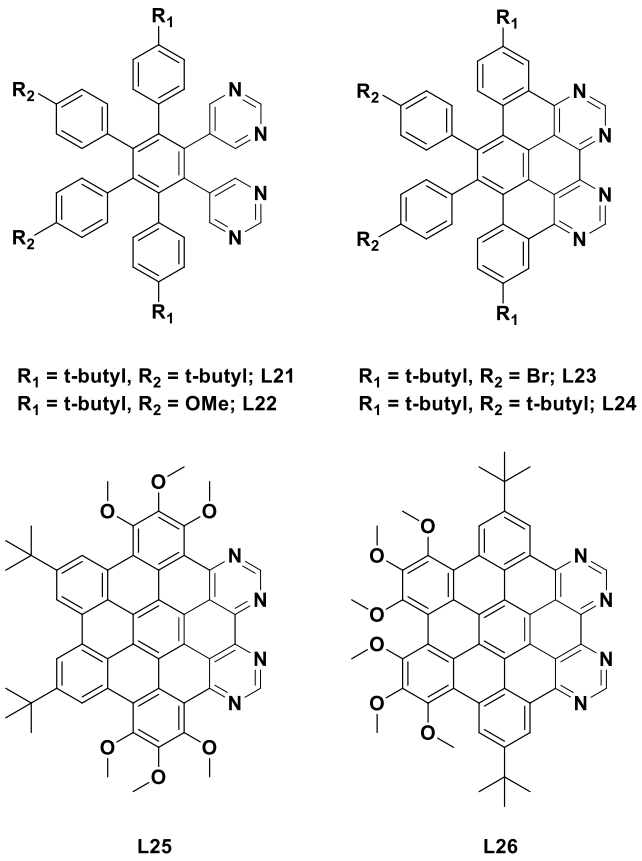

Chart 1. 4 Non-, partially-, and fully-fused Nitrogen-Heterosuperbenzene (NHSB) ligands.

1.1.5.2 Bipyridine and Terpyridine PAH-type Ligands

Further to the generation of the NHSBs, other PAH-type ligands have been synthesised featuring bidentate bipyridine functionality, or tridentate terpyridine functionality.

These systems are similar to the NHSB compounds, as (a) their syntheses typically generate unfused systems for initial study, and (b) they offer potential for further study through full or partial bond fusion. Chart 1.5 shows compounds of these kinds, incorporating the bi- or ter-pyridine functionality at the periphery of the compound, or within the PAH structure. **L27**, features a bipyridine ring system on the periphery of a tert-butyl substituted polyphenylene system, suitable for complexation to a range of metal centres. Designed and synthesised by Nolan *et al.*, the effect of the sterically encumbered nature of the ligand was investigated.[27] Use of a terminal acetylene on the bipyridine ring system generated a useful dienophile for reaction with the tetra-tert-butyl substituted cyclopentadienone, in a similar reaction procedure to the NHSBs discussed earlier.

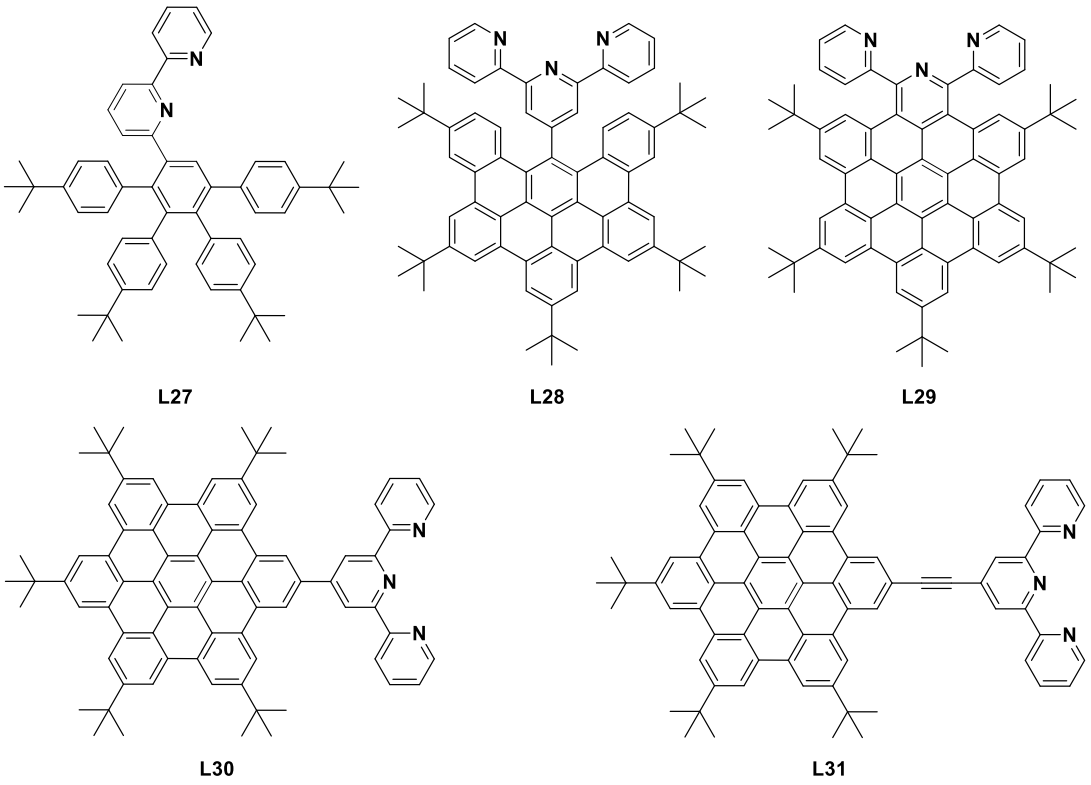

Chart 1. 5 Non, partially- and fully-fused bipyridine and terpyridine ligands.

Further to the bipyridine structure **L27**, several terpyridine structures are also reported. **L28**, featuring a large PAH-core, but without complete bond fusion around the terpyridine ring system was synthesised by Graczyk *et al.*[28] A second system, featuring bond closure to the middle pyridine ring of the terpyridine ring system **L29**, was also reported by the same authors.[28] In a similar preparation to the NHSBs discussed, synthetic access to these systems is through a tandem Diels-Alder cycloaddition, and $FeCl_3$ mediated cyclodehydrogenation reaction.

Two further systems **L30**, featuring the terpyridine ring system covalently appended to a hexaphenylbenzene system, and the terpyridine π-spacer compound **L31**, are shown in Chart 1.5. Both systems are the result of work by Murphy *et al.*,[29] and are once again synthesised through a tandem Diels-Alder cycloaddition, and $FeCl_3$ mediated cyclodehydrogenation reaction.

1.1.6 Ligand Structures *via* Further Synthetic Preparations

1.1.6.1 Pyridazine-substituted PAH Compounds & Ligands

Another method aimed generating PAH-type ligands is through inverse Diels-Alder cycloadditions with substituted tetrazines.

Chart 1.6 gives some examples of phenyl- and pyridine-substituted pyridazines derived from their respective tetrazines. Compared to the other examples of fully-and partially-fused PAH-type ligands, this is not a true representation of the quantity of pyridazine compounds in the literature, and these structures are simply chosen to discuss their synthesis and coordination functionality.

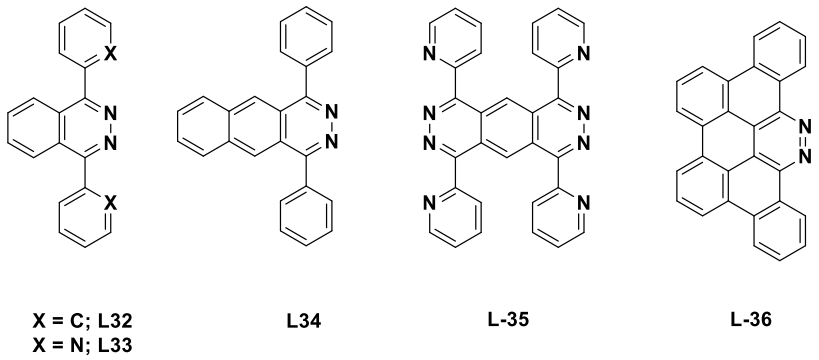

Chart 1. 6 Pyridazine-substituted PAH compounds and ligands.

1,4-diphenylphthalazine,[30] **L32**, 1,4-diphenylbenzo[g]phthalazine,[31] **L34**, 1,4-di(pyridin-2-yl)phthalazine,[32] **L33**, and 1,4,6,9-tetra(pyridin-2-yl)pyridazino[4,5-g]phthalazine,[33] **L35**, are generated *via* one of two methods. The first is through the generation of a highly reactive aryne system as the dienophile for reaction with the respective tetrazine. This is a common method for the generation of smaller phenyl- or pyridine-substituted pyridazine compounds. The second method is a double Schiff-base condensation between an equivalent amount of hydrazine hydrate and the necessary 1,4-diketone. The double condensation forms the pyridazine ring, further to the loss of two water molecules.

Benzo[h]benzo[5,6]tetraceno[11,12,1-cdef]cinnoline, **L36**, is a fully-fused PAH type molecule first synthesised by Tokita *et al.* in 1982.[34] Here, the pyridazine ring is generated through the reaction of a perylene-type compound with a highly reactive cyclic hydrazide, followed by an oxidation step to rearomatise the system.

1.1.7 Phenanthroline-Cyclone (PhenBlue)

It is apparent that there exists a limited number of synthetic methods towards PAH-type ligands, both of a fully- and partially-fused kind. The literature is dominated by Schiff base condensations, and normal and inverse Diels-Alder cycloadditions. As a result, the field has

made only limited progress towards a diverse library of compounds suitable for metal complexation and further study.

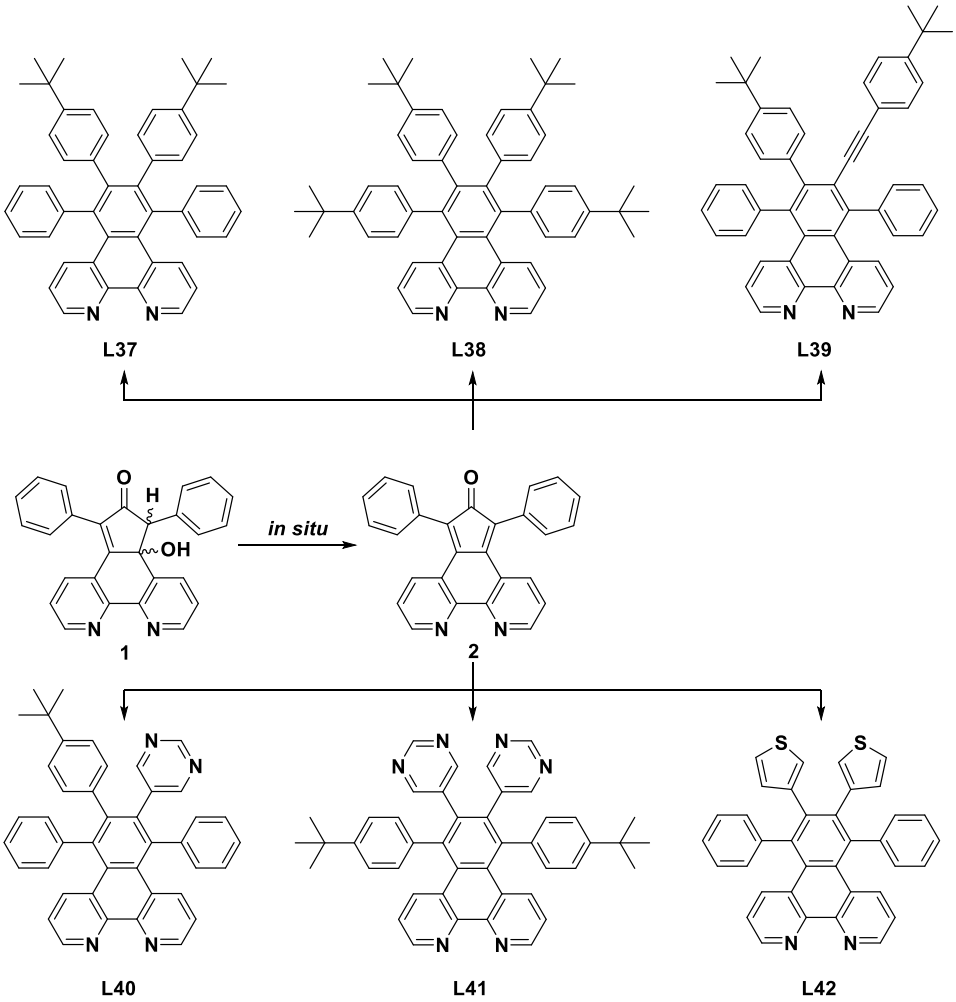

Scheme 1. 3 High temperature Diels-Alder cycloaddition route to extended 1,10-phenathroline ligands from the single hydroxyl compound **1**.

The aim therefore of this chapter is to attempt to begin the realisation of this diverse library of compounds, through the generation of a new route to 1,10-phenanthroline containing PAH-type ligands. To reduce the number of synthetic steps towards commercial applications, the work is paired with an investigation towards the use of partially-fused systems, thus not requiring the final cyclodehydrogenation step. The cyclodehydrogenation step was also not considered as increasing ring fusion correlates strongly to loss of solubility. Methods to overcome this solubility problem include the addition of alkyl chain or tertiary butyl groups to the para-position of the phenyl rings. However, the addition of these moieties results in a change to the optoelectronic properties of the total system. As this work is an initial study, a limited number of parameters were therefore considered. To achieve this goal, new synthetic

procedures and precursors are undoubtedly necessary. However, to overlook common literature preparations, including those detailed above would be short-sighted. As such, this volume of work will build on systems developed by the Draper research group from the last decade, *e.g.* the development of a phenanthroline-cyclone system, 5,7-diphenyl-6H-cyclopenta[f][1,10]phenanthrolin-6-one, **2**, consisting of the phenanthroline core ring system, and a cyclopentadienone moiety for further ligand growth. The naming of **2** as "PhenBlue" is in reference to the deep opaque blue colour of the cyclopentadienone ring in the structure. As these cyclopentadienone structures are more commonly deep purple or green, the influence of the nitrogen atoms on the optical properties of the cyclopentadienone structure is obvious to the naked eye.

2 is generated from the single hydroxyl product **1**. The product is generated *in situ* in high temperature reaction conditions (> 280 °C), and can be utilised as a diene for Diels-Alder cycloadditions reactions with acetylene-type dienophiles. The mechanism behind this synthetic step in unknown. However, attempts with acidic, basic, and neutral alumina generate considerably different results. Both acidic and basic alumina yield no appreciable yield of **2**, with only the neutral alumina capable of generating the desired product. This hints that the dehydration step is a surface-assisted process *versus* that of chemically-induced process. Scheme 1.3 demonstrates six compounds (unpublished) that have been successfully generated using this high temperature method in a benzophenone melt. However, due to the high reaction temperatures, the respective dienophile is limited to those with a high boiling point, or those resistant to thermal decomposition.

Due to this problem, this chapter concentrates on the attempt to circumvent the high temperature conditions currently necessary for the generation of **2**, and towards the generation of novel systems capable of generating partially-fused PAH-ligands by other synthetic means.

1.2 Attempted Development of "Phenaryne", 6

1.2.1 Retrosyntheses & Synthetic Challenges

High temperature routes to 5,7-diphenyl-6H-cyclopenta[f][1,10]phenanthrolin-6-one **2** currently exist from previous work by members of the Draper research group. However, due to these necessary high temperatures, diversification to partially-fused PAH-type ligands that require low boiling point, or temperature sensitive starting materials is difficult.

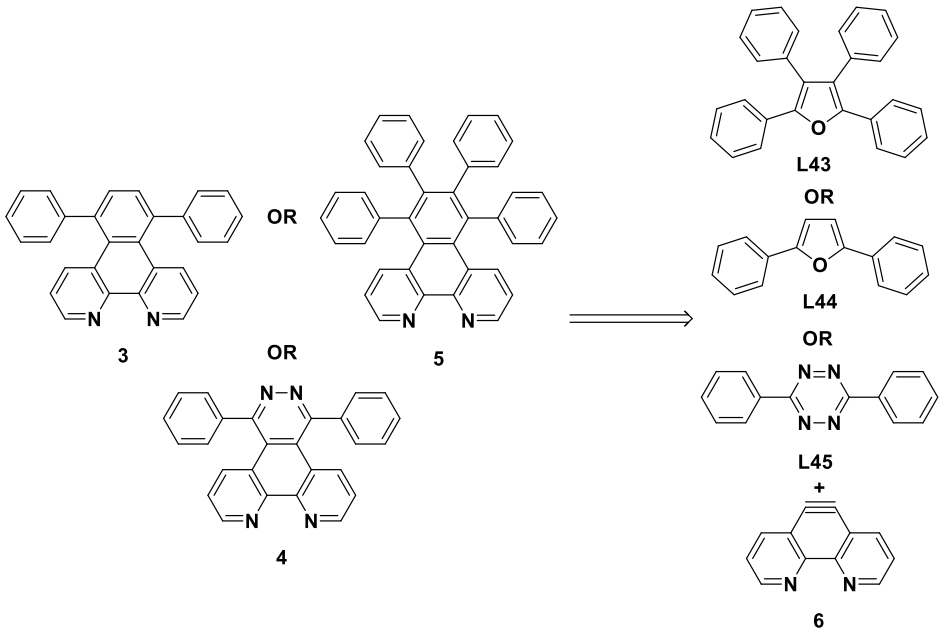

Scheme 1. 4 Retrosynthetic analysis towards extended 1,10-phenanthroline ligands *via* "phenaryne", **6**.

Scheme 1.4 demonstrates a retrosynthetic analysis of some potential candidates for this initial work. The middle ring of the PAH-type ligand can either be that of a single benzene ring **3**, a tetra-phenyl system **5**, or a pyridazine ring **4**. In Scheme 1.4, the retrosynthetic analysis attempts to generate these compounds using a 1,10-phenanthroline aryne system, **6**, with the aryne system at the 5- and 6-positions of the phenanthroline ring system. This reactive intermediate is not present in the literature, and was considered a strikingly simple target molecule to achieve the desired result. It is noted that the aryne system **6** may undergo a self [2+2] cycloaddition with a further molecule of **6**, potentially generating an interesting bridging ligand featuring an anti-aromatic core system. As shown, **3** and **5** are expected to be generated through a Diels-Alder reaction with either the commercially available 2,5-diphenylfuran **L43**, or 2,3,4,5-tetraphenylfuran **L44** respectively. The pyridazine system **4** is expected to be generated through an inverse Diels-Alder reaction with 3,6-diphenyl-1,2,4,5-tetrazine, **L45**. As these reagents are either commercially available or have literature-based synthetic preparations, the challenge of this work was therefore to generate the aryne precursor, which could be activated *in situ* generating the reactive aryne species.

Whilst the literature does not contain any synthetic preparations towards 1,10-phenanthroline aryne systems of this kind, generation of a similar aryne system in its all-carbon analogue phenanthrene have been carried out by many research groups. In addition to this, many synthetic strategies exist for simpler "benzyne" intermediates. A significant number of these reactions use either furan, or 2,3,4,5-tetraphenylcyclopenta-2,4-dien-1-one (hereafter referred

to as tetracyclone), as the reaction diene. As the phenanthroline aryne species **6** is expected to be highly reactive and not have a significant lifetime at room temperature, confirmation of the generation of this species would be through the successful formation of the Diels-Alder adduct. For this reason, both furan and tetracyclone were used as dienes. Similar synthetic procedures to the generation of the phenanthrene aryne species were used in attempting to generate **6**.

1.2.1.1 Attempted Synthesis of 6

Some general comments on the attempted syntheses of a number of aryne precursors from commercially available 1,10-phenanthroline are now discussed, and are shown *via* use of a retrosynthetic analysis in Scheme 1.5.

The first attempts to obtain **6** used 5-bromo-1,10-phenanthroline **7**,[35] and its treatment using several strong hydroxide or alkoxide bases. NaOH, KOH, nor potassium tert-butoxide generated the aryne species **6** on analysis of the reaction work up. Due to the low yields obtained of **7**, and safety concerns over the use of fuming nitric acid, this route was discontinued. Fortuitously however, the attempted preparations of **7** generated a significant quantity of 5,6-dibromo-1,10-phenanthroline **10**[35] the next suitable system for the generation of **6**. Dibrominated aromatics of this kind are typically converted to their aryne counterparts through the use of n-or t-butyl lithium, Rieke magnesium, or suitable small and commercially available Grignard organometallics. These methods were attempted with **10** in a range of temperatures, but no reaction between **6** and either the respective furan or tetracyclone dienes were observed. Attempts to generate 6-bromo-1,10-phenanthrolin-5-yl trifluoromethanesulfonate **9** were also unsuccessful. These attempts did not pass further than the formation of an epoxide at the 5- and 6-positons of phenanthroline (1a,9b-dihydrooxireno[2,3-f][1,10]phenanthroline),[36] as the epoxide ring opened product is extremely insoluble. This difficulty is noted by some authors in the literature.[37] The final series of attempts to generate **6** were undertaken *via* the formation of 1H-[1,2,3]triazolo[4,5-f][1,10]phenanthrolin-1-amine, **8**. This system, capable of aryne formation through reaction with $Pb(OAc)_2$, did not proceed past the suspected formation of the triazole ring, due to its insolubility. Despite a significant amount time and synthetic effort, the culmination of these attempts ultimately demonstrated that access to a 1,10-phenanthroline aryne system may not be realised due to the insolubility of its intermediate compounds. Some routes, including those that use a $NaNH_2$ base may prove successful in the future. However, as all the attempted syntheses proved unsuccessful, this route to a partially-fused PAH-type ligand was abandoned.

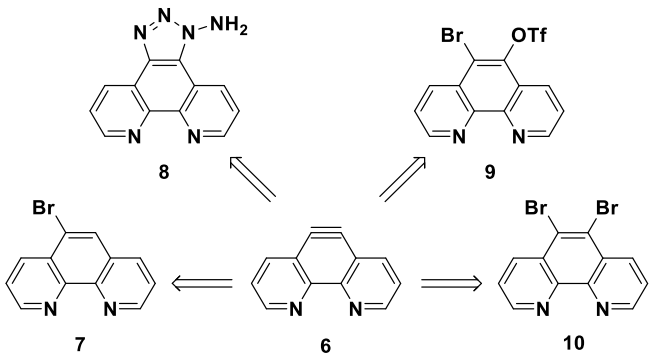

Scheme 1. 5 Retrosynthetic analysis towards the generation of "phenaryne", **6**.

1.3 Synthetic Access to 2 at Low Temperatures

1.3.1 Optimised Generation of 1

If the development of a 1,10-phenanthroline aryne system **6** could not be realised, the next logical step was to explore the possibility of generating the cyclopentadienone ring system at much lower temperatures.

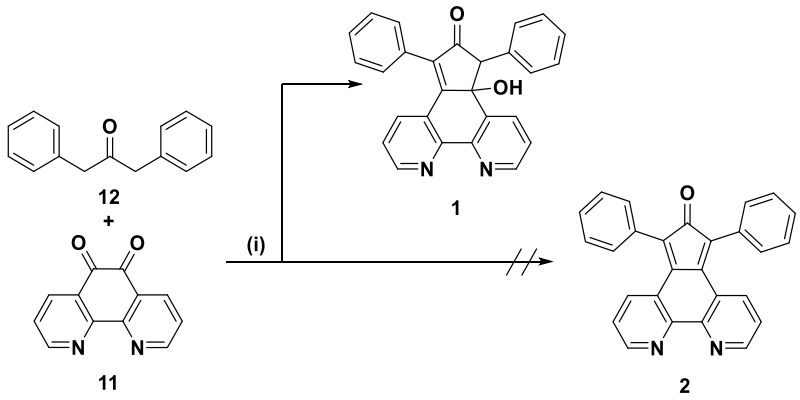

Scheme 1. 6 Attempted synthesis of **2**, with subsequent generation of **1**. (i) MeOH, piperidine, RT, 16 h, 78 %.

In Scheme 1.6, an optimised synthesis of the single-hydroxyl product **1** is shown. The failure to generate **2** is similar to observations of Warrener *et al.*,[38] using pentan-3-one as the reaction monoketone.

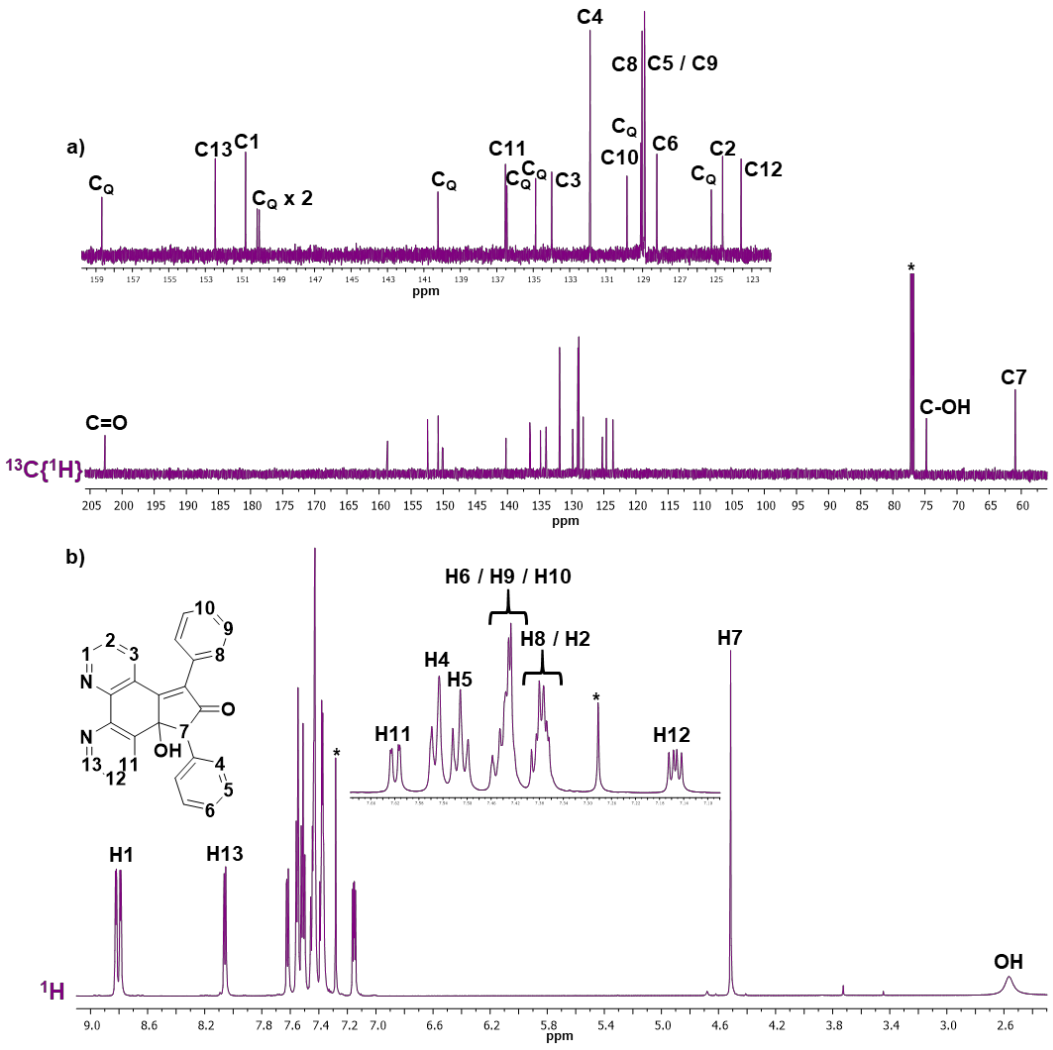

Figure 1. 2 a) $^{13}C\{^{1}H\}$ NMR (zoomed region as inset), and b) ^{1}H (zoomed region as inset) spectra of **1**. ($CDCl_3$. 600 MHz for ^{1}H, 150 MHz for $^{13}C\{^{1}H\}$. RT). C_Q = quaternary carbon.

Although **2** is analogous to the all-carbon 1,3-diphenyl-2H-cyclopenta[l]phenanthren-2-one, which is generated in 15 minutes through the addition of KOH to a MeOH solution at reflux,[39] increased temperatures did not appear to facilitate the generation of **1** or **2**. Increasing the reaction time only increased the formation of side products, and as such, future attempts were carried out at room temperature. Members of the Draper research group completed the synthesis of the single-hydroxyl product **1** through use of 1,10-phenanthroline-5,6-dione, **11**, and 1,3-diphenyl-2-propanone, **12**, in a KOH-catalysed Knoevenagel condensation in EtOH. However, the yields of this reaction varied considerably. The ^{1}H and $^{13}C\{^{1}H\}$ NMR spectra of **1** are given in Figure 1.2. Due to the unsymmetrical nature of **1**, numerous 1D studies including selective TOCSY and NOESY experiments were conducted to elucidate the separate spin systems. The reaction yield of **1** depended on a number of factors. Heating the reaction mixture above that of ambient temperature appears to decrease the reaction yield,

while use of high volumes of reaction solvent affect the precipitation process used to collect the product **1**. Finally, substitution of the KOH base to the softer piperidine base gave more consistent yields. Further to these optimised conditions, attention now turned to the low temperature generation of the cyclopentadienone product **2**.

1.3.2 Low Temperature Generation of 2; Attempts & Challenges

The high temperature conditions of the benzophenone melt method generates the cyclopentadienone product **2** *in situ*. The reduction of this high temperature of this step is the focus of attention. Table 1.1 demonstrates work towards the generation of **2** at lower temperatures of < 200 °C.

Entries 1 and 2 attempted to generate **2** by forcing the reaction with KOH in either a MeOH or EtOH solvent. However, this did not work, and appeared to only destroy **1**. Entry 3 switched to the use of an acidic dehydrating agent in H_2SO_4. This also appeared to destroy **1**, hinting that the compound may not be as stable as expected. Entries 4 to 9 then attempted to generate **2** without the use of a dehydrating agent, choosing solvents of increasing boiling points. As the auto-dehydration of **2** must have already occurred for those high temperature Diels-Alder reactions at 280-300 °C, it was hoped this solvent screening attempt would reveal an approximate auto-dehydration temperature, but these attempts were unsuccessful. Entry 9, using the high temperature boiling point solvent glycerol, appeared to cause further reaction, but the reaction product(s) remain unidentified.

Some common synthetic preparations exist by which to generate cyclopentadienone rings from their single-hydroxyl products. These were systematically considered, with entries 10 and 11 demonstrating the use of a pyridine/$SOCl_2$ mixture. Here, the thionyl chloride replaces the hydroxyl group with a chloride. This is facilitated by the pyridine base, which can also force the generation of the cyclopentadienone ring through a basic attack at the tertiary carbon α to the newly-formed chloride. This reaction was attempted at room temperature, and at 0 °C, but were unsuccessful. Notably however, at 0 °C, an intense blue colour characteristic of **2** was seen immediately on the addition of pyridine. After a few minutes, the colour reverted to pale yellow. Efforts to characterise this transient blue product through NMR and high-resolution mass spectrometry (HRMS) proved unsuccessful. Further heating of this reaction mixture also generated a mixture of unidentified products. Another common preparation of cyclopentadienones is with an acetic anhydride/H_2SO_4 reagent mixture. Here, an acid assisted protection of the hydroxyl group occurs, forming the acetyl protecting group. Subsequent protonation of this acetyl protecting group results in an elimination step generating the desired alkene bond. From entries 12 and 13, it can be seen that this route was also found to be

unproductive. To ensure that insufficient thermal activation was not the cause of the persistent failure, entries 14 and 15 were undertaken with the organic acid 4-methylbenzenesulfonic acid in 1,2-dichlorobenzene at 180 °C. Entry 14 proved unsuccessful, but attempts with 2,3,4,6,7,8,9,10-octahydropyrimido[1,2-a]azepine (DBU) in Entry 15 showed some promise. Here, the use of the base serves to "mop up" any remaining acid that may prevent the reaction of **2** with a chosen dienophile. However, yields were low and unreliable.

At this point, rather than continuing with synthetic preparations to force the generation of the alkene bond, attention turned to the use of heterogeneous drying agents used in other laboratory syntheses. The first attempts were those using the powerful desiccant phosphorus pentoxide (Entries 16 and 17). Initial attempts with this drying agent in toluene and xylenes had some limited success, but the work up proved exceptionally difficult. On cooling, the product was seen to accumulate on the surface of the P_2O_5, and attempts to destroy the phosphorus pentoxide with water was sufficiently exothermic to destroy the product. Multiple attempts to remove the phosphorus pentoxide both in-solution, or after the removal of the reaction solvent proved unsatisfactory. Entries 18 to 23 detail unsuccessful attempts at generating **2** with common laboratory drying agents, but yielded no reaction. Of note, Entry 23 uses a pre-activated acidic silica generated from the literature preparation of Rasheed *et al.*[40] It was hoped that the high surface area of the silica, combined with its acidic properties might be helpful in promoting the formation of **2**. In a last series of attempts, heterogeneous alumina was considered worth trying. Activated basic or acidic technical grade alumina did not generate **2** in refluxing xylenes, but remarkably, switching to neural technical grade alumina in refluxing xylenes, gives **2** minutes on achieving the reflux temperature.

Table 1.1. Attempted low temperature syntheses towards **2**.

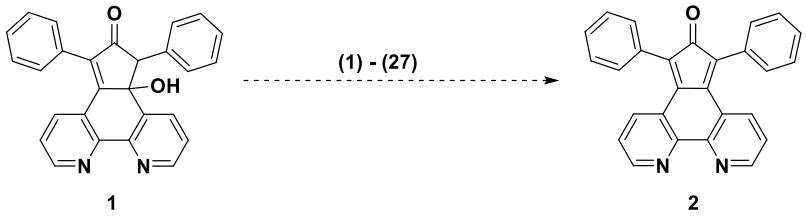

1 2

Entry	Solvent	Dehydrating Agent	Temp(°C)	Time(h)	1	2
1	MeOH	KOH	65	16	✕	✕
2	EtOH	KOH	78	16	✕	✕
3	EtOH	H_2SO_4	78	16	✕	✕
4	Toluene	---	110	16	✓	✕
5	Xylenes	---	140	16	✓	✕
6	1,2-dichlorobenzene	---	180	16	✓	✕
7	Glycerol	---	200	16	✓	✕
8	Glycerol	---	250	16	✕	✕
9	Diphenyl Ether	---	258	16	✕	✕
10	Pyridine	$SOCl_2$	20	2	✕	✕
11	Pyridine	$SOCl_2$	0	2	✕	✕
12	Ac_2O	H_2SO_4	20	2	✕	✕
13	Ac_2O	H_2SO_4	0	2	✕	✕
14	1,2-dichlorobenzene	p-TSA	180	16	✕	✕
15	1,2-dichlorobenzene	p-TSA/TEA	180	16	✕	✓[a]
16	Toluene	P_2O_5	140	16	✕	✓[a]
17	Xylenes	P_2O_5	110	16	✕	✓[a]
18	Toluene	$MgSO_4$	110	16	✓	✕
19	1,2-dichlorobenzene	$MgSO_4$	180	16	✓	✕
20	Toluene	Molecular Sieves; 4A	110	16	✓	✕
21	1,2-dichlorobenzene	Molecular Sieves; 4A	180	16	✓	✕
22	Xylenes	Silica[41]	140	16	✓	✕
23	Xylenes	Silica; Acidic[40]	140	16	✕	✕
24	Xylenes	Al_2O_3; Basic	140	16	✓	✕
25	Xylenes	Al_2O_3; Acidic	140	16	✓	✕
26	**Xylenes**	**Al_2O_3; Neutral**	**140**	**16**	✕	✓
27	**Chlorobenzene**	**Al_2O_3; Neutral**	**130**	**16**	✕	✓

[a] The entries did not give consistent results, or failed in repeated attempts.

On optimising the conditions using neutral alumina, it was clear that side products form when xylenes is used as the reaction solvent. These were difficult to remove by silica-based column chromatography. The slightly lower boiling point solvent chlorobenzene seemed to overcome these problems, and under strict anhydrous and anaerobic conditions, the optimal generation of **2** is seen over 3-4 hours. Shorter reaction times give rise to the intense blue colour of **2**, but lower overall yields due to the presence of the single hydroxyl starting material **1** which requires further time to undergo full dehydration. It was found that the addition of the dienophile to **2** can be added with the alumina still in the reaction mixture, or if required, following the alumina being filtered off under an inert atmosphere. The filtrate remains available for subsequent reaction if used quickly at elevated temperatures. These conditions are presented in Scheme 1.7.

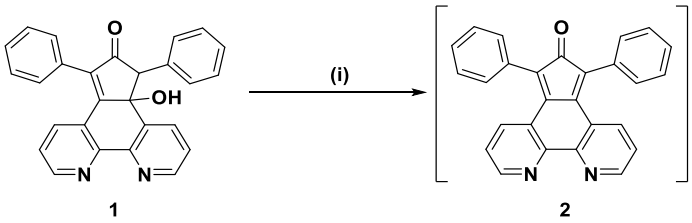

Scheme 1. 7 *In situ* synthesis of **2**. (i) Chlorobenzene, Al_2O_3, 4 h.

The cyclopentadienone product **2** is very sensitive to atmospheric conditions, reverting back to the single hydroxyl product **1** on contact with moisture. It appears only to exist in solution, and even when isolated under anhydrous and anaerobic conditions, reversion to **1** still occurs precluding spectroscopic analysis. The evaluation of the reaction yield is therefore only possible on reacting it further. On adopting microwave assisted methods, the preparation of **2** was found to be poorest in high dielectric polar solvents like MeOH and EtOH. Ultimately, a 1:9 mixture of CH_2Cl_2:THF was found to be the most successful solvent system for conversion of **1** to **2** when combined with the alumina dehydrating agent at 135 °C. The moderate dielectric constant of THF allows for the required temperature to be reached, while the small amount of CH_2Cl_2 aids in the solubility of **1**.

1.4 Synthetic Attempts, Results, & Discussion; Partially-fused PAH-type Ligands

1.4.1 Proposed Synthesis of Phenanthroline-core PAH-type Ligands

Following the successful generation of **2**, the five postulated novel ligands from Scheme 1.8 were proposed to allow for detailed preliminary studies of this kind of PAH-type ligand. The

reduction of two phenyl rings from the already synthesised 5,6,7,8-tetraphenylbenzo[f][1,10]phenanthroline**, 5**, to 5,8-diphenylbenzo[f][1,10]phenanthroline, **3**, would also allow the study of the effect of ring rotation on the optical and electrochemical properties of the systems in their own right, and as ligands in metal complexes.

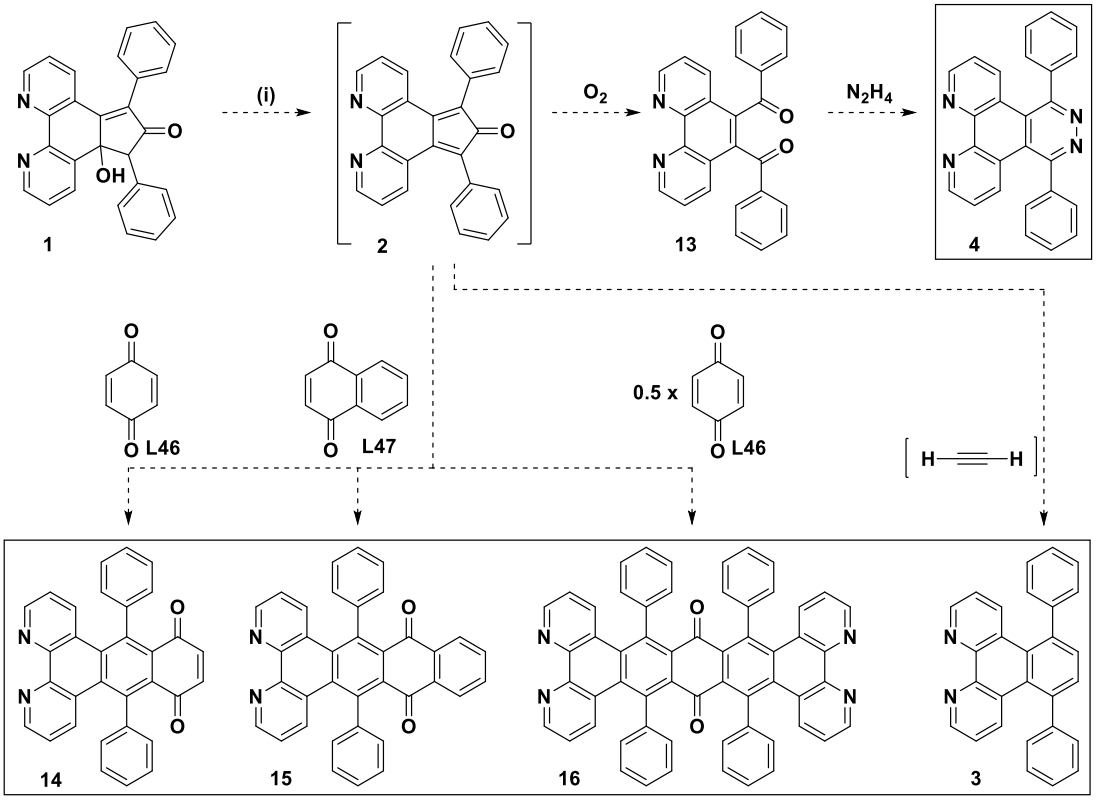

Scheme 1. 8 Proposed synthetic routes to the five extended 1,10-phenanthroline ligands.

Scheme 1.8 illustrates how the synthetic preparation of **14**, **15**, **16**, and **3** could be readily achieved through Diels-Alder reactions with their respective dienophiles. Whilst the pyridazine-containing system **4** could be generated through a ring opening reaction of **2** to **13**, and a subsequent ring closure with hydrazine hydrate. The safety implications of using ethyne at elevated temperatures meant this simplistic route to **3** was not undertaken. Therefore, to achieve the successful synthesis of **3**, the reaction with "acetylene-type" reagents had to be considered.

1.4.2 Synthesis of Phenyl-Coupled Quinone Phenanthroline-core PAH-type Ligands

1.4.2.1 Synthesis of 14

14 was first attempted under the optimised conditions discussed earlier. On generating cyclopentadienone **2**, benzoquinone **L46** was added *in situ*. Despite the lower reaction temperature (130 °C), it was still feared that the temperature might be a problem for **L46**, due to its known tendency to form both quinhydrone charge transfer complexes (1:1 complex with hydroquinone), and its melting point (115 °C). Given that **14** contains the quinone moiety in a terminal position, the reaction temperature of **2** and **L46** was brought to room temperature as quickly as possible. On cooling, a sample of the crude reaction mixture was analysed by HRMS, and found to contain a mixture of products consisting of **17**, **18**, and **14** (Scheme 1.9; Table 1.2).

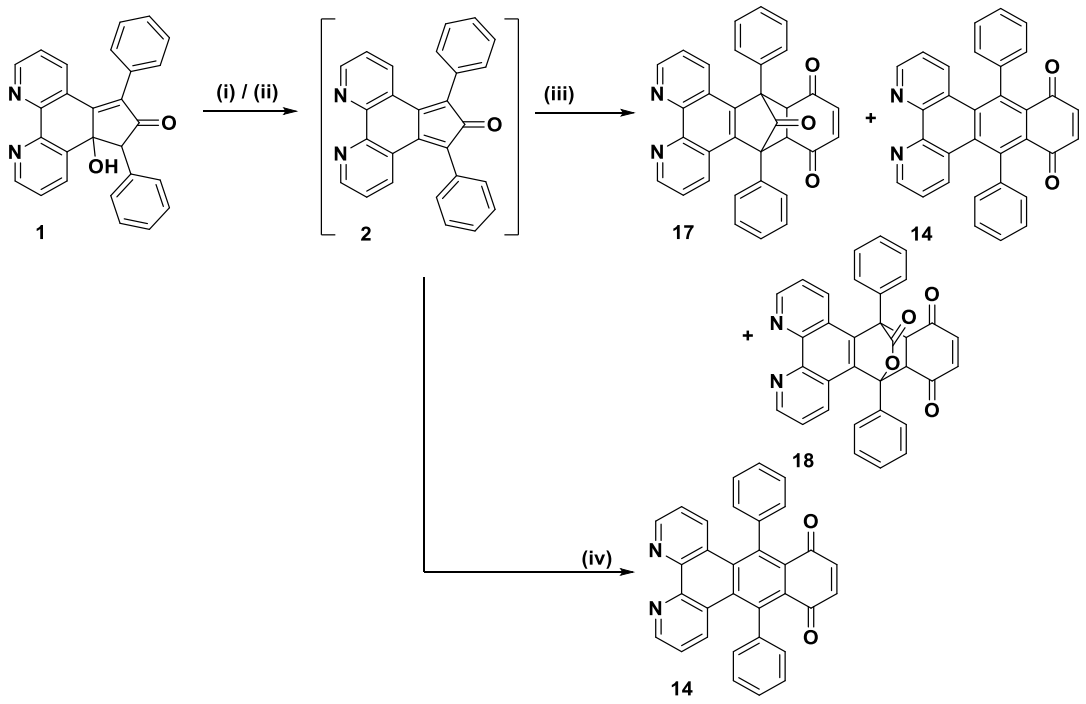

Scheme 1. 9 Attempted, and successful syntheses towards **14**. (i) Chlorobenzene, Al_2O_3, 130 °C, 4 h. (ii) xylenes, Al_2O_3, 130 °C, 4 h. (iii) benzoquinone **L46**, N_2, 1 h. (iv) benzoquinone **L46**, N_2, 140 °C, 1 h → air, 16 h, 83 %.

As predominantly the desired product **14** and its incomplete DA product **17** were formed, it was thought that the reflux temperature of chlorobenzene was either not sufficient to allow for the chelotrophic expulsion of CO, or that the reaction had been stopped prematurely. It was decided to attempt to force the reaction to proceed *via* the expulsion of the bridging CO

in a solvent of a higher reflux temperature. **17** was dissolved in degassed xylenes and refluxed overnight under anaerobic conditions, however no significant change in the ratio of products was seen. The same reaction mixture was refluxed again overnight in air. Surprisingly, on analysis of the products after the work up by ^{1}H NMR, full conversion to the desired product **14** had been achieved (attempts summarised in Scheme 1.9).

Table 1.2. High resolution mass spectrometry analysis of **17**, **18**, and **14**. (ESI, CH_2Cl_2)

Compound	Molecular Formula	Calculated Mass $[M+H]^+$	m/z
17	$C_{33}H_{20}N_2O_3$	493.1552	493.1547
18	$C_{33}H_{20}N_2O_4$	509.1501	509.1498
14	$C_{32}H_{18}N_2O_2$	463.1447	463.1447

As the only difference in the xylenes attempts was the presence of atmospheric oxygen, it is assumed that this oxygen plays a role in the expulsion of the bridging CO, as indicated by the presence of **18** in the original HRMS of the crude.

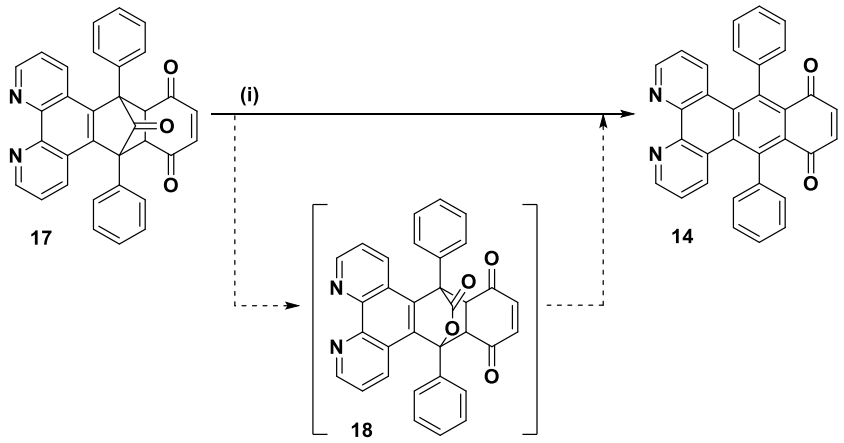

Scheme 1. 10 Potential formation of a bridging CO_2 reaction intermediate **18**.

In this regard, expulsion of the bridging CO would result in a tandem dehydration-decarbonylation process, whereas the bridging CO_2 would result in a tandem dehydration-decarboxylation process. These two processes may have significantly different activation energies, with the bridging CO_2 compound potentially capable of this process at the reflux temperature of xylenes. The possible role of a photochemical process (in ambient light) cannot be ruled out.

14 is as the first 1,10-phenanthroline phenyl-coupled quinone ligand of its kind. It is capable of metal coordination with the quinone in a terminal position, featuring the cyclic-alkene of the quinone moiety. The isolation of **14** *via* column chromatography proved challenging, as the use of silica required significant amounts of either MeOH or triethylamine to elute **14**. Neither solvent as the mobile phase is desirable. After drying *in vacuo*, a second column using alumina was attempted, yielding the pure compound **14** as a dark orange solid (through the sequential use of methylene chloride, chloroform, and acetone).

1.4.2.2 Structural Characterisation of 14

1.4.2.3 Crystallographic Analysis of 14

Crystals of **14** suitable for single crystal X-ray diffraction studies were obtained from the slow evaporation of a toluene/hexanes solution of the compound. Data collection and refinement was conducted by Dr. Brendan Twamley in Trinity College Dublin.

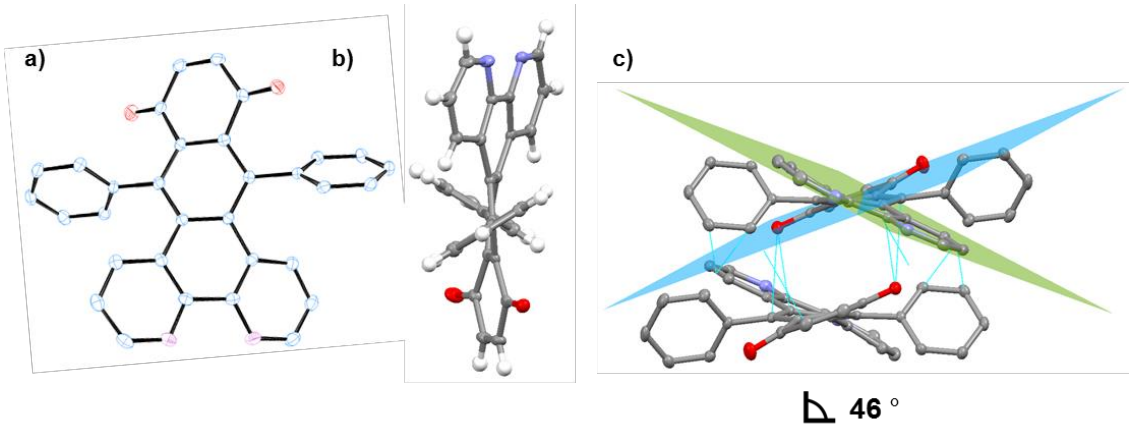

Figure 1. 3 Molecular representations of **14**. (a) Asymmetric unit (thermal ellipsoids shown at 50% probability; hydrogen atoms removed for clarity). (b) Asymmetric unit (thermal ellipsoids shown at 50% probability) viewed parallel to the central phenanthroline ring system. (c) Representation demonstrating quinone ring twist from expected planarity. Short contacts, where the intermolecular contact is shorter than the sum of the van der Waals radii of the atoms involved, are also shown (blue lines).

A clear orange block-like specimen of $C_{32}H_{18}N_2O_2$, of approximate dimensions of 0.120 mm x 0.170 mm x 0.180 mm, was used for the X-ray crystallographic analysis. The structure was solved using the space group $P2_1/n$, with Z = 4 for the formula unit, $C_{32}H_{18}N_2O_2$. The final

anisotropic full-matrix least-squares refinement on F^2 with 325 variables converged at R1 = 4.39%, for the observed data and wR2 = 14.62% for all data. The goodness-of-fit was 1.049.

Figure 1.3(a)-(b) shows representations of the asymmetric unit of **14**. In Figure 1.3(c), two planes (one averaged across the phenanthroline ring system, and the second averaged across the quinone ring) show a twist from expected planarity of 46 °. The twist is the result of the steric demands of the two free phenyl rings. Both of the free phenyls are twisted out of the plane of the middle benzene ring by approximately 57 ° and 60 °. Short contacts between two molecules are also shown (blue lines, Figure 1.3(c)). The intermolecular interactions which stabilise this lattice are in the range of 3 – 3.7 Å. No hydrogen bonding is seen in the crystal lattice.

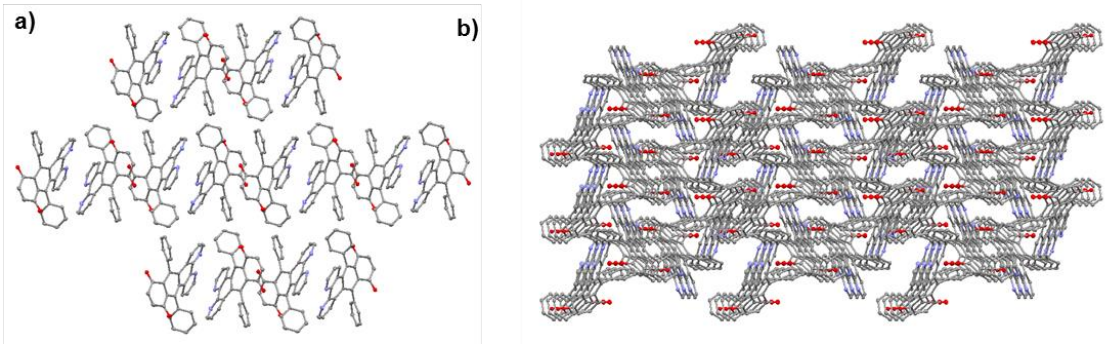

Figure 1. 4 (a) 2x2x2 packing structure of **14**. (b) 3x3x3 packing structure of **14**.

Figure 1.4(a) shows the 2x2x2 packing structure of **14**, viewed along the b axis. Figure 1.4(b) increases the packing structure to 3x3x3, viewed along the reciprocal cell axis a*. The close intermolecular distances of 3 Å results in the inter-layer spacing being quite close. Inter-layer spacing of these distances indicates stacking stability, expected of the partially-fused nature of **14**. However, it is noted that this simplistic explanation of intermolecular stacking between the aromatic planar components of **14** contrasts with the work of Wheeler *et al.*, which states that stacking stability is a result of the electrostatic interaction between a ring's substituent and another ring, rather than between both rings.[42]

1.4.2.4 Multinuclear NMR Analysis of 14

The first of the generated phenyl-coupled quinone ligands, **14**, was spectroscopically characterised by multinuclear NMR studies, and ATR-FTIR. The ^{1}H and $^{13}C\{^{1}H\}$ NMR spectra in $CDCl_3$ are shown in Figure 1.5. The symmetrical structure of **14** aids in the assignment of the respective ^{1}H and $^{13}C\{^{1}H\}$ signals.

The three phenanthroline signals follow the typical pattern of this ring system seen for phenanthroline systems in the literature, with the most downfield signal corresponding to H2 at δ 8.97 ppm. The three phenyl signals are confirmed through use of the HSQC spectrum (Figure 1.6). The three phenyl signals follow the *o*, *p*, *m* sequence found for phenyl systems covalently attached to an electron withdrawing substituent or ring. The shifts are characteristic of aromatic rings of this kind. The cyclic alkene ^{1}H signal is clearly visible as a singlet at δ 6.87 ppm.

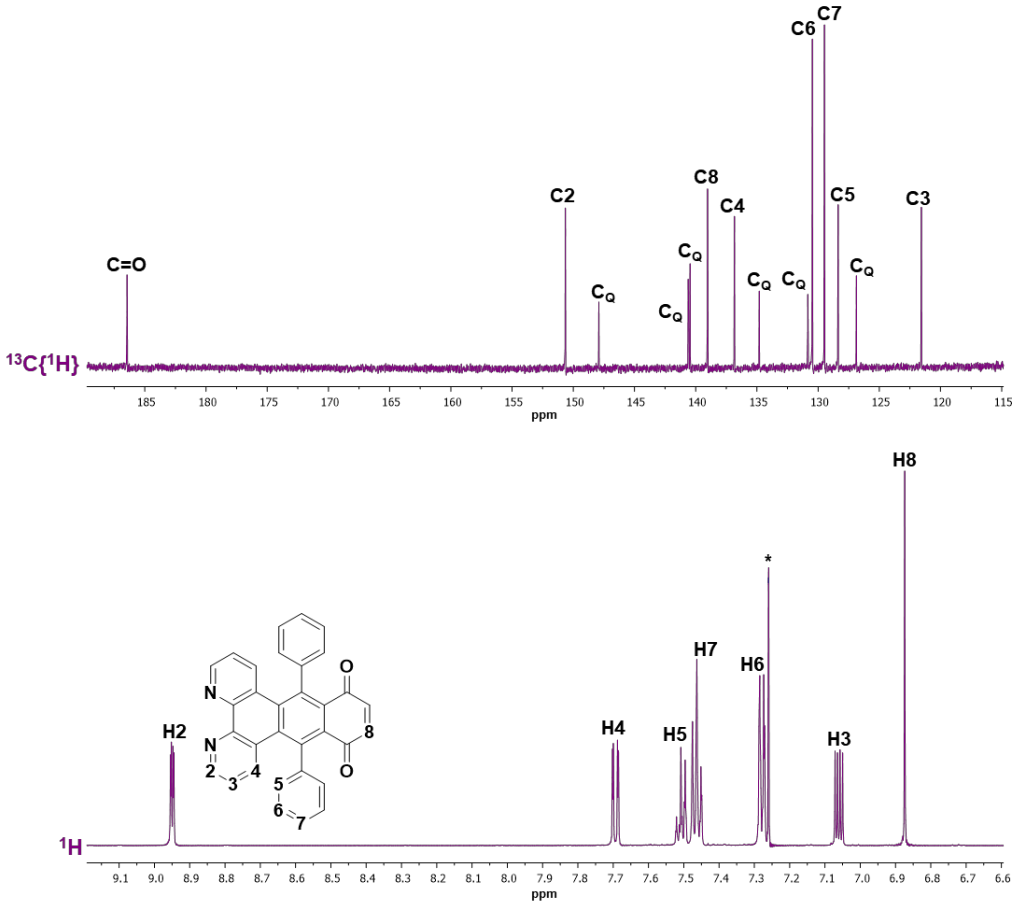

Figure 1. 5 $^{13}C\{^1H\}$ and ^1H NMR spectra of **14**. ($CDCl_3$. 400 MHz for ^1H, 100 MHz for $^{13}C\{^1H\}$. RT). C_Q = quaternary carbon.

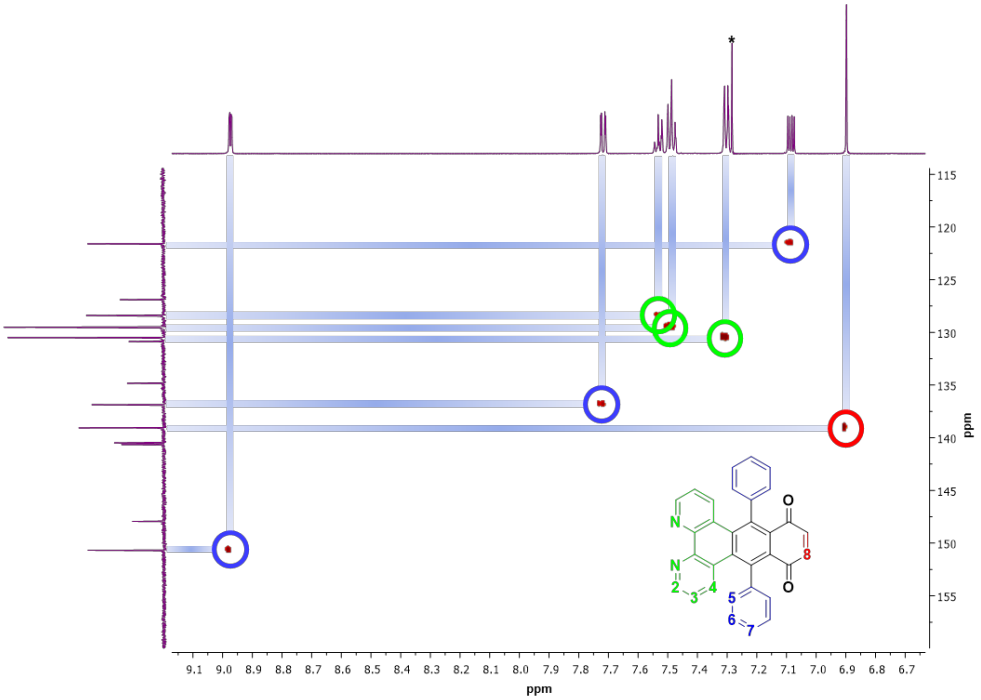

Figure 1. 6 HSQC spectrum of **14** showing the direct ^{1}H and $^{13}C\{^{1}H\}$ signal correlations. ($CDCl_3$. 400 MHz for ^{1}H, 100 MHz for $^{13}C\{^{1}H\}$. RT)

1.4.2.5 Synthesis of 15

Following the successful synthesis of **14**, use of a different quinone dienophile was chosen to mirror the more common "naphthoquinone" quinone-type ligand found in the pyrazine-coupled quinone examples in the literature.

15 is a "naphthoquinone" in which the 1,4-quinone moiety is contained between two aromatic rings. The structure of **15** was expected to be easily generated from **2**, using **L47** as the reaction dienophile *via* reflux overnight under N_2. Analysis of the crude reaction mixture was undertaken with HRMS, revealing a mixture of the desired product **15**, and the bridging CO product **19** (Scheme 1.11, Table 1.3). As in the generation of **14**, the use of refluxing xylenes in air gave complete conversion to the desired product **15**. Unlike for **14** however, no bridging CO_2 product was found in either ^{1}H NMR or HRMS studies. The isolation of **15** using silica-based column chromatography was challenging, requiring significant amounts of either MeOH or triethylamine as eluting solvents **15**. Secondary column chromatography using alumina yielded a bright yellow solid (through the sequential use of methylene chloride, chloroform, and acetone).

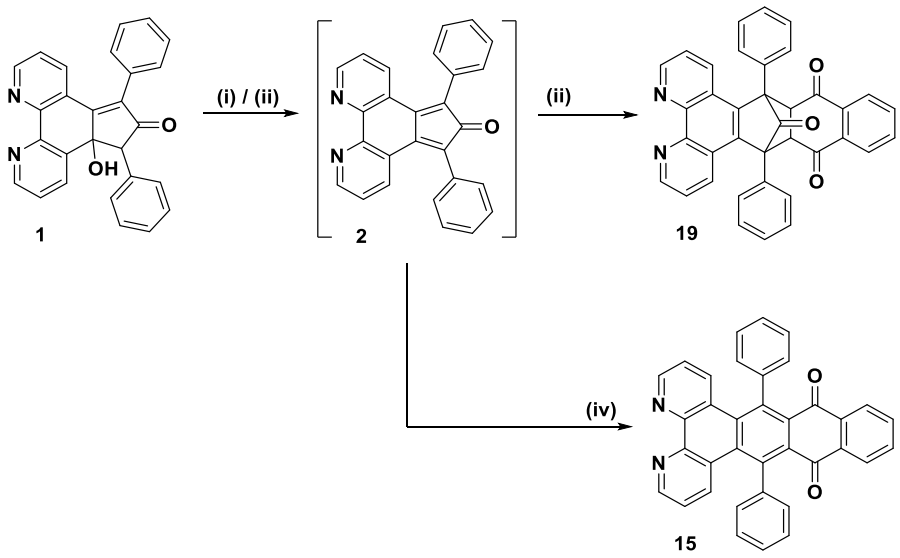

Scheme 1. 11 Attempted, and successful syntheses towards **15**. (i) Chlorobenzene, Al_2O_3, 130 °C, 4 h. (ii) xylenes, Al_2O_3, 130 °C, 4 h. (iii) naphthoquinone **L47**, N_2, 1 h. (iv) naphthoquinone **L47**, N_2, 140 °C, 1 h → air, 16 h, 22 %.

Table 1.3. High resolution mass spectrometry analysis of **19**, and **15**. (ESI, CH_2Cl_2)

Compound	Molecular Formula	Calculated Mass $[M+H]^+$	m/z
19	$C_{37}H_{22}N_2O_3$	543.1709	543.1707
15	$C_{36}H_{20}N_2O_2$	513.1603	513.1606

1.4.2.6 Structural Characterisation of 15

1.4.2.7 Crystallographic Analysis of 15

Crystals of **15** suitable for single crystal X-ray diffraction studies were obtained from the slow evaporation of a $CDCl_3$ solution of the compound. Data collection and refinement was conducted by Dr. Brendan Twamley in Trinity College Dublin.

A specimen of $C_{39}H_{20}D_4Cl_{10}N_2O_2$ (contains disordered dueterated solvent molecules), approximate dimensions 0.070 mm x 0.080 mm x 0.430 mm, was used for the X-ray crystallographic analysis. The structure was solved using the space group $P\bar{1}$, with Z = 2 for the formula unit, $C_{39}H_{20}D_4Cl_{10}N_2O_2$. The final anisotropic full-matrix least-squares refinement on F^2 with 490 variables converged at R1 = 3.97%, for the observed data and wR2 = 9.55% for all data. The goodness-of-fit was 1.037.

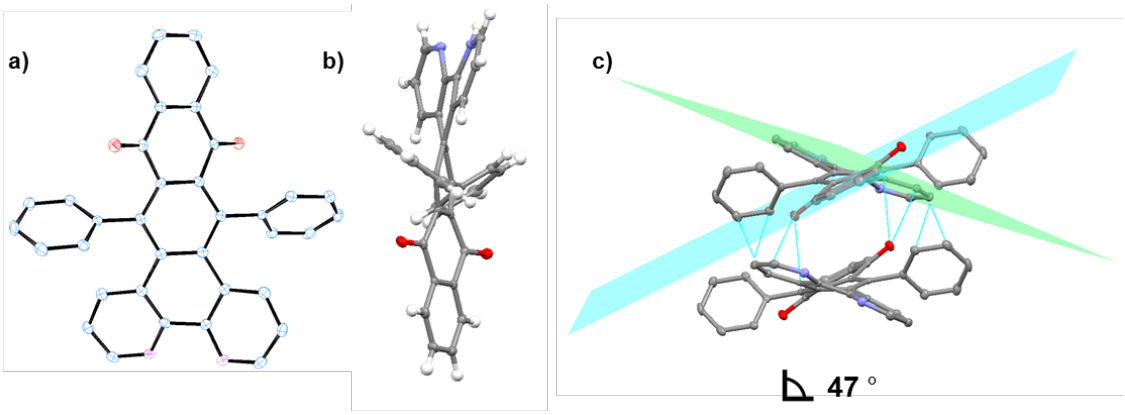

Figure 1. 7 Molecular representations of **15** (disordered solvent removed for clarity). (a) Asymmetric unit (thermal ellipsoids shown at 50% probability; hydrogen atoms removed for clarity). (b) Asymmetric unit (thermal ellipsoids shown at 50% probability) viewed parallel to the central phenanthroline ring system. (c) Representation demonstrating quinone ring twist from expected planarity. Short contacts, where the intermolecular contact is shorter than the sum of the van der Waals radii of the atoms involved, are also shown (blue lines).

Figure 1.7(a)-(b) shows representations of the asymmetric unit of **15**. In Figure 1.7(c), two planes (one averaged across the phenanthroline ring system, and the second averaged across the naphthoquinone ring) show a twist from expected planarity of 47 °. This twist is once again due to the steric demands of the two free phenyl rings. The added phenyl ring compared to **14** has little influence on the size of this twist. Both of the free phenyls are twisted out of the plane of the middle benzene ring (by approximately 54 ° and 56 °). Short contacts between two molecules are also shown (blue lines, Figure 1.7(c)). The intermolecular interactions which stabilise this lattice are approximately 3.2 Å. Hydrogen bonding is observed in the crystal lattice between molecules of **15** and the disordered $CDCl_3$ solvent.

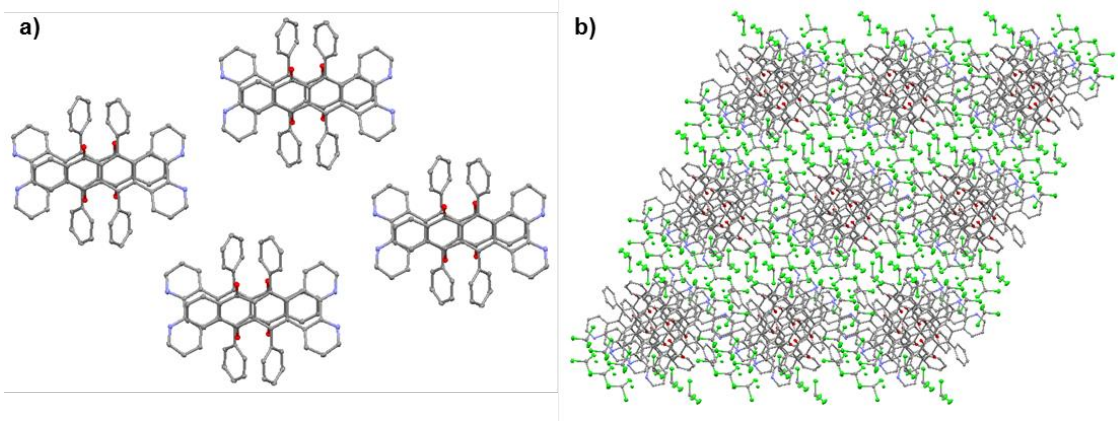

Figure 1. 8 (a) 2x2x2 packing structure of **15**. (b) 3x3x3 packing structure of **15**.

As in the packing structure of **14**, the close intermolecular distances of 3 Å results in the inter-layer spacing being quite close, again indicating stacking stability as expected of the partially-fused **15**. This is seen in detail in Figure 1.8(a) which shows the 2x2x2 packing structure of **15**, viewed along the a axis. Here, a dimer-like structure is observed, with the full length of a **15** molecule "pairing" with another molecule in a head to tail fashion. Figure 1.8(b) increases the packing structure to 3x3x3, as viewed along the reciprocal cell axis a*, and demonstrates "pockets" of these stacked structures, with the intermediate space between the pockets being occupied by the disordered $CDCl_3$ solvent.

1.4.2.8 Multinuclear NMR Analysis of 15

The second phenyl-coupled quinone ligand, **15**, was spectroscopically characterised by multinuclear NMR studies, and the ATR-FTIR (See Chapter 5, Experimental).

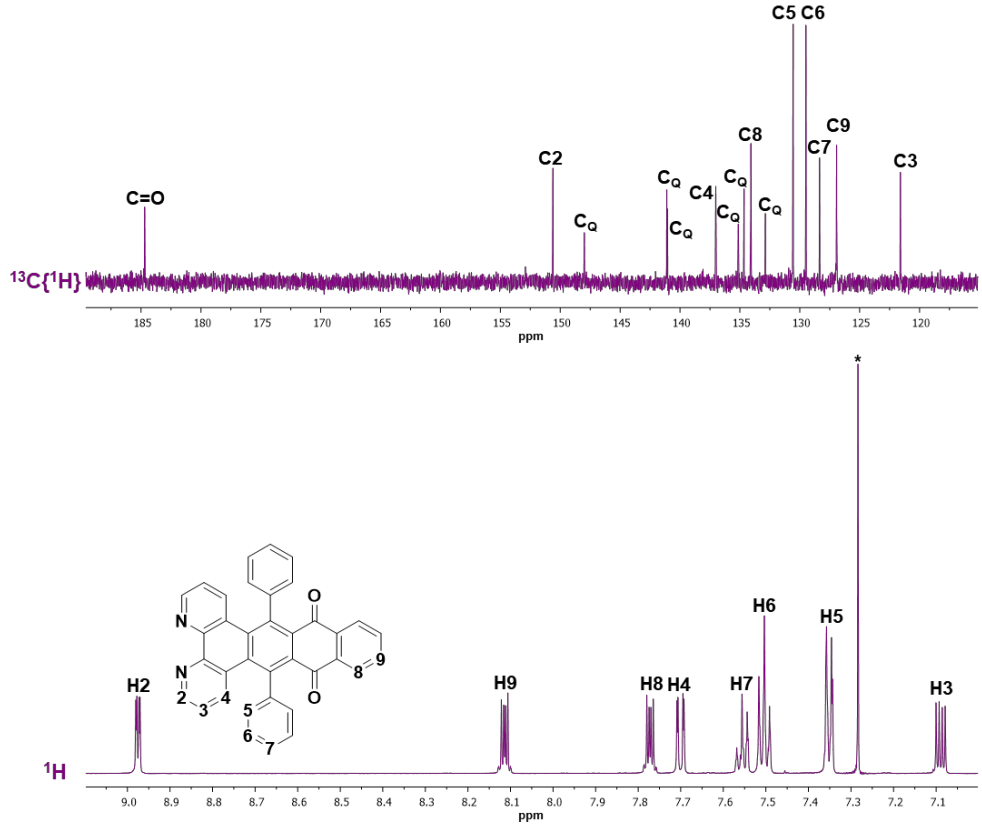

Figure 1. 9 $^{13}C\{^1H\}$ and ^1H NMR spectra of **15**. ($CDCl_3$. 400 MHz for ^1H, 100 MHz for $^{13}C\{^1H\}$. RT). C_Q = quaternary carbon.

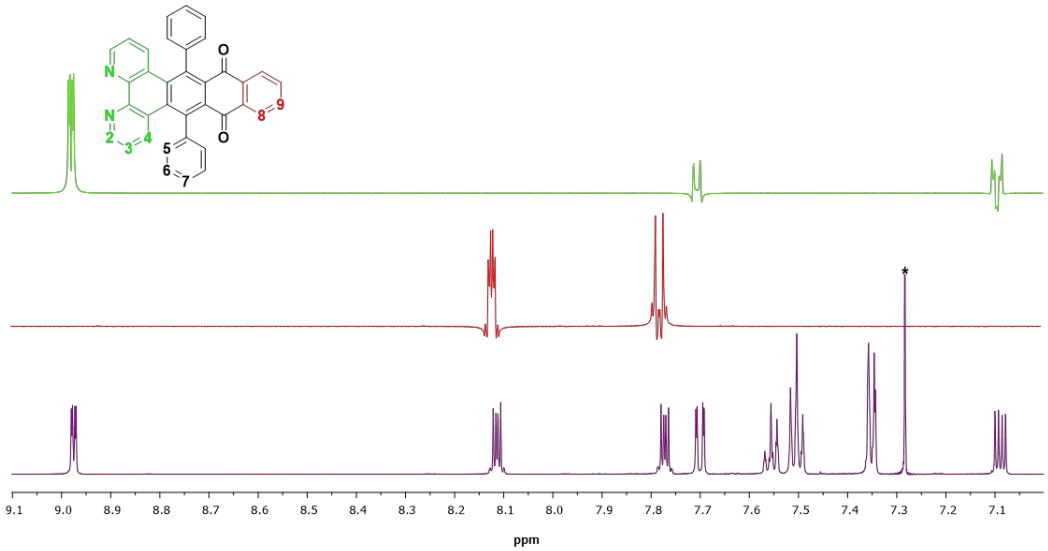

Figure 1. 10 Selective 1D TOCSY experiments revealing the spin systems of **15**, with full aromatic ^{1}H region (purple spectrum). ($CDCl_3$. 400 MHz for ^{1}H, RT)

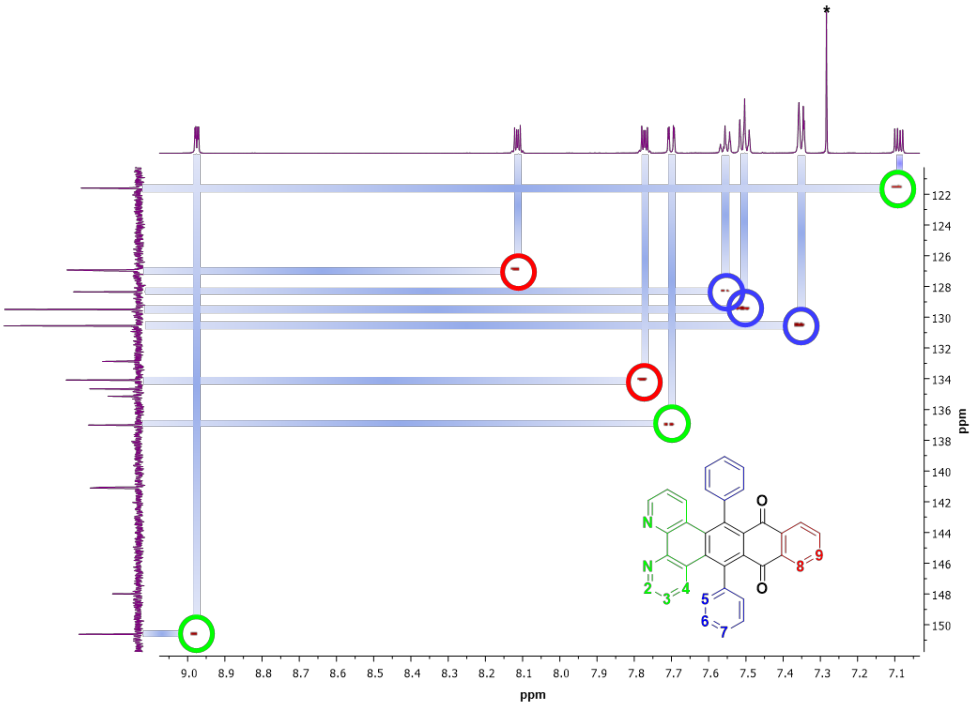

Figure 1. 11 HSQC spectrum of **15** showing the direct ^{1}H and $^{13}C\{^{1}H\}$ signal correlations. ($CDCl_3$. 400 MHz for ^{1}H, 100 MHz for $^{13}C\{^{1}H\}$. RT)

The ^{1}H and $^{13}C\{^{1}H\}$ NMR spectra in $CDCl_3$ are shown in Figure 1.9. The symmetrical structure of **15** once again aids in the assignment of the respective ^{1}H and $^{13}C\{^{1}H\}$ signals. The three phenanthroline signals again follow the typical pattern, with the most downfield

signal corresponding to H2 at δ 8.98 ppm. The three phenyl signals were expected the follow a similar sequence to **14** (*o*, *p*, *m*), but this was not the case. Whilst the ^{1}H spectrum is well resolved, use of selective TOCSY experiments (Figure 1.10) were required to distinguish the respective signals originating from the phenanthroline and "naphthalene-quinone" ring, before successfully determining those signals of the free phenyl rings. The sequence followed here appears as *p*, *m, o*.

1.4.2.9 Attempted Synthesis of 18

Further to the generation of the two 1,10-phenanthroline-quinone compounds in the preceding sections, attempts were made towards the generation of the bis-1,10-phenanthroline compound **16**. Using chlorobenzene or xylenes as the reaction solvent, it was assumed that **16** would be easily obtained from using 0.5 equivalents of **L46**.

On multiple attempts however, **16** was not found, with just **14** found *via* HRMS or NMR analysis of the crude reaction mixture. It was hypothesised that the problem was the inadequate formation of **2**, meaning that the 0.5 equivalents of **L46** were rapidly used up in the formation of **14**. Multiple attempts with lower equivalents of **L46** were undertaken but did not generate any significant amounts of **16** for further study. The failure of the regular alumina method here prompted investigations towards new methods to **16**. The attempted syntheses are summarised in Scheme 1.12.

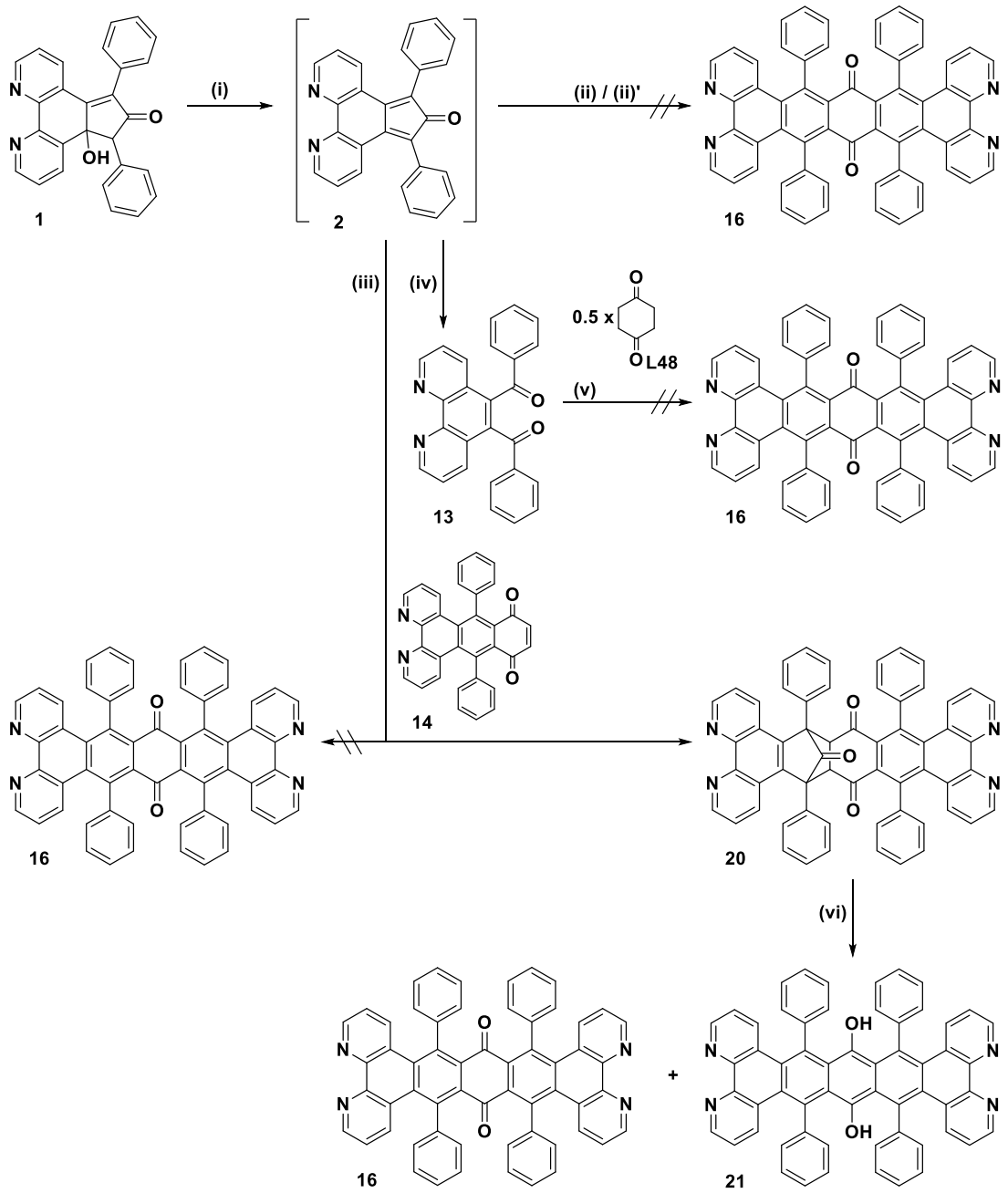

Scheme 1. 12 Attempted syntheses towards **16**. (i) Chlorobenzene, Al_2O_3, 130 °C, 4 h. (ii) benzoquinone **L46**, N_2, 1 h. (ii)' benzoquinone **L46**, benzophenone, N_2, 300 °C, 1 h. (iii) xylenes, naphthoquinone **L47**, N_2, 140 °C, 1 h → air, 16 h, 34 %. (iv) KOH, MeOH/EtOH, 80 °C, 16 h. (v) dichlorobenzene, 180 °C, 16 h.

The first attempt was undertaken in a benzophenone melt at 300 °C, using an electrically-heated sand bath. This method was not ideal due to problems encountered in degassing the reaction mixture, and the limited size of the sand bath. On heating **1** and **L46** together at 300 °C under anaerobic conditions, no detectable amounts of **16** (or **14**) were found across different reaction times. A similar reaction was tried with the high boiling point solvent diphenyl ether. On heating above its melting point of 25 °C, the diphenyl ether solvent could

be degassed with argon by bubbling, and was further degassed on addition of **1** and **L46**. The reaction was brought to its reflux temperature of 259 °C under argon, with HRMS studies indicating the successful synthesis of **16**. However, significant amounts of unidentified impurities (from side reactions) were also present. For this reason, the high temperature methods were abandoned.

A low temperature route was attempted using **13** and the commercially available cyclohexane-1,4-dione, **L48**. Mirroring a synthetic preparation from Einholz *et al.*[43] for the synthesis of heptacene-7,16-dione, it was hoped that the use of catalytic KOH would result in an entropically-driven quadruple aldol reaction between **13** and 0.5 equivalents of **L48**, generating **16**. However, attempts at this preparation in both MeOH and EtOH did not yield the desired product. It was postulated that **14** might act as a suitable dienophile for the DA reaction with **2**, but this route gave only a trace amount of the desired product **16**, and large amounts of the single CO bridging structure **20** (Table 1.4).

Table 1.4. High resolution mass spectrometry analysis of **16**, **20**, and **21**. (MALDI-TOF, CH_2Cl_2)

Compound	Molecular Formula	Calculated Mass $[M+Na]^+$	m/z
16	$C_{58}H_{32}N_4O_2$	839.2423	839.2378
20	$C_{59}H_{34}N_4O_3$	869.2529	869.2565
21	$C_{58}H_{34}N_4O_2$	841.2579	841.2605

As per the other two quinone-coupled products, it was assumed that this CO bridge could be removed in a brute force type synthesis through heating. For this reason, the reaction mixture was redissolved in xylenes and refluxed in air overnight. Upon cooling HRMS studies revealed an increased yield of the desired product **16**, a new diol product **21**, and a significant amount of the CO bridging product **20**. Results from further attempts in the higher boiling point solvent 1,2-dichlorobenzene did not sufficiently show any further formation of **16**. However, a large increase in side product formation was observed. Due to time constraints, further attempts to generate **16** were not attempted in this work, however the work undertaken indicates that the higher temperature expulsion of the bridging CO is not viable, and the formation of **16** may require chemical techniques at lower temperatures. The lack of **16** was regrettable as it would make an attractive ligand for comparison against the known pyrazine-coupled phenanthroline ligand structures in the literature.

1.4.2.10 Possible Development of Trimer 22

Past attempts in the early 2000's by previous members of the Draper group, using the high temperature method of the benzophenone melt detailed above, failed to successfully synthesise compound **16**. In one attempt by Dr. Pablo Fernández-Garcia, a small red crystal was generated, and was found to be suitable for single crystal diffraction studies. This was undertaken *via* the Small Molecule Crystallography Service at the CCLRC Daresbury Laboratory.

Refinement of the structure was carried out for this thesis by Drs. Gearóid Ó Máille, Brendan Twamley, and Sunil Varughese to reveal a fascinating *cyclo*-trimerisation product **22**, arising from three equivalents of **14**.

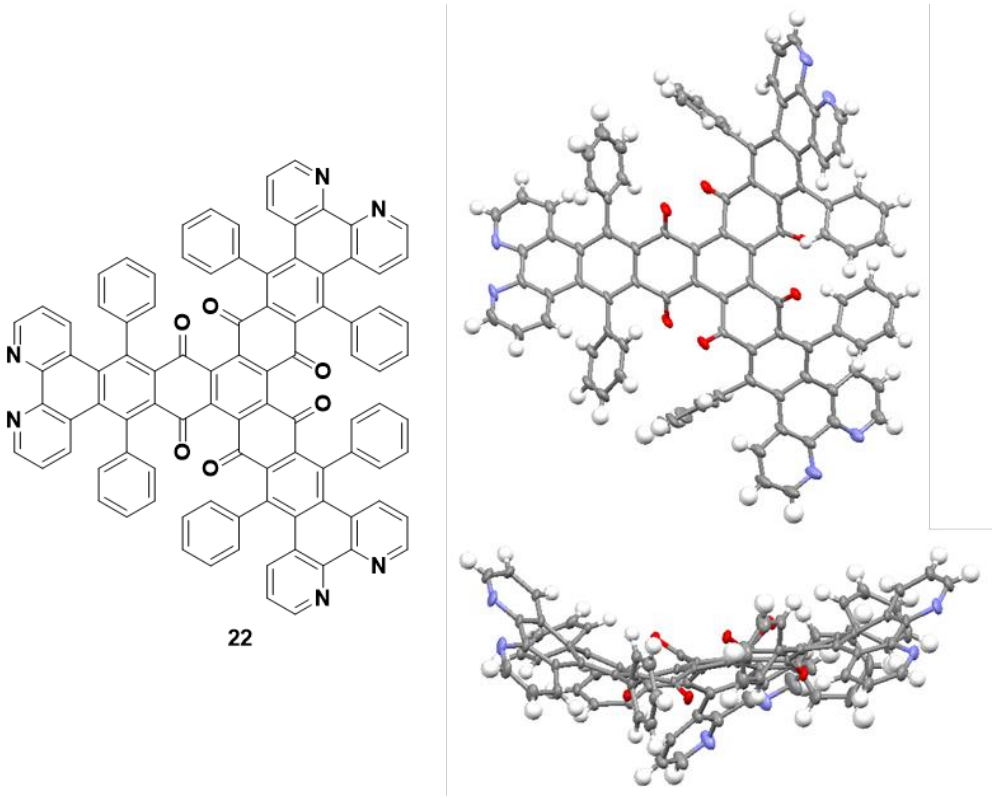

Figure 1. 12 Molecular structure, and two representations of the single crystal X-ray diffraction asymmetric unit (simplified) of the cyclo-trimerisation product, **22**.

22 appears to be the largest *cyclo*-trimerisation product of its kind, and the first to demonstrate N^N bidentate coordination capabilities through the inclusion of its 1,10-phenanthroline moieties. As a result of the research undertaken, a proposed synthetic mechanism is put forward (Scheme 1.13).

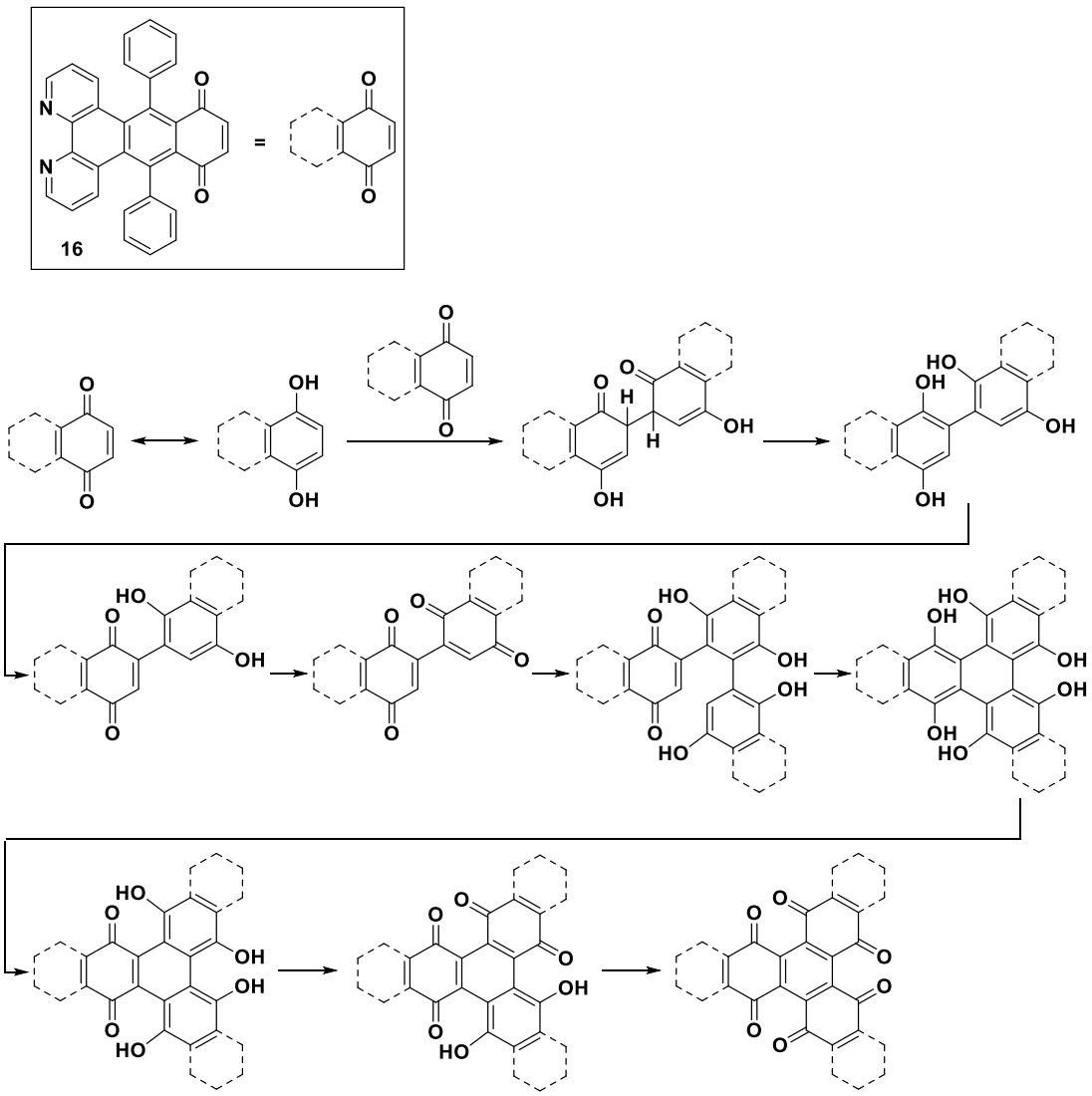

Scheme 1. 13 Postulated reaction mechanism for the cyclo-trimerisation reaction of **14** to **22**.

The mechanism is modified from that discussed by Brockmann *et al.* for the *cyclo*-trimerisation of naphthalene-1,4-dione to trinaphthylene-5,6,11,12,17,18-hexaone.[44] The proposed mechanism only proceeds through the cooperation of the sequential quinone/hydroquinone additions, and the redox reactions of the same, assisted by a continuous decreasing oxidation potential of the redox mixture. Whilst Brockmann deliberately adds the respective hydroquinone to start the reaction, in this case, the high temperature of 300 °C may generate this species spontaneously, allowing the reaction to proceed. The reaction ends with the regeneration of the tris-quinone structure as the most thermodynamically stable form.

1.4.3 Synthesis of Extended Phenanthroline-core PAH-type Ligands

1.4.3.1 Synthesis of 3

Following the successful synthesis of the quinone-coupled PAH-type ligands **14** and **15**, initial attempts towards the generation of **3** were made through use of the optimised low temperature conditions detailed earlier, using ethynyltrimethylsilane as the reaction dienophile. This silyl-acetylene has a low boiling point, but was deemed viable as a result of recent work by Wang *et al*.[45] who utilised ethynyltrimethylsilane in a pressurised reaction vessel. For this reason, attempts were made towards the generation of 5,8-diphenyl-6-(trimethylsilyl)benzo[f][1,10]phenanthroline, **23**. The attempted and future reaction steps are summarised in Scheme 1.14.

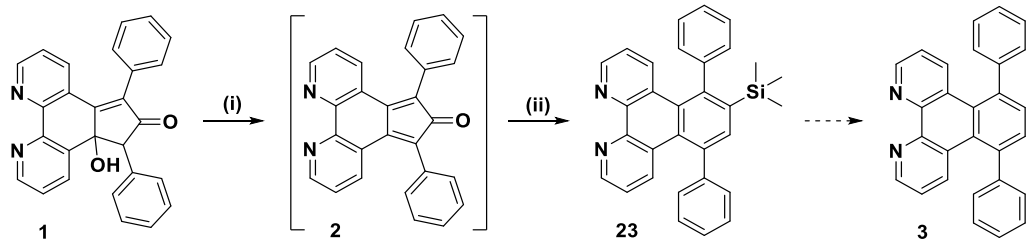

Scheme 1. 14 Attempted syntheses towards **3**. (i) Chlorobenzene, Al_2O_3, 130 °C, 4 h. (ii) ethynyltrimethylsilane, N_2, 135 °C, 16 h.

Here, use of pressure tube conditions, allowed the ethynyltrimethylsilane reagent to be reacted with **2**, maintaining the optimised low temperature conditions detailed earlier. **2** is initially generated over the course of four hours in chlorobenzene with alumina in a pressure tube at 135 °C, under N_2. The pressure tube was then cooled to room temperature, with subsequent addition of the ethynyltrimethylsilane. This was carried out under a stream of Ar in an attempt to maintain the required inert conditions. The tube was then brought back to the reaction temperature of 135 °C overnight. Despite **23** being found by HRMS (Table 1.5), the pressure tube conditions led to largely increased amounts of undesired side products.

Table 1.5. High resolution mass spectrometry analysis of **23**. (ESI, CH_2Cl_2)

Compound	Molecular Formula	Calculated Mass $[M+H]^+$	m/z
23	$C_{31}H_{26}N_2Si$	455.1944	455.1940

Attempts to isolate the silyl-product **23** were unsuccessful. For this reason, and with numerous other methods available towards the generation of **3**, this route was discontinued. Had the isolation of **23** proven successful, the silyl-group would be removed *via* acidic conditions, through the use of refluxing concentrated H_2SO_4 in THF overnight.

The second synthon chosen in place of ethyne was (allylsulfonyl)benzene, **L49**, used by Kumar *et al.* as an acetylene synthon for reaction with 1,3-diphenyl-2H-cyclopenta[l]phenanthren-2-one.[46] Here, the terminal alkene is the reaction dienophile, which undergoes a further thermal elimination of the phenyl sulfone moiety, allowing the chelotrophic expulsion of CO to proceed. The attempted reaction of **2** with **L49** is detailed in Scheme 1.15.

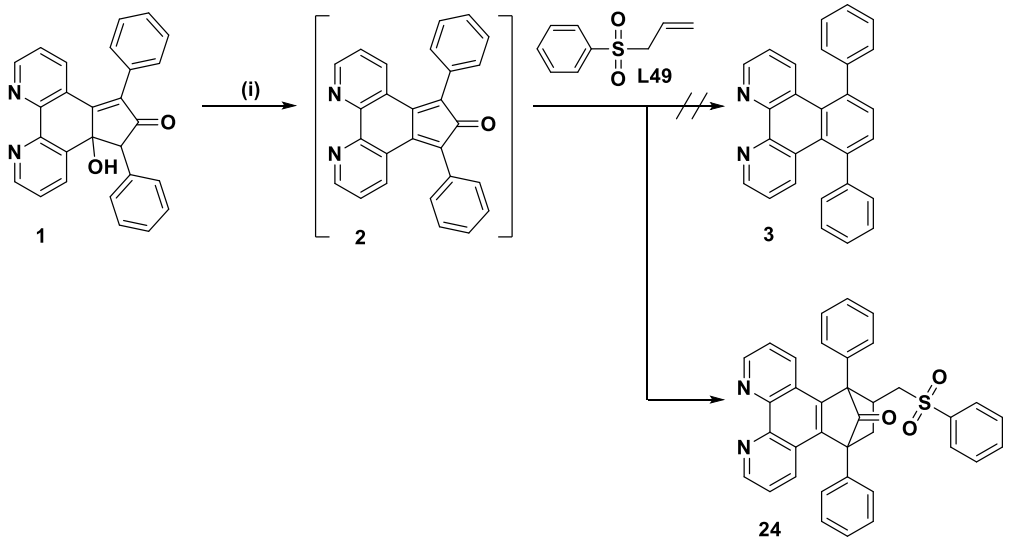

Scheme 1. 15 Attempted syntheses towards **3**. (i) Chlorobenzene, Al_2O_3, 130 °C, 4 h. (ii) N_2, 135 °C, 16 h.

As can be seen in Scheme 1.15, the use of (allylsulfonyl)benzene generated exclusively **24**; a novel sulfone containing-intermediate. This intermediate had not been observed by Kumar *et al.*

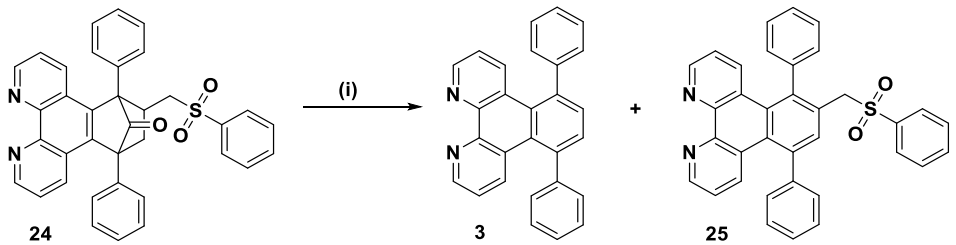

Scheme 1. 16 Attempted syntheses towards **3**. (i) 1,2-dichlorobenzene, 180 °C, 24 h.

Table 1.6. High resolution mass spectrometry analysis of **3**, **24**, and **25**. (ESI, CH_2Cl_2)

Compound	Molecular Formula	Calculated Mass $[M+H]^+$	m/z
3	$C_{28}H_{18}N_2$	383.1548	383.1553
24	$C_{36}H_{26}N_2O_3S$	567.1742	567.1728
25	$C_{35}H_{24}N_2O_2S$	537.1637	537.1633

24 was not isolated as it was assumed that the generation of **3** from **24** could be simply promoted at higher temperatures. For this reason, **24** was redissolved in 1,2-dichlorobenzene, and refluxed in anaerobic conditions for 24 hours. Further to the reaction work up, a number of products were identified by HRMS (Table 1.6). Whilst the generation of **3** was successful, a further novel incomplete reaction product was also found, **25**. Due to both products containing the 1,10-phenanthroline core system, silica-based column chromatography proved inadequate for separation, as the iminic nitrogens of the phenanthroline ring system require high percentages of MeOH to facilitate elution, and both products run together. Further attempts to remove the sulfone under aerobic conditions did not achieve the desired results, with no appreciable loss of sulfone occurring. The loss of the CO bridge without the loss of the sulfone group suggests two competing aromatisation pathways exist, and as such, this route was discontinued.

The next attempt to generate the desired ligand system **3** was through the use of a preparation with bicyclo[2.2.1]hepta-2,5-diene, **L50**. This reagent initially acts as a dienophile for Diels-Alder reactions, before undergoing a subsequent retro Diels-Alder reaction at elevated temperatures to give cyclopenta-1,3-diene as a reaction product. It was hoped that its use here would avoid the issues seen with the generation of **25**, where the loss of the CO bridge did not occur.

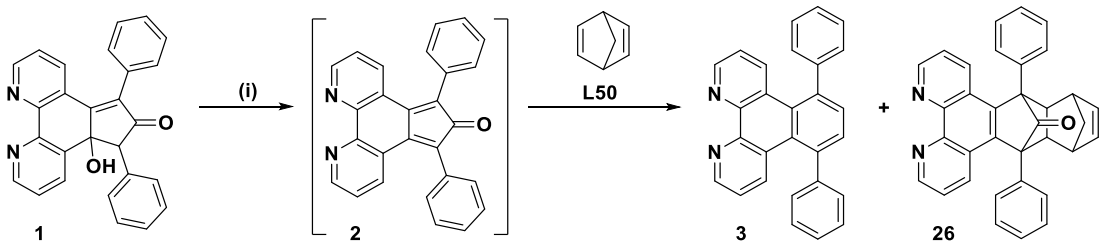

Scheme 1. 17 Attempted syntheses towards **3**. (i) Chlorobenzene, Al_2O_3, 130 °C, 4 h. (ii) N_2, 130 °C, 16 h.

Table 1.7. High resolution mass spectrometry analysis of **3**, and **26**. (ESI, CH_2Cl_2)

Compound	Molecular Formula	Calculated Mass $[M+H]^+$	m/z
3	$C_{28}H_{18}N_2$	383.1548	383.1560
26	$C_{34}H_{24}N_2O$	477.1967	477.1974

It was postulated that if the reaction proceeded *via* the loss of the CO bridge first, then the retro Diels-Alder would be unaffected, and could still be forced at high temperatures. As shown in Scheme 1.17, on generating the cyclopentadienone product **2** *in situ*, the addition of **L50** results in both the desired ligand **3**, and the CO bridged product 9,14-diphenyl-9,9a,10,13,13a,14-hexahydro-9,14:10,13-dimethanonaphtho[2,3-f][1,10]phenanthrolin-15-one, **26**. HRMS samples taken after 1 hour, and after 16 hours, showed this mixture did not change over time at the reflux temperature of 130 °C (Table 1.7).

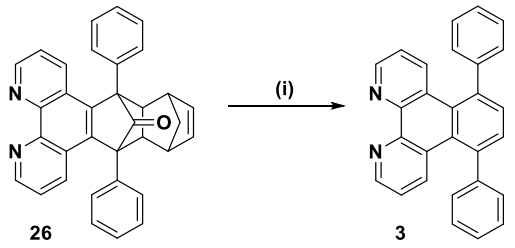

Scheme 1. 18 Final synthesis towards **3**. (i) 1,2-dichlorobenzene, 180 °C, Ar, 24 h, 23 %.

As no change was observed with the chlorobenzene solvent reflux temperature, this solvent was removed *in vacuo* and exchanged for the higher boiling point 1,2-dichlorobenzene. The reaction was continued under Ar for a further 24 hours to give **3**. Clearly, the retro Diels-Alder step was necessary for the expulsion of CO, and the generation of the middle benzene

ring (Scheme 1.18). Silica-based column chromatography facilitated the collection of **3** as an analytically pure off-white solid, structurally characterised by NMR and HRMS studies.

1.4.3.2 Structural Characterisation of 3

1.4.3.3 Crystallographic Analysis of 3

Crystals of **3** suitable for single crystal X-ray diffraction studies were obtained from the slow evaporation of a toluene/hexane solution of the compound. Data collection and refinement was conducted by Dr. Brendan Twamley in Trinity College Dublin.

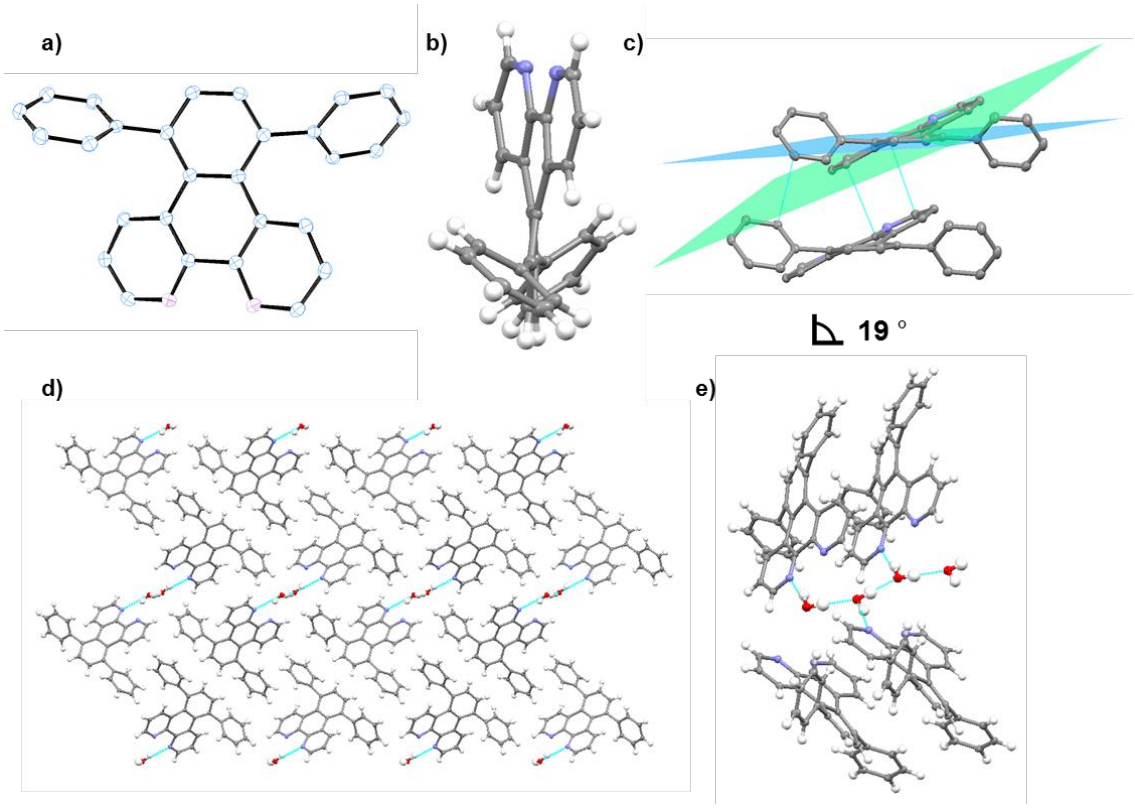

Figure 1. 13 Molecular representations of **3**. (a) Asymmetric unit (thermal ellipsoids shown at 50% probability; hydrogen atoms removed for clarity). (b) Asymmetric unit (thermal ellipsoids shown at 50% probability) viewed parallel to the central phenanthroline ring system. (c) Representation demonstrating quinone ring twist from expected planarity. Short contacts, where the intermolecular contact is shorter than the sum of the van der Waals radii of the atoms involved, are also shown (blue lines). (d) 2x2x2 packing structure of **3** showing interstitial H_2O. (e) Simplified "dimer" structures of **3** showing interstitial H_2O.

A specimen of $C_{28}H_{20}N_2O$, approximate dimensions 0.080 mm x 0.080 mm x 0.230 mm, was used for the X-ray crystallographic analysis. The structure was solved using the space group $P2_1/c$, with Z = 4 for the formula unit, $C_{28}H_{20}N_2O$. The final anisotropic full-matrix least-squares refinement on F^2 with 288 variables converged at R1 = 3.88%, for the observed data and wR2 = 10.62% for all data. The goodness-of-fit was 1.024.

Figure 1.13(a)-(b) shows representations of the asymmetric unit of **3**. In Figure 1.13(c), two planes (one averaged across the phenanthroline ring system, and the second averaged across the middle benzene ring) shows a twist from expected planarity of 19 °. This twist is once again due to the steric demands of the two free phenyl rings. Both of the free phenyls are twisted out of the plane of the middle benzene ring (by approximately 50 ° and 57 °). Short contacts between two molecules are also shown (blue lines, Figure 1.13(c)). The intermolecular interactions between two phenanthroline ring systems are between 3.3-3.6 Å, while the intermolecular interactions between two free phenyl rings is 4.9 Å. Figure 1.13(d) shows the hydrogen bonding observed (in the calculated 2x2x2 packing structure viewed along the b axis) between molecules of **3** and interstitial H_2O. Figure 1.13(e) shows a simplified version of this hydrogen bonding, demonstrating O ⋯ H bonds between two H_2O molecules, and N ⋯ H bonds between the phenanthroline nitrogens and water hydrogens.

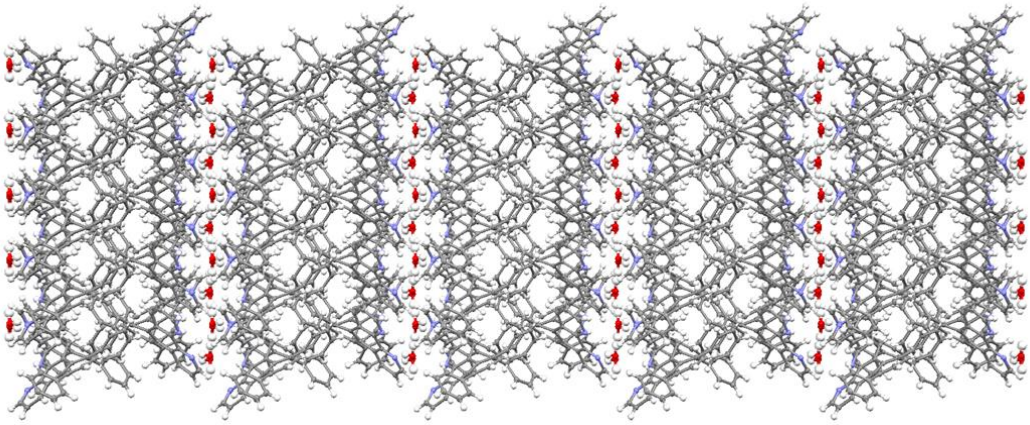

Figure 1. 14 5x5x5 crystal packing structure of **3**.

The calculated (multiple unit cells of the same space group) 5x5x5 packing structure of **3** viewed along the c axis (Figure 1.14) visualises the interstitial H_2O in much greater detail. Here, the molecules of H_2O can be observed to form linear columns between the tight-knit columns of the packed molecules of **3**. Similarly to the two quinone-coupled structures **16** and **17**, the close intermolecular distances of approximately 3 Å indicate stacking stability, expected of the partially-fused nature extended phenanthroline ring systems.

1.4.3.4 Multinuclear NMR Analysis of 3

The first of the generated extended 1,10-phenanthroline ligands, **3**, was spectroscopically characterised by multinuclear NMR studies, and the ATR-FTIR spectrum (See Chapter 5, Experimental). The ^{1}H and $^{13}C\{^{1}H\}$ NMR spectra in $CDCl_3$ are shown in Figure 1.15. The symmetrical structure of **3** aids in the assignment of the respective ^{1}H and $^{13}C\{^{1}H\}$ signals. The three phenanthroline signals again follow the typical pattern, with the most downfield signal corresponding to H2 at δ 8.97 ppm. The three phenyl signals are surprisingly contained within a large *quasi*-singlet at δ 7.47 ppm. This strange phenomenon of the three signals appearing at essentially the same ppm value was determined from the HSQC spectrum (Figure 1.16), and confirmed by the use of the integration value. The singlet expected of the central benzene ring is clearly visible at δ 7.62 ppm.

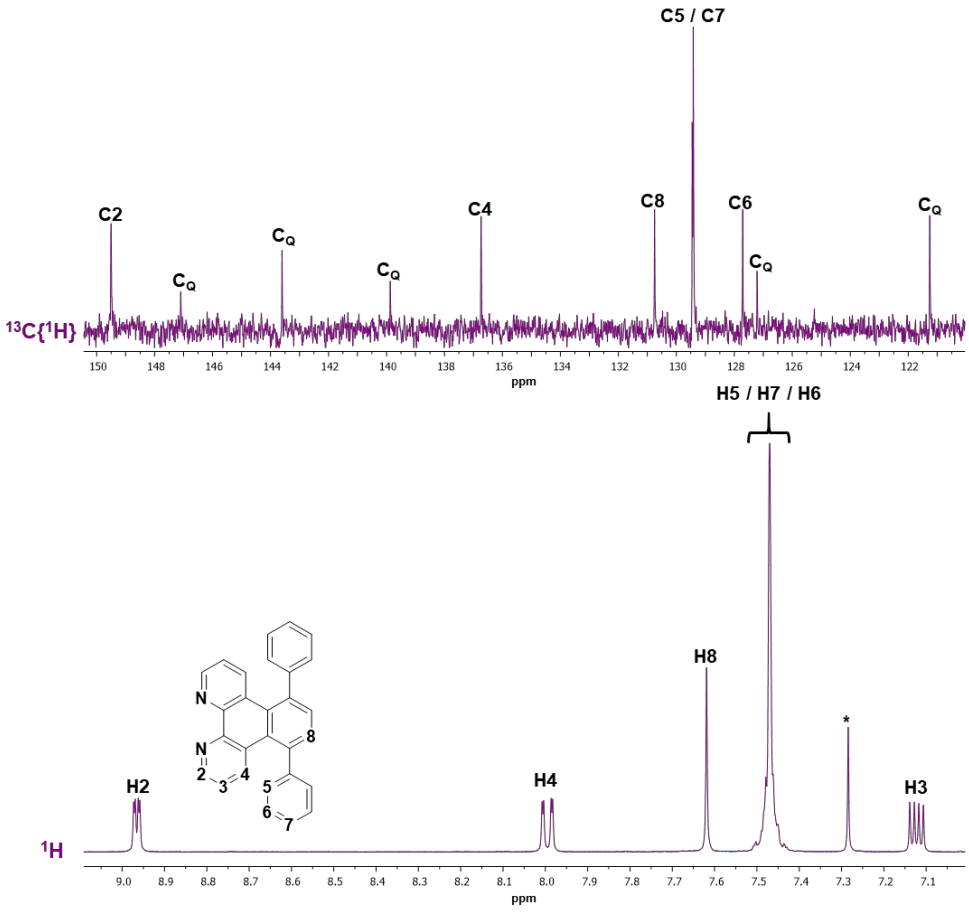

Figure 1. 15 $^{13}C\{^{1}H\}$ and ^{1}H NMR spectra of **3**. ($CDCl_3$. 400 MHz for ^{1}H, 100 MHz for $^{13}C\{^{1}H\}$. RT). C_Q = quaternary carbon.

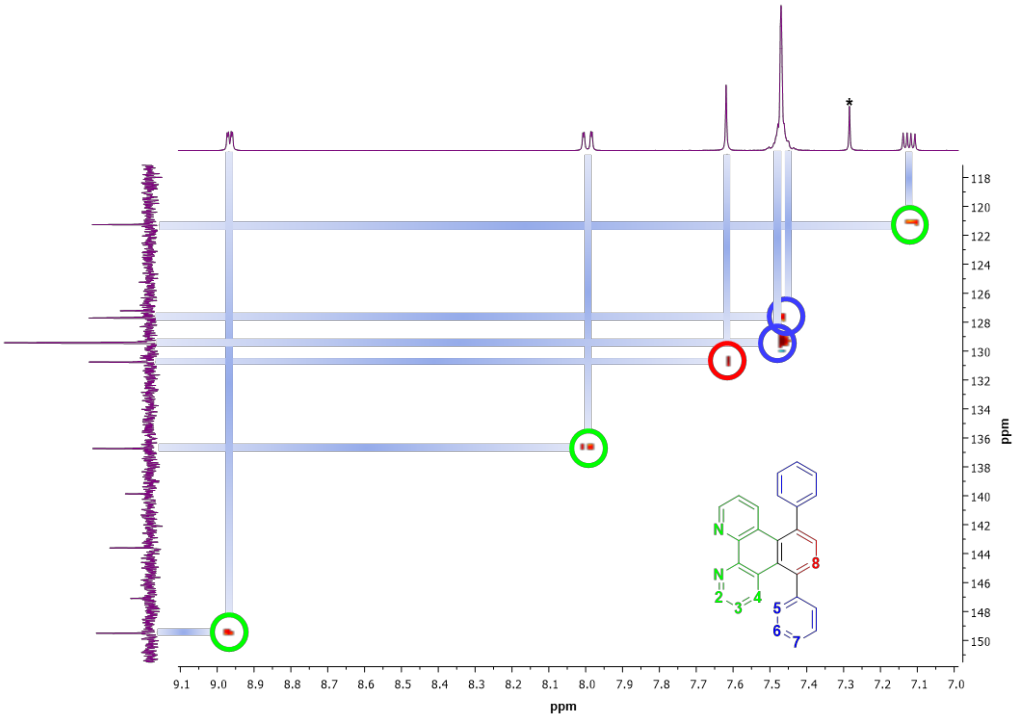

Figure 1. 16 HSQC spectrum of **3** showing the direct ^{1}H and $^{13}C\{^{1}H\}$ signal correlations. ($CDCl_3$. 400 MHz for ^{1}H, 100 MHz for $^{13}C\{^{1}H\}$. RT)

1.4.3.5 Synthesis of 4

With the successful generation of **3**, attention turned to the potential formation of a further ligand, that incorporated a second heterocyclic ring system, 5,8-diphenylpyridazino[4,5-f][1,10]phenanthroline **4**. This is a PAH-type ligand comprising a phenanthroline system, and a pyridazine ring, and would allow further insight into the effect of the additional heteroatoms in the molecular structure. The similarity of both of these systems would allow for a direct comparison of their respective optoelectronic and electrochemical properties. The pyridazine ring was considered to be most accessible *via* the ring opened product (1,10-phenanthroline-5,6-diyl)bis(phenylmethanone), **13**. A proposed synthetic route to **13** is given in Scheme 1.20.

As the ring opening reaction of the commercially available tetraphenylcyclopentadienone to its corresponding diketone form can be carried out by a number of routes, it was hoped to apply one of these routes to **2**. One promising route was its reaction in dry MeOH with $^{1}O_2$ (generated in situ from the reaction of chloramine-T hydrate and hydrogen peroxide).[47] The reaction is a standard Diels-Alder [4+2] cycloaddition with the consecutive ring opening likely driven by the chelotrophic elimination of carbon monoxide. Utilising this route in an attempt to form **13** seemed very promising. As a Diels-Alder [4+2] concerted cycloaddition is spin-forbidden using $^{3}O_2$ as a reactive species, $^{1}O_2$ was expected to be a definitive

requirement. However, the optimisation of this reaction proved quite difficult. After an aqueous work-up, only starting material **1** was found. On review of the reaction conditions, a number of issues were noted. As hydrogen peroxide is supplied as an aqueous solution, water is delivered to the reaction vessel in a considerable volume rendering the ring-opening of **2** unlikely. The reaction was attempted in a number of non-protic solvents including CH_2Cl_2, THF and hexanes but no successful reaction was observed. The polar and protic nature of MeOH seems to be required for successful reaction.

Knowing that the ring opening reaction would provide an extremely simple synthetic route to **4**, further attempts were made. A literature review of papers from the early 20th century demonstrated that the ring opening of tetracyclone (and other all carbon-based PAH-type cyclopentadienone structures) could be carried out in air at elevated temperatures. However, "self" Diels-Alder reactions between two cyclopentadienone system molecules was expected to be an issue at these elevated temperatures. On an attempt to determine a mechanism for this seemingly simple addition of $^3O_2$ to the cyclopentadienone ring system of **2**, a literature source of the phenanthrene version of the diketone was found.[48] Strikingly, the authors had seen a similar reaction with 1,3-diphenyl-2H-cyclopenta[l]phenanthren-2-one in air, in the same refluxing solvents used for the dehydration step of **13**, xylenes or chlorobenzene. They proposed a mechanism accounting for the formation of the diketone whilst also carrying out a control experiment in the dark to confirm that the photoactivation of $^3O_2$ to $^1O_2$ in ambient lighting was not responsible for the successful diketone formation. A modified mechanism is proposed in Scheme 1.19.

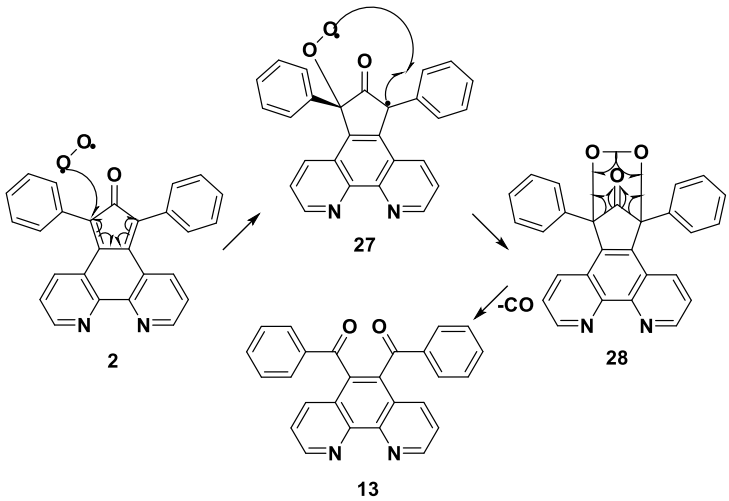

Scheme 1. 19 Postulated reaction mechanism for the $^3O_2$ mediated ring opening of **2** to **13**.

As this reaction required no specialist conditions, a solution of **1** in chlorobenzene, with the requirement of alumina to generate **2**, was refluxed in air overnight (Scheme 1.20). Following a work-up, analysis with HRMS and NMR showed the diketone **13** was successfully synthesised. Whilst the yield is modest, the lack of chloramine-T hydrate made the work up very simple with a small aqueous wash and precipitation from acetone with hexanes being all that was required (See Chapter 5, Experimental). The reaction was also attempted in xylenes, but unidentified side products were generated, similar to the earlier reactions. **13** was perfectly stable in atmospheric conditions, and its conversion to the pyridazine ring system was achieved through reaction with commercially available hydrazine hydrate in EtOH, with a catalytic amount of KOH (Scheme 1.20). Aware of the safety concerns, hydrazine hydrate was used with a total hydrazine content of not more than 60 %.

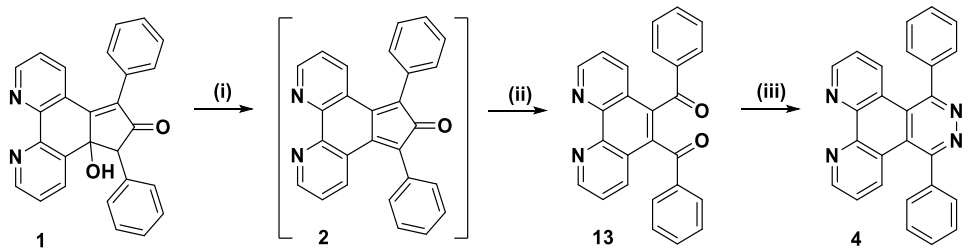

Scheme 1. 20 Synthesis of **4**. (i) Chlorobenzene, Al_2O_3, 130 °C, 4 h. (ii) air, 130 °C, 16 h, 29 %. (iii) Hydrazine hydrate (60 %), KOH, EtOH, 78 °C, 2 h, 92 %.

Table 1.8. High resolution mass spectrometry analysis of **13**, and **4**. (ESI, CH_2Cl_2)

Compound	Molecular Formula	Calculated Mass $[M+H]^+$	m/z
13	$C_{26}H_{16}N_2O_2$	389.1290	389.1298
4	$C_{26}H_{16}N_4$	385.1453	385.1452

As demonstrated, a double Schiff-type condensation reaction of one hydrazine molecule generates the pyridazine ring to form **4**. Whilst hydrazine hydrate and KOH are common reagents for the reductive deoxygenation of carbonyls, it is thought that the entropically favoured formation of the six-membered ring prevents this from occurring. This entropic driving force is due to the loss of two water molecules in the double condensation, accounting for the generation of three molecules from two starting materials. The formation of the pyridazine ring also appears to be irreversible, thus preventing the deoxygenation reaction occurring. As any excess hydrazine hydrate or KOH are water soluble, a simple aqueous wash

followed by precipitation from acetone with hexanes yielded an analytically pure sample of **4** in good yield. This was characterised by HRMS and NMR studies.

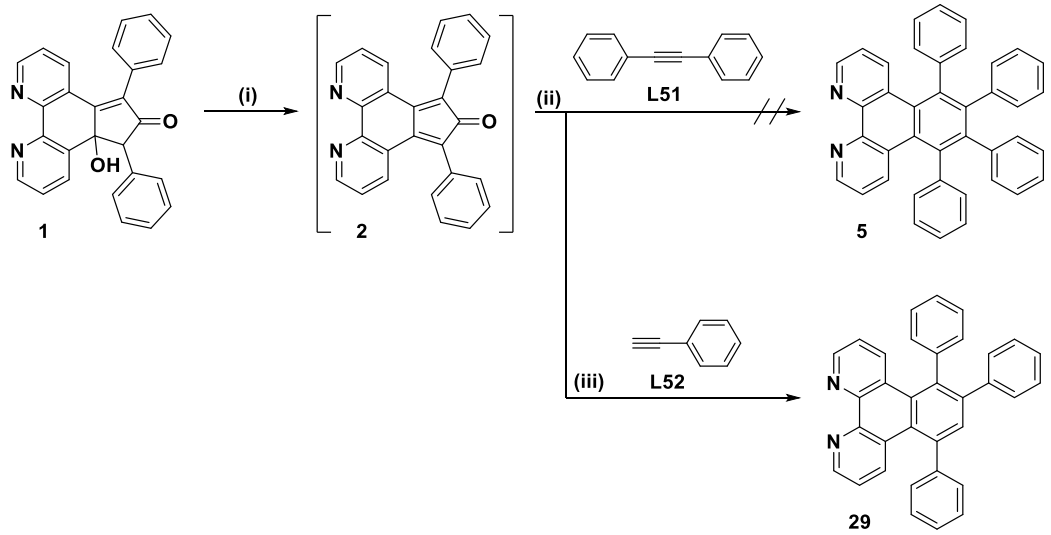

Scheme 1. 21 Attempted syntheses towards **5** and **29**. (i) Chlorobenzene, Al_2O_3, 130 °C, 4 h. (ii) Chlorobenzene, 130 °C, 16 h. (iii) Chlorobenzene, 130 °C, 16 h.

Attempts were made to generate 5,6,7,8-tetraphenylbenzo[f][1,10]phenanthroline, **5** *via* the optimised synthetic method, with heterogeneous alumina in refluxing chlorobenzene (Scheme 1.21). This reaction, using the cyclopentadienone precursor **2** and 1,2-diphenylethyne **L51**, appears unable to proceed due to the reaction temperature. Although not completely unexpected, it had been hoped that the increased reactivity of **2** over the all-carbon tetracyclone would allow the reaction to proceed. On repeat in the higher boiling point solvent, 1,2-dichlorobenzene, no product was retrieved.

Whilst the use of 1,2-diphenylethyne as the Diels-Alder dienophile does appear to require elevated temperatures in a significant number of literature reaction preparations,[49,50] other phenyl-type acetylenes, including the single-phenyl acetylene ethynylbenzene **L52** were used and do appear to react within the range offered by the optimised conditions with alumina (Table 1.9).[51] These results offer an insight into the activation energies required for low-temperature Diel-Alder reactions with 1,10-phenanthroline systems.

Table 1.9. High resolution mass spectrometry analysis of **29**. (ESI, CH_2Cl_2)

Compound	Molecular Formula	Calculated Mass $[M+H]^+$	m/z
29	$C_{34}H_{22}N_2$	459.1861	459.1849

1.4.3.6 Structural Characterisation of 4

1.4.3.7 Crystallographic Analysis of 4

Crystals of **4** suitable for single crystal X-ray diffraction studies were obtained from the slow evaporation of a CH_2Cl_2/MeOH solution of the compound. Data collection and refinement was conducted by Dr. Brendan Twamley in Trinity College Dublin.

A specimen of $C_{26}H_{16}N_4$, approximate dimensions 0.130 mm x 0.150 mm x 0.160 mm, was used for the X-ray crystallographic analysis. The structure was solved using the space group C2/c, with Z = 8 for the formula unit, $C_{26}H_{16}N_4$. The final anisotropic full-matrix least-squares refinement on F^2 with 271 variables converged at R1 = 4.79%, for the observed data and wR2 = 12.18% for all data. The goodness-of-fit was 1.022.

Figure 1.17(a)-(b) shows representations of the asymmetric unit of **4**. In Figure 1.17(c), two planes (one averaged across the phenanthroline ring system, and the second averaged across the pyridazine ring) show a twist from expected planarity of 16 °. The twist is from the steric demands of the two free phenyl rings. Both of the free phenyls are twisted out of the plane of the middle pyridazine ring (by approximately 51 ° and 52 °). Short contacts between two molecules are also shown (blue lines, Figure 1.17(c)). The intermolecular interactions between the phenanthroline ring system, and the pyridazine ring is a distance of 3.2 Å. No hydrogen bonding is seen in the crystal lattice.

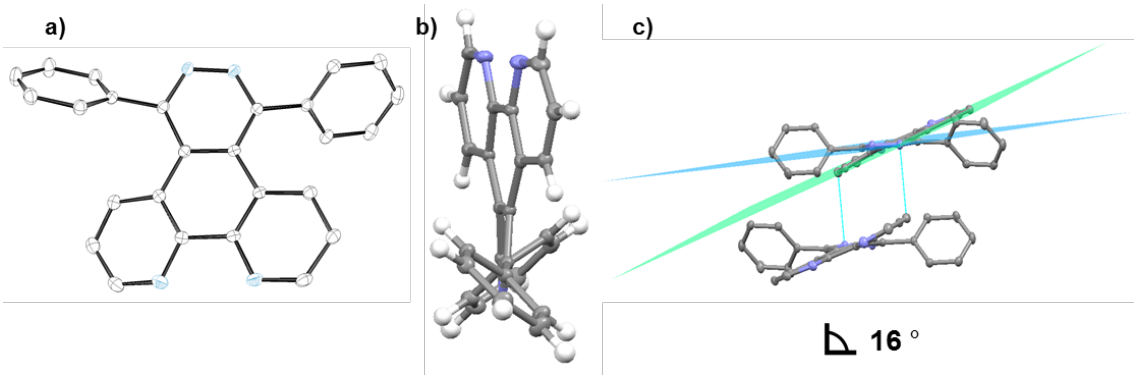

Figure 1. 17 Molecular representations of **4**. (a) Asymmetric unit (thermal ellipsoids shown at 50% probability; hydrogen atoms removed for clarity). (b) Asymmetric unit (thermal ellipsoids shown at 50% probability) viewed parallel to the central phenanthroline ring system. (c) Representation demonstrating quinone ring twist from expected planarity. Short contacts, where the intermolecular contact is shorter than the sum of the van der Waals radii of the atoms involved, are also shown (blue lines).

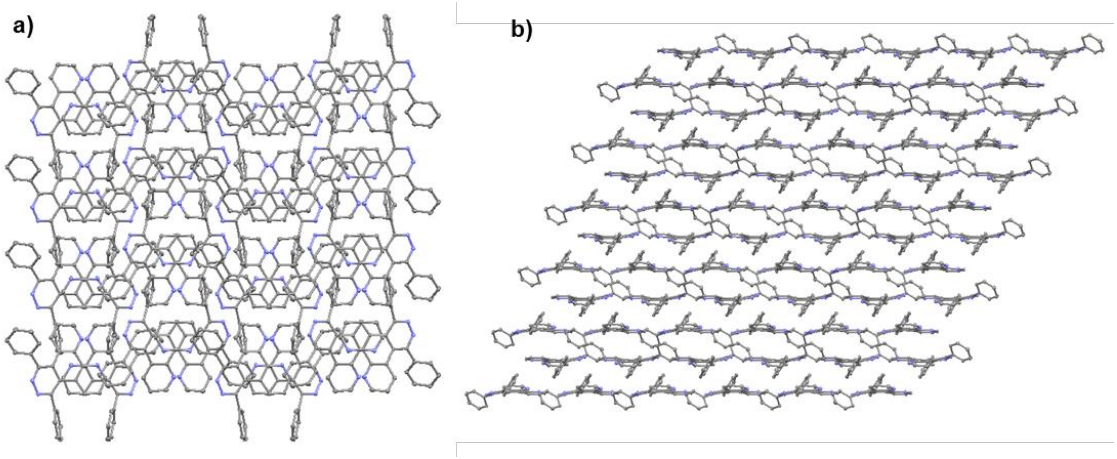

Figure 1. 18 (a) 2x2x2 crystal packing structure of **4**. (b) 3x3x3 crystal packing structure of **4**.

Figure 1.18(a) shows the 2x2x2 packing structure of **4**, viewed along the a axis. Figure 1.18(b) increases the packing structure to 3x3x3, and is viewed along the b axis. The close intermolecular distances of 3 Å illustrate stacking stability, similar to that of the other three previous structures. Figure 1.18(a) reveals a wave-like "W" pattern in the crystal lattice.

1.4.3.8 Multinuclear NMR Analysis of 4

The second generated extended 1,10-phenanthroline ligand, **4**, was spectroscopically characterised by multinuclear NMR studies, and the ATR-FTIR (See Chapter 5, Experimental). The ^{1}H and $^{13}C\{^{1}H\}$ NMR spectra in $CDCl_3$ are shown in Figure 1.19. The symmetrical nature of **4** aided the assignment its respective ^{1}H and $^{13}C\{^{1}H\}$ signals.

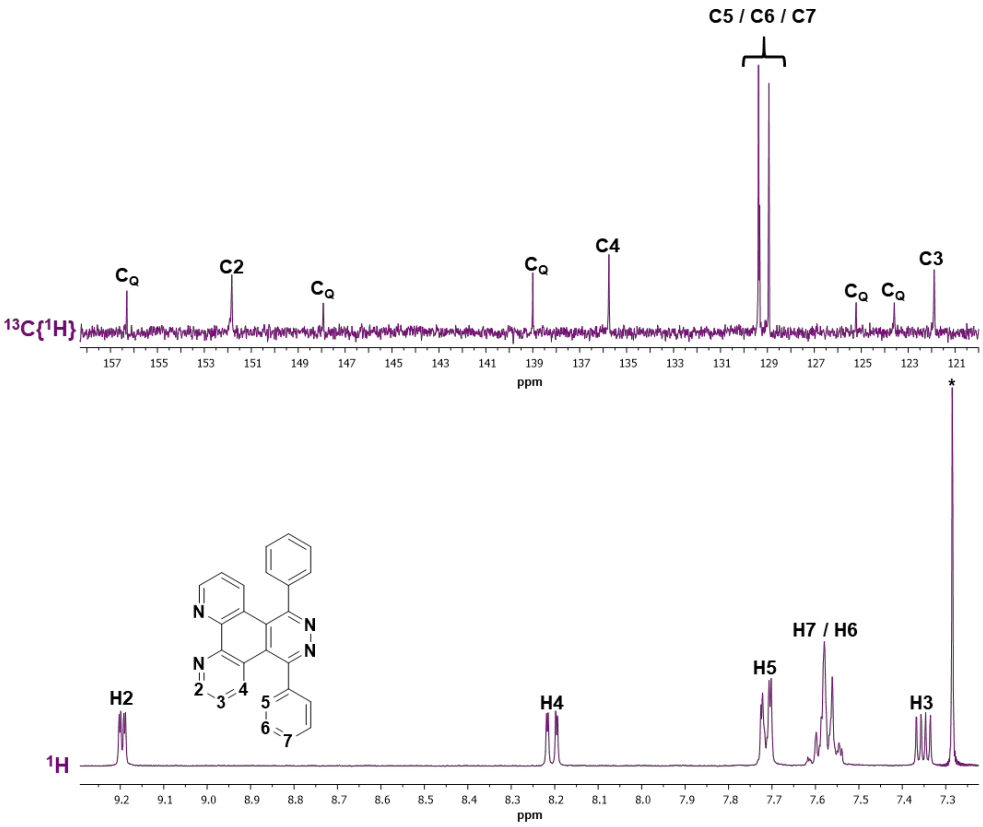

Figure 1. 19 $^{13}C\{^1H\}$ and ^1H NMR spectra of **4**. ($CDCl_3$. 400 MHz for ^1H, 100 MHz for $^{13}C\{^1H\}$. RT). C_Q = quaternary carbon.

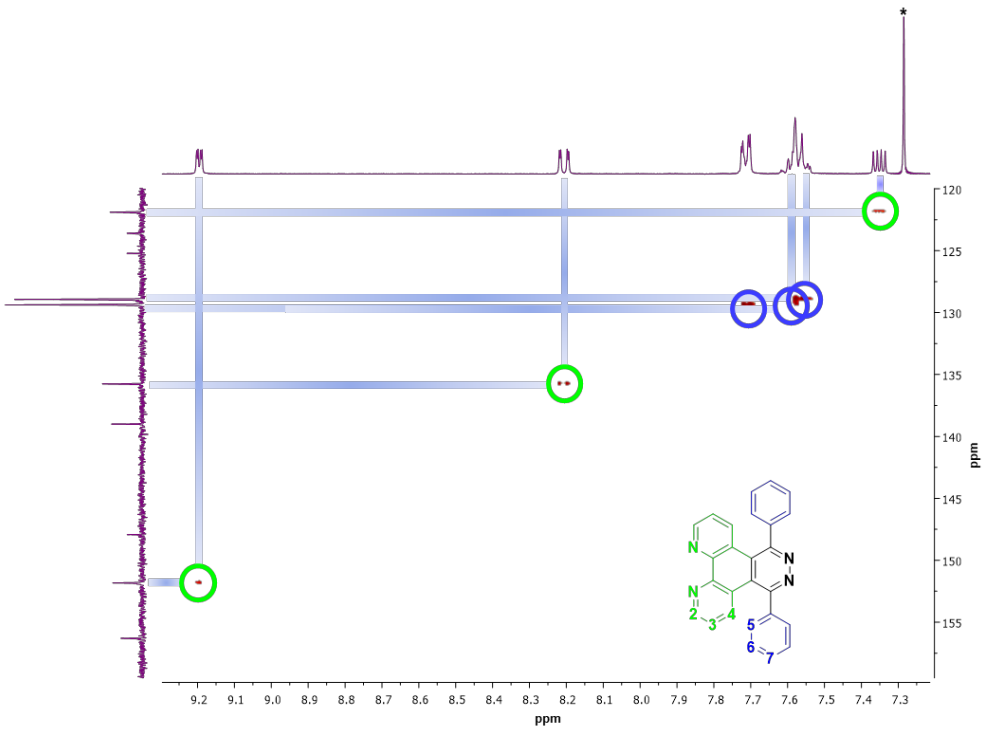

Figure 1. 20 HSQC spectrum of **4** showing the direct ^1H and $^{13}C\{^1H\}$ signal correlations. ($CDCl_3$. 400 MHz for ^1H, 100 MHz for $^{13}C\{^1H\}$. RT)

The three phenanthroline signals again follow the typical pattern of this ring system, with the most downfield signal corresponding to H2 at δ 9.2 ppm. Of all the generated compounds, the ^{1}H spectrum of **4** is the simplest, with the unusual *quasi*-singlet seen for **3** not visible here. The three phenyl signals follow the *o*, *p*, *m* sequence found for phenyl systems covalently attached to an electron withdrawing substituent or ring. This was confirmed through the use of the HSQC spectrum (Figure 1.20). The shifts are characteristic for aromatic rings of this kind.

1.4.4 Electrochemical Investigation of 14, 15, 3, and 4

Cyclic Voltammetry (CV) studies were carried out on 1x10^{-4} M solutions of **14**, **15**, **3**, and **4**, in CH_2Cl_2 (0.1 M nBu_4NPF_6). CV studies at concentrations of 1mM solutions did not give satisfactory resolution of the voltammogram. Cyclic voltammograms were recorded using an Ag/AgCl reference electrode, a Pt wire counter electrode, and a glassy carbon working electrode (See Chapter 5, Experimental).

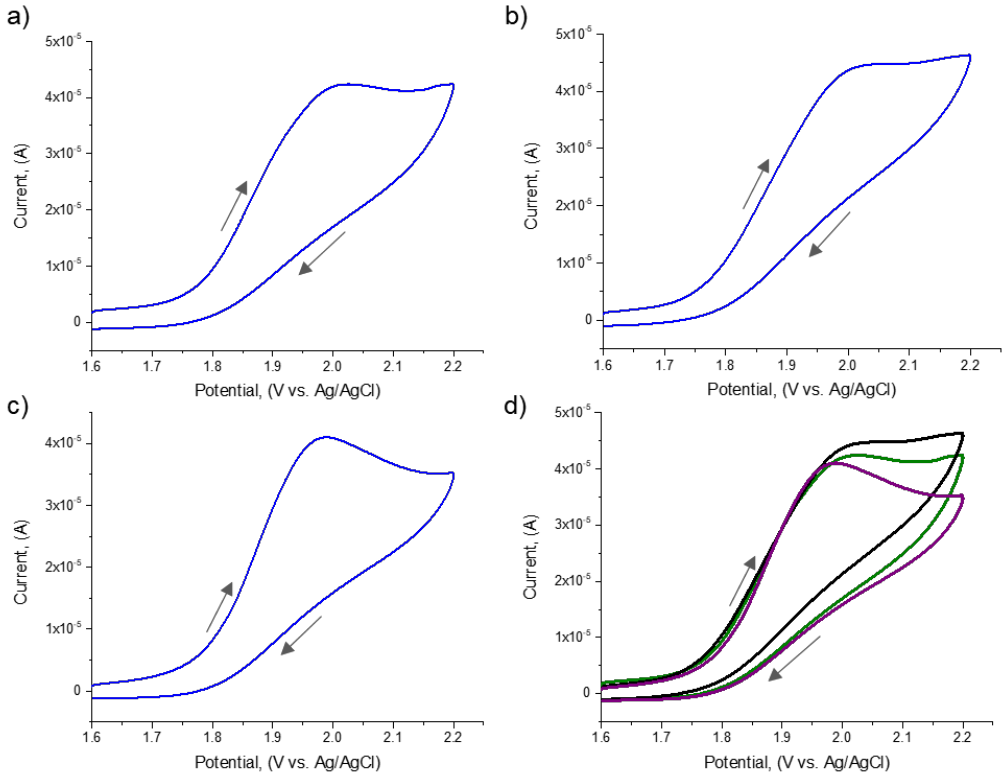

Figure 1. 21 Oxidative cyclic voltammograms of **14** (a), **15** (b), and **4** (c), in CH_2Cl_2 and 0.1 M $TBAPF_6$. Scan rate = 0.1 V/s. (d) Overlaid oxidative cyclic voltammograms of **14**, **15**, and **4**.

Figure 1.21(a)-(c) shows the oxidative cyclic voltammograms of **14**, **15**, and **4**. The oxidation of **3** appears to be beyond that of the solvent window of the CH_2Cl_2 solvent used its measurement. The three compounds in Figure 1.21 show irreversible oxidation processes at essentially the same oxidation potential (~2 V). This is shown in Figure 1.21(d). The similarity of these values suggests that the oxidation of each respective compound occurs at the phenanthroline ring system, *i.e.* the component found in all systems. These results suggest the HOMO of each compound is located on the phenanthroline ring system, and is little affected by the modification of the 5- and 6-positions of the ring system.

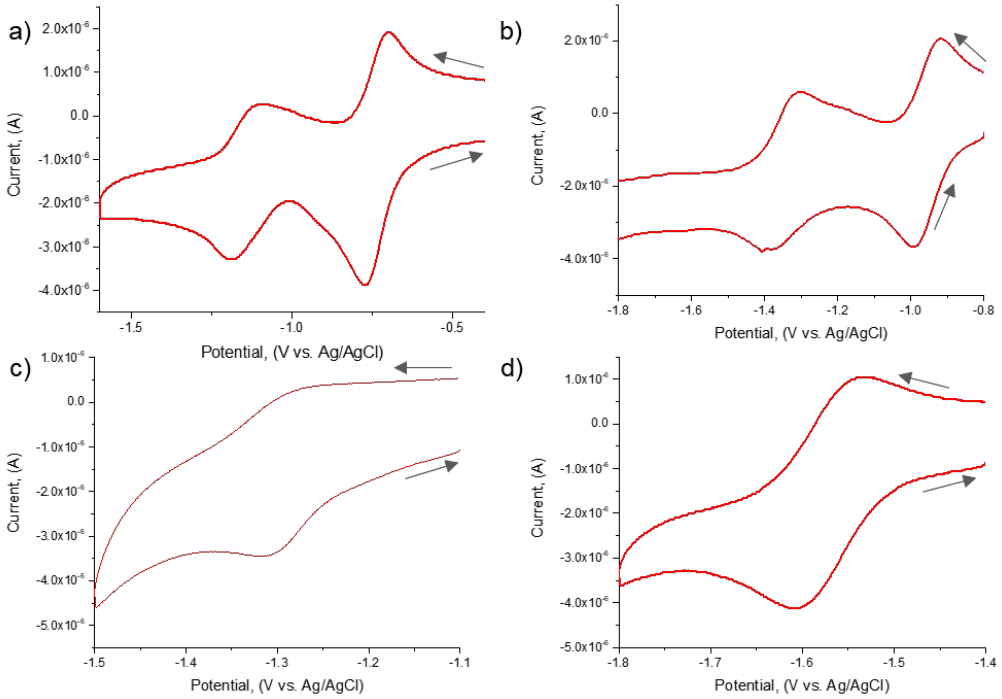

Figure 1. 22 Reductive cyclic voltammograms of **14** (a), **15** (b), **3** (c), and **4** (d), in CH_2Cl_2 and 0.1 M $TBAPF_6$. Scan rate = 0.1 V/s.

Reductive cyclic voltammograms were collected for **14**, **15**, **3**, and **4**. Unlike the oxidative processes shown earlier, many of the reductive processes are found to be reversible. Table 1.10 summarises the electrochemical data of each compound. **3** and **4** each show one reductive process respectively. The difference in the reduction potentials is undoubtedly due to the presence of the pyridazine ring within the PAH structure of **4**. **14** and **15**, comprising a quinone moiety, feature two reductive processes at very low values compared to **3** and **4**. A large amount of study has been carried out on quinone containing compounds,[52–54] with an agreement between authors that two reductive processes occur in a stepwise fashion, converting the quinone moiety to the semi-quinone, and then to the dianion.[55] The terminal

nature of the quinone moiety of **14** appears to facilitate the reductive processes at lower energies. Comparison to a number of literature compounds confirms this assignment in compounds **14** and **15**. Starting with the most basic system, para-benzoquinone, the first reductive process to the semi-quinone is observed at -0.45 V, with the second reductive process occurring at -1.07 V (*versus* Ag/AgCl).[56] The first system to introduce a quinone and an aromatic ring is 1,4-naphthoquinone, which undergoes the two step reduction at reduction potentials of -0.61 V and -1.04 V respectively (*versus* Ag/AgCl).[56] The effect of the aromatic ring on the electrochemical behaviour of the quinone system is immediately apparent. While there is essentially no change to the reduction potential of the second step to the dianion, the first reductive process occurs at a higher reduction potential (150 mV). This indicates that the first reduction to the semi-quinone is now more difficult compared to the non-aromatic benzoquinone. The effect of adding a second aromatic ring, in the construction of anthraquinone, continues this trend, with the first reductive process occurring at -0.77 V, and the second at -1.46 V (*versus* Ag/AgCl).[57] In this case, there is now a greater energetic challenge to generate the dianion, *versus* the semi-quinone. The compounds **14** and **15** sit neatly within similar reduction potentials. With **14**, the first process is of a similar energy to anthraquinone, but with the large PAH structure lowering the energy required for the second process. Compound **15** undergoes both processes with more difficulty when compared to **14**, but only shares similar reduction potentials with anthraquinone for the second reductive process. Larger structures bearing anthraquinone moieties feature generally similar values,[53,54] potentially indicating that modifications to the structure of the anthraquinone, beyond that of incorporating the quinone within a larger PAH ring system, has little effect on the quinone → semi-quinone → dianion energies. This suggests that future efforts to modulate the reductive processes of internal quinone moieties should be undertaken *via* PAH architectures *versus* that of appended systems.

Table 1.10. Electrochemical data for **14**, **15**, **3**, and **4**. (CH_2Cl_2. 0.1 M $TBAPF_6$. Scan rate = 0.1 V/s.). Samples prepared in air and purged with N_2 for 10 mins and for the duration of measurement.

Compound	Oxidation	Reduction
	E_{pa}/V	$E_{1/2}$/V, [ΔE_p/mV]
14	+2.02	-0.74 [77], -1.1 [188]
15	+1.98	-0.96 [60], -1.34 [60]
3	--	-1.35 [50]
4	+1.96	-1.58 [70]

1.4.5 Photophysical Investigation of 14, 15, 3, and 4

1.4.5.1 UV-visible Absorption Spectra of 14, 15, 3, and 4

The UV-visible absorption spectra of **14**, **15**, **3**, and **4** are shown in Figure 1.23, with data summarised in Table 1.11.

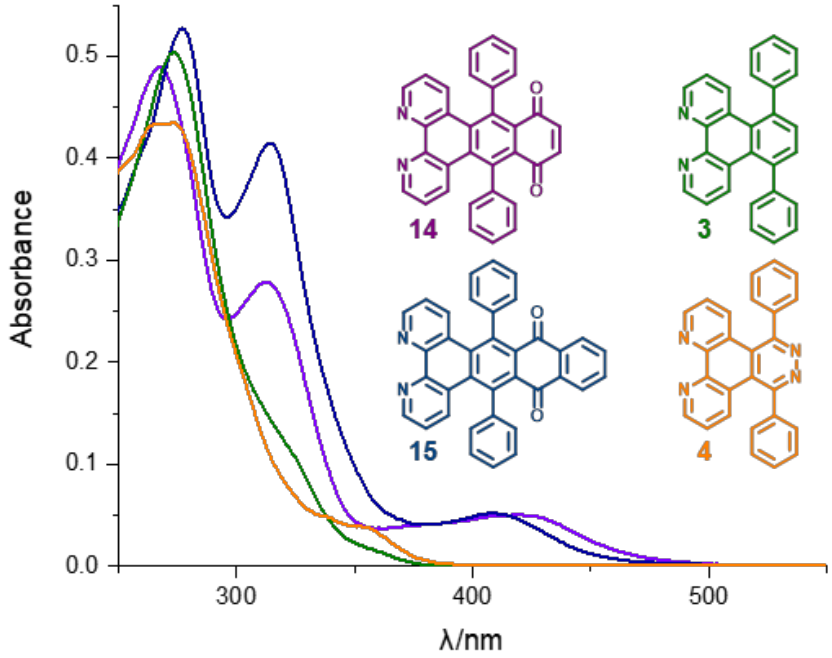

Figure 1. 23 UV-visible absorption spectra of **14**, **15**, **3**, and **4** in CH_2Cl_2 (10^{-5} M).

The quinone-containing compounds **14** and **15**, show similar absorption profiles, with low energy absorptions at λ_{abs} = 420 nm and λ_{abs} = 410 nm respectively. A second higher energy absorption is seen at *circa.* λ_{abs} = 315 nm for both compounds. With the final, and highest energy absorptions occurring for **14** at λ_{abs} = 268 nm, and λ_{abs} = 275 nm for **15**. The highest energy absorptions are assigned to the π-π* transitions within the phenanthroline ring system, and the pendant phenyl rings.[58] The weaker bands at *circa.* λ_{abs} = 315 nm for both quinone containing compounds contain transitions from the lower energy π-π* transitions. Some of these transitions are postulated as originating from the HOMO orbital located on the phenanthroline ring system, to the LUMO orbital of the quinone moiety. This assignment is aided by the CV data of the compounds presented earlier. The lowest energy transitions are assigned as n- π* transitions within the quinone moiety.[55] This assignment is aided by the lack of these transitions occurring in the non-quinone containing compounds **3** and **4**. As quinone moieties absorb in the visible region, the transitions in the visible region of the spectra of **14** and **15** confirm their inclusion in the molecular structure.

The absorption spectra of **3** and **4** are comparable also. Both feature intense absorptions at *circa.* λ_{abs} = 270 nm, once again assigned as π-π* transitions within the phenanthroline ring system and the pendant phenyl rings.[58] In **3**, this absorption band is also considered to include transitions within the middle benzene ring. In **4**, the modification of the middle ring to that of a pyridazine ring has a noticeable effect on the absorption spectra, with a small absorption band appearing at λ_{abs} = 355 nm. This is also observed for the similar structure of 1,4-diphenylphthalazine,[59] and occurs from transitions within the pyridazine ring.

Table 1.11. UV-visible spectral data for compounds **14**, **15**, **3**, and **4** in CH_2Cl_2 at RT (10^{-5} M).

Compound	**λ_{abs}/nm [ϵ x 10^4/M^{-1} cm^{-1}]**
14	268 [4.88], 310 [2.78], 420 [0.52]
15	275 [5.27], 315 [4.15], 410 [0.52]
3	275 [5.03], 325_{sh} [1.03], 360 [0.15]
4	265 [4.33], 270 [4.33], 355 [0.37]

Solvatochromism studies were performed for the four compounds, with their respective absorption profiles given in Figure 1.24. Solvents of varying polarity were chosen; CH_2Cl_2, MeOH, Diethyl ether, and THF. Maintaining a concentration of 10^{-5} M for all solutions, no significant change was seen for any of the compounds, indicating that the ground state energies of each of the respective compounds is unaffected by the solvent polarity. Charge transfer (CT) character is not observed for **14** and **15**, with the phenanthroline → quinone transition not involving a significant charge separation of the HOMO and LUMO orbitals.

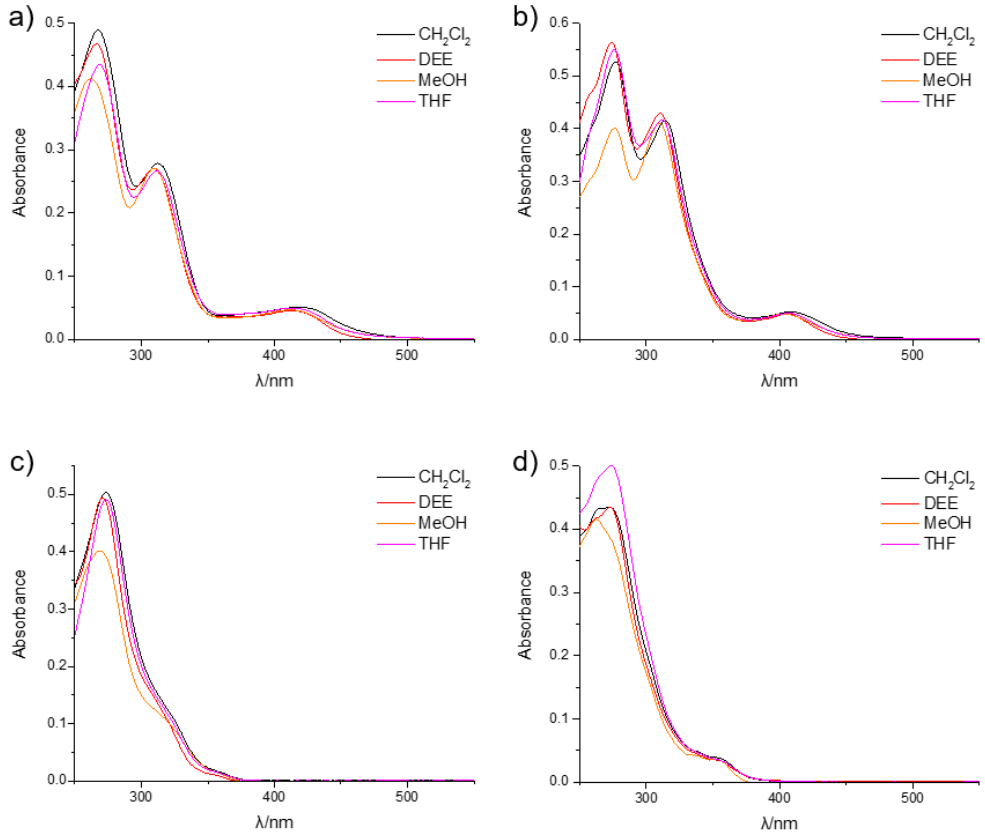

Figure 1. 24 Solvatochromism studies (UV-visible absorption spectra) of **14** (a), **15** (b), **3** (c), and **4** (d), in CH_2Cl_2, DEE, MeOH, and THF (10^{-5} M). DEE = Diethyl ether.

1.4.5.2 Emission Studies of 3

As compounds **14**, **15**, and **4** are non-emissive, or very weakly emissive, no emission studies could be obtained for these compounds. However, **3** is emissive, and the steady state emission spectra was recorded. The excitation spectra monitored at the peak emission wavelength was also collected. These are given in Figure 1.25(a).

On excitation at λ_{ex} = 275 nm, a single sharp emission band is observed at λ_{em} = 405 nm. The excitation spectrum, collected through monitoring the emission at λ_{em} = 405 nm, gives λ_{max} = 305 nm. The corresponding Stokes shift of **3** in CH_2Cl_2 is therefore 100 nm, or 8095 cm^{-1}.

Solvatochromism studies were performed for **3**, with the respective emission profiles given in Figure 1.25(b). Those solvents of varying polarity chosen for the UV-visible spectra were again chosen; CH_2Cl_2, MeOH, Diethyl ether, and THF. Maintaining a concentration of 10^{-5} M for all solutions, no significant change was seen for the peak emission wavelength, indicating that the ground state energy of **3** is unaffected by the solvent polarity. A broadening of the emission profile is observed in MeOH.

Due to the emissive nature of **3**, the fluorescence quantum yield was measured using the single-point relative method, using quinine sulfate as the reference, in CH_2Cl_2 at RT. The single-point method was utilised through calculation of the integrated emission intensities of both **3** and quinine sulfate, measured on the same instrument, with identical entrance and exit slit values. Optically dilute samples (Abs = ~0.1) of both **3** and quinine sulfate were prepared. The quantum yield of **3** *via* the single-point method was calculated as 0.02. Emission data is summarised in Table 1.12. For this method, see Experimental.

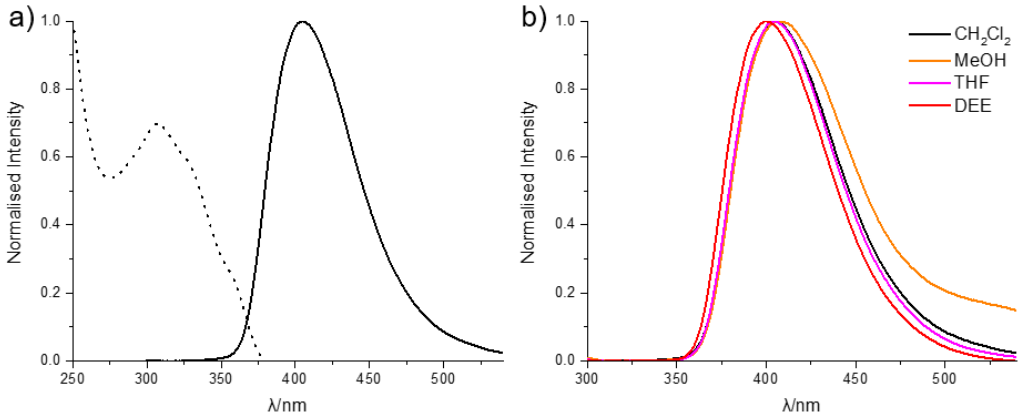

Figure 1. 25 (a) Normalised emission spectrum (solid line, λ_{ex} = 275 nm), and excitation spectrum (dashed line, λ_{em} = 405 nm) of **3** in CH_2Cl_2 (10^{-5} M). (b) Solvatochromism studies (emission spectra) of **3** in CH_2Cl_2, DEE, MeOH, and THF (10^{-5} M). DEE = Diethyl ether.

Table 1.12. Emission data for **3** in CH_2Cl_2 at RT (10^{-5} M).

Compound	λ_{ex}/nm	λ_{em}/nm	Φ
3	275	405	0.02

1.5 Further Synthetic Attempts & Future Work

Concurrent to the synthetic work summarised in the preceding sections, extensive attempts were made to devise synthetic routes to partially-fused PAH-type ligands from derivatives of the cyclopentadienone **2**. These were unsuccessful, but offer significant promise should they be realised towards a massive diversification of these ligand systems.

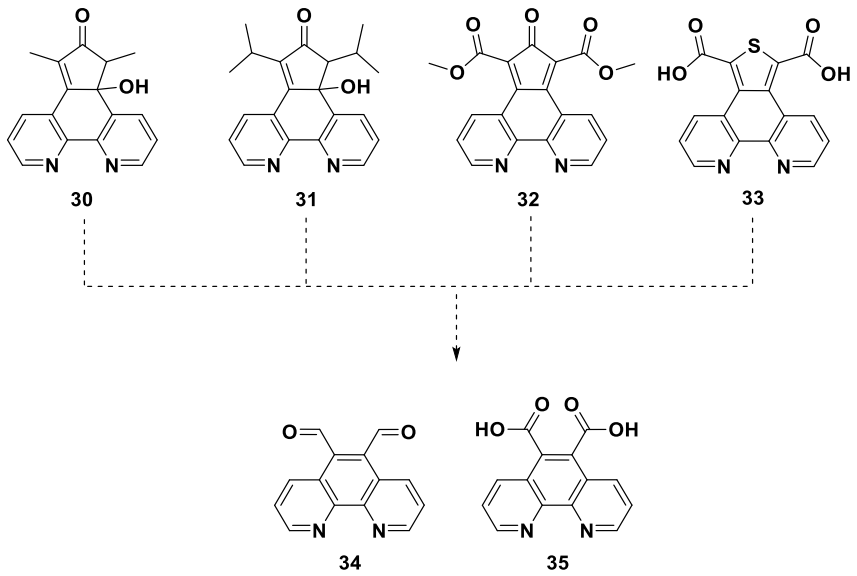

Scheme 1. 22 Unsuccessful synthetic attempts towards the "gateway" compounds **34** and **35**.

Scheme 1.22 shows four target molecules (**30**, **31**, **32**, and **33**) whose syntheses were attempted following either modified literature procedures for the all-carbon phenanthrene product, or synthetic preparations designed especially. These four target molecules would have allowed the generation of two "gateway" compounds, **34** and **35**. These gateway compounds could then be used to generate a range of novel ligand structures, giving access to the 5- and 6-positions of the phenanthroline ring system. **30** has already been referred to in this chapter, in discussion of the work of Warrener *et at*.[38] Attempts to ring open the compound at lower than 100 °C were unsuccessful, with dimerisation and rearrangement seen above this temperature. It was hoped that the generation of **31**, with the increased sterics of the isopropyl group (facilitated through synthetic modification of the monoketone precursor for the Knoevenagel reaction), would allow the ring opening reaction to occur using the newly optimised chlorobenzene/alumina method. However, this was not the case, and a similar result to the thermal rearrangement to **30** was observed. **30** and **31** would be converted to the gateway ligands **36** and **37** *via* modified haloform-type reactions. Here, the methyl or isopropyl ketones would be halogenated before undergoing nucleophilic acyl substitution on the addition of a base. The ring-opened products therefore require an α-hydrogen to the carbonyl. Use of the phenyl-containing ring opened product **13** from this chapter is therefore unsuitable.

As an intermediate between the isopropyl system **31** and the phenyl system **13** could not be found, attention turned to the tris-carbonyl system **32**. Here, the monoketone precursor to the Knoevenagel reaction is the commercially available dimethyl 3-oxopentanedioate. It was hoped that similar to the successful Knoevenagel reaction to generate cyclopentadienone **2**,

subsequent ring opening would generate the di-methyoxoacetate product. However, despite finding this product by HRMS studies, negligible yields were found across the numerous reaction conditions attempted, and this target was abandoned. A literature procedure exists to synthetically access the carboxylic acid product from methyoxoacetate systems,[60] and it was hoped to use this to achieve the desired target molecule **35**. Finally, attempts were made to generate the phenanthroline-thiophene target compound **33** in a similar fashion to the preceding Knoevenagel preparations. However, despite multiple attempts, the existence of this product was never found. Should the synthesis have been successful, several oxidative ring-opening preparations exist for thiophene-type ting systems, facilitating the generation of both gateway compounds **34** and **35**.

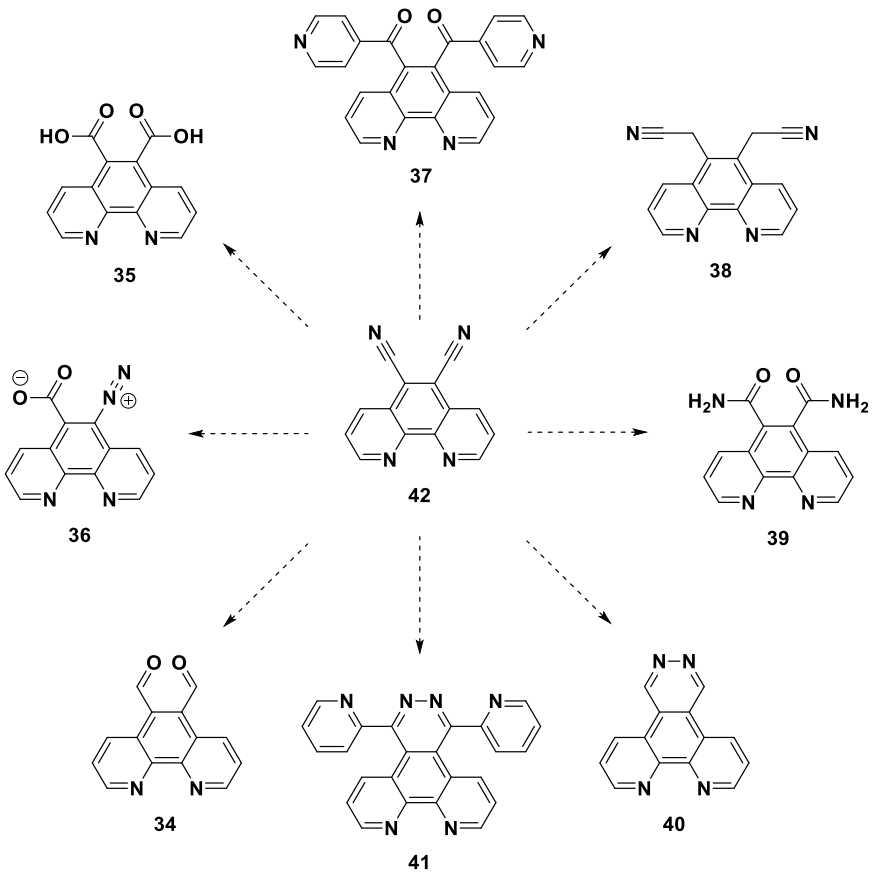

Scheme 1. 23 Potential ligands or compounds for further reaction from the "gateway" ligand **42**.

42 was chosen as the ideal target ligand for this study. Here, nitrile substitution at the 5- and 6-positions of the 1,10-phenanthroline ring system would act as readily changeable functional groups. Acid or base catalysed conversion of the nitriles to their corresponding amides would further allow their conversion to the corresponding carboxylic acids *via* hydrolysis. This

would give the di-carboxylic acid product **35** shown earlier in Scheme 1.22, which may be reduced to the corresponding di-aldehyde **34** (also given in Scheme 1.22), or further utilised towards the compounds given in Scheme 1.23 through their respective synthetic preparations. Of note, **36**, the diazonium-carboxylate product, offers a potentially facile route to the "phenaryne" system **6** presented earlier in this chapter.

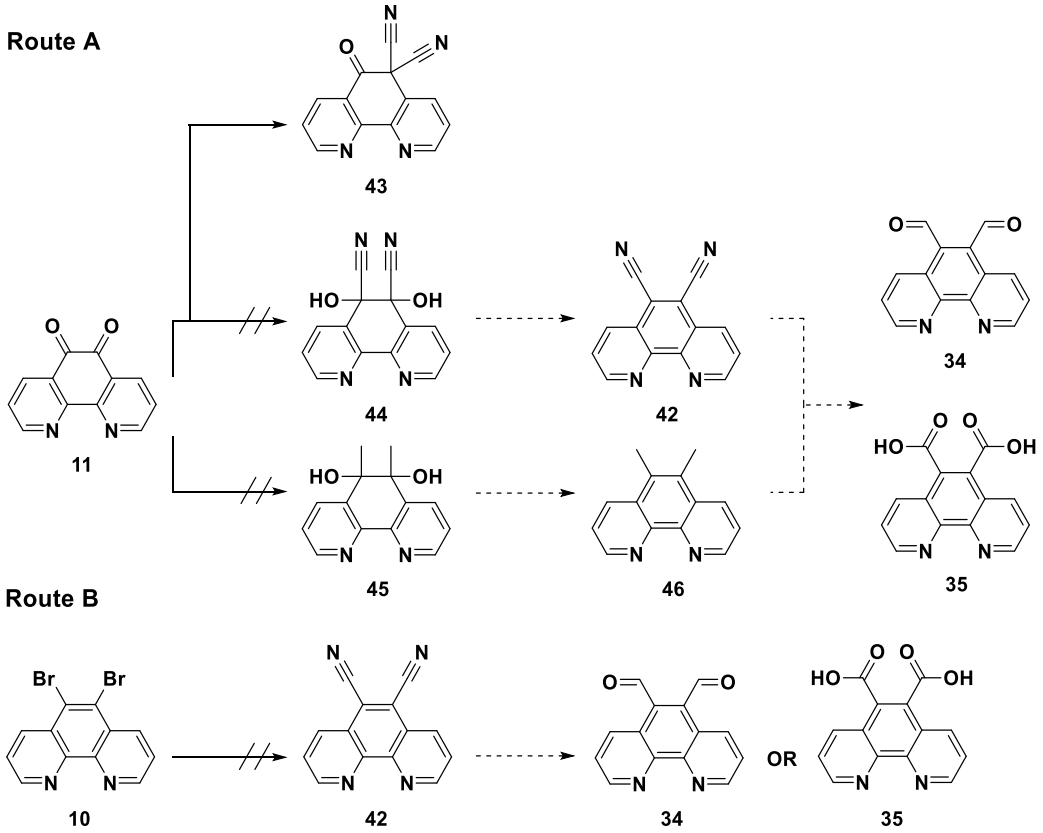

Scheme 1. 24 Unsuccessful synthetic attempts towards the "gateway" compounds **34** and **35**.

Scheme 1.24 shows two routes attempted towards the generation of the di-nitrile product **42**. Route A was initially attempted since the phendione product **11** could be generated in large quantities, and meant numerous reactions could be attempted simultaneously. Reaction of **11** with two different alkoxide reagents, delivering either methyl or nitrile functionalisation, would have allowed subsequent rearomatisation of the middle phenanthroline ring through loss of the hydroxyl groups. In the case of **44**, the target molecule would have been the desired di-nitrile product **42**, whereas with **46**, further oxidation of the methyl groups would have generated the respective di-aldehyde or di-carboxylic acid products. Neither reactions gave sufficient amounts of the diol products (**44** and **45**) necessary for further reaction. With respect to the di-nitrile product **44**, nucleophilic attack at one of the carbonyl moieties

appeared to occur rapidly in protic solvents, with the necessary second nucleophilic attack not occurring at ambient temperatures. Attempts to increase the reaction temperature appear to have facilitated this secondary step, but on analysis of the reaction mixture, the increased temperature also facilitated a pinacol-type rearrangement, regenerating one of the carbonyl moieties, **43**. As this process is irreversible, this route was reluctantly abandoned. The pinacol rearrangement problem was not seen for the dimethyl product, where it had been expected to be a problem.

Route B in Scheme 1.24 shows another attempted route, using the di-bromo product **10** used in earlier attempts to generate the "phenaryne" system **6**. Whilst conversion of ortho di-bromo species to their respective di-nitrile products is common, attempts here with a 1,10-phenanthroline system proved unsuccessful. Metalation at the iminic nitrogens with a Ru(II) centre, also did not yield any di-nitrile product when **50** was used as a ligand.

These routes offer potential rewards and the opportunity to realise 1,10-phenanthroline systems of varying functionalisation at the 5- and 6-positions. Synthetic access to these positions is crucial to realise a diverse library of extended phenanthroline ligands. Work is ongoing towards this goal.

1.6 Conclusion

An optimised route to **1** is reported through a room temperature Knoevenagel reaction with the soft base piperidine. The low-temperature generation of a 1,10-phenanthroline cyclopentadienone system **2** was realised, and further reacted with low boiling point or temperature sensitive dienophiles. This successfully increased the number of possible ligand architectures *versus* those generated *via* typical Diels-Alder reaction temperatures.

Optimisation of the synthetic route to **2** allowed for the successful synthesis of four partially-fused PAH-type ligands. These were characterised by a range of techniques including exhaustive NMR studies and single crystal X-ray diffraction. The two quinone-coupled ligands **14** and **15**, exhibit remarkable twists between the quinone ring and the phenanthroline ring system, with **14** being the first ligand structure combining phenanthroline complexation functionality, and a terminal quinone moiety. Two extended phenanthroline ligands, **3** featuring a fused benzene ring, and **4** featuring a fused pyridazine ring, allow the study influence of the heteroatom substitution in partially-fused PAH-type ligands.

Electrochemical and photophysical measurements of the four compounds were also conducted, revealing only **3** to be emissive.

1.7 References

1 S. M. Draper, D. J. Gregg and R. Madathil, *J. Am. Chem. Soc.*, 2002, **124**, 3486–3487.

2 V. Jurcik and R. Wilhelm, *Org. Biomol. Chem.*, 2005, **3**, 239–244.

3 A.-C. Knall and C. Slugovc, *Chem. Soc. Rev.*, 2013, **42**, 5131–5142.

4 C. R. Mayer, E. Dumas and F. Secheresse, *Chem. Commun.*, 2005, **0**, 345–347.

5 M.-J. Li, T.-Y. Lan, X.-H. Cao, H.-H. Yang, Y. Shi, C. Yi and G.-N. Chen, *Dalton Trans.*, 2014, **43**, 2789–2798.

6 A. Chouai, S. E. Wicke, C. Turro, J. Bacsa, K. R. Dunbar, D. Wang and R. P. Thummel, *Inorg. Chem.*, 2005, **44**, 5996–6003.

7 A. Rudi, Y. Benayahu, I. Goldberg and Y. Kashman, *Tetrahedron Lett.*, 1988, **29**, 6655–6656.

8 A. Plodek and F. Bracher, *Tetrahedron Lett.*, 2015, **56**, 1445–1447.

9 S. Jakobsen and M. Tilset, *Tetrahedron Lett.*, 2011, **52**, 3072–3074.

10 X. Li, D. Zhang, G. Lu, G. Xiao, H. Chi, Y. Dong, Z. Zhang and Z. Hu, *J. Photochem. Photobiol. A Chem.*, 2012, **241**, 1–7.

11 M. Carmeli and S. Rozen, *J. Org. Chem.*, 2005, **70**, 2131–2134.

12 S. A. De Pascali, D. Migoni, P. Papadia, A. Muscella, S. Marsigliante, A. Ciccarese and F. P. Fanizzi, *Dalton Trans.*, 2006, 0, 5077–5087.

13 C. Wang, L. Lystrom, H. Yin, M. Hetu, S. Kilina, S. A. McFarland and W. Sun, *Dalton Trans.*, 2016, **45**, 16366–16378.

14 W. Travis, C. E. Knapp, C. N. Savory, A. M. Ganose, P. Kafourou, X. Song, Z. Sharif, J. K. Cockcroft, D. O. Scanlon, H. Bronstein and R. G. Palgrave, *Inorg. Chem.*, 2016, **55**, 3393–3400.

15 Y.-J. Cho, S.-Y. Kim, M. Cho, K.-R. Wee, H.-J. Son, W.-S. Han, D. W. Cho and S. O. Kang, *Phys. Chem. Chem. Phys.*, 2016, **18**, 15162–15169.

16 J. M. Aslan, M. Yousufuddin, D. J. Boston and F. M. MacDonnell, *Inorg. Chim. Acta*, 2017, **454**, 216–221.

17 S. Singh, N. R. de Tacconi, N. R. G. Diaz, R. O. Lezna, J. Muñoz Zuñiga, K. Abayan and F. M. MacDonnell, *Inorg. Chem.*, 2011, **50**, 9318–9328.

18 Y. Chen, W. Lei, G. Jiang, Q. Zhou, Y. Hou, C. Li, B. Zhang and X. Wang, *Dalton Trans.*, 2013, **42**, 5924–5931.

19 Y. Na, P. Lincoln, J. R. Johansson and B. Nordén, *ChemCatChem*, 2012, **4**, 1746–1750.

20 S. P. Foxon, C. Green, M. G. Walker, A. Wragg, H. Adams, J. A. Weinstein, S. C. Parker, A. J. H. M. Meijer and J. A. Thomas, *Inorg. Chem.*, 2012, **51**, 463–471.

21 M.-J. Kim, R. Konduri, H. Ye, F. M. MacDonnell, F. Puntoriero, S. Serroni, S. Campagna, T. Holder, G. Kinsel and K. Rajeshwar, *Inorg. Chem.*, 2002, **41**, 2471–2476.

22 S. Singh, N. R. de Tacconi, D. Boston and F. M. MacDonnell, *Dalton Trans.*, 2010, **39**, 11180–11187.

23 D. J. Gregg, C. M. A. Ollagnier, C. M. Fitchett and S. M. Draper, *Chem. – Eur. J.*, 2006, **12**, 3043–3052.

24 C. Delaney, G. M. Ó Máille, B. Twamley and S. M. Draper, *Org. Lett.*, 2016, **18**, 88–91.

25 D. J. Gregg, E. Bothe, P. Höfer, P. Passaniti and S. M. Draper, *Inorg. Chem.*, 2005, **44**, 5654–5660.

26 L. P. Wijesinghe, B. S. Lankage, G. M. O. Maille, S. D. Perera, D. Nolan, L. Wang and S. M. Draper, *Chem. Commun.*, 2014, **50**, 10637–10640.

27 D. Nolan, B. Gil, L. Wang, J. Zhao and S. M. Draper, *Chem. – Eur. J.*, 2013, **19**, 15615–15626.

28 A. Graczyk, F. A. Murphy, D. Nolan, V. Fernandez-Moreira, N. J. Lundin, C. M. Fitchett and S. M. Draper, *Dalton Trans.*, 2012, **41**, 7746–7754.

29 F. A. Murphy and S. M. Draper, *J. Org. Chem.*, 2010, **75**, 1862–1870.

30 S.-E. Suh, S. A. Barros and D. M. Chenoweth, *Chem. Sci.*, 2015, **6**, 5128–5132.

31 L. Xin, J. Xue, G. Lei and J. Qiao, *RSC Adv.*, 2015, **5**, 42354–42361.

32 D. Margetić, Y. Murata, K. Komatsu and Ž. Marinić, *Helv. Chim. Acta*, 2009, **92**, 298–312.

33 F. Thebault, A. J. Blake, C. Wilson, N. R. Champness and M. Schroder, *New J. Chem.*, 2006, **30**, 1498–1508.

34 S. Tokita, K. Hiruta, S. Ishikawa, K. Kitahara and H. Nishi, *Synthesis*, 1982, **10**, 854–855.

35 S. Monro, J. Scott, A. Chouai, R. Lincoln, R. Zong, R. P. Thummel and S. A. McFarland, *Inorg. Chem.*, 2010, **49**, 2889–2900.

36 E. N. Dixon, M. Z. Snow, J. L. Bon, A. M. Whitehurst, B. A. DeGraff, C. Trindle and J. N. Demas, *Inorg. Chem.*, 2012, **51**, 3355–3365.

37 G. A. Slough, V. Krchňák, P. Helquist and S. M. Canham, *Org. Lett.*, 2004, **6**, 2909–2912.

38 R. N. Warrener, M. A. Houghton, A. C. Schultz, F. R. Keene, L. S. Kelso, R. Dash and D.

N. Butler, *Chem. Commun.*, 1996, **0**, 1151–1152.

39 G. Y. Wooi and J. M. White, *Org. Biomol. Chem.*, 2005, **3**, 972–974.

40 S. Rasheed, D. N. Rao, A. S. Reddy, R. Shankar and P. Das, *RSC Adv.*, 2015, **5**, 10567–10574.

41 U. Siemeling, T. Klemann, C. Bruhn, B. Neumüller and K. Dehnicke, *Zeitschrift für Anorg. und Allg. Chemie*, 2008, **634**, 895–900.

42 S. E. Wheeler and K. N. Houk, *J. Am. Chem. Soc.*, 2008, **130**, 10854–10855.

43 R. Einholz, T. Fang, R. Berger, P. Grüninger, A. Früh, T. Chassé, R. F. Fink and H. F. Bettinger, *J. Am. Chem. Soc.*, 2017, **139**, 4435–4442.

44 H. Brockmann, *Liebigs Ann. der Chemie*, 1988, **1988**, 1–7.

45 H. Wang, Y. Liang, Y. Wang, H. Xie, L. Feng, H. Lu and S. Feng, *RSC Adv.*, 2014, **4**, 17171–17178.

46 P. R. Kumar, *J. Chem. Soc., Chem. Commun.*, 1989, 509–510.

47 D. F. Evans and M. W. Upton, *J. Chem. Soc., Dalt. Trans.*, 1985, 1141–1145.

48 A. P. Marchand, G. Srinivas and W. H. Watson, *Arkivoc*, 2002, **3**, 8.

49 X. Wang, L. Xu, D. Mu, H. Wang and S. Feng, *RSC Adv.*, 2016, **6**, 23335–23339.

50 T. H. Vo, U. G. E. Perera, M. Shekhirev, M. Mehdi Pour, D. A. Kunkel, H. Lu, A. Gruverman, E. Sutter, M. Cotlet, D. Nykypanchuk, P. Zahl, A. Enders, A. Sinitskii and P. Sutter, *Nano Lett.*, 2015, **15**, 5770–5777.

51 L. Li, M. Chen, H. Zhang, H. Nie, J. Z. Sun, A. Qin and B. Z. Tang, *Chem. Commun.*, 2015, **51**, 4830–4833.

52 N. Gupta and H. Linschitz, *J. Am. Chem. Soc.*, 1997, **119**, 6384–6391.

53 J. E. Gautrot, P. Hodge, D. Cupertino and M. Helliwell, *New J. Chem.*, 2007, **31**, 1585–1593.

54 J. E. Gautrot, P. Hodge, D. Cupertino and M. Helliwell, *New J. Chem.*, 2006, **30**, 1801–1807.

55 R. Díaz, O. Reyes, A. Francois, A. M. Leiva and B. Loeb, *Tetrahedron Lett.*, 2001, **42**, 6463–6467.

56 M. Martínez-Cifuentes, R. Salazar, O. Ramírez-Rodríguez, B. Weiss-López and R. Araya-Maturana, *Molecules*, 2017, **22**, 577.

57 J. Tsunetsugu, S. Tanaka, S. Ebine and K. Morinaga, *J. Chem. Soc., Perkin Trans.*, 1988, 1541–1545.

58 J. M. Stanley, C. K. Chan, X. Yang, R. A. Jones and B. J. Holliday, *Polyhedron*, 2010, **29**, 2511–2515.

59 J. Li, J. Gao, W.-W. Xiong and Q. Zhang, *Tetrahedron Lett.*, 2014, **55**, 4346–4349.

60 A. K. Padala, V. Saikam, A. Ali and Q. N. Ahmed, *Tetrahedron*, 2015, **71**, 9388–9395.

Chapter 2

Transition Metal Complexes Bearing Extended 1,10-Phenanthroline PAH-type Ligands

Part 2 of 2

2.1 Introduction

2.1.1 Ru(II) and Ir(III) Photochemistry

Of all the transition metals photochemically studied, ruthenium has long stood as the most widely investigated and studied, of which the class of polypyridine complexes holds the highest research interest.[1,2] This extensive interest is due to a number of favourable characteristics of Ru(II) polypyridine complexes including their redox properties and their chemical stability in a vast number of solvents.[1] This is in tandem with both their tuneable luminescence emission and relatively long excited state lifetimes. The latter is often desired for photochemical applications, as a long excited state lifetime allows further reactions to occur.[1,3] Common reactions for the photoexcited complex include energy transfer and reductive and oxidative quenching.[4,5] Particularly useful is the ability to use $[Ru(bpy)_3]^{2+}$ as a model system for most Ru(II) complexes comprising of six coordinate aromatic ring-containing nitrogen atoms in an octahedral coordination environment.[1]

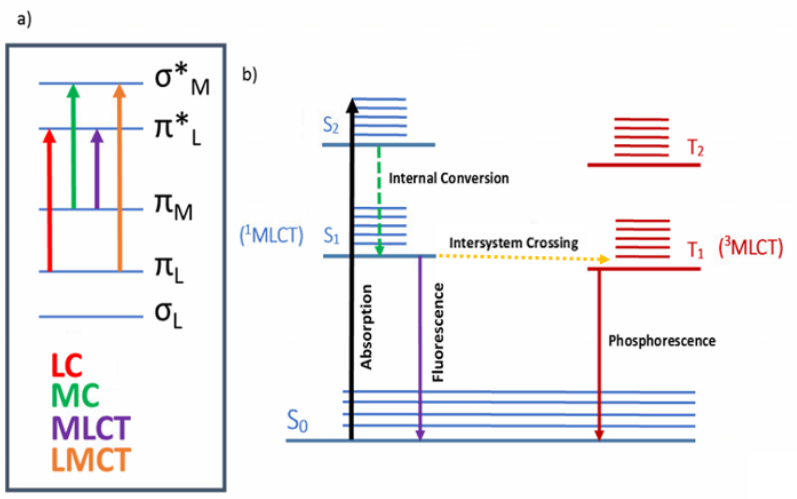

Figure 2. 1 a) Simplified molecular orbital diagram for typical Ru(II) polypyridine complexes in an octahedral coordination environment. b) Simplified Jablonski diagram showing some common radiative and non-radiative processes.

Beginning in the 1940's, the development of Ligand Field Theory (LFT) quickly paved the way for the development of photophysical behaviour being described *via* electronic configurations, energy level diagrams and selection rules. When these conditions are applied to photochemical systems, the systems response to the absorption of light may be described by use of a molecular orbital (MO) diagram. In Figure 2.1, a standard MO diagram for d^6 octahedral complexes is shown. Further detail is given by Figure 2.2. Whilst each orbital is

molecular in nature, each orbital can be distinguished as being essentially ligand or metal, due to the larger contribution of one or the other's atomic orbitals. On the absorption of an appropriate energy photon, the promotion of an electron can transition through one of four common types of transitions in the generation of an excited state. These four types are Ligand Centred (LC), Metal Centred (MC), Ligand-to-Metal Charge Transfer (LMCT) and Metal-to-Ligand Charge Transfer (MLCT) and are all shown in Figure 2.1. The lowest energy transition is often the most important for the determination of the excited state properties and expected reactivity, and therefore it can be said that the greatest effect to the orbital energies can be found in the oxidation state of the metal, and the electronic properties of the ligand.

In the $[Ru(bpy)_3]^{2+}$ model complex, and indeed most Ru(II) polypyridine complexes, it is found that the lowest energy transition is a Metal-to-Ligand Charge Transfer (MLCT) transition.[6] MLCT absorption bands of Ru(II) polypyridine centres are usually intense due to their allowed nature by both spin and Laporte selection rules.[7] If the excited electron is not consumed by a secondary process, relaxation of the excited state will occur to its natural ground state. This relaxation may occur *via* a radiative or non-radiative process which are summarised in Figure 2.1. Although ligand photosubstitution can occur for Ru(II) polypyridine complexes,[8] the rigid nature of its bidentate based octahedral binding, and its low energy MLCT prevents substitution from readily occurring.[1] This correlates with the Frank-Condon principle, which states that electronic transitions occur at a faster rate than atomic movements.[9] The basis of this principle is that transitions occur faster if there is an overlap of the initial and final vibrational excited state. As the excited state geometry of the Ru(II) complex is confined to that of its ground state, there is a large overlap in the states, and as such there is a low energy barrier to electronic transitions. As electronic transitions often populate higher excited states, rapid internal conversion (IC) occurs to the lowest singlet state (S_1, ^{1}MLCT), and thus obeys Kasha's rule allowing for further photon emission.[10,11] As can be seen in Figure 2.1, photon emission from S_1 can occur directly through fluorescence, returning the molecule to its ground state (S_0), or can undergo intersystem crossing (ISC) to its triplet excited state (T_1, ^{3}MLCT). For Ru(II) polypyridine complexes, the efficiency of the formation of the lowest excited state, ^{3}MLCT, is expected to be essentially unity due to spin-orbit coupling caused by the heavy Ru atom.[1] The triplet excited state also exists at a lower energy due to Hund's rule, which states that minimum repulsion occurs between electrons of the same spin in separate orbitals.[9] As phosphorescence requires both an emission of a photon similar to fluorescence, but also the secondary inversion of the electron spin to return to the ground state, the excited state lifetime is much longer than that of the excited singlet state and it is this extended lifetime that allows for further reaction to occur.[3,12,13]

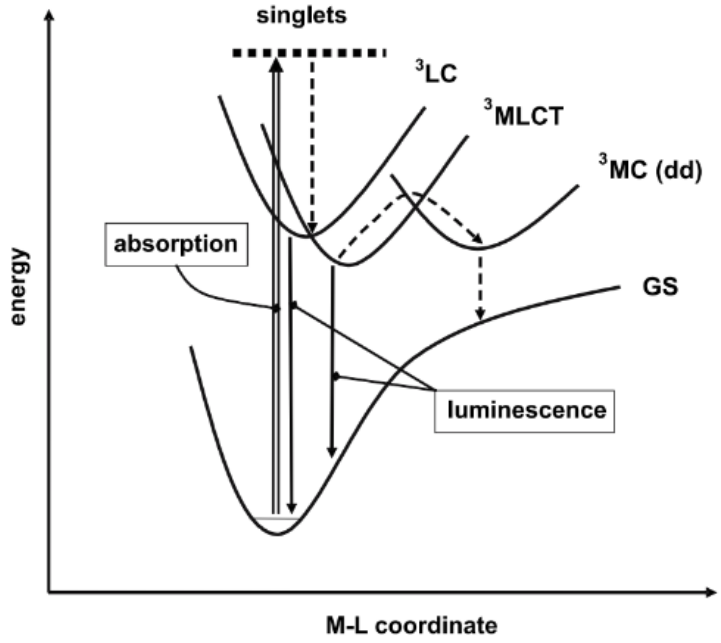

Figure 2. 2 Electronic transitions of d^6 complexes. LC, MLCT, and MC are shown. MC levels are not emissive. GS = ground state.[14]

Ir(III) centres, comprising of the general formula $[Ir(C^N)_2(N^N)]^+$, are increasingly used in fields typically historically dominated by Ru(II) polypyridine complexes, due to their similar photophysical properties,[14] and enhanced photostabilities.[15,16] Whilst commonly suffering from poorer absorption in the visible region, increased Turnover Number (TON) and Turnover Frequency (TOF) values are often observed for Ir(III) centres *versus* Ru(II) centres bearing the same participating ligand, and similar ancillary ligands. In these cases, TONs are defined as the number of moles of H_2 formed per mole of catalyst, while the TOF is defined as the turnover per time. The emergence of cyclometalated Ir complexes for use in Organic Light Emitting Diode applications has also resulted in a dramatic increase in the synthetic preparations of a large range of Ir complexes.[14,17,18] Similar to Ru(II), luminescence is often exclusively phosphorescent in character, due to the large spin orbit coupling of the 3rd row transition metal. Also, whilst MC levels are often thermally accessible to Ru(II) centres, the ligand field splitting is quite large for Ir(III), and thus the MC levels are pushed too high to be involved in the emission properties of Ir(III) centres.[14] As the Δ_{Oct} increases down a group, there is a large octahedral splitting for Ir as a third row transition metal. Further to this, the cyclometalating nature of the phenylpyridine ancillary ligands also result in a large Δ_{Oct}. Whilst Ru(II) compounds typically do not undergo direct transitions from S_0 to T_1, this transitions well documented for Ir(III) compounds.[16,19,20]

2.1.2 General Introduction

As per Chapter 1, there is a lack of partially-fused PAH-type ligands in the literature which offers an opportunity to rapidly expand this field in an exploration of ligands and complexes of this type. As mentioned, the goal of this study is to then determine if those partially-fused systems may be used in the place of fully-fused ligand systems, without loss of their desirable photophysical properties. As the field of PAH-type ligands lacks significant numbers of transition metal complexes bearing partially-fused ligands compared to fully-fused systems, discussion of both will again be necessary. As a detailed introduction to the ligands is given in Chapter 1, this chapter will comment only on close literature comparators, before the introduction of Ru(II) and Ir(III) centres bearing the novel ligands generated in Chapter 1. As many of these systems are utilised in the photocatalytic reduction of protons to H_2, studies towards this goal will also be discussed.

2.1.3 Ru(II) Complexes Bearing 1,10-Phenanthroline-Pyrazine Ligand Structures

Chart 2.1 shows some Ru(II) complexes bearing 1,10-phenanthroline-pyrazine ligand structures.

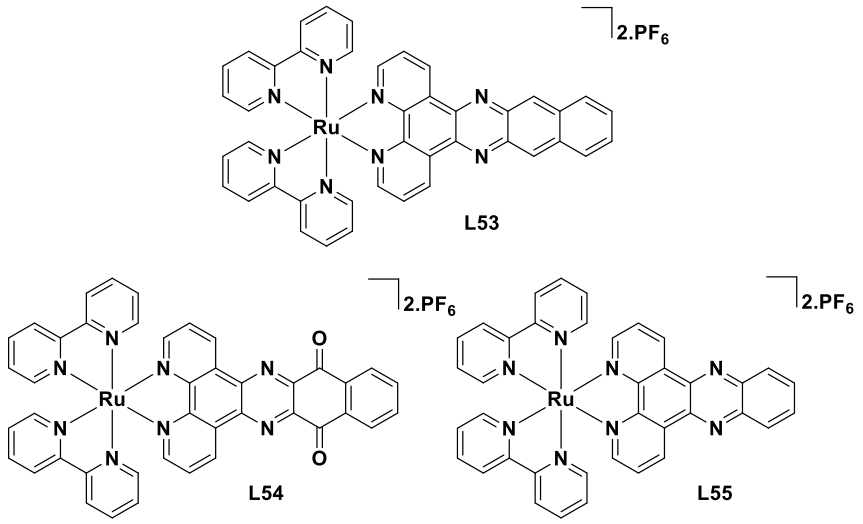

Chart 2. 1 Literature examples of Ru(II) complexes bearing 1,10-phenanthroline-pyrazine ligand structures.

L53, bearing the large benzo[i]dipyrido[3,2-a:2',3'-c]phenazine (dppz) ligand is well documented as an efficient photocleaver of DNA.[2] As large conjugated PAH-type ligands are often used as intercalators for DNA, the long planar structure assists in the binding of the

complex with DNA. The complex is then photoexcited, generating singlet oxygen, which acts as the reactive oxygen species (ROS) during the photodynamic therapy process.[21] As **L53** is a fully-fused system, the extensive delocalisation of the π-system assists with the lowering of the absorption wavelength to lower energies.

This lowering of the ^{1}MLCT absorption is a fundamental aspect of DNA intercalation chemistry, with many other systems designed with this crucial consideration being the primary goal of the work. This focus is due to the desire for low energy wavelengths, which can reach deeper into human tissue *versus* that of high energy wavelengths. **L54**, similar in structure to **L53**, is comprised of a "naphthoquinone" moiety, and is not used towards DNA intercalation. Work by Na *et al.* utilises **L54** as a multi-electron collector towards the catalysis of CO_2 to MeOH, using a Co-based catalyst.[22] As most Ru(II) centres only undergo a single electron processes on excitation, this process is not overly efficient for the multi-electron reduction of CO_2. The authors report collection of two electrons into the quinone moiety (reduction firstly to the semi-quinone, and secondly to the hydroquinone), before the transfer of both electrons to the Co catalyst. Whilst the authors do admit the turnover numbers are quite low, this was the first attempted use of a quinone-containing ligand towards catalysis. The important conclusion of their work indicated that multi-electron transfer systems outperformed their single-electron transfer analogues.

The final system in Chart 2.1 is **L55**, with the participating ligand as dipyrido[3,2-a:2',3'-c]phenazine (dppz). First developed by Friedman *et al.*,[23] dppz was used as a "molecular light switch" for DNA. The complex, which shows no luminescence as the free species in aqueous solutions, becomes intensely luminescent on binding to DNA. The reason for this "switching" behaviour is that in aqueous solutions, hydrogen bonding with the pyrazine nitrogen atoms quenches the luminescence of the complex. Upon intercalation, no H-bonding can occur, and the luminescence of the compound is unaffected.[24] As the prototypical pyrazine-PAH system, dppz has found numerous research uses, most involving studies of DNA or nucleic acid interaction. One interesting study by Li *et al.*, encapsulates **L55** into apoferrin, a small protein capable of encapsulating Fe.[25] The loaded nanocomposites showed reduced cytotoxicity, enhanced cellular uptake, and improved water solubility. The nanocomposites were then investigated towards targeted tumour delivery, showing promise for the bioapplication of protein nanocages containing photoactive Ru(II) complexes.[25]

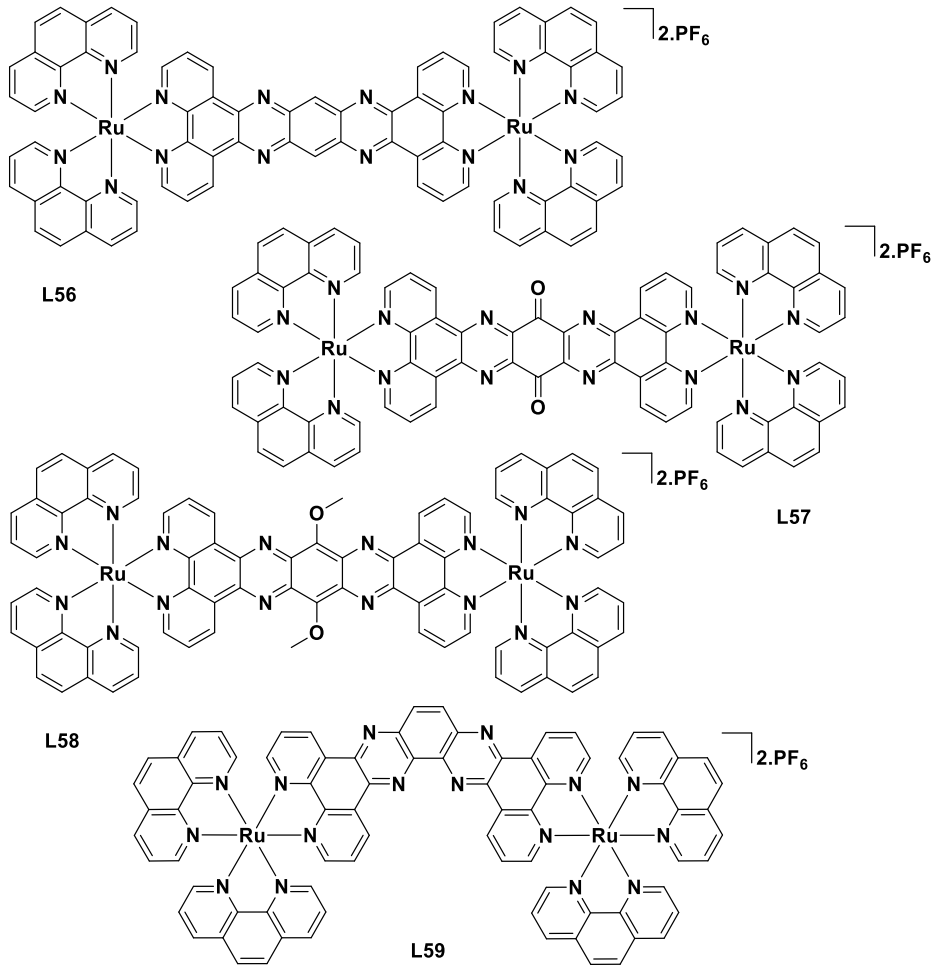

Chart 2. 2 Literature examples of bimetallic Ru(II) complexes via phenanthroline-pyrazine bridging ligand structures.

Chart 2.2 shows four bimetallic complexes bearing large PAH-type ligands. **L56**,[26] **L57**,[26] **L58**,[27] and **L59**[28] were all investigated towards photoinitiated electron collection (PEC).

L56 and **L57** were generated as part of work by Kim *et al.*,[26] with extensive photophysical, electrochemical, and computational work revealing the existence of low lying acceptor orbitals in the centre portion of the ligands, which effectively quench all expected luminescence. As the luminescence was expected to be that originating from a Ru(II) ^{1}MLCT excitation, the authors propose an intramolecular charge transfer mechanism to specific parts of the bridging ligand as responsible for the luminescence quenching. **L57** may be generated from the "on-complex" oxidation of the large bridging ligand of **L56**, using ammonium persulfate.[26] **L58**, may be considered a trapped form of **L57**, as the di-methoxy functionality in the central component of the bridging ligand may be converted to that of the quinone bridging ligand in **L57** through excitation of the Ru(II) centres. This photoinduced transformation occurs both with or without a triethylamine (TEA) sacrificial agent. This

work, by Singh *et al*.,[27] demonstrates that **L57** and **L58** are capable of reversibly storing two, and four electrons respectively. **L59**, a "bent" version of **L56** is reported once again by Singh *et al*.[28] In the study of the direct comparison of **L56** and **L59**, **L59** reports some advantages over the linear **L56**. Capable of a reversible two-electron storage, **L59** stores the electrons at reduction potentials 500 mV more negative than **L56**. However, **L59** suffers from radical-dianion dimerisation side reactions not seen for **L56**. The authors propose that this issue may be overcome through careful inclusion of steric bulk at the likely sites of the dimerisation.

Whilst not exhaustive, the small selection of complexes shown in Charts 2.1 and 2.2 demonstrate the most common uses for complexes (and PAH-type ligands) of this kind. Of great interest for these complex types is the research field of the photocatalytic reduction of protons into H_2, and this will now be discussed. This interest is driven mainly by the high research interest of the corresponding photooxidation of H_2O, which can ideally be combined into a single device.

2.1.4 TM Complexes Bearing PAH-type Ligands for Photocatalytic Proton Reduction

Chart 2.3 shows six bimetallic compounds suitable for the photocatalytic reduction of protons to molecular H_2. While photocatalytic proton reduction will be discussed in detail later, the introduction of these bimetallic systems here offers an opportunity to discuss the synthetic diversity of fully- and partially-fused PAH-type ligands towards this research goal.

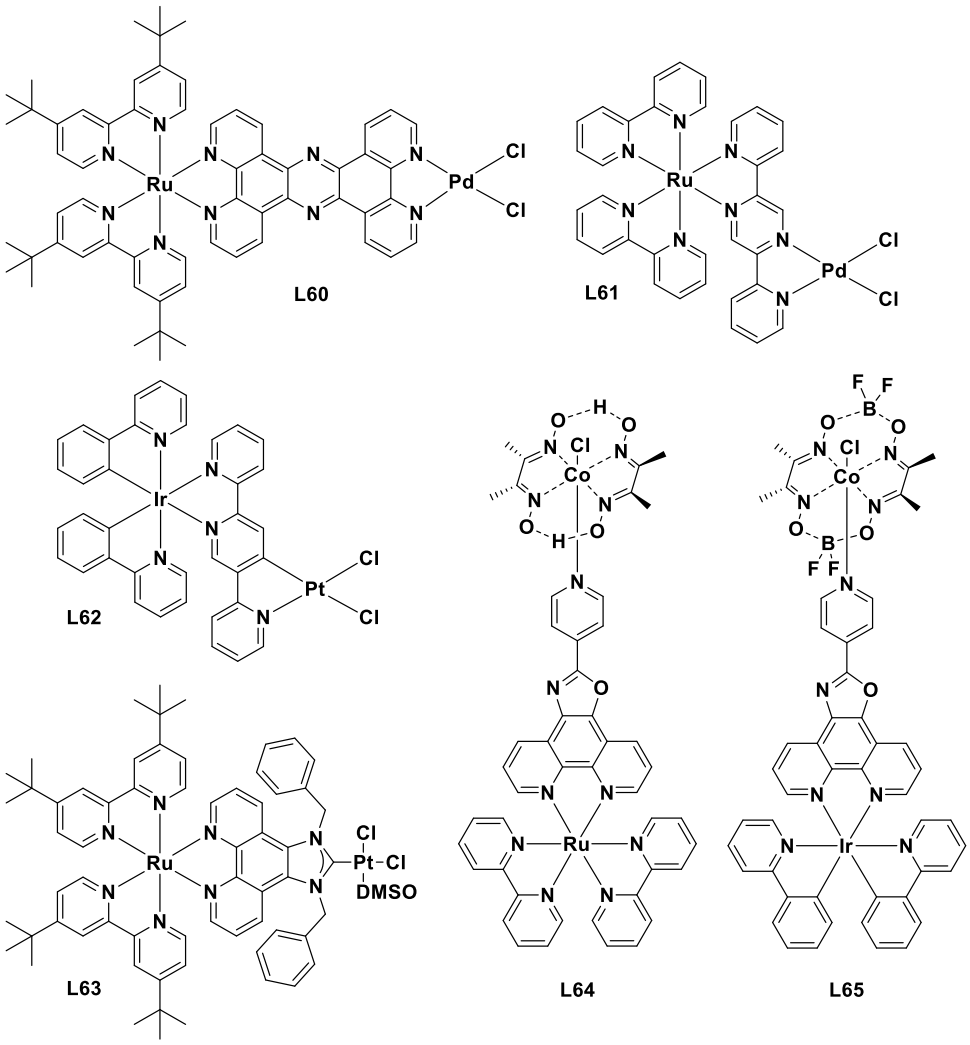

Chart 2. 3 Literature examples of bimetallic transition metal complexes bearing fully- or partially-fused PAH-type ligands for the photocatalytic reduction of protons to H_2.

One of the most ubiquitous ligands towards photocatalytic proton reduction in the literature is tetrapyrido[3,2-a:2',3'-c:3",2"-h:2"',3"'-j]phenazine, or tpphz.[29–32] **L60**, shows tpphz as a bridging ligand between a Ru(II) photosensitiser centre, and a Pd(II) proton reduction centre. The fully fused nature of tpphz allows efficient electron transfer from the Ru metal centre, to that of the Pd metal centre.

L61 and **L62**, while not strictly PAH-type ligands, show two binding modes of the proton reduction catalyst centre. Whilst **L61** includes a Ru(II) centre, and **L62** includes an Ir(III), the binding mode is the same, with N^N-type bidentate coordination to both metals. **L61** repeats this N^N binding mode for the proton reduction catalyst (Pd). However, **L62** shows a C^N cyclometalation coordination of the proton reduction catalyst centre (Pt). Both systems were also tested without the deliberate coordination of the proton reduction centre, *i.e.* simply

as a normal photosensitiser. However, in both instances, lower turnover numbers were observed for these systems.

L63 is a partially-fused PAH-type ligand showing a standard N^N type coordination site for the photosensitiser centre at the phenanthroline ring system of the ligand, with a substantially rarer N-heterocyclic carbene-type binding to the proton reduction centre (Pt). Developed by Kaufhold *et al.,*[33] an *in situ* ligand exchange of the chlorides to iodides results in a 500-fold increase in the turnover frequency of the photocatalyst. The authors note the stability of the carbene-Pd bond *versus* that of the normal N^N bidentate-type coordination.

The final two systems in Chart 2.3, **L64**[34] and **L65**[35] both incorporate a PAH-type oxazole ligand, 2-(pyridin-4-yl)oxazolo[4,5-f][1,10]phenanthroline. **L64** features a Ru(II) photosensitiser centre, while **L65** features an Ir(III) photosensitiser centre. Both feature a Co proton reduction catalyst, which itself has structural modifications between **L64** and **L65**. The former Co centre is constructed as a H-bridged cobaloxime, while the latter is constructed as a BF_2-bridged cobaloxime. This BF_2-bridged cobaloxime facilitates a more easily reduced Co^{II} centre, resulting in more effective electron transfer from the photosensitiser centre to the Co proton reduction centre.[34]

2.1.5 Proposed TM Complexes Bearing Partially-fused PAH-type Ligands

Further to the successful synthesis of two quinone-containing partially-fused PAH-type compounds (**14** and **15**), and two extended phenanthroline ligands (**3** and **4**) in Chapter 1, the development of Ru(II) and Ir(III) complexes of the same was undertaken. As highlighted in both chapters, literature examples of partially-fused PAH-type complexes are rare in the literature, with applications even more rare.

Chart 2.4 shows eight proposed complexes bearing those ligands generated in Chapter 1. Quinone-containing ligands in the literature are typically coordinated to Ru(II) centres, with the coordination environment almost exclusively satisfied using bpy or phen ancillary ligands. For this reason, both bpy and phen were chosen as ancillary ligands towards the generation of the proposed complexes. Generation of **47** or **48** will allow the study of the first system showing a terminal quinone moiety, with **49** and **50** comprising of the quinone in the more typical “naphthoquinone” construction.

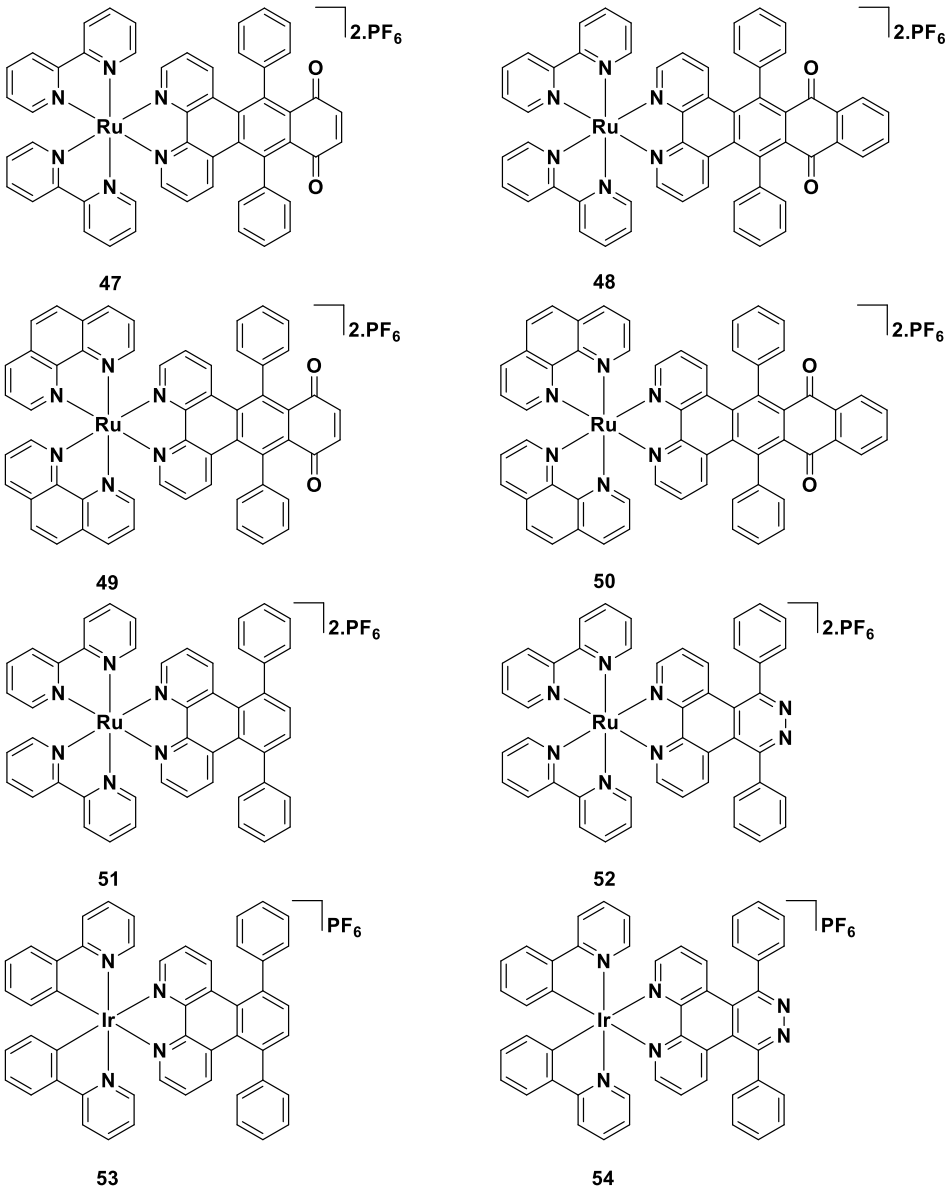

Chart 2. 4 Proposed Ru(II) and Ir(III) complexes bearing partially-fused PAH-type ligands.

Further to this, the generation of Ru(II) and Ir(III) complexes of the extended phenanthroline ligands **3** and **4** will allow the study of (a) the effect of the free phenyl rings in the ligand, (b) the effect of the partially-fused nature of the ligand, and (c) the effect of the modification of the central benzene ring of **3**, to the pyridazine ring of **4**. As these systems are smaller than their quinone-containing counterparts, complexes **51**, **52**, **53**, and **54**, may find immediate use as photosensitisers for a number of photoactive processes, in place of their respective $[Ru(bpy)_3]^{2+}$ or $[Ir(ppy)_2(bpy)]^{+}$ model complexes. **52** and **54** are proposed as photosensitisers for the photocatalytic reduction of protons into molecular H_2.

2.6 Photocatalytic Proton Reduction Experiments with 52 and 54

2.6.1 Photocatalytic Proton Reduction Introduction

As briefly discussed earlier in this chapter, the use of small heteroleptic Ru(II) and Ir(III) complexes as photosensitisers for the photocatalytic reduction of aqueous protons to H_2 is an established research field. Hydrogen has been long sought after as an everyday fuel type for use in both consumer and commercial sectors rather than simply a research interest, due to its environmentally friendly nature.[36] Hydrogen as a fuel type is well suited to the current infrastructure of fuel delivery, and to replace the various fractions of crude oil in use today. As the waste product of hydrogen fuel use is water, and is therefore inherently carbon neutral, it again demonstrates the potential of hydrogen as the fuel of the future.[37] The current bottleneck for the use of hydrogen as a common fuel is undeniably in its generation. The vast majority of current production is from the formation of syngas from coal gasification, or the steam reforming of methane; processes requiring both large amounts of energy and with serious negative side effects for the environment.[38] To truly increase the use of hydrogen as a viable fuel option requires the development of novel methods for its generation. One of the most obvious sources of hydrogen is from the splitting of water.[36,38] This research avenue becomes infinitely more viable if coupled with current desalination research of seawater, thus providing a colossal source of cheap, clean water.[39,40]

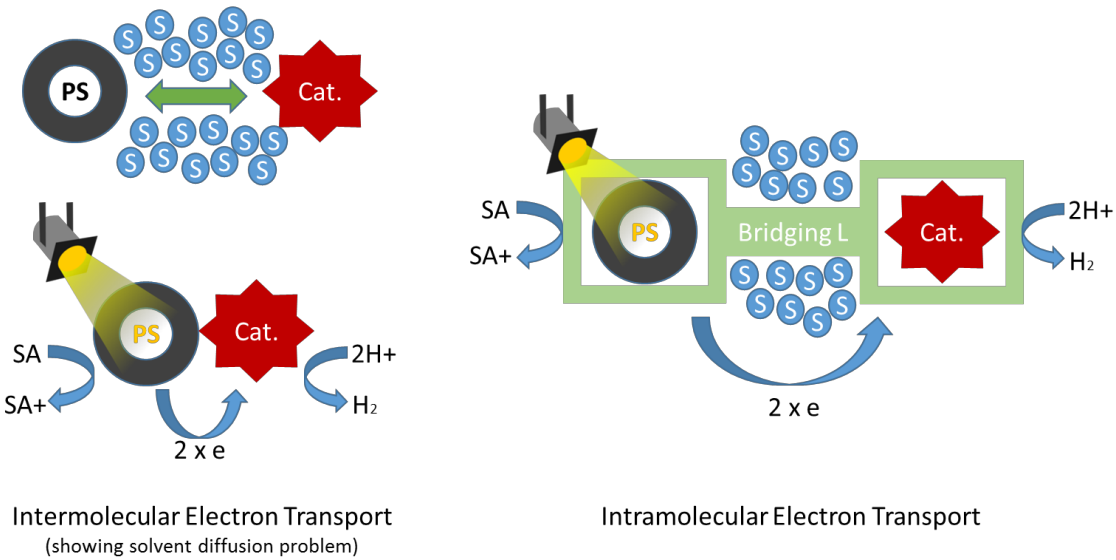

Figure 2. 3 Intermolecular *versus* Intramolecular proton reduction. SA = Sacrificial Agent, SA^+ = Reduced Sacrificial Agent, S = Solvent, PS = Photosensitiser, Cat. = Catalyst.

When combined with an electron sacrificial agent, a light harvesting centre (the photosensitiser) may be coupled with a catalyst for the effective reduction of two protons into molecular hydrogen.[36,38,41] Both the photosensitiser and catalytic centre are almost always late transition metals in combinations such as Ru/Pd, Ru/Pt, Ir/Pd and Ir/Rh.[42] Some work is also being carried out on earlier transition metals such as iron and cobalt.[43]

The composition of components that constitute a "photocatalyst" may be intermolecular *versus* intramolecular in nature as can be seen in Figure 2.32. The intramolecular photocatalyst architecture must then include a bridging ligand.[44–46] In both systems, the process of proton reduction is performed by electron transfer from the excited state of the photosensitiser to the catalytic centre, where the excited state is generated by an incident photon from either the visible or UV spectrum.[36] As the intermolecular system requires two separate components to be free in solution, diffusion processes limit the contact between the photosensitiser and the catalytic centre and consequently this affects the rate of electron transfer. This is not a problem in the intramolecular system as the two metal centres are held at a fixed distance from each other. However, synthetic challenges are compounded in the intramolecular set up, as often the bis-metalation reactions must occur separately. The issue of complex stability is also of great importance, as an unstable photocatalytic system is not commercially desirable and a diminution in catalyst concentration in solution will result in a decrease in catalytic activity. Whilst a long excited-state lifetime is necessary for effective electron transfer to the proton reduction catalyst, if the electron transfer does not take place quickly enough, ligand dissociation can occur whilst the LUMO located on that ligand is populated. Vacant sites on the metal centre are then filled by coordinating solvent, often MeCN, thus generating a new complex incapable of the necessary light absorption for photocatalytic hydrogen generation. Therefore, the generation of hydrogen by metal complexes is often not limited by their ability to facilitate low energy transitions, but rather the stability of the entire photosensitiser component. As discussed, this problem has resulted in the increased use of Ir(III) *versus* Ru(II) centres.

An issue common to both systems is that of the sacrificial agent. Whilst the sacrificial agent is necessary to allow the catalytic cycle to take place, the decomposition products of the agent may play a role in the cycle. A common sacrificial agent is triethylamine (TEA), which is known to produce protons and electrons in its decomposition pathway, and in future work its use will hopefully be avoided.[45,47] Ancillary ligands have also been found to play a large role in the control of the photophysical and catalytic properties, with special regard to their effect on the excitation wavelength of the photosensitiser.[36] The presence (or absence) of electron donating or electron withdrawing functional groups on the ancillary ligands also can have the

dramatic effect of preventing electron transport into the participating ligand, and thus essentially block hydrogen evolution.[48]

The scope of changing the ancillary ligands, the participating ligand, the sacrificial agent, and indeed the solvent choice is consequently enormous. To allow for a detailed study of a photocatalytic assembly, some constant parameters must be sought. For this reason, **52** and **54** were chosen as the photosensitisers for initial study, with bpy or ppy chosen as suitable ancillary ligands respectively. For the catalytic centre, a tetrachloroplatinate proton reduction centre was chosen, with triethylamine (TEA) as the sacrificial agent, in MeCN. As the processes at the catalytic centre are the least understood, these will not be discussed in detail. However, a general mechanism for hydrogen evolution from a double proton reduction is proposed. This mechanism is a modified form of a possible mechanism put forward by Rau *et al.* for the tpphz bridging ligand complex of Ru/Pd.[45] The proposed mechanism implies that while the participating ligand "holds" the electron after a photoinduced electron transfer from the photosensitiser centre, the centre is rapidly reduced by the sacrificial agent, preventing the back-transport of the electron. Loss of a labile Cl^- anion allows the electron to be held by the catalyst centre. A repeat of this process essentially stores two electrons in the catalyst centre, which may be used to reduce two protons from the aqueous solution. A competing process exists where the oxidised product of the sacrificial agent transfers one electron to the singly reduced catalyst. Currently, no method exists to determine between these two mechanisms.

2.2 Results & Discussion

Whilst the synthesis of the ligands had proved challenging in parts, the coordination reactions of both Ru(II) and Ir(III) precursors is well documented in the literature, and typically follow very similar synthetic preparations.

2.2.1 Synthesis & Structural Characterisation of 47, 48, 49, and 50

2.2.2 Synthesis of 47 and 48

The synthesis of four novel Ru(II) complexes was undertaken. As most work in this area focuses on those ancillary ligands of 2,2'-bipyridine (bpy) or 1,10-phenanthroline (phen), both were chosen for the direct comparison of their electrochemical and photophysical properties.

Scheme 2.1 shows the synthetic preparation of **48** and the attempted synthesis of **47**, from the Ru(II) precursor $[Ru(bpy)_2Cl_2]$. Both were attempted through use of a microwave-assisted

process (See Chapter 5, Experimental) due to both the short reaction time, and facile work up.

The unsuccessful synthesis of **47** may be due to the terminal nature of the quinone moiety, as the high reaction temperature of 160 °C may allow significant side product formation to occur. HRMS studies do show the successful synthesis of **47**, however purification methods attempted (both silica- and alumina-based column chromatography) proved unsuccessful towards the collection of an analytically pure sample of **47** for further study.

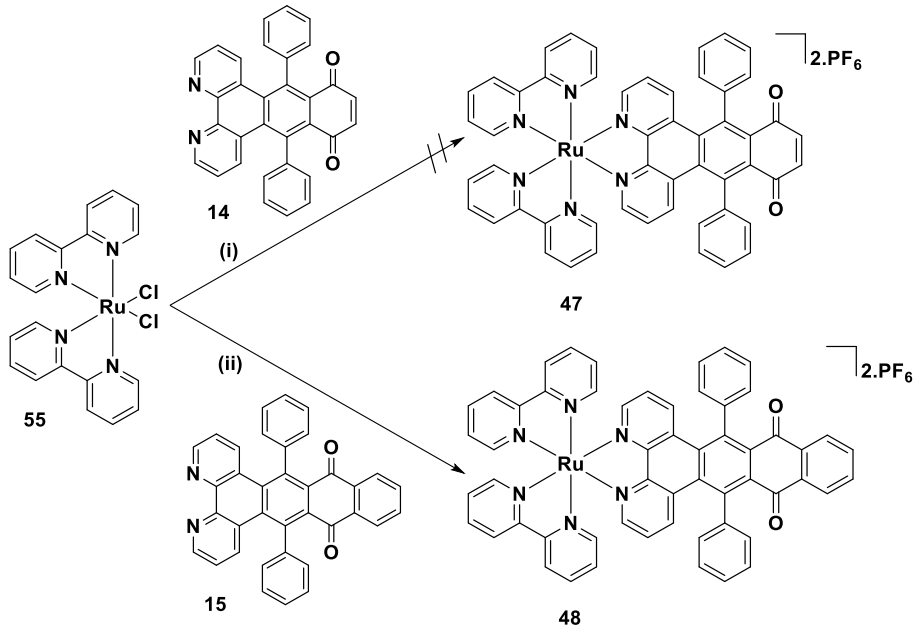

Scheme 2. 1 (i) ethane-1,2-diol, KPF_6, 160 °C, 150 W, 1 h. (ii) ethane-1,2-diol, KPF_6, 160 °C, 150 W, 1 h, 27 %.

Table 2. 1 High resolution mass spectrometry analysis of **47**, and **48**. (ESI, CH_2Cl_2)

Compound	Molecular Formula	Calculated Mass [M]	m/z
47	$C_{52}H_{34}F_{12}N_6O_2P_2Ru$	1166.1070	876.1813 [M-2PF_6]
48	$C_{56}H_{36}F_{12}N_6O_2P_2Ru$	1216.1227	1071.1636 [M-PF_6]

2.2.3 Structural Characterisation of 48

2.2.4 Multinuclear NMR Analysis of 48

The first of the generated Ru(II) complexes **48**, was spectroscopically characterised by multinuclear NMR studies, and the ATR-FTIR (See Chapter 5, Experimental). The ^{1}H and $^{13}C\{^{1}H\}$ NMR spectra in acetone-d_6 are shown in Figure 2.3.

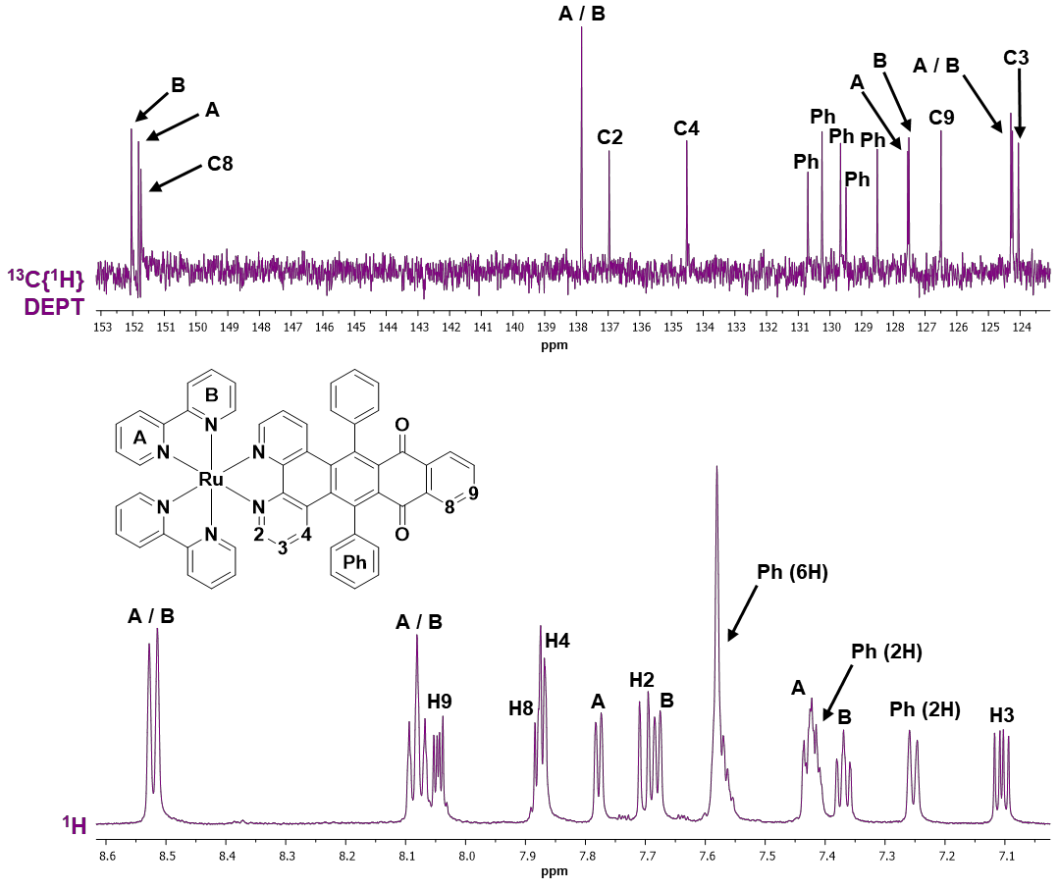

Figure 2. 4 $^{13}C\{^{1}H\}$ DEPT (90°), and ^{1}H NMR spectra of **48**. (acetone-d_6. 600 MHz for ^{1}H, 150 MHz for $^{13}C\{^{1}H\}$. RT)

Due to the symmetrical nature of the large ligands **15**, and the symmetry of the polypyridine Ru(II) centre, the ^{1}H spectrum was assumed to be relatively simple to assign. However, the presence of an extra two signals complicated the assignment. On careful inspection of a number of 2D experiments (Figure 2.5), it was revealed that the expected three spin system of the free phenyl rings is now a five-spin system. This loss of equivalency between the proton signals typically assigned of the ortho, meta, and para positions, is postulated as a loss, or significant slowing, of the rotation of the free phenyl rings. As restricted rotation, or "slowed" rotation often generates a broadening of the proton signals, the apparent resolution of the

signals here indicates that the phenyl rings are locked, and cannot spin. From the X-ray structure of **15** in Chapter 1, a large twist is observed in the free ligand system. This is undoubtedly enhanced in the metal complex, and is seen for later discussed complexes also. It is this twisting that is tentatively put forward as the reason for trapping the phenyl rings, and locking their position. Variable temperature studies did not give any significant change in the temperature range tested (DMSO-d_6, 25 - 60 °C) for **48**. However, further 2D EXchange SpectroscopY (EXSY) studies allowed the successful NMR characterisation of **48**. The 2D EXSY technique uses the same pulse sequence to a 2D NOESY spectrum, providing off-diagonal responses for spins which exchange slowly with one another. This can be conformationally or chemically, and is especially useful for confirming the presence of "rotamers", or rotational isomers. Careful choice of the experimental conditions allows for the exchange peak signals to be significantly more intense than those due to the NOEs, giving clear cross peaks in the 2D spectrum. For **48**, use of the 2D EXSY experiment demonstrated that the free phenyl rings are slow turning rotamers *versus* locked rings (Figure 2.4).

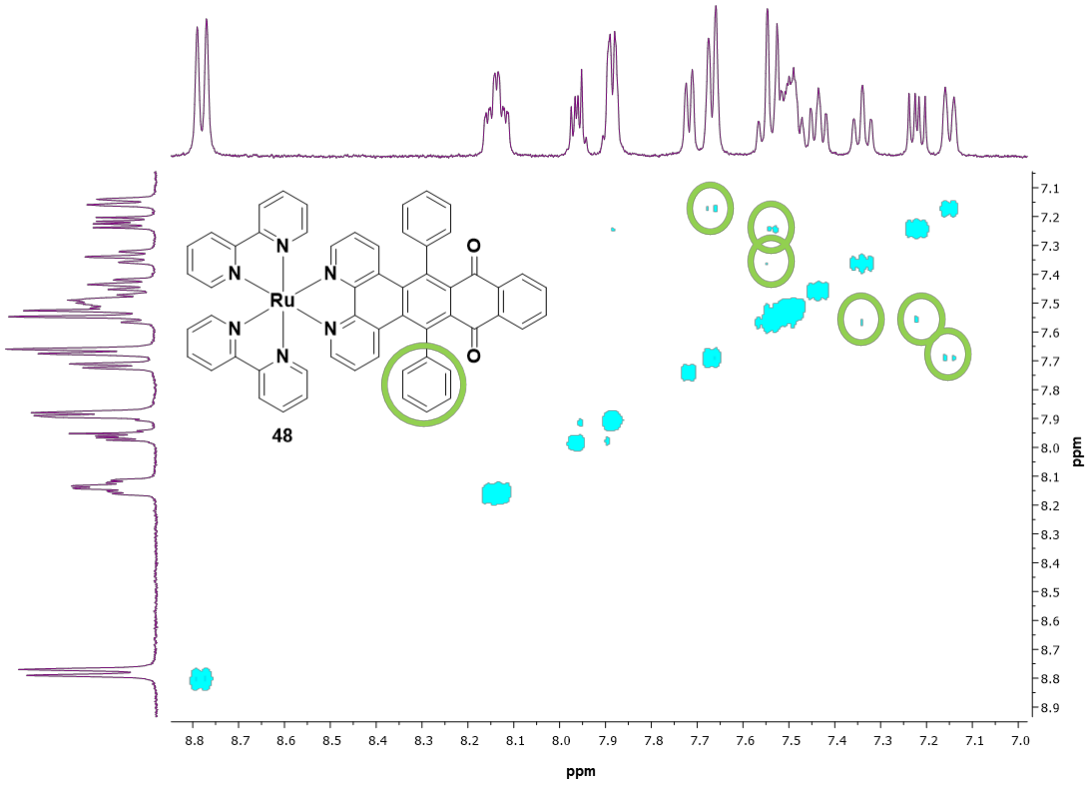

Figure 2. 4 2D EXSY spectrum of **48**. Off-diagonal cross peaks are visualised by a green circle, which correspond to the freely rotating phenyl ring (DMSO-d_6. 400 MHz for ^{1}H. 25 °C).

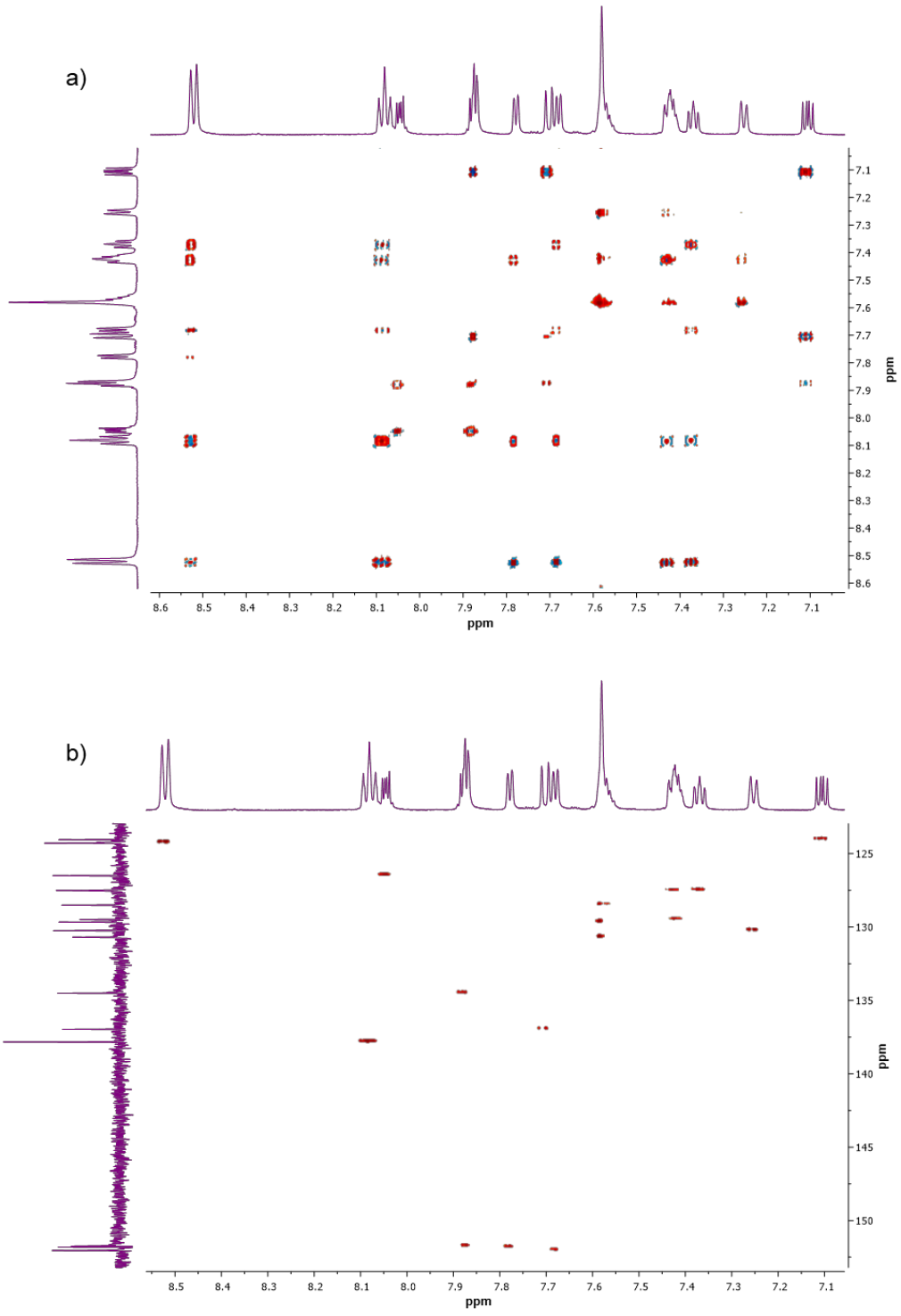

Figure 2. 5 a) ^{1}H-^{1}H COSY, and b) HSQC, spectra of **48** (acetone-d_6. 600 MHz for ^{1}H, 150 MHz for ^{13}C{^{1}H}. RT).

The symmetry of the Ru(II) centre is similar to other systems in the literature of the structure $[Ru(N^N)_2(N'^N')]^{2+}$.[49] The respective rings of the bpy ancillary ligands are denoted as A

and B, and the respective signals of the separate spin systems are assigned through use of the ^{1}H-^{1}H COSY (Figure 2.5(a)).

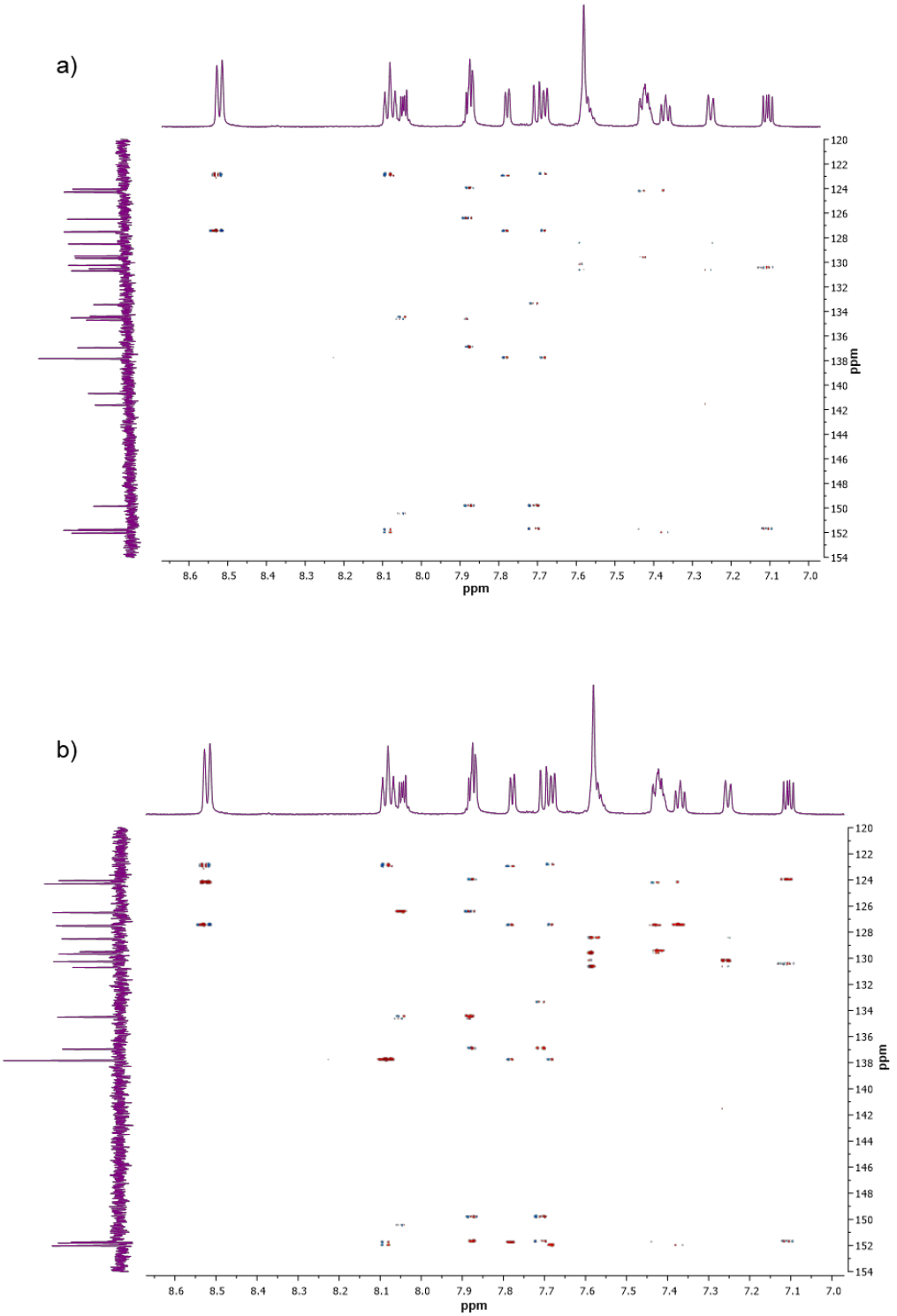

Figure 2. 6 a) HMBC, and b) overlaid HSQC and HMBC spectra of **48** (acetone-d_6. 600 MHz for ^{1}H, 150 MHz for $^{13}C\{^{1}H\}$. RT).

2.2.5 Synthesis of 49 and 50

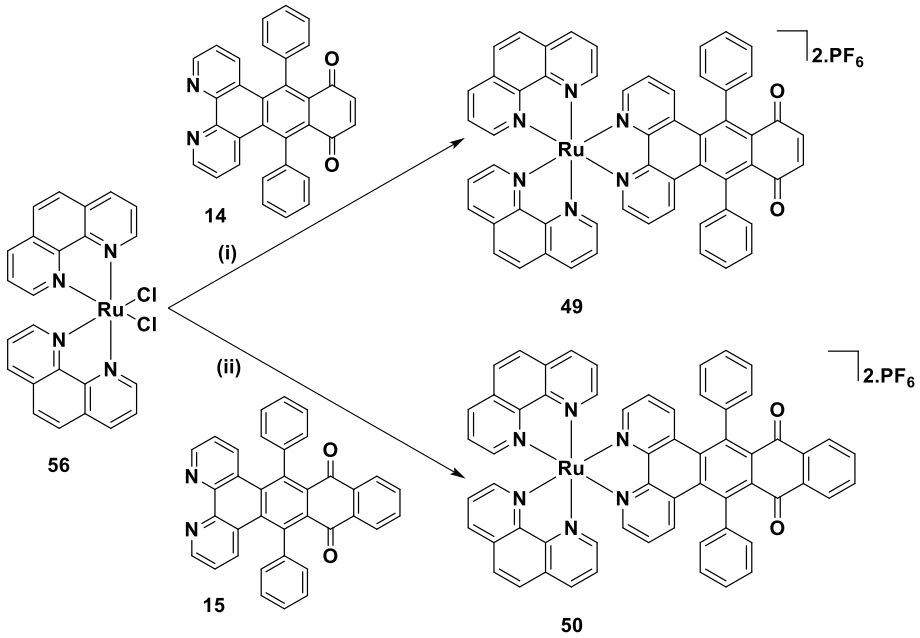

Scheme 2. 2 (i) ethane-1,2-diol, KPF_6, 160 °C, 150 W, 1 h, 28 %. (ii) ethane-1,2-diol, KPF_6, 160 °C, 150 W, 1 h, 43 %.

Scheme 2.2 shows the synthetic preparation of **49**, and **50**, from the Ru(II) precursor $[Ru(phen)_2Cl_2]$. Once again, the use of the microwave-assisted process for the synthesis of **47** and **48** was utilised due to the short reaction time, and facile work up.

Table 2. 2 High resolution mass spectrometry analysis of **49**, and **50**. (ESI, CH_2Cl_2)

Compound	Molecular Formula	Calculated Mass [M]	m/z
49	$C_{56}H_{34}F_{12}N_6O_2P_2Ru$	1214.1070	924.1822 [M-2PF_6]
50	$C_{60}H_{36}F_{12}N_6O_2P_2Ru$	1264.1227	1119.1609 [M-PF_6]

2.2.6 Structural Characterisation of 49 and 50

2.2.7 Multinuclear NMR Analysis of 49

The first of the generated Ru(II) complexes bearing phen ancillary ligands **49**, was spectroscopically characterised by multinuclear NMR studies, and the ATR-FTIR (See Chapter 5, Experimental). The ^1H and $^{13}C\{^1H\}$ NMR spectra in acetone-d_6 are shown in Figure 2.7.

The symmetry of the Ru(II) centre with the ancillary phen ligands is again similar to the structure $[Ru(N^N)_2(N'^N')]^{2+}$, observed for that of the bpy ancillary ligands earlier. The respective rings of the phen ancillary ligands are denoted as A and B again, and the respective signals of the separate spin systems are assigned through use of the ^1H-^1H COSY (Figure 2.8(a)). The expected singlet of the free ligand phen, is split into two doublets, showing very strong "roofing", as are denoted as the S signals in Figure 2.7.

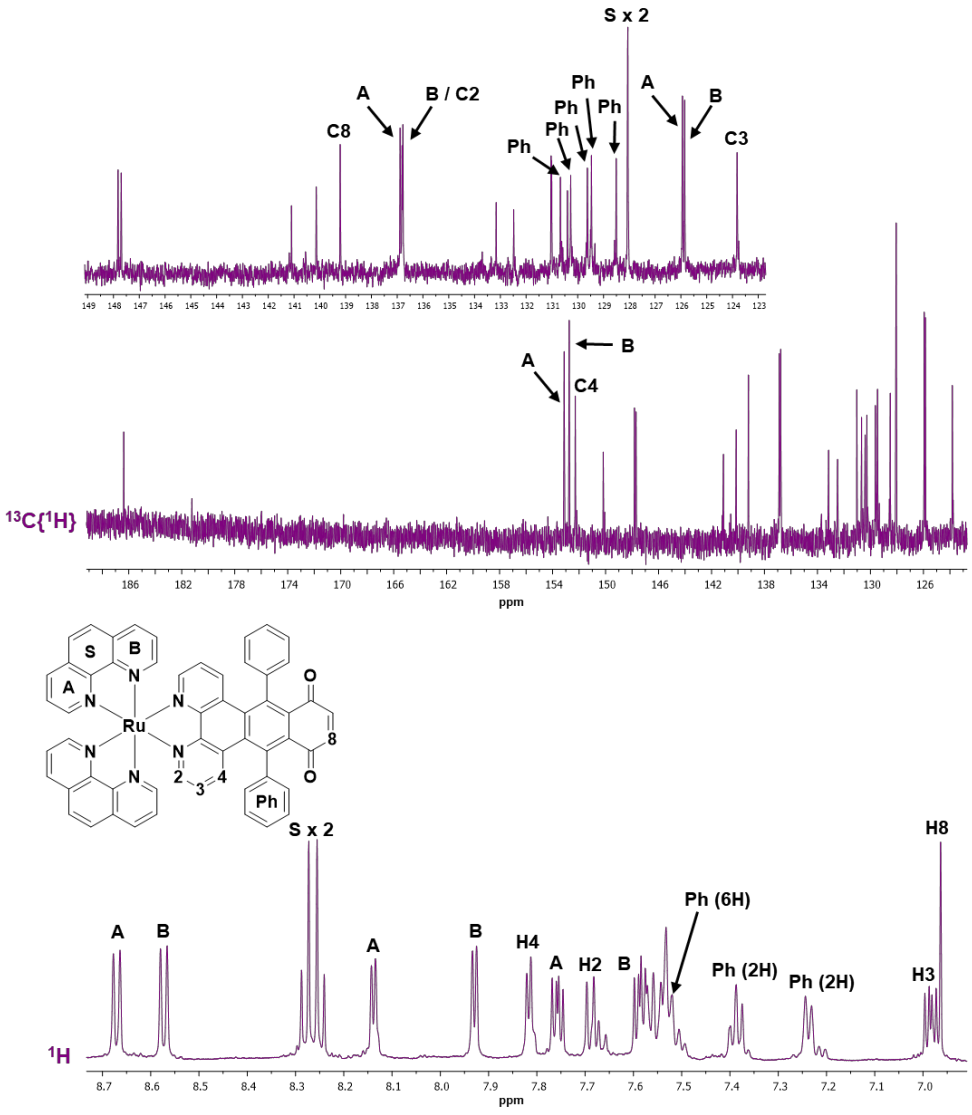

Figure 2. 7 $^{13}C\{^1H\}$ and ^1H NMR spectra of **49**. Zoomed region inset. (acetone-d_6. 600 MHz for ^1H, 150 MHz for $^{13}C\{^1H\}$. RT). Unlabelled peaks in the $^{13}C\{^1H\}$ spectra are quaternary carbons.

Once again, the appearance of a further two signals was postulated as the loss of equivalency between the proton signals typically assigned of the ortho, meta, and para positions of the

free phenyl rings, due to their slow rotation (seen for **48**). Similar to the X-ray structure of **15** in Chapter 1, **14** also demonstrates a large twist, which again is undoubtedly enhanced in the metal complex. Further to the assignment of **48**, this allows the successful NMR characterisation of **49**. Variable temperature studies did not give any significant change in the temperature range tested (DMSO-d_6, 25 - 60 °C). The singlet of the cyclic alkene of the quinone moiety is observed at δ 6.96 ppm.

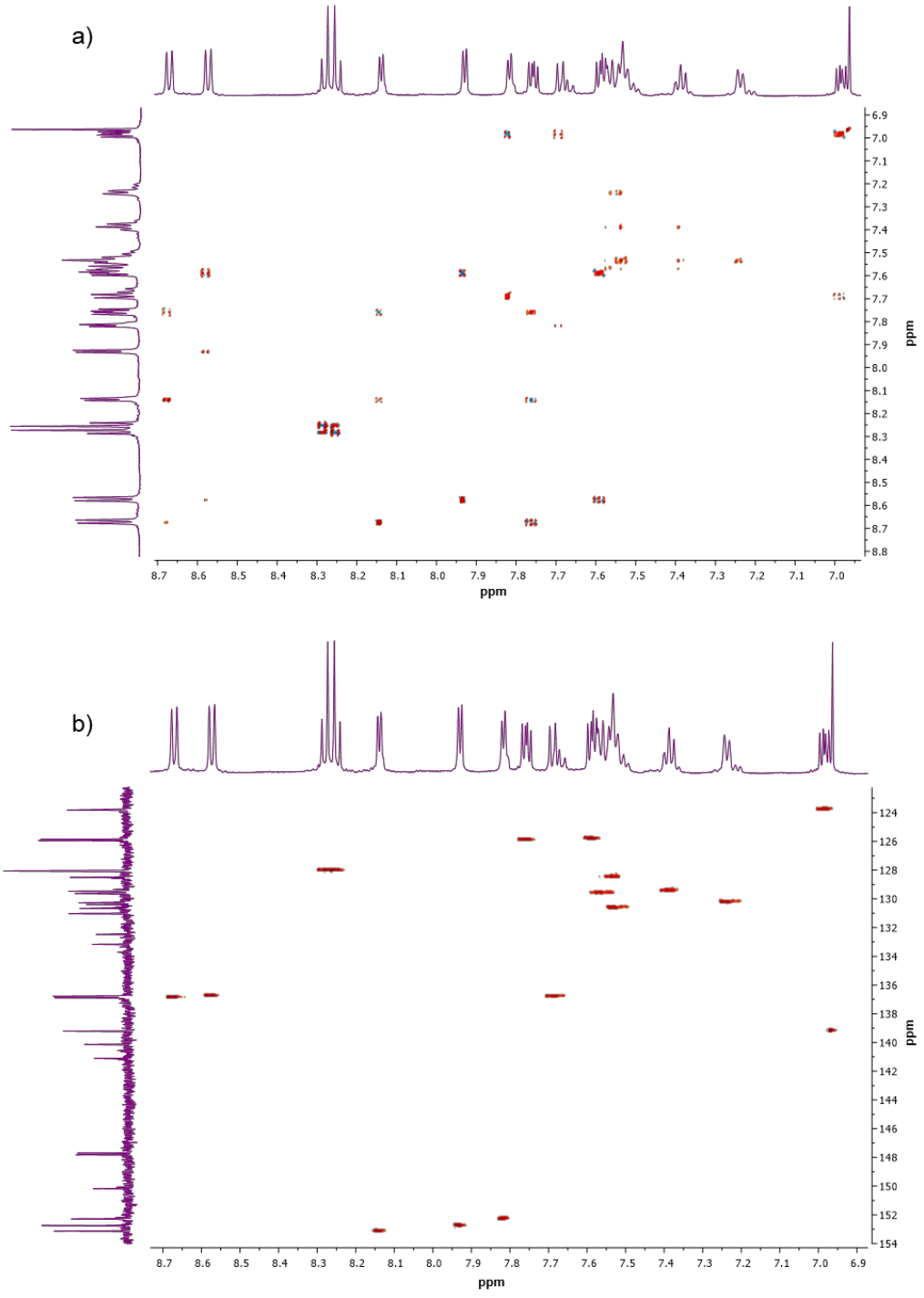

Figure 2. 8 a) ^{1}H-^{1}H COSY, and b) HSQC, spectra of **49** (acetone-d_6. 600 MHz for ^{1}H, 150 MHz for ^{13}C{^{1}H}. RT).

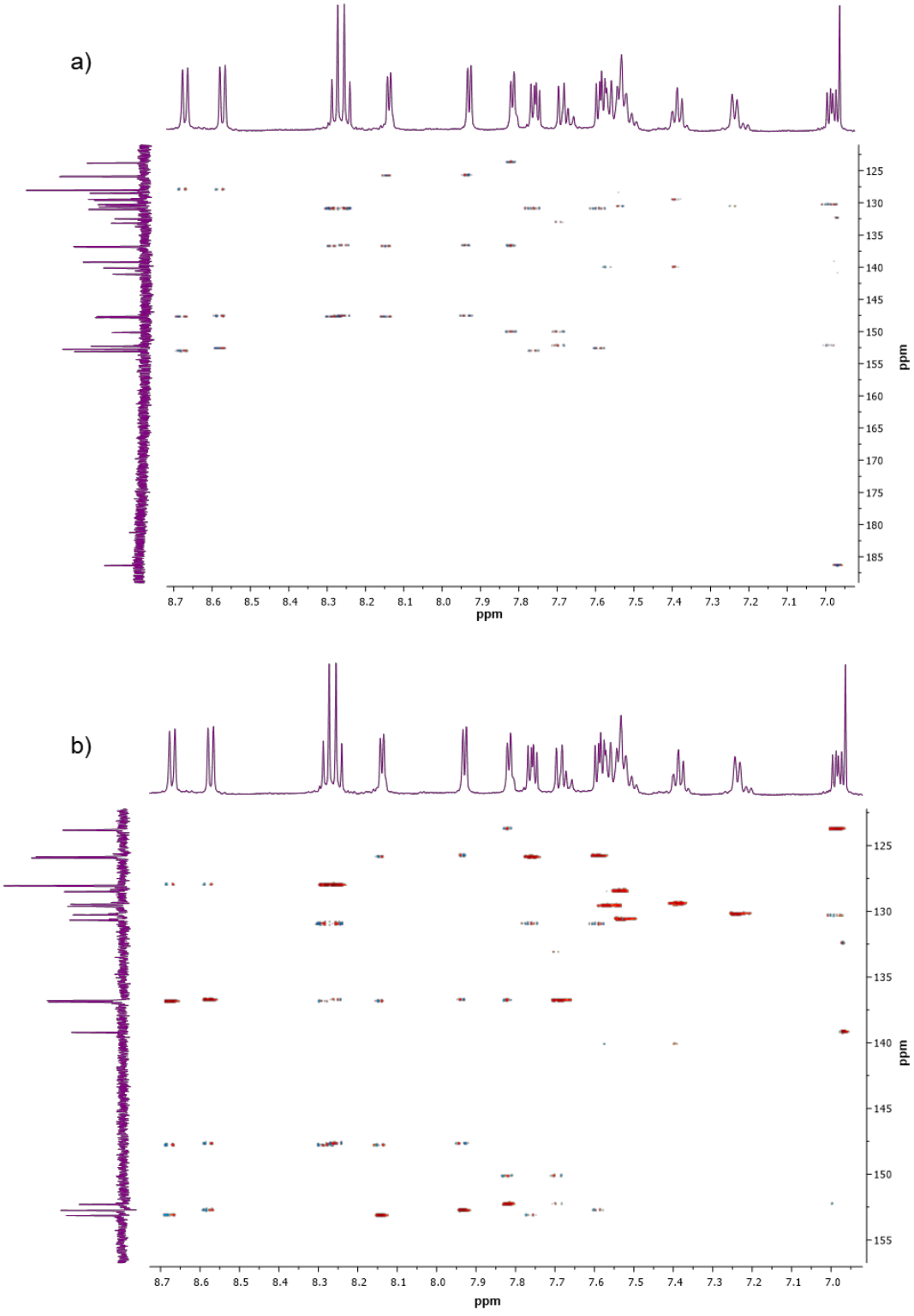

Figure 2. 9 a) HMBC, and b) overlaid HSQC and HMBC spectra of **49** (acetone-d_6. 600 MHz for ^{1}H, 150 MHz for $^{13}C\{^{1}H\}$. RT).

2.2.8 Multinuclear NMR Analysis of 50

The second of the generated Ru(II) complexes bearing phen ancillary ligands **50**, was spectroscopically characterised by multinuclear NMR studies, and the ATR-FTIR (See Chapter 5, Experimental). The ^{1}H and $^{13}C\{^{1}H\}$ NMR spectra in acetone-d_6 are shown in Figure 2.10.

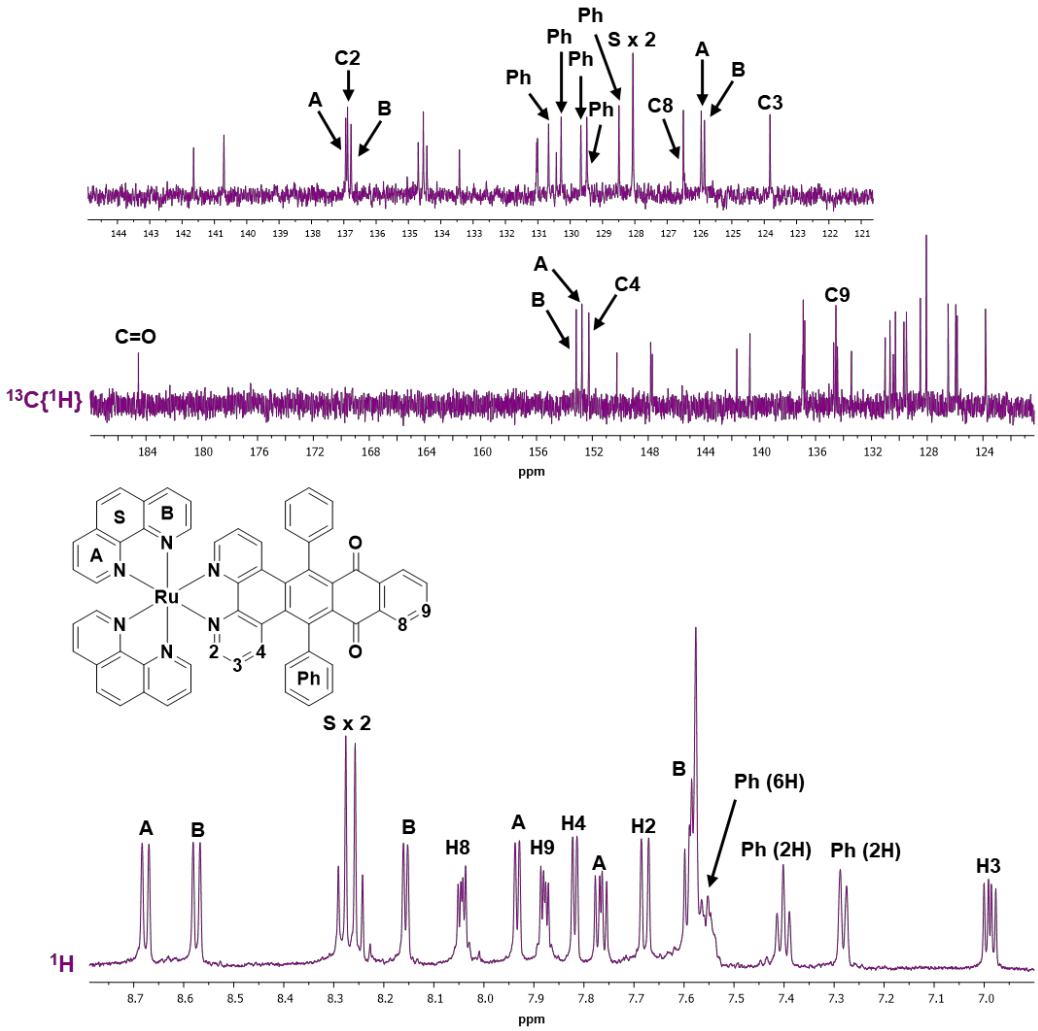

Figure 2. 10 $^{13}C\{^{1}H\}$ and ^{1}H NMR spectra of **50**. Zoomed region inset. (acetone-d_6. 600 MHz for ^{1}H, 150 MHz for $^{13}C\{^{1}H\}$. RT). Unlabelled peaks in the $^{13}C\{^{1}H\}$ spectra are quaternary carbons.

The symmetry of the Ru(II) centre with the ancillary phen ligands is again similar to the structure $[Ru(N^N)_2(N'^N')]^{2+}$, observed for **49**. The respective rings of the phen ancillary ligands are denoted as A and B again, and the respective signals of the separate spin systems are assigned through use of the HMBC (Figure 2.11(a)). Once again, the appearance of a

further two signals was postulated as the loss of equivalency between the proton signals typically assigned of the ortho, meta, and para positions of the free phenyl rings, due to their slowed rotation seen in **48** and **49**. Variable temperature studies did not give any significant change in the temperature range tested (DMSO-d_6, 25 - 60 °C).

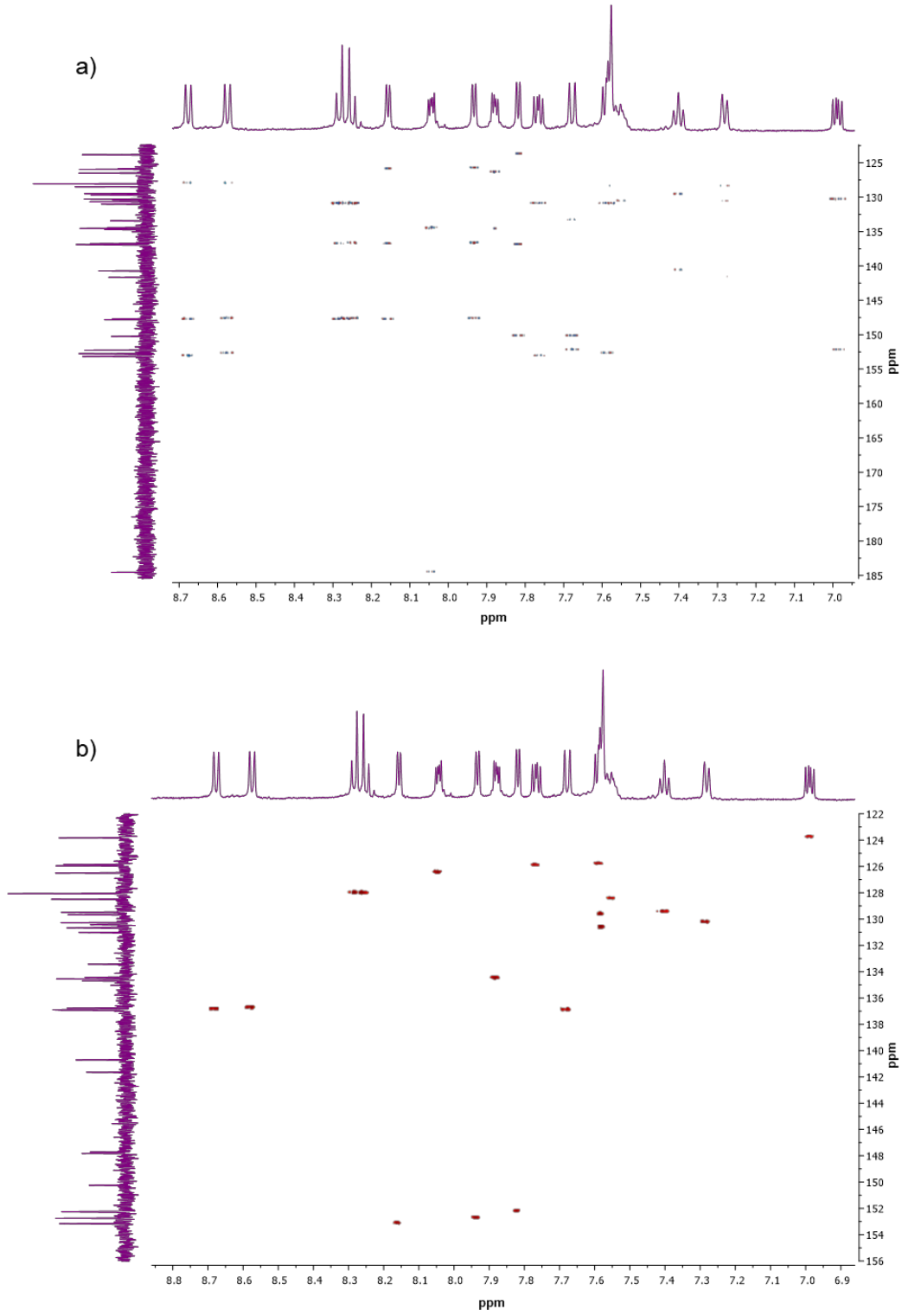

Figure 2. 11 a) HMBC, and b) HSQC spectra of **50** (acetone-d_6. 600 MHz for ^{1}H, 150 MHz for $^{13}C\{^{1}H\}$. RT).

2.2.9 Synthesis of 51, 52, 53, and 54

2.2.10 Synthesis of 51 and 52

Scheme 2.3 shows the synthetic preparation of **51**, and **52**, from the Ru(II) precursor $[Ru(phen)_2Cl_2]$. Once again, the use of the microwave-assisted process was used for the synthesis of **51**, with a conventional synthesis in a mixed solvent of 2-ethoxyethanol and H_2O used for the synthesis of **52**.

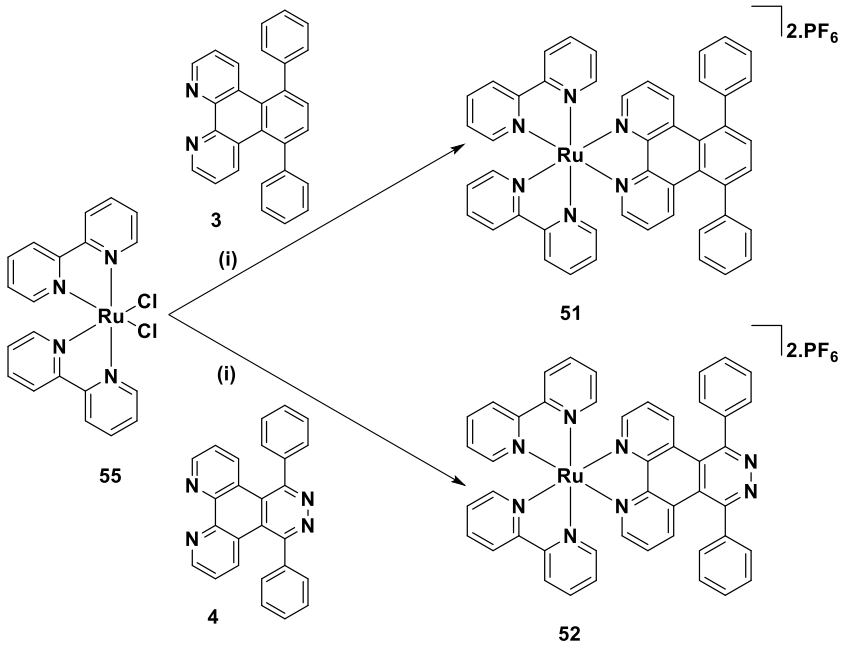

Scheme 2. 3 (i) ethane-1,2-diol, KPF_6, 160 °C, 150 W, 1 h, 72 %. (ii) 2-ethoxyethanol, H_2O, KPF_6, 145 °C, 24 h, 39 %.

Table 2. 3 High resolution mass spectrometry analysis of **51**, and **52**. (ESI, CH_2Cl_2)

Compound	Molecular Formula	Calculated Mass [M]	m/z
51	$C_{48}H_{34}F_{12}N_6P_2Ru$	1086.1172	398.0963 [M/2;-2PF_6]
52	$C_{46}H_{32}F_{12}N_8P_2Ru$	1088.1077	798.1794 [M-2PF_6]

2.2.11 Structural Characterisation of 51 and 52

2.2.12 Multinuclear NMR Analysis of 51

The first of the generated Ru(II) complexes bearing the extended phenanthroline ligand **3**, **51**, was spectroscopically characterised by multinuclear NMR studies, and the ATR-FTIR (See

Chapter 5, Experimental). The ^{1}H and $^{13}C\{^{1}H\}$ NMR spectra in acetone-d_6 are shown in Figure 2.12.

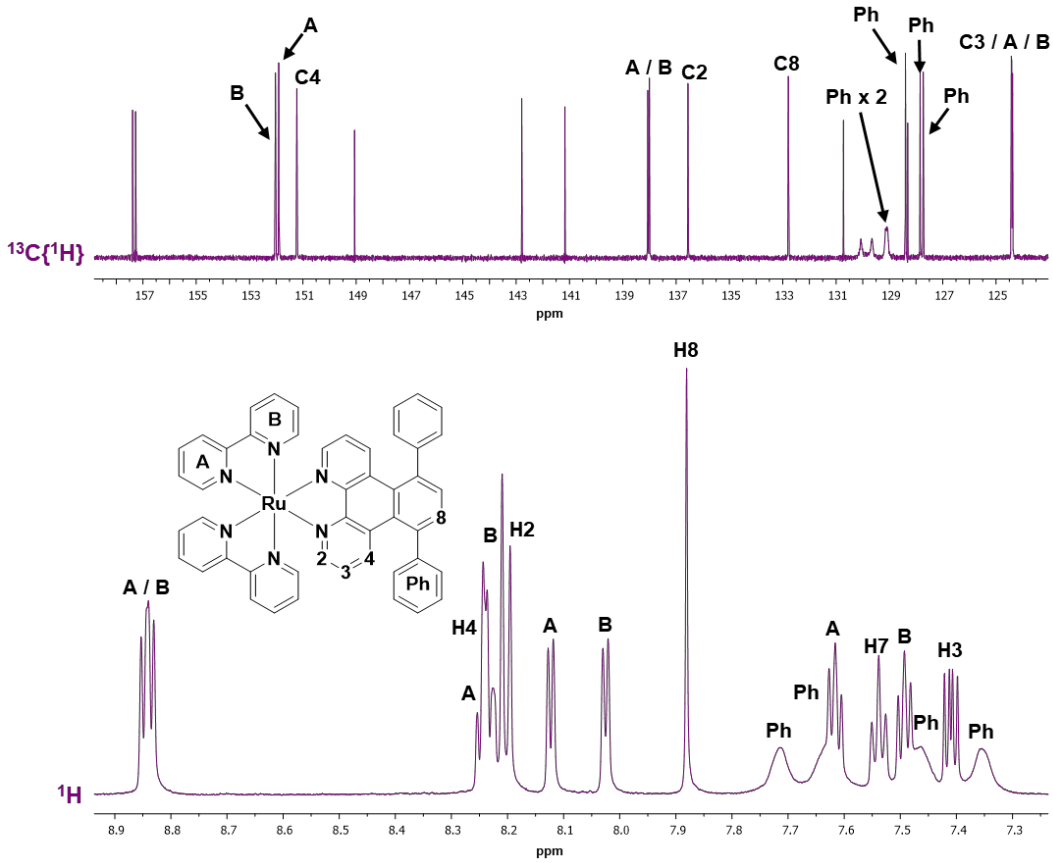

Figure 2. 12 $^{13}C\{^{1}H\}$ and ^{1}H NMR spectra of **51**. (acetone-d_6. 600 MHz for ^{1}H, 150 MHz for $^{13}C\{^{1}H\}$. RT). Unlabelled peaks in the $^{13}C\{^{1}H\}$ spectrum are quaternary carbons.

As **51** no longer includes a quinone moiety within its core structure, the slowing of the rotation of the free phenyl rings was not expected to be as pronounced, but this effect appears to actually be enhanced (Figure 2.12). A broadening of the phenyl signals is observed, with normal resolution observed for the remaining signals corresponding to the ancillary bpy rings, and the phenanthroline ring system. Use of the ^{1}H-^{1}H COSY (Figure 2.13(a)) demonstrates that these signals corresponding to a single spin system, confirming their position in the molecule versus that of an impurity. The expected singlet of the central benzene ring is observed in the ^{1}H spectrum at δ 7.88 ppm.

As the spectroscopic study for the remaining compounds in this chapter follow similar assignments to those discussed earlier, most comments will not be repeated further. As such, most spectra will be included but not discussed. Details of note however will be mentioned where appropriate.

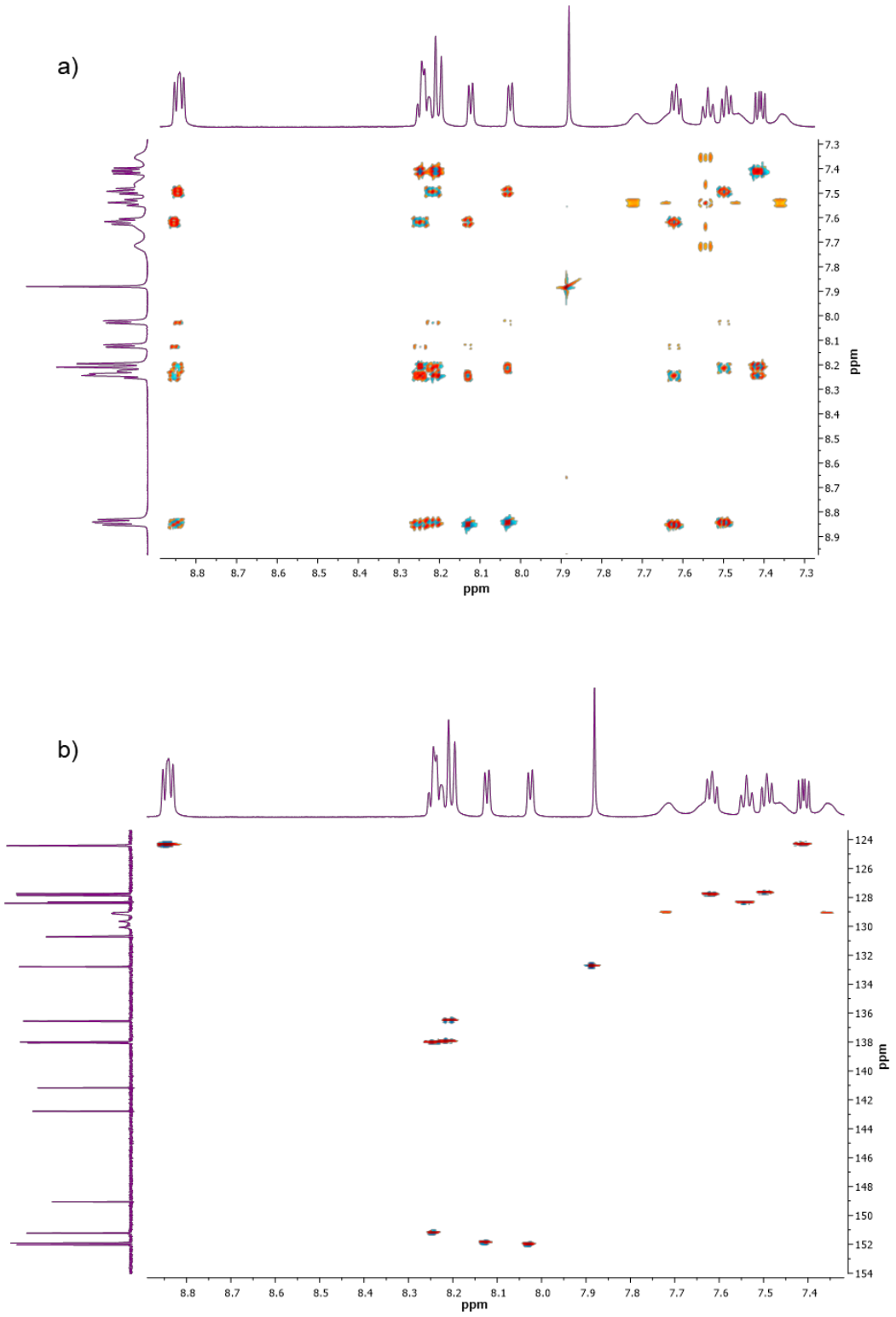

Figure 2. 13 a) ^{1}H-^{1}H COSY, and b) HSQC spectra of **51** (acetone-d_6. 600 MHz for ^{1}H, 150 MHz for ^{13}C{^{1}H}. RT).

Variable temperature studies were not used for **51**, but will be discussed in detail later for **53**, as the complex bears the same ligand. However, the slowed rotation of the free phenyl rings

once again explains the the loss of equivalency between the proton signals typically assigned of the ortho, meta, and para positions.

2.2.13 Multinuclear NMR Analysis of 52

The second of the generated Ru(II) complexes bearing the extended phenanthroline ligand **4**, now including a central pyridazine ring, **52**, was spectroscopically characterised by multinuclear NMR studies, and the ATR-FTIR (See Chapter 5, Experimental). The ^{1}H and $^{13}C\{^{1}H\}$ NMR spectra in MeCN-d_3 are shown in Figure 2.14.

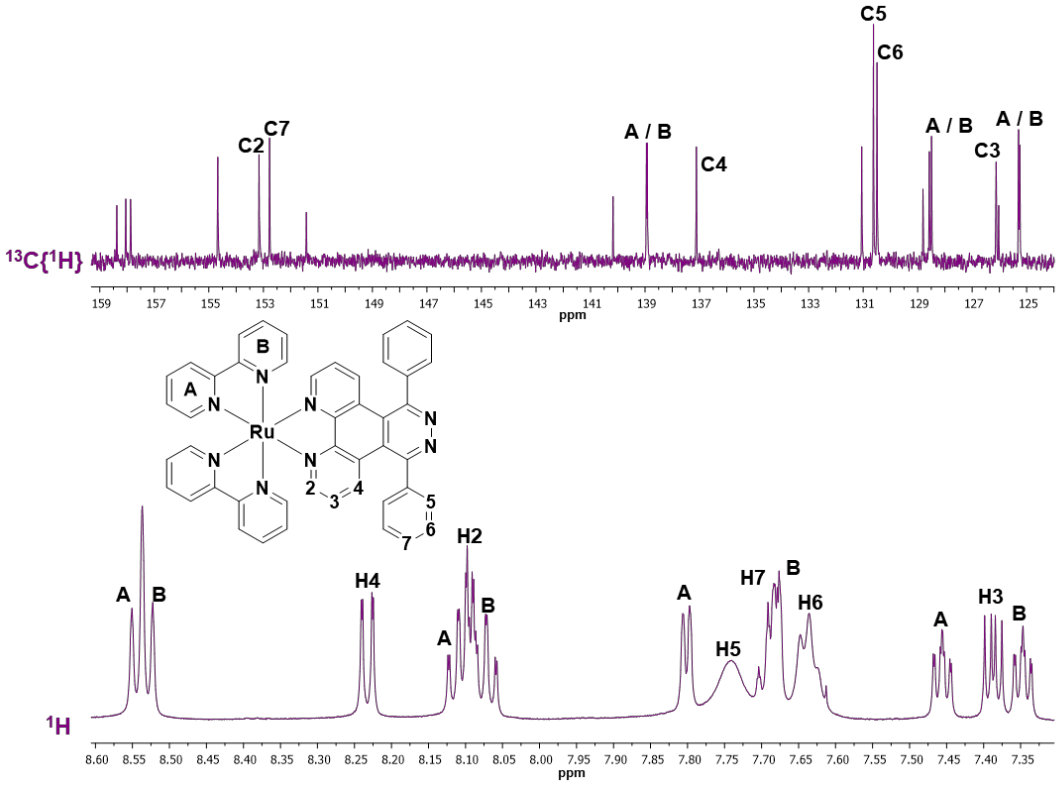

Figure 2. 14 $^{13}C\{^{1}H\}$ and ^{1}H NMR spectra of **52**. (MeCN-d_3. 600 MHz for ^{1}H, 150 MHz for $^{13}C\{^{1}H\}$. RT). Unlabelled peaks in the $^{13}C\{^{1}H\}$ spectrum are quaternary carbons.

In direct comparison to the ^{1}H spectrum of **51**, a dramatic loss of the broadening of the phenyl signals is observed for **52**. With the exception of the broad signal corresponding to H5, H6 and H7 integrate for two protons each, following the expected symmetrical pattern of the ligand **4**. This allowed the full assignment of each respective signal, not fully possible with those earlier systems.

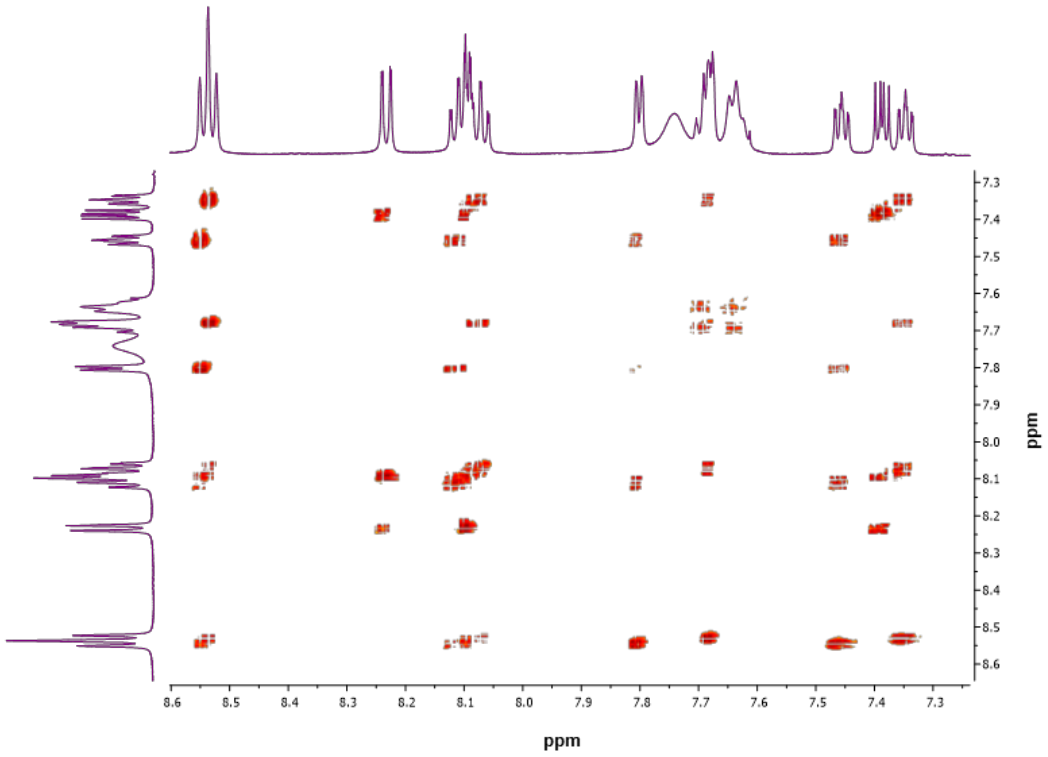

Figure 2. 15 ^{1}H-^{1}H COSY spectrum of **52** (MeCN-d_3. 600 MHz for ^{1}H, 150 MHz for ^{13}C{^{1}H}. RT).

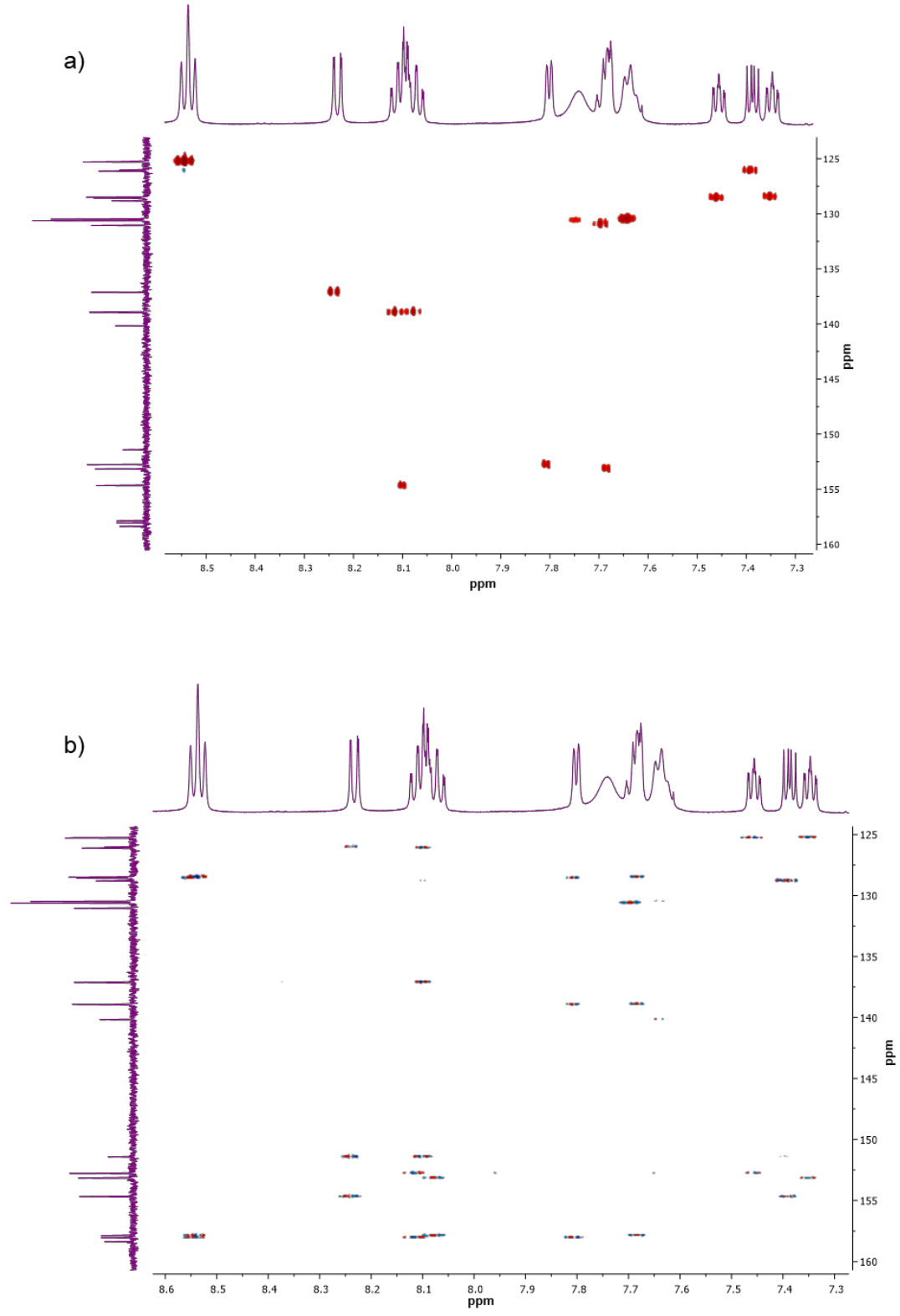

Figure 2. 16 (a) HSQC, and (b) HMBC spectra of **52** (MeCN-d_3. 600 MHz for ^{1}H, 150 MHz for $^{13}C\{^{1}H\}$. RT).

2.2.14 Synthesis of 53 and 54

Scheme 2.4 shows the synthetic preparation of **53**, and **54**, from the Ir(III) precursor [Ir(2-phenylpyridine)$_2$Cl]$_2$. Both syntheses followed a conventional synthesis in $CHCl_3$.

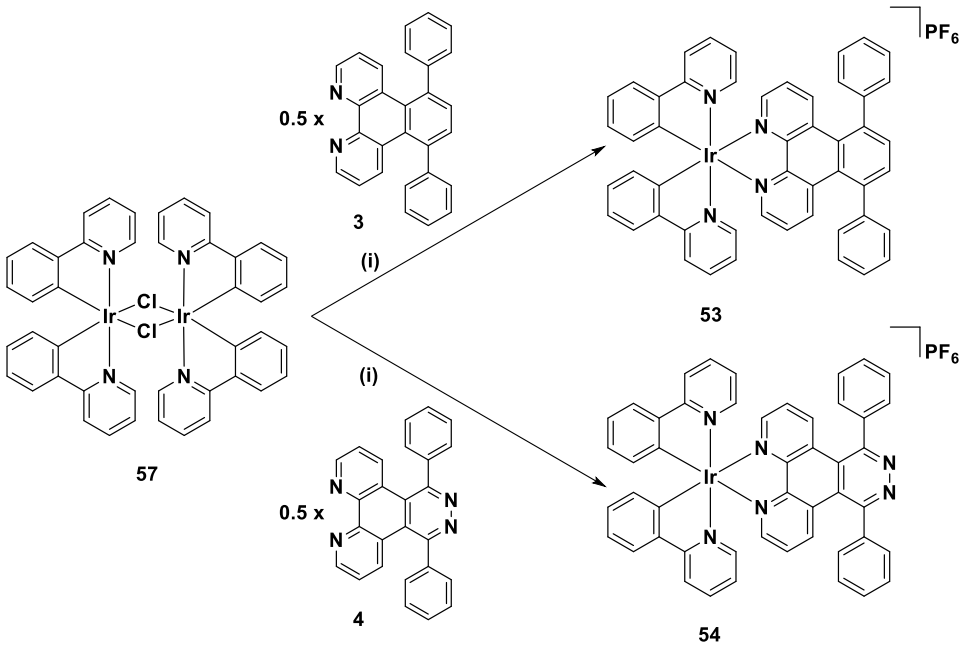

Scheme 2. 4 (i) $CHCl_3$, KPF_6, 60 °C, 16 h, 56 %. (ii) $CHCl_3$, KPF_6, 60 °C, 16 h, 88 %.

Table 2. 4 High resolution mass spectrometry analysis of **53**, and **54**. (ESI, CH_2Cl_2)

Compound	Molecular Formula	Calculated Mass [M]	m/z
53	$C_{50}H_{34}F_6IrN_4P$	1028.2055	883.2445 [M-PF_6]
54	$C_{48}H_{32}F_6IrN_6P$	1030.1959	885.2328 [M-PF_6]

2.2.15 Structural Characterisation of 53 and 54

2.2.16 Multinuclear NMR Analysis of 53 and 54

The two generated Ir(III) complexes bearing the extended phenanthroline ligands **3** and **4**, were spectroscopically characterised by multinuclear NMR studies, and the ATR-FTIR (See Chapter 5, Experimental). The ^1H and $^{13}C\{^1H\}$ NMR spectra of both complexes in acetone-d_6 are shown in the proceeding figures.

For **53**, the broadening of the phenyl signals is once more observed, with four small broad signals appearing in the ^1H spectrum (Figure 2.17). This suggests that the central benzene ring plays a significant role in the restricted rotation of these rings, and this effect is less

pronounced in those complexes (both Ru(II) and Ir(III)) bearing the central pyridazine ring ligand **4** (See Figure 2.22 for **54**).

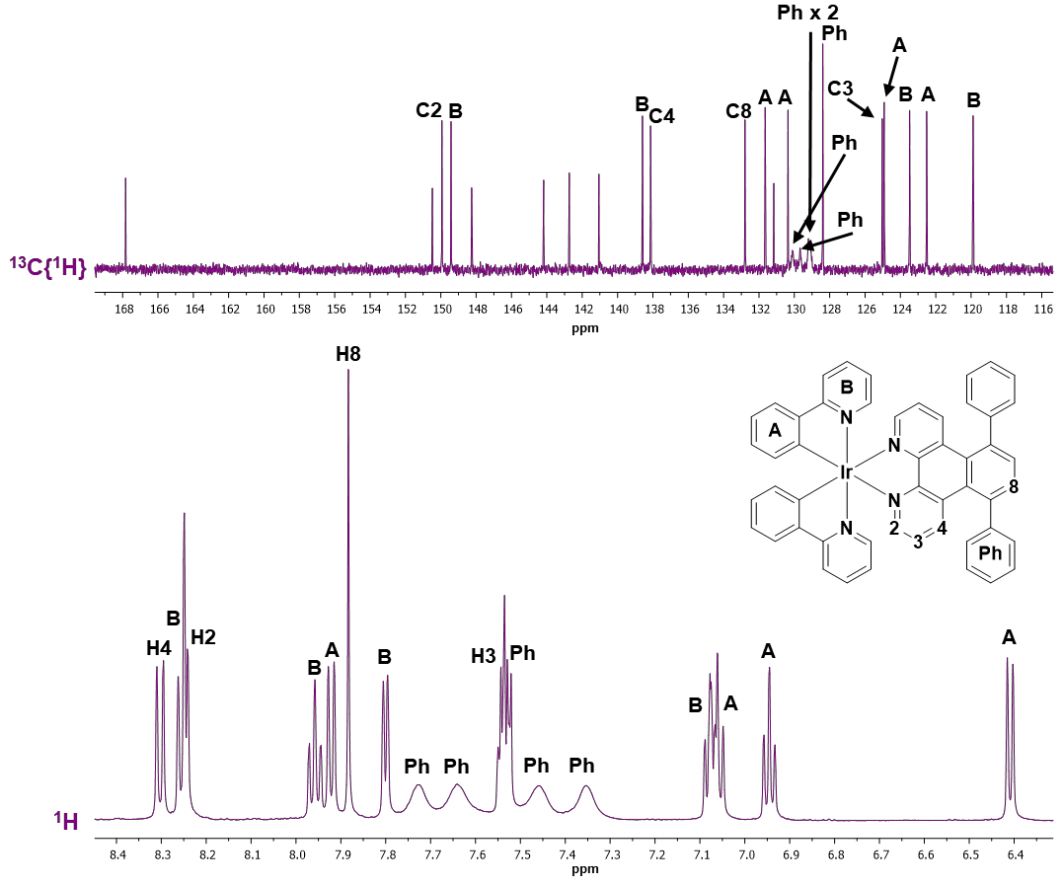

Figure 2. 17 $^{13}C\{^{1}H\}$ and ^{1}H NMR spectra of **53**. (acetone-d_6. 600 MHz for ^{1}H, 150 MHz for $^{13}C\{^{1}H\}$. RT). Unlabelled peaks in the $^{13}C\{^{1}H\}$ spectrum are quaternary carbons.

As previously mentioned, variable temperature studies were undertaken for **53** (DMSO-d_6, 25 - 60 °C). Figure 2.19 shows the broad signals of the freely rotating phenyls (rotamers) at 25 °C in DMSO-d_6. However, these are not as well defined as the broad signals in acetone-d_6. On increasing the temperature to 60 °C, a significant change in the spectrum is observed. There is a sharpening of all bar one of the peaks. This is unlikely to be resolved through increasing the temperature further. This confirms that the free phenyl signals are slowed at room temperature (25 °C), but rotate much more quickly at elevated temperatures. This was further confirmed with a 2D EXSY experiment. As for **48**, use of the 2D EXSY experiment with **53** demonstrated that the free phenyl rings are slow turning rotamers *versus* locked rings (Figure 2.20).

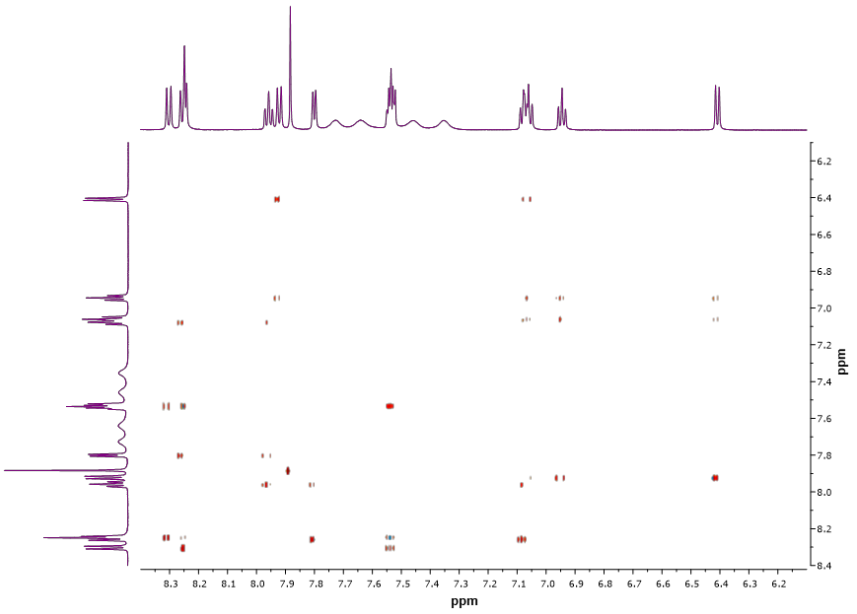

Figure 2. 18 ^{1}H-^{1}H COSY spectrum of **53** (acetone-d$_6$. 600 MHz for ^{1}H, 150 MHz for ^{13}C{^{1}H}. RT).

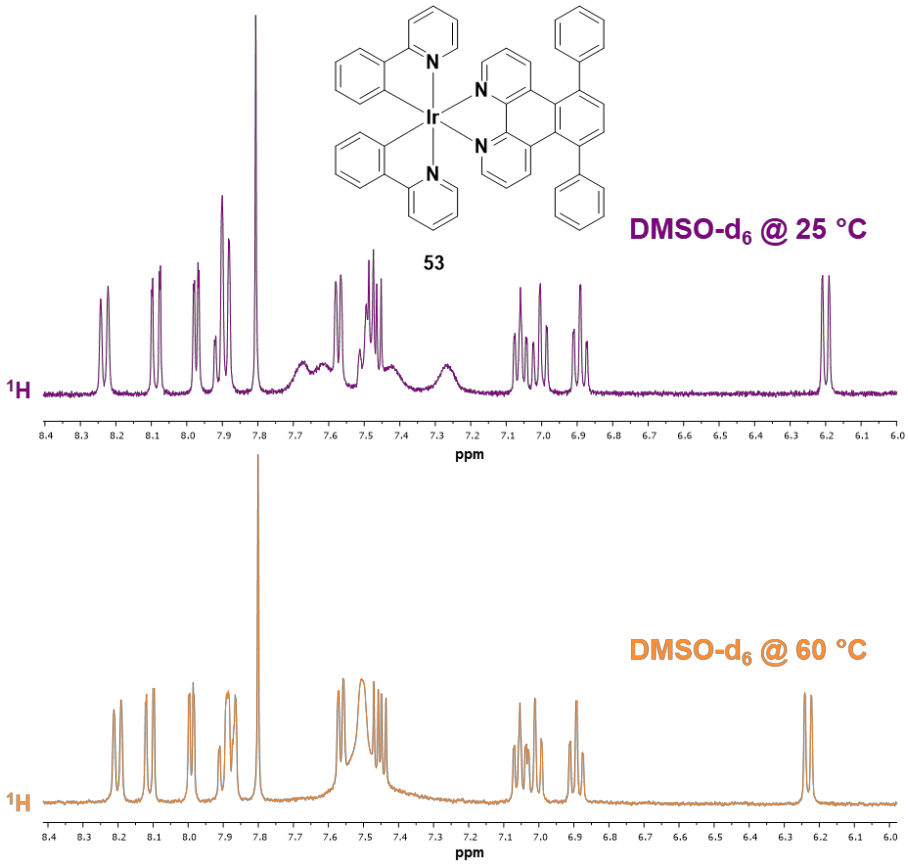

Figure 2. 19 Variable temperature studies of 53. (DMSO-d$_6$. 400 MHz for ^{1}H.).

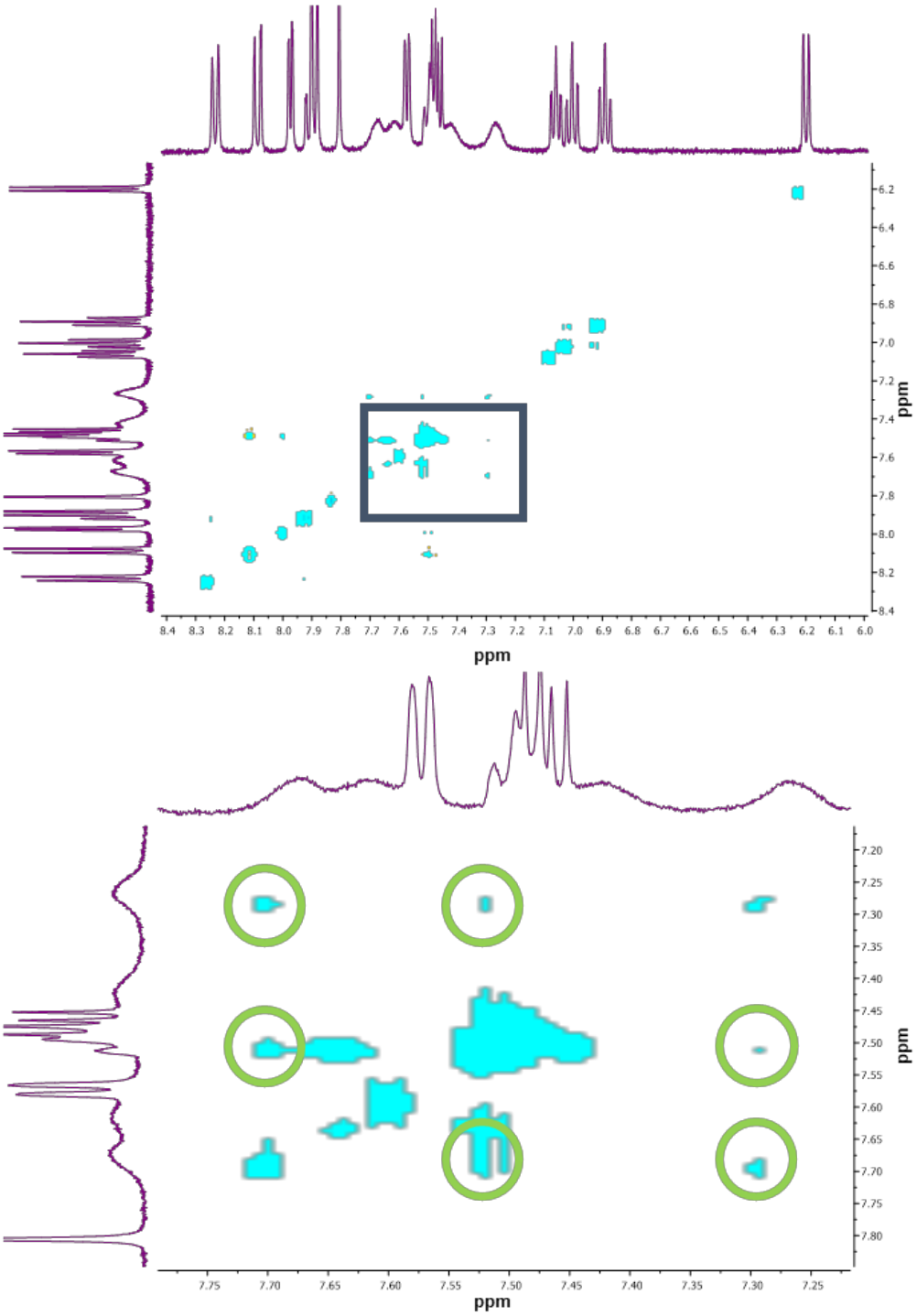

Figure 2. 20 2D EXSY spectrum of **53**. Off-diagonal cross peaks are visualised by green circles, which correspond to the freely rotating phenyl ring (DMSO-d_6. 400 MHz for ^{1}H. 25 °C).

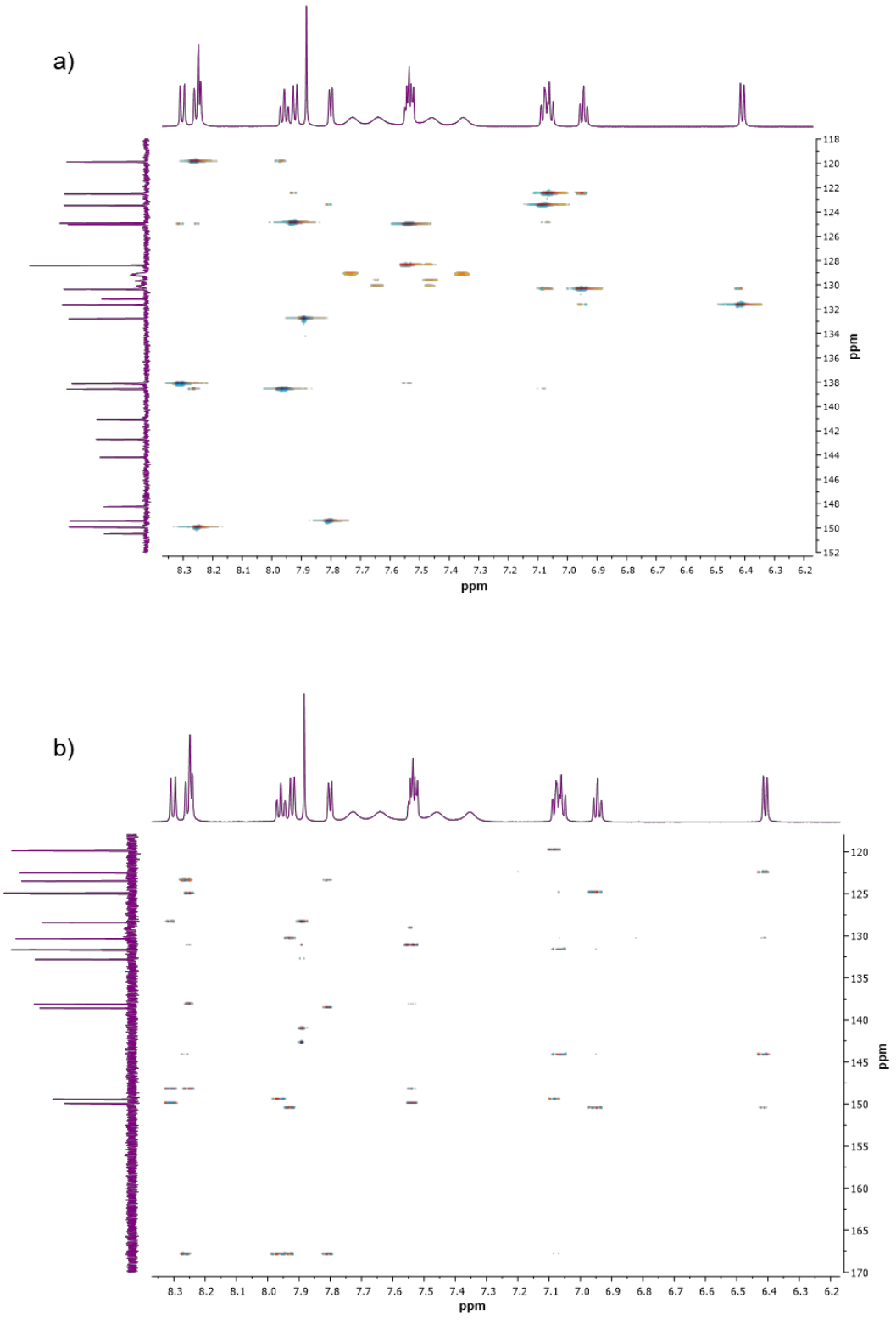

Figure 2. 21 (a) HSQC, and (b) HMBC spectra of **53** (MeCN-d_3. 600 MHz for ^{1}H, 150 MHz for $^{13}C\{^{1}H\}$. RT).

For both Ir(III) complexes **53** and **54**, the cyclometalated $^{13}C\{^{1}H\}$ signal appears as the most deshielded, and thus most downfield, for each complex in their respective $^{13}C\{^{1}H\}$ spectra.

These values correspond to δ 167.8 ppm for **53**, and δ 168.3 ppm for **54**. The expected singlet of the central benzene ring is observed in the ^{1}H spectrum at δ 7.88 ppm. This is the same value to this signal position for the Ru(II) complex **51**, and may suggest that the periphery of the extended phenanthroline ligand **3** is little affected by the choice of metal in the octahedral centre.

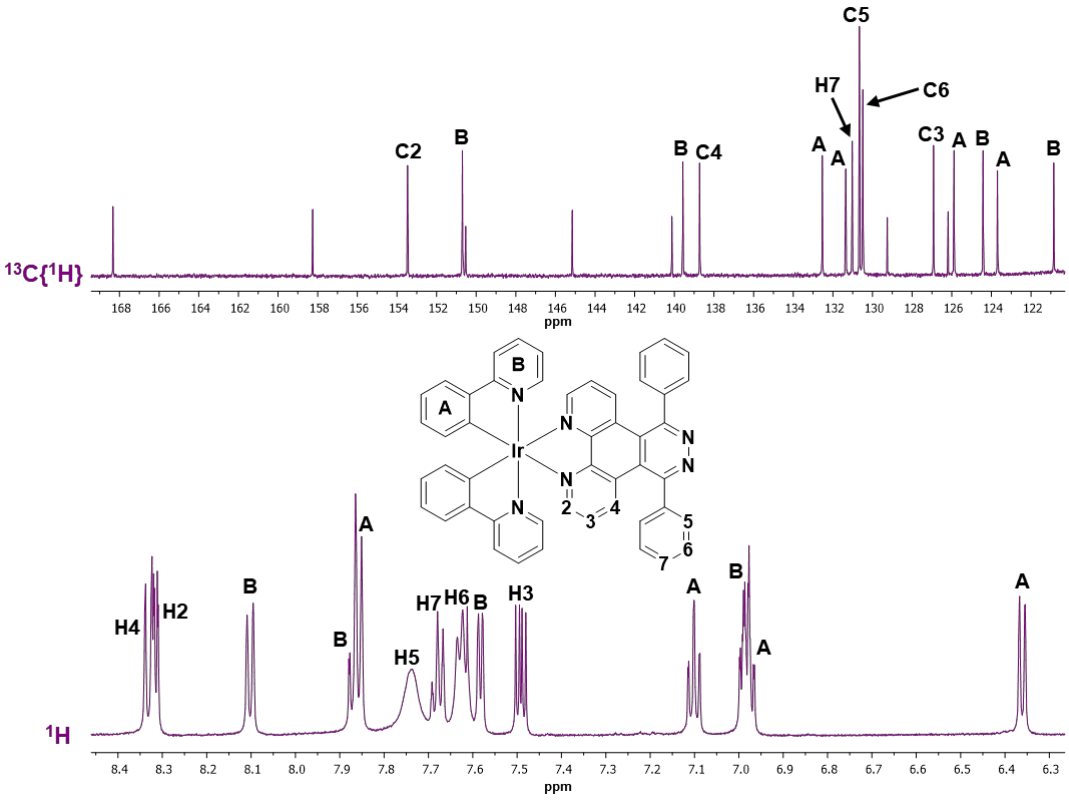

Figure 2. 22 ^{13}C{^{1}H} and ^{1}H NMR spectra of **54**. (acetone-d_6. 600 MHz for ^{1}H, 150 MHz for ^{13}C{^{1}H}. RT). Unlabelled peaks in the ^{13}C{^{1}H} spectrum are quaternary carbons.

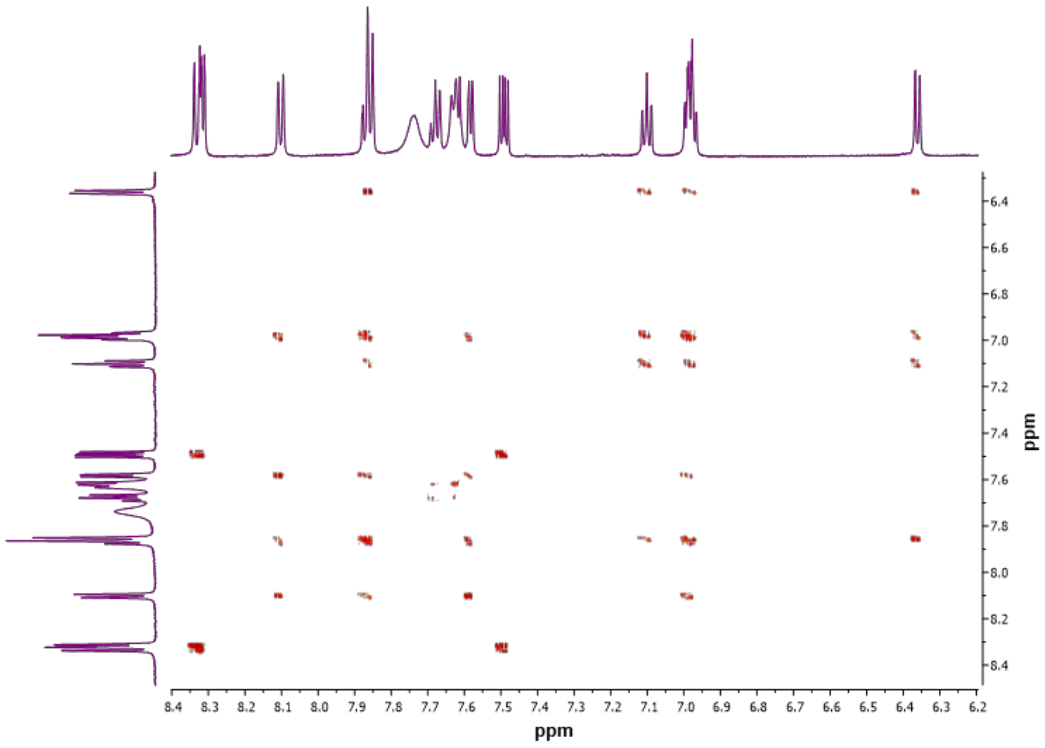

Figure 2. 23 ^{1}H-^{1}H COSY spectrum of **54** (acetone-d_6. 600 MHz for ^{1}H, 150 MHz for ^{13}C{^{1}H}. RT).

2.2.17 Crystallographic Analysis of 52 and 54

2.2.18 Crystallographic Analysis of 52

Crystals of **52** suitable for single crystal X-ray diffraction studies were obtained from the slow evaporation of a small sample of the crude reaction solution of the compound. For that reason, the unit cell contains a mixture of solvents (2-ethoxyethanol, acetone, and MeOH) which have been treated as a diffuse contribution to the overall scattering without specific atom positions by SQUEEZE/PLATON. Data collection and refinement was conducted by Dr. Brendan Twamley in Trinity College Dublin.

A specimen of $C_{46}H_{32}F_{12}N_8P_2Ru$, approximate dimensions 0.040 mm x 0.060 mm x 0.190 mm, was used for the X-ray crystallographic analysis. The structure was solved using the space group P21/c, with Z = 4 for the formula unit, $C_{46}H_{32}F_{12}N_8P_2Ru$. The final anisotropic full-matrix least-squares refinement on F^2 with 622 variables converged at R1 = 5.22%, for the observed data and wR2 = 12.51% for all data. The goodness-of-fit was 1.036.

Figure 2.24(a)-(b) shows representations of the asymmetric unit of **52**. In Figure 2.24(b), two planes (one averaged across the phenanthroline ring system, and the second averaged across the pyridazine ring) show a twist from expected planarity of 18 °. The twist is from the steric

demands of the two free phenyl rings. Both of the free phenyls are twisted out of the plane of the middle pyridazine ring (by approximately 58 ° and 56 °). No hydrogen bonding is seen in the crystal lattice. Figure 2.25 shows the 2x2x2 packing structure of **52**, viewed along the c axis. A pairing of two complexes in a "head to head" pattern is observed in the crystal packing structure.

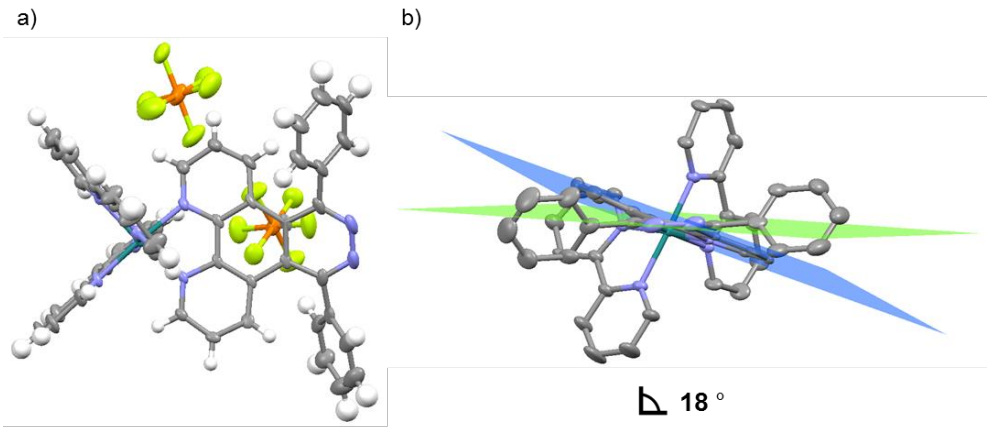

Figure 2. 24 Molecular representations of **52**. (a) Asymmetric unit (thermal ellipsoids shown at 50% probability). (b) Representation demonstrating the pyridazine ring twist from expected planarity (PF_6 anions removed for clarity).

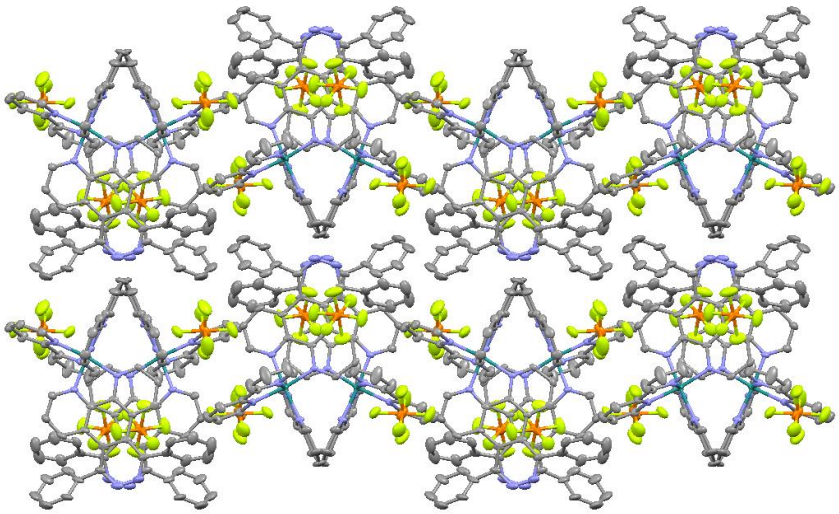

Figure 2. 25 (a) 2x2x2 crystal packing structure of **52**, viewed along the c axis.

2.2.19 Crystallographic Analysis of 54

Crystals of **54** suitable for single crystal X-ray diffraction studies were obtained from the slow evaporation of a THF/diethyl ether solution of the compound. Data collection and refinement was conducted by Dr. Brendan Twamley in Trinity College Dublin. The two phenylpyridine ligands coordinated to Ir3 are disordered and this was modelled with both restraints and constraints. The disordered moiety occupancy for each phenylpyridine was refined at 61% and 57%. Several solvent molecules were disordered and modelled with both restraints and constraints. The less occupied part of a disordered THF (55:45% occupied) was modelled (only the oxygen atom) to maintain the molecule in a reasonable H-bonding position.

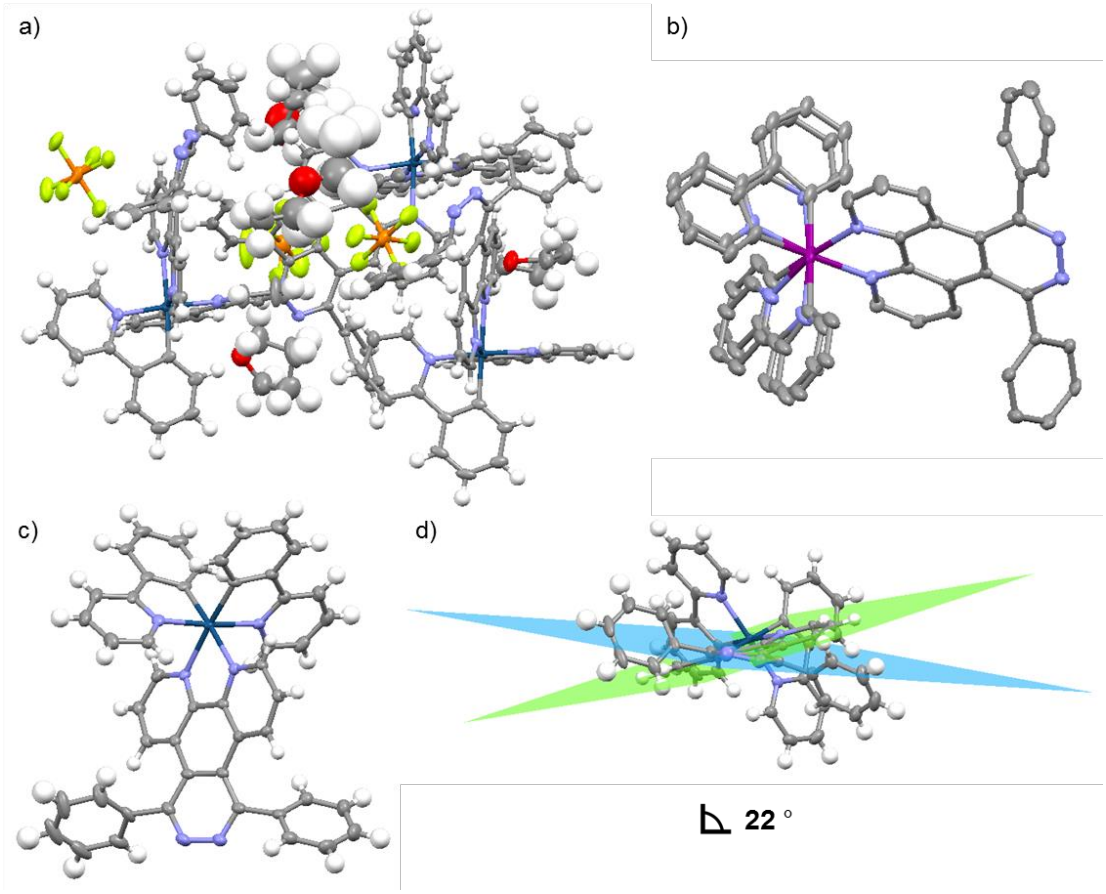

Figure 2. 26 Representations of **54**. (a) Asymmetric unit (thermal ellipsoids shown at 50% probability) showing three Ir(III) centres, and disordered solvent. (b) Representation of **54** showing the disordered moiety occupancy for each phenylpyridine ancillary ligand. (c) Representation of **54** (thermal ellipsoids shown at 50% probability). (d) Representation demonstrating the pyridazine ring twist from expected planarity (PF_6 anions removed for clarity).

A specimen of $C_{164}H_{138}F_{18}Ir_3N_{18}O_5P_3$, approximate dimensions 0.040 mm x 0.140 mm x 0.320 mm, was used for the X-ray crystallographic analysis. The structure was solved using the space group P21/c, with Z = 4 for the formula unit, $C_{164}H_{138}F_{18}Ir_3N_{18}O_5P_3$. The final anisotropic full-matrix least-squares refinement on F^2 with 1813 variables converged at R1 = 4.03%, for the observed data and wR2 = 10.09% for all data. The goodness-of-fit was 1.102.

Figure 2.26(a)-(c) shows representations of **54**. In Figure 2.26(d), two planes (one averaged across the phenanthroline ring system, and the second averaged across the pyridazine ring) show a twist from expected planarity of 22 °. The twist is from the steric demands of the two free phenyl rings. Both of the free phenyls are twisted out of the plane of the middle pyridazine ring (by approximately 48 ° and 60 °). No hydrogen bonding is seen in the crystal lattice. Figure 2.26(b) shows the disordered moiety occupancy for each phenylpyridine ancillary ligand for Ir3.

2.3 Electrochemical Investigation of 48, 49, 50, 51, 52, 53, and 54

Cyclic Voltammetry (CV) studies were carried out on $1x10^{-4}$ M solutions of **48**, **49**, **50**, **51**, **52, 53**, and **54** in MeCN (0.1 M nBu_4NPF_6). Cyclic Voltammetry (CV) studies were carried out on $1x10^{-4}$ M solutions in MeCN. Cyclic voltammograms were recorded using an Ag/AgCl reference electrode, a Pt wire counter electrode, and a glassy carbon working electrode (See Chapter 5, Experimental). The cyclic voltammograms for the respective compounds are now shown, with a summary of the electrochemical data presented in Table 2.5. The voltammograms were initially run from 0 to +2, and then from 0 to -2. The voltammograms were then selectively run at smaller windows to increase the resolution of the trace, and to aid in the determination of the $E_{1/2}$, and ΔE_p values.

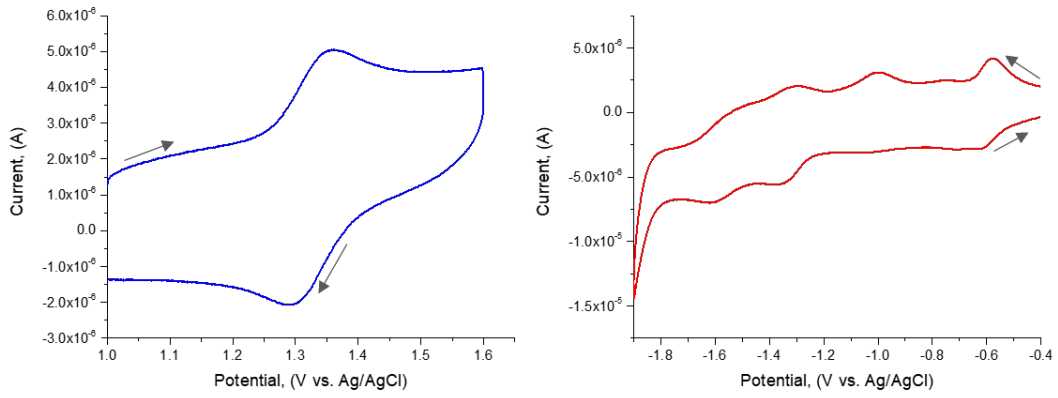

Figure 2. 27 Oxidative (blue) and reductive (red) cyclic voltammograms of **48** in MeCN and 0.1 M $TBAPF_6$. Scan rate = 0.1 V/s.

The first system, **48**, bearing a terminal quinone moiety shows one reversible oxidation at +1.33 V (Figure 2.27). As can be seen in Table 2.5, all of the oxidation potentials for the Ru(II) complexes generated in this chapter show very similar oxidation potentials. This is undoubtedly the Ru^{II} to Ru^{III} oxidation,[50] effectively demonstrating that the HOMO of the Ru(II) complexes is located in the Ru(II) centre, with the orbital almost exclusively of metal character. As all of the participating ligands are phenanthroline ring systems, there is little difference in this value. The effect of using phen or bpy as the respective ancillary ligands also shows little effect on the HOMO energy of the complexes. The reductive processes are much less clear for **48** (Figure 2.27), and may be due to the terminal nature of the quinone, which is assumed to be less stable than that of the naphthoquinone structure.

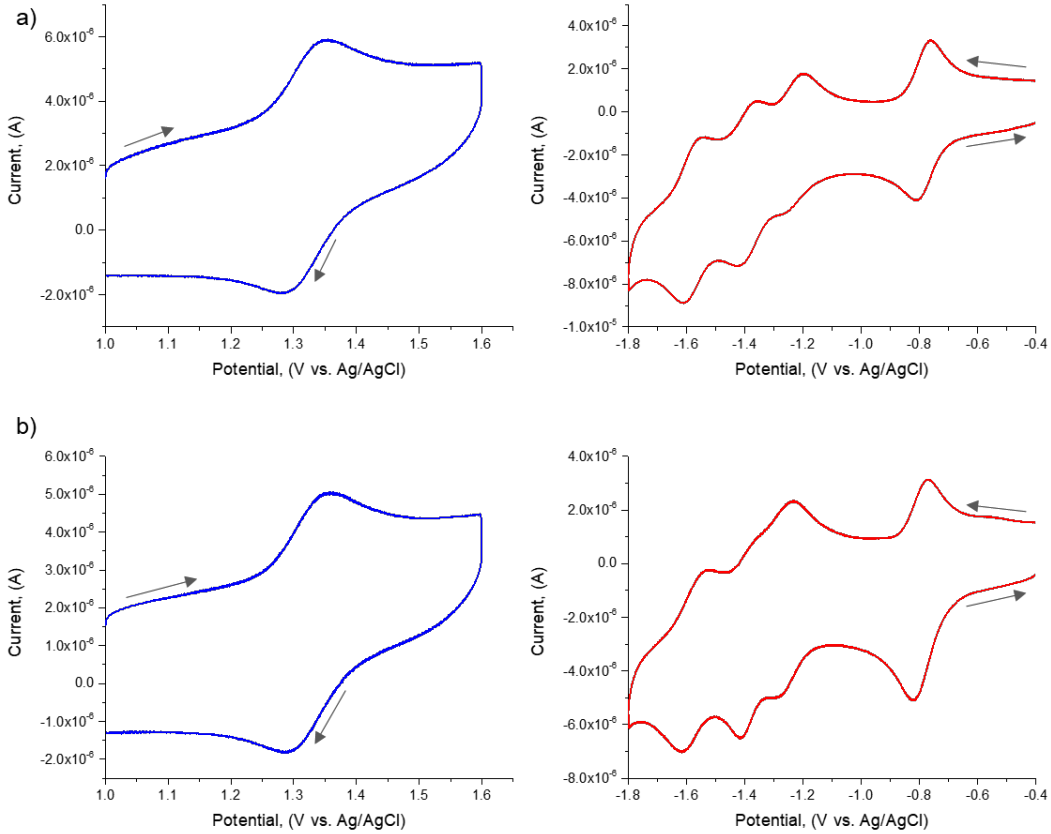

Figure 2. 28 (a) Oxidative (blue) and reductive (red) cyclic voltammograms of **49**. (b) Oxidative (blue) and reductive (red) cyclic voltammograms of **50**. MeCN and 0.1 M $TBAPF_6$. Scan rate = 0.1 V/s.

A clear reversible reduction can be observed at -0.79 V for **49** (Figure 2.28(a)). As per the ligand **14** assignment in Chapter 1, this was first assumed to be the conversion of the quinone moiety first to the semi-quinone, with the subsequent conversion to the dianion being masked

by the reductive processes occurring at the ancillary ligands.[51] These three reversible reductions are assigned as one electron reductions to each of the three bidentate ligands around the Ru(II) centre.[50] However, comparison to literature complexes composed of a polypyridine Ru(II) centre, and an appended benzo- or anthra-quinone, suggests that on metal complexation, the conversion of the quinone to the hydroquinone occurs in one step *versus* two (*i.e*. a two electron process).[52–54] A single reversible oxidation is observed at +1.32 V. Almost identical electrochemical activity is observed for **50**.

Comparing the electrochemical behaviour of **49** and **50** to that of their quinone-containing ligands **14** and **15**, reveals the effect of the metal complexation on the quinone of each ligand structure. The first reductive process of each complex and ligand is postulated to be conversion of the quinone to the semi-quinone. In the free ligands **14** and **15**, this occurs at a -0.74 V and -0.96 V respectively (See Chapter 1). On metal complexation, the first reductive process for **49** and **50** both occur at approximately -0.80 V. This suggests that the semi-quinone is considerably stabilised in **50** by the complexation of the metal centre, with essentially no change for **49**. As **49** bears a terminal quinone, with **50** bearing a "naphthoquinone" moiety, this would suggest that the terminal quinone is little affected by the metal complexation. For the naphthoquinone-type quinone, work by Díaz *et al.* with **L18**, shows the interesting effect of changing the metal centre with respect to the quinone-containing ligand.[55] In MeCN, depending on the ancillary ligands coordinated to a rhenium carbonyl centre, the free ligand **L18** semi-quinone reduction at -0.65 V changes to either -0.8 V or -0.43 V. As **49** is the first PAH-type compound bearing a terminal quinone moiety, there are no similar structures to compare or contrast.

In comparison to the literature previous mentioned regarding Ru(II) centre compounds bearing appended quinone moieties,[52–54] the quinone electrochemical behaviour appears buried in the baseline of the cyclic voltammetry trace, and not fully reversible, and thus may hint that those compounds do not have significant electron accepting capabilities. However, in this work, the electrochemical behaviour of the internal PAH-quinone structures is well-defined and fully reversible despite a wide potential window. This suggests that the dianion generated in **49** and **50** is exceptionally stable, *versus* those of appended anthraquinone structures currently in the literature. Further work is therefore necessary to investigate the use of **49** and **50** in photoinitiated electron collection studies for photocatalysis and photovoltaic applications, where the electrochemical behaviour of the novel quinone-containing structures may outperform the best current literature compounds. Work in this area is ongoing.

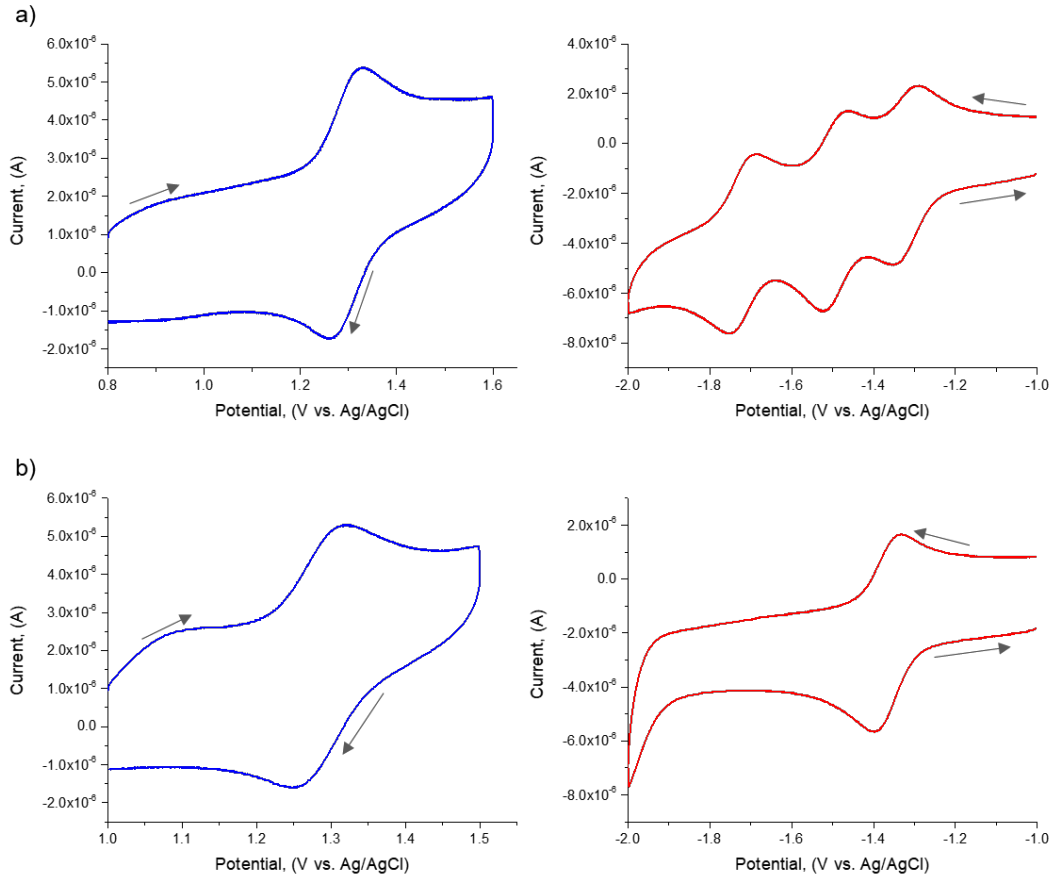

Figure 2. 29 (a) Oxidative (blue) and reductive (red) cyclic voltammograms of **51**. (b) Oxidative (blue) and reductive (red) cyclic voltammograms of **53**. MeCN and 0.1 M $TBAPF_6$. Scan rate = 0.1 V/s.

Figure 2.29(a)-(b) shows the oxidation and reduction behaviour of **51** and **53** respectively, both bearing the participating ligand **3**. **51** shows three reversible reduction potentials, again assigned as one electron reductions to each of the respective three bidentate ligands around the Ru(II) centre.[50] This is not observed for the Ir(III) centre for **53**. The cyclometalating ppy ancillary ligands likely show reductions outside of the solvent window of the MeCN solvent. A single reversible reduction is observed at -1.36 V, and is assigned as a one electron reduction of the only N^N ligand, **3**. A similar one electron process is observed for $[Ir(ppy)_2(phen)][PF_6]$.[56]

Figure 2.30(a)-(b) shows the oxidation and reduction behaviour of **52** and **54** respectively, both bearing the participating ligand **4**. The effect of the pyridazine ring substitution for **54** is immediately apparent, with a lowering of the reduction potential of **54** to -1.11 V, *versus* -1.36 V for the other Ir(III) centre complex **53**. A single irreversible oxidation for **54** is observed at +1.16 V.

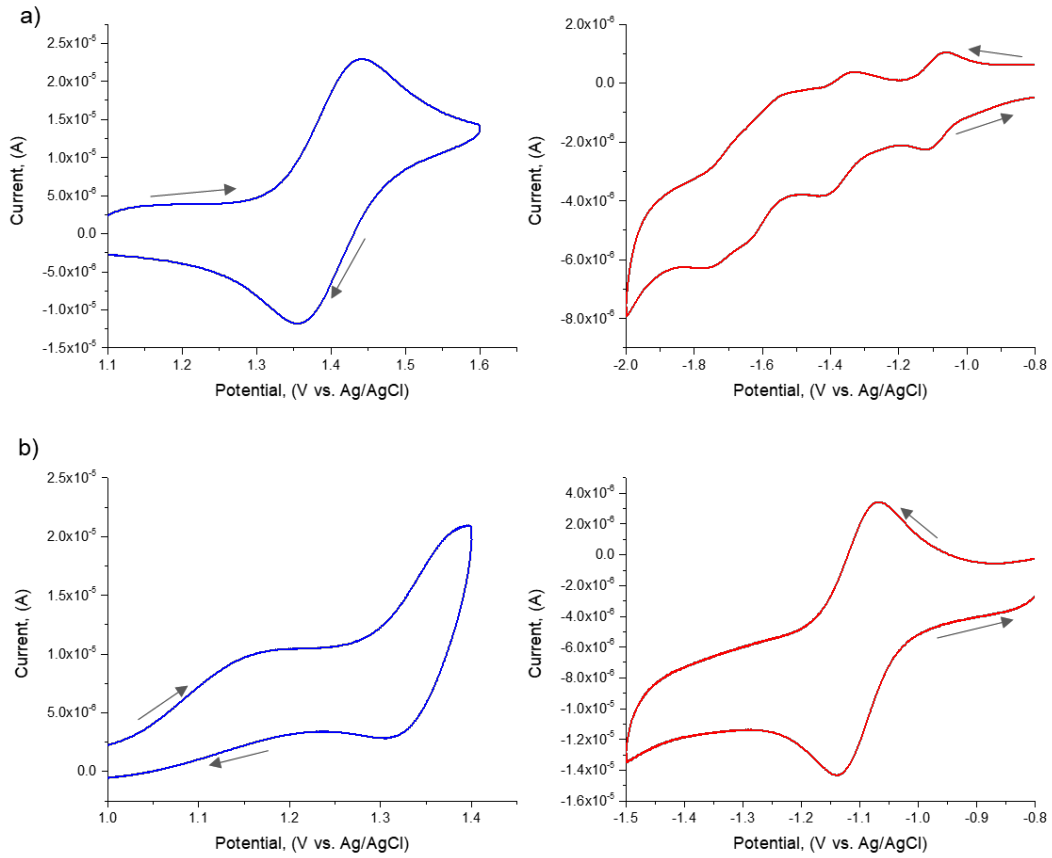

Figure 2. 30 (a) Oxidative (blue) and reductive (red) cyclic voltammograms of **52**. (b) Oxidative (blue) and reductive (red) cyclic voltammograms of **54**. MeCN and 0.1 M $TBAPF_6$. Scan rate = 0.1 V/s.

Table 2. 5 Electrochemical data for **48**, **49**, **50**, **51**, **52**, **53**, and **54**. (MeCN. 0.1 M $TBAPF_6$. Scan rate = 0.1 V/s.). Samples prepared in air and purged with N_2 for 10 mins and for the duration of measurement.

Compound	Oxidation; $E_{1/2}$/V, [ΔE_p/mV]	Reduction; $E_{1/2}$/V, [ΔE_p/mV]
48	+1.33 [80]	-1.33 [60], -1.59 [70]
49	+1.32 [60]	-0.79 [60], -1.23 [50], -1.39 [40], -1.58 [60]
50	+1.31 [70]	-0.80 [50], -1.26 [40], -1.41 [E_{pa}], -1.58 [80]
51	+1.32 [110]	-1.31 [50], -1.49 [60], -1.72 [60]
52	+1.4 [80]	-1.1 [50], -1.38 [90], -1.62 [160]
53	+1.29 [70]	-1.36 [70]
54	+1.16 [E_{pc}]	- 1.11 [70]

2.4 Photophysical Investigation of 48, 49, 50, 51, 52, 53, and 54

2.4.1 UV-visible Absorption Spectra of 48, 49, 50, 51, 52, 53, and 54

The UV-visible absorption spectra of **48**, **49**, **50**, **51**, **52**, **53**, and **54** are shown in Figure 2.31, with data summarised in Table 2.6.

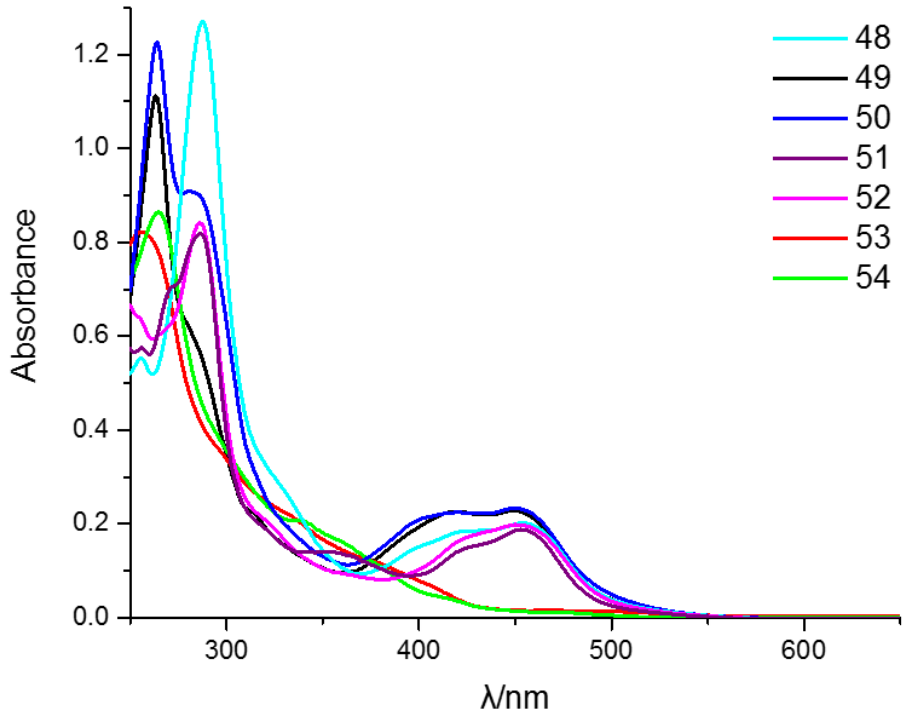

Figure 2. 31 UV-visible absorption spectra of **48**, **49**, **50**, **51**, **52**, **53**, and **54** in deaerated MeCN (Ar; 10^{-5} M).

It is clear from Figure 2.31 that the UV-visible absorption profiles are dominated by metal-assigned processes. For the Ru(II) complexes, the expected metal-to-ligand charge transfer (MLCT) transitions are immediately visible. **48**, **49**, and **50**, those Ru(II) complexes bearing quinone-containing ligands, show two MLCT absorptions that may include some n-π* transitions from within the quinone moiety. **49** and **50**, with ancillary phen ligands show very similar absorption profiles, with the lowest energy transition (^{1}MLCT) observed at λ_{abs} = 450 nm. A second transition (again assigned as ^{1}MLCT) is observed at λ_{abs} = 420 nm. These transitions are assigned with use of the $[Ru(bpy)_3]^{2+}$ model complex. The remaining Ru(II) complexes have their lowest energy transition at λ_{abs} = 455 nm, with their second lowest energy transition observed at λ_{abs} = 420 nm. Again, these are assigned at ^{1}MLCT transitions.

The Ir(III) complexes **53** and **54** do not show a similar ^{1}MLCT profile. The absorption profile of these complexes is predominately in the UV region of the spectra. A significant absorption is observed between λ_{abs} = 300-400 nm, with absorption in the visible region extending to

circa. 450 nm. All of the complexes show intense π-π* transitions < 300 nm, which occur within the π-structure of both the participating, and ancillary ligands.

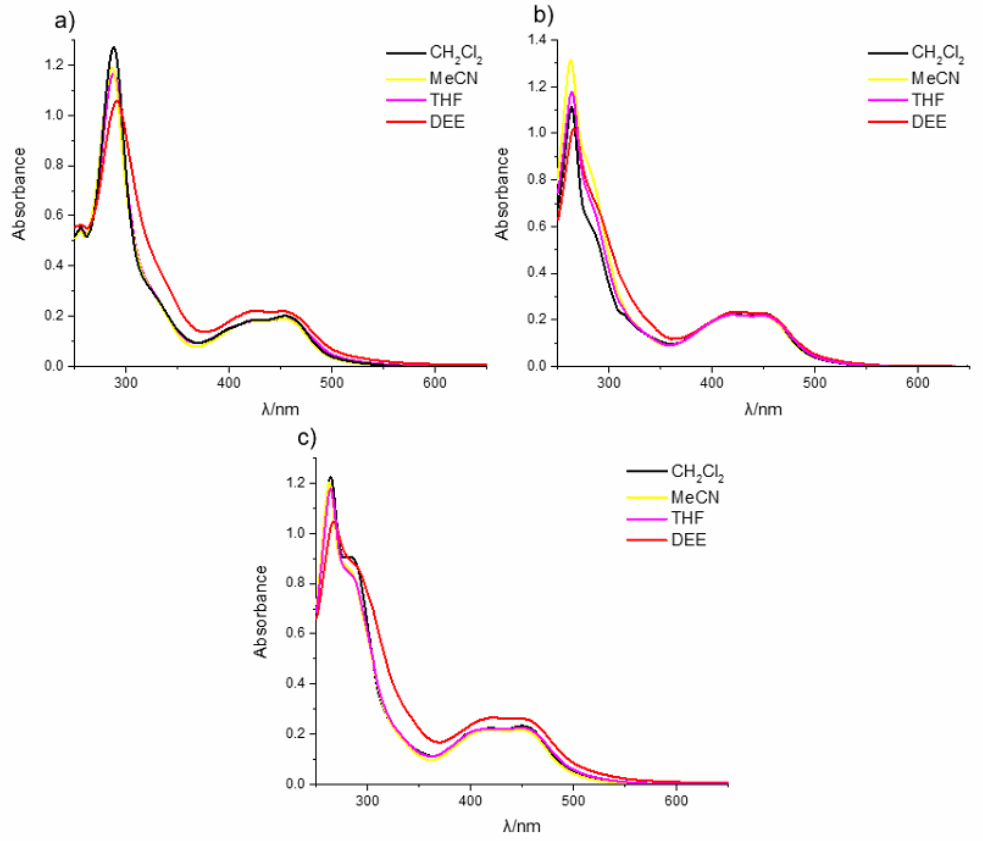

Figure 2. 32 Solvatochromism studies (UV-visible absorption spectra) of **48** (a), **49** (b), and **50** (c) in CH_2Cl_2, MeCN, THF, and DEE (10^{-5} M). DEE = Diethyl ether.

Solvatochromism studies were performed for **48**, **49**, **50**, **51**, **52**, **53**, with their respective absorption profiles given in Figures 2.32 and 2.33. Solvents of varying polarity were chosen; CH_2Cl_2, MeCN, THF, and diethyl ether. Maintaining a concentration of 10^{-5} M for all solutions, no significant change was seen for any of the complexes, indicating that the ground state energies of each of the respective complexes is unaffected by the solvent polarity. The ^{1}MLCT transition of **51** is observed to increase in diethyl ether, with a corresponding decrease in the π-π* transition band at λ_{abs} = 295 nm. A red shift of 10 nm is seen for the π-π* transition band, with a 5 nm shift observed for the ^{1}MLCT transition bands. This change is postulated as a result of a decrease in solubility of **51** in DEE *versus* that of the other solvents, which may result in an aggregation of the compound in solution. Typically, aggregation studies can be determined through the careful addition of known amounts of H_2O, but this was not performed here due to the immiscibility with DEE. No other significant differences are observed *via* the solvatochromism studies undertaken.

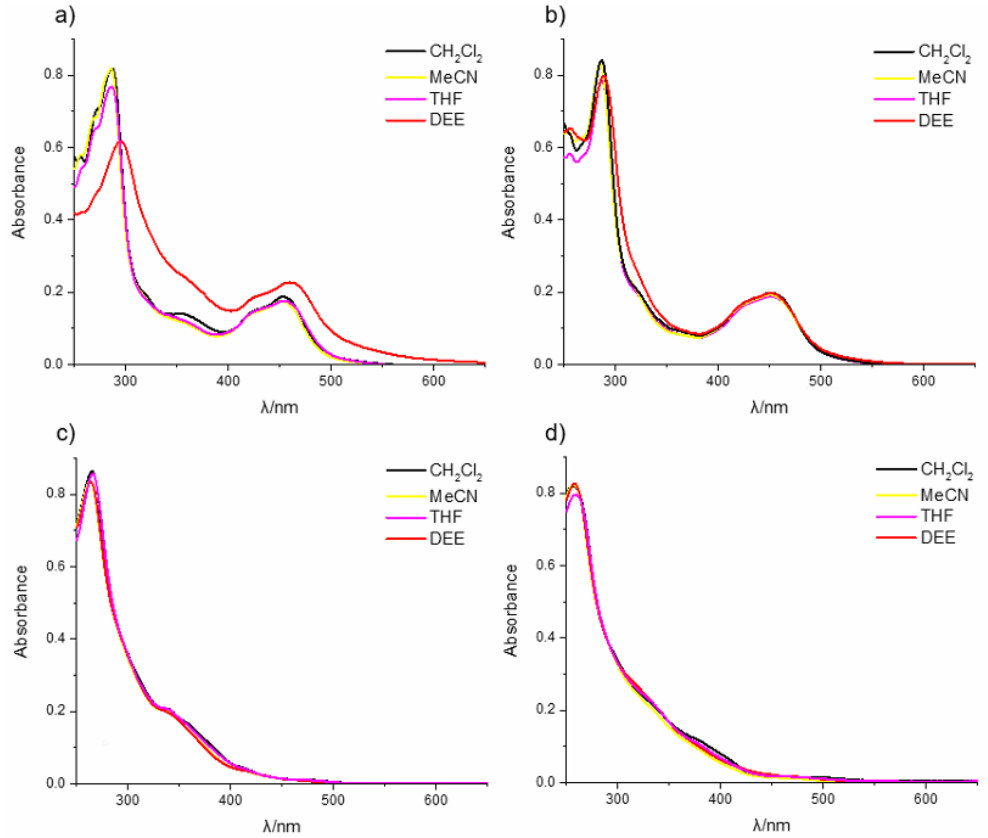

Figure 2. 33 Solvatochromism studies (UV-visible absorption spectra) of **51** (a), **52** (b), **53** (c), and **54** (d) in CH_2Cl_2, MeCN, THF, and DEE (10^{-5} M). DEE = Diethyl ether.

Table 2. 6 UV-visible spectral data for compounds **48**, **49**, **50**, **51**, **52**, **53**, and **54** in deaerated MeCN (Ar; 10^{-5} M).

Compound	**λ_{abs}/nm** **[ϵ x 10^4/M^{-1} cm^{-1}]**
48	255 [5.54], 285 [11.8], 420 [1.82], 455 [2.03]
49	265 [13.1], 290_{sh} [7.05], 420 [2.21], 450 [2.24]
50	262 [12.1], 285 [8.37], 420 [2.29], 450 [2.16]
51	285 [8.18], 420 [1.46], 450 [1.91]
52	285 [8.42], 420 [1.64], 450 [2.03]
53	265 [8.66], 340 [2.06], 360 [1.62], 415 [0.36]
54	255 [8.22], 405 [0.64]

2.5 Emission Studies of 48, 49, 50, 51, 52, 53, and 54

As all of the complexes **48**, **49**, **50**, **51**, **52**, **53**, and **54** are emissive, the steady state emission spectra were recorded. The excitation spectra monitored at the peak emission wavelength were also collected. These are given in Figure 2.34, with data summarised in Table 2.7.

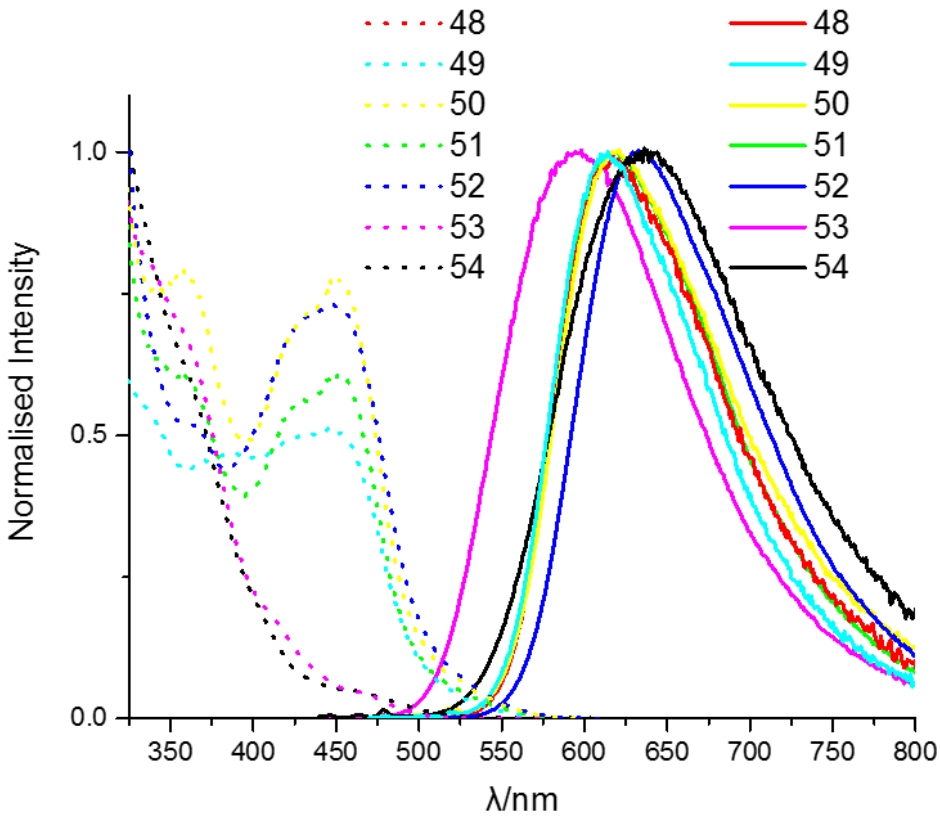

Figure 2. 34 Normalised emission spectra (solid line, λ_{ex} given in Table 2.7), and excitation spectrum (dashed line) of **48**, **49**, **50**, **51**, **52**, **53**, and **54** in MeCN (RT. 10^{-5} M).

The excitation spectra for all of the generated complexes match well with their respective UV-visible transitions, with the clear MLCT transition observable for those comprised of a Ru(II) centre. The emission spectra of the generated complexes show broad and featureless emission profiles, indicative of ^{3}MLCT character. This was expected as the large atomic mass of the Ru(II) and Ir(III) centres essentially guarantees 100 % intersystem crossing of the ^{1}MLCT excited state to that of the ^{3}MLCT excited state *via* significant spin-orbit coupling. The majority of the complexes show a single emission peak at *circa.* λ_{em} = 615 nm (**48**, **49**, **50**, and **51**). **54** shows the lowest energy emission at λ_{em} = 640 nm, while highest energy emission is observed for **53** at λ_{em} = 595 nm. A single emission peak for **52** is seen at λ_{em} = 630 nm.

Table 2. 7 Emission data of **48**, **49**, **50**, **51**, **52**, **53**, and **54** in deaerated MeCN at RT (10^{-5} M).

Compound	λ_{ex}/nm	λ_{em}/nm	Φ	τ (μs)
48	450	615	0.003	--
49	450	615	0.006	--
50	450	615	--	--
51	450	615	--	--
52	450	630	0.077[a,c]	1.51
53	420	595	0.25	--
54	420	640	0.04[b,c]	0.64

[a] Standard Deviation = 0.0068; [b] Standard Deviation = 0.0057; [c] Recorded using an integrating sphere method (See Chapter 5, Experimental).

To confirm the emissive nature of **48**, **49**, **50**, **51**, **52**, **53**, and **54** being from a triplet excited state (^{3}MLCT), degassing studies were undertaken for all of the generated compounds (Figures 2.35 and 2.36).

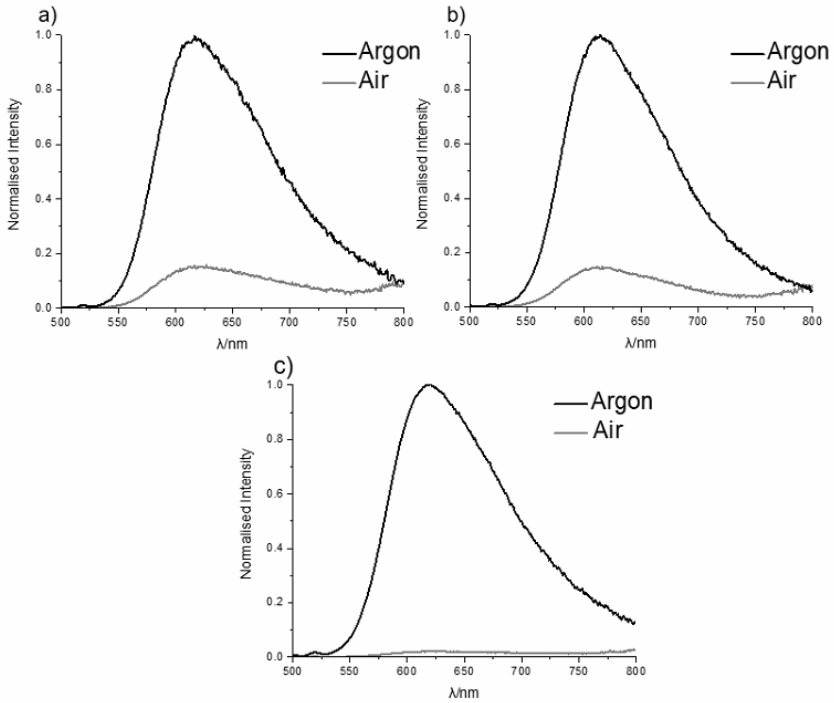

Figure 2. 35 Degassing studies (emission spectra) of **48** (a), **49** (b), and **50** (c) in MeCN (RT. 10^{-5} M).

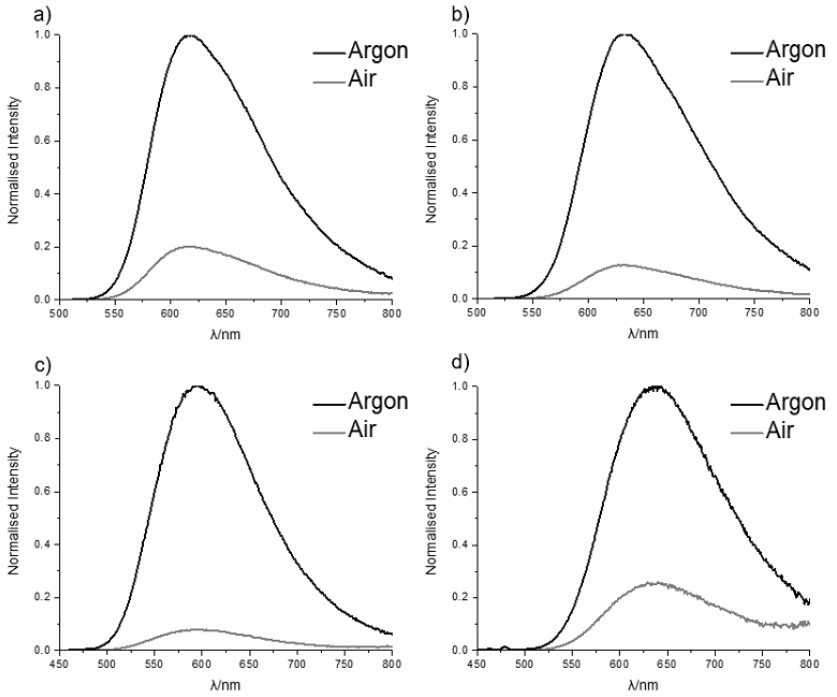

Figure 2. 36 Degassing studies (emission spectra) of **51** (a), **52** (b), **53** (c), and **54** (d) in MeCN (RT. 10^{-5} M).

It is immediately apparent that significant quenching of the luminescence of each respective complex occurs in the presence of atmospheric O_2. As the triplet excited state interacts with the triplet ground state of O_2, this confirms the luminescence of each complex at phosphorescent in nature.

Due to the emissive nature of **48**, **49**, **50**, **51**, **52**, **53**, and **54**, the phosphorescence quantum yield was measured using the single-point relative method, using $[(Ru(bpy)_3(Cl)_2]$ as the reference, in MeCN at RT. The single-point method was utilised through calculation of the integrated emission intensities of both the respective complex and $[(Ru(bpy)_3(Cl)_2]$, measured on the same instrument, with identical entrance and exit slit values. Optically dilute samples (Abs = ~0.1) of both the respective complex and $[(Ru(bpy)_3(Cl)_2]$. The quantum yields *via* the single-point method are summarised in Table 2.7.

Of note, the quantum yields of the quinone-containing compounds **49** and **50** are very low. This suggests that photoinduced electron transfer is occurring within these compounds, from the Ru(II) centre into the quinone moiety. This is unsurprisingly, as the closest literature compound **L57** is non-luminescent, with the authors describing an efficient photoinduced electron transfer from the Ru(II) centres into the central quinone core of the pyrazine bridging ligand.[27] Attempts to determine the excited state lifetimes of the compounds was unsuccessful due to their faint luminescence.

2.6 Photocatalytic Proton Reduction Experiments

The photocatalytic measurements were carried out through collaboration with Dr. Mary Pryce of Dublin City University. Sample preparation and photocatalytic measurements were carried out by Dr. Nivedita Das.

52 and **54** were assessed for their ability to act as a photosensitiser for hydrogen production *via* a double proton reduction in aqueous media using visible light. The intermolecular reactions were carried out in mixtures containing MeCN/TEA/H_2O (8:1:1), with a K_2PtCl_4 co-catalyst. Two irradiation wavelengths were employed; λ_{ex} = 350 and λ_{ex} = 470 nm, and the respective turnover numbers (TONs) were determined. Control vials containing no **52** or **54** produced negligible amounts of hydrogen. The TON is defined as number of moles of H_2 formed per mole of catalyst.

52 generated a total TON of 35 after irradiation at 470 nm for 18 hours. This low value is surprising, as irradiation at 470 nm should effectively populate the ^{3}MLCT excited state, allowing for successful electron transfer to the tetrachloroplatinate co-catalyst. **54** showed a reasonably high TON of 160 when irradiated at 470 nm after 18 hours. It is not uncommon for an Ir(III) complex to show improved performance compared to its Ru(II) analogue, due to an increased photostability of the cyclometalating phenylpyridines of the Ir(III) centre, *versus* the bipyridines of the Ru(II) centre, but it was surprising in this case due to the poor absorbance of **54** at 470 nm. For both **52** and **54**, negligible hydrogen production was seen when irradiated at 355 nm. This is unsurprising due to the poor absorption of the ^{1}MLCT absorption band at this wavelength value. For the purpose of these studies, it is assumed that electron transfer is occurring in a similar process to those in the related literature (discussed in the introduction to this work).

2.6.1 Attempted Syntheses of 58 and 59

The successful photocatalytic proton reduction studies with **52** and **54** prompted an investigation towards the generation of the respective bis-metallic intramolecular photocatalysts **58**, and **59**. Scheme 2.5 shows the attempted syntheses of these compounds, with the proton reduction catalyst (Pt), assembled in a cyclometallated fashion using one of the free phenyl moieties, and the central pyridazine ring. Similar to other literature intramolecular catalysts, the coordination environment of the catalytic metal is satisfied *via* the coordination of a solvent molecule (MeCN).[38]

Unfortunately, the synthesis of these compounds was not realised, with no product detected by NMR or HRMS on completion of a number of synthetic preparations used. As the

generated complexes exist as μ-Cl dimers in the solid state,[38] it was postulated that the large size, and twist, of the PAH-type ligand precluded the generation of this product.

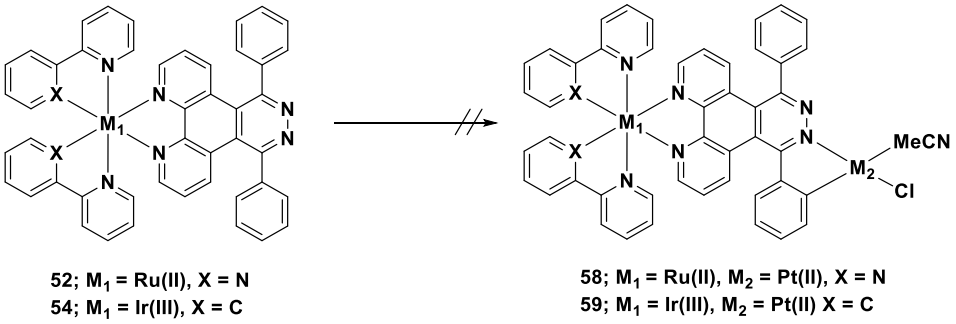

Scheme 2. 5 Unsuccessful synthetic attempts towards the bimetallic cyclometalated Pt(II) photocatalyst complexes **58** and **59**.

2.6.2 Attempted Syntheses of 68 and 70

In an attempt to address this issue, efforts were made to synthesise a bis-N^N ligand capable of bimetallic coordination, comprised still of a phenanthroline core ring system, and the central pyridazine ring.

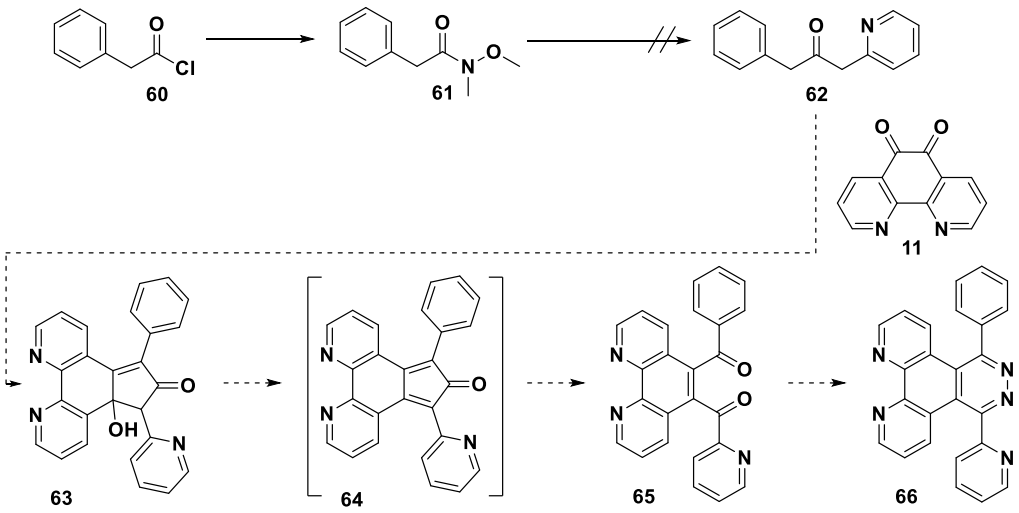

Scheme 2. 6 Unsuccessful synthetic attempts towards the "pyridine-monoketone" **62**. Postulated synthetic route to ligand **66**.

Scheme 2.6 describes the attempted synthesis of this compound **66**, through substitution of a free phenyl ring with that of a pyridine ring. However, attempts undertaken were

unsuccessful, as the bromo-pyridine compound, 2-(bromomethyl)pyridine, appears to not undergo facile or efficient lithiation. The synthesis of the Weinreb amide **61** was deliberately undertaken in an effort to prevent over-addition of the lithiated pyridine compound to the carbonyl moiety.

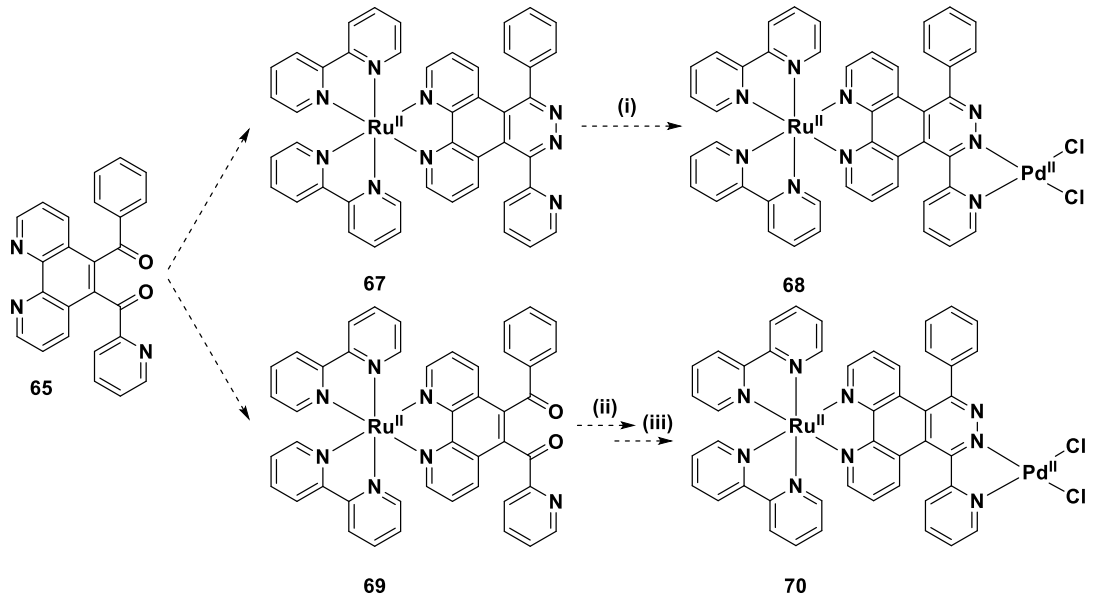

Scheme 2. 7 Postulated selective synthetic access to each bidentate coordination site of ligand **66.**

Scheme 2.7 further details the synthetic pathway that could have been attempted should the successful synthesis of **66** been realised. As the ligand **66** now has two bidentate N^N coordination sites, Scheme 2.7 visualises two potential synthetic routes to control metalation of the photosensitiser centre, and the proton reduction catalyst centre. Route B demonstrates that should metalation be carried out on the ring opened ligand **65** first, only the phenanthroline coordination site is available for complexation. This allows the singular coordination of the photosensitiser centre, with subsequent ring closure with hydrazine hydrate required to generate the second coordination site. This would allow the strict control of the respective coordination of the two centres. Exchange of the photosensitiser centre to that of the proton reduction centre with the ring opened ligand **65** allows the generation of a further class of compounds, with the proton reduction catalyst located on the phenanthroline ring system, with the photosensitiser coordination to the central pyridazine ring. Generation of both forms would facilitate the study of the effects of these "isomers" on the TON of these photocatalysts.

2.7 Further Synthetic Attempts & Future Work

Further the successful generation of a number of Ru(II) and Ir(III) complexes bearing partially-fused PAH-type ligands, opportunities now exist towards further functionalisation of the ligands towards a range of diverse applications. As already briefly explored in this chapter, complexes for photocatalytic proton reduction have been generated, confirming their suitability towards further work in this area. As photocatalytic proton reduction requires the formal transfer of an electron, the generation of quinone-containing complexes may assist in the transfer of electrons to the co-catalyst through photoinitiated electron collection within the quinone moiety. Work with **48**, **49**, and **50** is ongoing in this area.

Chart 2.5 shows three compounds incorporating a quinone moiety, but with secondary diol or carboxylic acid functionality for surface adsorption. Whilst the proton reduction work earlier was in-solution, an opportunity exists to study the effect of decoupling the photosensitiser and proton reduction catalyst. Assembly of a photo-electrode with **71**, **72**, or **73**, and an indium tin-oxide, titanium dioxide, or a nickel oxide surface, may facilitate effective electron transfer into the electrode, for use in a secondary Pd or Pt electrode capable of proton reduction. The effect of electron collection within the quinone moiety may assist electron injection into the surface, or may hinder the process. Further experimental work is therefore needed to explore this topic. However, it is apparent in Chart 2.5 that a number of synthetic strategies remains unrealised towards this exciting study.

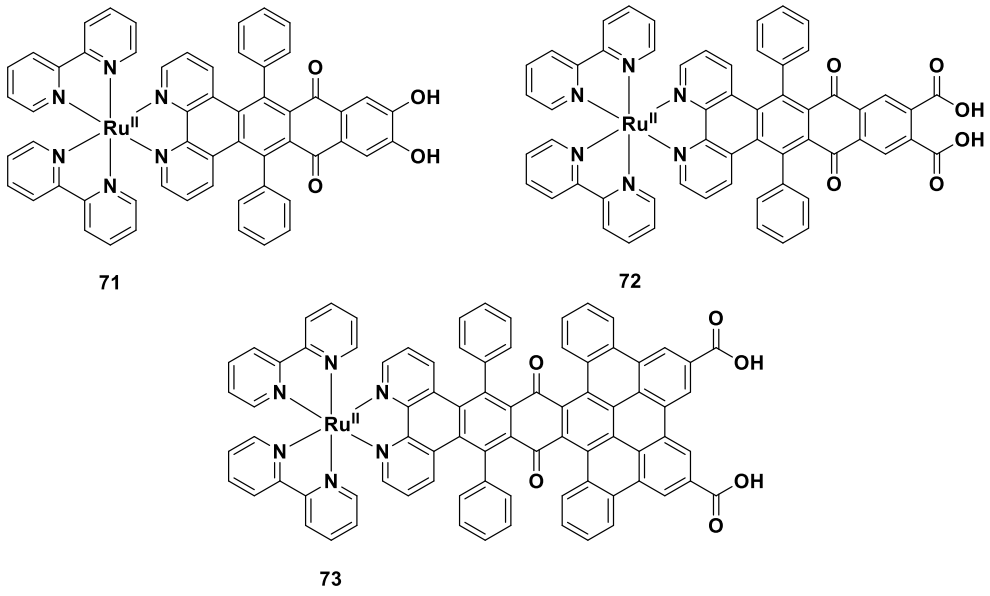

Chart 2. 5 Future work showing diol (**71**) or carboxylic acid (**72-73**) functionalisation of quinone-containing partially-fused PAH-type ligands.

Further work on systems generated in this, and the preceding chapter, is not limited to the quinone-containing ligands **14** and **15**. The extended phenanthroline ligands **3** and **4** offer potential use as "slow-threading" DNA intercalation complexes.[57] Threading intercalation is a DNA binding mode that displays extremely slow dissociation kinetics. As slow dissociation rates correlate to strong DNA affinity, the measure of this phenomenon is important regarding cytotoxicity.[57]

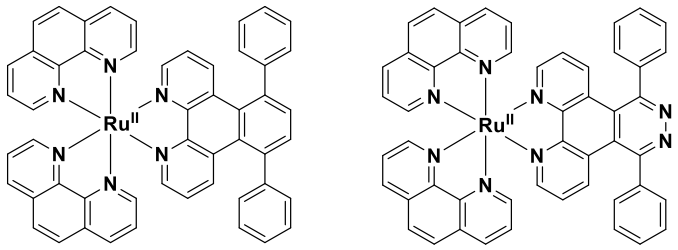

74 **75**

Chart 2. 6 Future work showing partially-fused PAH-type complexes potentially suitable for "slow threading" DNA intercalation studies.

Work by Li *et al.* demonstrates the use of a partially-fused PAH-type ligand, with two free phenyl rings assembled in a similar way to ligands **3** and **4**.[57] The authors use a 10,13-diphenyldipyrido[3,2-a:2',3'-c]phenazine ligands, with a Ru(II) centre. Phen ancillary ligands are chosen due to their higher affinity to DNA *versus* that of bpy. The generation therefore of **74** and **75** offers potential to study the effect of smaller partially-fused PAH-type systems for DNA intercalation. The effect of the restricted rotation of the free phenyls (observed in the NMR spectra of the respective complexes) may assist in the intercalation, and dissociation processes.

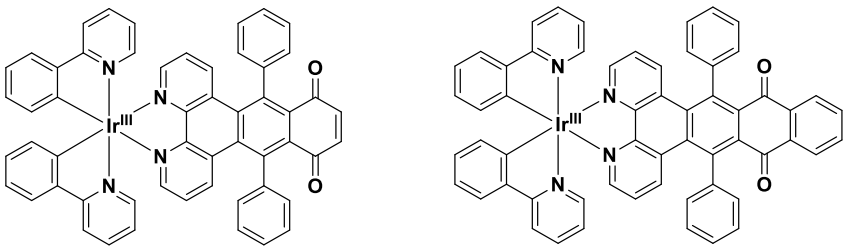

76 **77**

Chart 2. 7 Future work showing Ir(III) centred quinone-containing complexes towards their potential use as multi-electron photocatalysts.

As discussed earlier, quinone-containing ligand structures have been used to assist in the photocatalytic reduction of CO_2 to MeOH.[22] However, this work has relied exclusively on Ru(II) centres, and there appears to be no work towards multi-electron catalysis using Ir(III) centres. Chart 2.7 shows two Ir(III) complexes **76** and **77**, bearing the quinone-containing ligand **15** developed in Chapter 1. Whilst the higher cost of the Ir precursor may suggest its unsuitability towards commercial use, the higher photostability of the Ir(III) centre *versus* that of the Ru(II) centres in the literature may indicate its more favourable use.

2.8 Conclusion

The successful generation of three quinone-containing complexes of a Ru(II) centre is described. Further generation of Ru(II) and Ir(III) centred extended phenanthroline ligands is also documented. Extensive multinuclear NMR characterisation was performed on all complexes, revealing a ring slowing of the free phenyl rings for those complexes comprising a quinone moiety and the extended phenanthroline ligands, when complexed to a metal centre. This was not seen for the free ligands. Electrochemical and photophysical studies were carried out for all systems, revealing normal and expected optoelectronic behaviour of the generated complexes to their respective $[Ru(bpy)_3]^{2+}$ or $[Ir(ppy)_2(bpy)]^{+}$ model complexes.

Photocatalytic proton reduction studies carried out to **52** and **54** revealed TONs of 35 and 160 respectively. Detailed further synthetic work is included, with some active future work also described.

2.9 References

1 S. Campagna, F. Puntoriero, F. Nastasi, G. Bergamini and V. Balzani, *Photochemistry and Photophysics of Coordination Compounds I*, Springer Berlin Heidelberg, Berlin, Heidelberg, 2007, vol. 280.

2 Y. Chen, W. Lei, G. Jiang, Q. Zhou, Y. Hou, C. Li, B. Zhang and X. Wang, *Dalton Trans.*, 2013, **42**, 5924–5931.

3 M. A. Ischay, M. E. Anzovino, J. Du and T. P. Yoon, *J. Am. Chem. Soc.*, 2008, **130**, 12886–12887.

4 C. Creutz and N. Sutin, *Inorg. Chem.*, 1976, **15**, 496–499.

5 G. S. Laurence and V. Balzani, *Inorg. Chem.*, 1974, **13**, 2976–2982.

6 D. W. Thompson, A. Ito and T. J. Meyer, *Pure Appl. Chem.*, 2013, **85**, 1257–1305.

7 A. O. Adeloye and P. A. Ajibade, *Molecules*, 2014, **19**, 12421–60.

8 D. V. Pinnick and B. Durham, *Inorg. Chem.*, 1984, **23**, 1440–1445.

9 J. W. Verhoeven, *Pure Appl. Chem.*, 1996, **68**, 2223–2286.

10 M. Kasha, *Discuss. Faraday Soc.*, 1950, **9**, 14.

11 M. ABRAHAMSSON, Uppsala Universitet, 2006.

12 M. A. Ischay, Z. Lu and T. P. Yoon, *J. Am. Chem. Soc.*, 2010, **132**, 8572–8574.

13 J. D. Parrish, M. A. Ischay, Z. Lu, S. Guo, N. R. Peters and T. P. Yoon, *Org. Lett.*, 2012, **14**, 1640–1643.

14 L. Flamigni, A. Barbieri, C. Sabatini, B. Ventura and F. Barigelletti, in *Photochemistry and Photophysics of Coordination Compounds II*, eds. V. Balzani and S. Campagna, Springer Berlin Heidelberg, Berlin, Heidelberg, 2007, pp. 143–203.

15 C. Jin, J. Liu, Y. Chen, R. Guan, C. Ouyang, Y. Zhu, L. Ji and H. Chao, *Sci. Rep.*, 2016, **6**, 22039.

16 R. D. Costa, E. Ortí, H. J. Bolink, F. Monti, G. Accorsi and N. Armaroli, *Angew. Chemie Int. Ed.*, 2012, **51**, 8178–8211.

17 C.-H. Yang, Y.-M. Cheng, Y. Chi, C.-J. Hsu, F.-C. Fang, K.-T. Wong, P.-T. Chou, C.-H. Chang, M.-H. Tsai and C.-C. Wu, *Angew. Chemie Int. Ed.*, 2007, **46**, 2418–2421.

18 C.-F. Chang, Y.-M. Cheng, Y. Chi, Y.-C. Chiu, C.-C. Lin, G.-H. Lee, P.-T. Chou, C.-C. Chen, C.-H. Chang and C.-C. Wu, *Angew. Chemie Int. Ed.*, 2008, **47**, 4542–4545.

19 K. Hasan, J. Wang, A. K. Pal, C. Hierlinger, V. Guerchais, H. Sen Soo, F. García and E. Zysman-Colman, *Sci. Rep.*, 2017, **7**, 15520.

20 C. M. Brown, M. J. Kitt, Z. Xu, D. Hean, M. B. Ezhova and M. O. Wolf, *Inorg. Chem.*, 2017, **56**, 15110-15118.

21 Q.-X. Zhou, W.-H. Lei, J.-R. Chen, C. Li, Y.-J. Hou, X.-S. Wang and B.-W. Zhang, *Chem. - Eur. J.*, 2010, **16**, 3157–3165.

22 Y. Na, P. Lincoln, J. R. Johansson and B. Nordén, *ChemCatChem*, 2012, **4**, 1746–1750.

23 A. E. Friedman, J. C. Chambron, J. P. Sauvage, N. J. Turro and J. K. Barton, *J. Am. Chem. Soc.*, 1990, **112**, 4960–4962.

24 M. R. Gill and J. A. Thomas, *Chem. Soc. Rev.*, 2012, **41**, 3179–92.

25 X. Li, Y. Zhang, H. Chen, J. Sun and F. Feng, *ACS Appl. Mater. Interfaces*, 2016, **8**, 22756–22761.

26 M.-J. Kim, R. Konduri, H. Ye, F. M. MacDonnell, F. Puntoriero, S. Serroni, S.

Campagna, T. Holder, G. Kinsel and K. Rajeshwar, *Inorg. Chem.*, 2002, **41**, 2471–2476.

27 S. Singh, N. R. de Tacconi, D. Boston and F. M. MacDonnell, *Dalton Trans.*, 2010, **39**, 11180–11187.

28 S. Singh, N. R. de Tacconi, N. R. G. Diaz, R. O. Lezna, J. Muñoz Zuñiga, K. Abayan and F. M. MacDonnell, *Inorg. Chem.*, 2011, **50**, 9318–9328.

29 T. Kowacs, Q. Pan, P. Lang, L. O'Reilly, S. Rau, W. R. Browne, M. T. Pryce, A. Huijser and J. G. Vos, *Faraday Discuss.*, 2015, **185**, 143–170.

30 M. Karnahl, C. Kuhnt, F. W. Heinemann, M. Schmitt, S. Rau, J. Popp and B. Dietzek, *Chem. Phys.*, 2012, **393**, 65–73.

31 M. G. Pfeffer, C. Pehlken, R. Staehle, D. Sorsche, C. Streb and S. Rau, *Dalton Trans.*, 2014, **43**, 13307–13315.

32 M. Karnahl, C. Kuhnt, F. Ma, A. Yartsev, M. Schmitt, B. Dietzek, S. Rau and J. Popp, *ChemPhysChem*, 2011, **12**, 2101–2109.

33 S. Kaufhold, D. Imanbaew, C. Riehn and S. Rau, *Sustain. Energy Fuels*, 2017, **1**, 2066–2070.

34 A. Fihri, V. Artero, M. Razavet, C. Baffert, W. Leibl and M. Fontecave, *Angew. Chemie Int. Ed.*, 2008, **47**, 564–567.

35 A. Fihri, V. Artero, A. Pereira and M. Fontecave, *Dalton Trans.*, 2008, 5567–5569.

36 Y. Halpin, M. T. Pryce, S. Rau, D. Dini and J. G. Vos, *Dalton Trans.*, 2013, **42**, 16243–54.

37 A. Bailey, L. Andrews, A. Khot, L. Rubin, J. Young, T. D. Allston and G. A. Takacs, *J. Chem. Educ.*, 2015, **92**, 688-692.

38 S. Soman, G. Singh Bindra, A. Paul, R. Groarke, J. C. Manton, F. M. Connaughton, M. Schulz, D. Dini, C. Long, M. T. Pryce and J. G. Vos, *Dalton Trans.*, 2012, **41**, 12678–80.

39 S. Porada, L. Weinstein, R. Dash, A. van der Wal, M. Bryjak, Y. Gogotsi and P. M. Biesheuvel, *ACS Appl. Mater. Interfaces*, 2012, **4**, 1194–9.

40 M. Zhou, P. R. Nemade, X. Lu, X. Zeng, E. S. Hatakeyama, R. D. Noble and D. L. Gin, *J. Am. Chem. Soc.*, 2007, **129**, 9574–5.

41 G. S. Bindra, M. Schulz, A. Paul, R. Groarke, S. Soman, J. L. Inglis, W. R. Browne, M. G. Pfeffer, S. Rau, B. J. MacLean, M. T. Pryce and J. G. Vos, *Dalton Trans.*, 2012, **41**, 13050–9.

42 D. R. Whang, K. Sakai and S. Y. Park, *Angew. Chem. Int. Ed.*, 2013, **52**, 11612–5.

43 M. Wang, Y. Na, M. Gorlov and L. Sun, *Dalton Trans.*, 2009, **0**, 6458–67.

44 T. Stoll, M. Gennari, J. Fortage, C. E. Castillo, M. Rebarz, M. Sliwa, O. Poizat, F. Odobel, A. Deronzier and M.-N. Collomb, *Angew. Chem. Int. Ed.*, 2014, **53**, 1654–8.

45 S. Rau, B. Schäfer, D. Gleich, E. Anders, M. Rudolph, M. Friedrich, H. Görls, W. Henry and J. G. Vos, *Angew. Chem. Int. Ed.*, 2006, **45**, 6215–8.

46 C. V. Suneesh, B. Balan, H. Ozawa, Y. Nakamura, T. Katayama, M. Muramatsu, Y. Nagasawa, H. Miyasaka and K. Sakai, *Phys. Chem. Chem. Phys.*, 2014, **16**, 1607–16.

47 T. S. Teets and D. G. Nocera, *Chem. Commun.*, 2011, **47**, 9268–74.

48 G. Singh Bindra, M. Schulz, A. Paul, S. Soman, R. Groarke, J. Inglis, M. T. Pryce, W. R. Browne, S. Rau, B. J. Maclean and J. G. Vos, *Dalton Trans.*, 2011, **40**, 10812–4.

49 W. Huang and T. Ogawa, *Polyhedron*, 2006, **25**, 1379–1385.

50 S. Monro, J. Scott, A. Chouai, R. Lincoln, R. Zong, R. P. Thummel and S. A. McFarland, *Inorg. Chem.*, 2010, **49**, 2889–2900.

51 R. Díaz, O. Reyes, A. Francois, A. M. Leiva and B. Loeb, *Tetrahedron Lett.*, 2001, **42**, 6463–6467.

52 K. A. Opperman, S. L. Mecklenburg and T. J. Meyer, *Inorg. Chem.*, 1994, **33**, 5295–5301.

53 M. Borgström, O. Johansson, R. Lomoth, H. B. Baudin, S. Wallin, L. Sun, B. Åkermark and L. Hammarström, *Inorg. Chem.*, 2003, **42**, 5173–5184.

54 J. Hankache, M. Niemi, H. Lemmetyinen and O. S. Wenger, *Inorg. Chem.*, 2012, **51**, 6333–6344.

55 R. Díaz, A. Francois and B. Loeb, *Polyhedron*, 2011, **30**, 697–701.

56 J. R. Ochola and M. O. Wolf, *Org. Biomol. Chem.*, 2016, **14**, 9088–9092.

57 M. Li, P. Lincoln and J. Andersson, *J. Phys. Chem. B*, 2011, **115**, 7923–7931.

Chapter 3

Towards Pyridazine-substituted GNRs

3.1 Introduction

3.1.1 Technical Introduction

Graphene Nanoribbons (GNRs) may be considered as narrow strips of graphene, with the reduction of the 2D structure of graphene to the 1D structure of GNR resulting in interesting electronic properties,[1–4] with promising potential applications in polymer composites[5] and electrode materials for energy storage.[6,7] Two main synthetic methodologies have emerged towards the generation of processable GNRs; top down and bottom up. The top down strategy often includes the generation of Single Walled Carbon Nanotubes (SWNTs), or Multi-Walled Carbon Nanotubes (MWCNTs), before their chemically induced "unzipping", generating GNRs suitable for potential investigation and commercialisation.[8–11] Figure 3.1(a) shows modifications of SWNTs, which are often carried out before the inducement of unzipping. Introduction of nitrogen-substitution can also be achieved through this method, with substitution occurring during the nanotube synthesis (discussed shortly). Figure 3.1(b) shows the different types of nitrogen-substitution in nitrogen-GNRs (N-GNRs). Two types of "graphitic" substitution can be seen, bulk- or edge-based, with pyridinic and pyrrolic also visible. The absence of pyridazine substitution is noted, and will be discussed later.

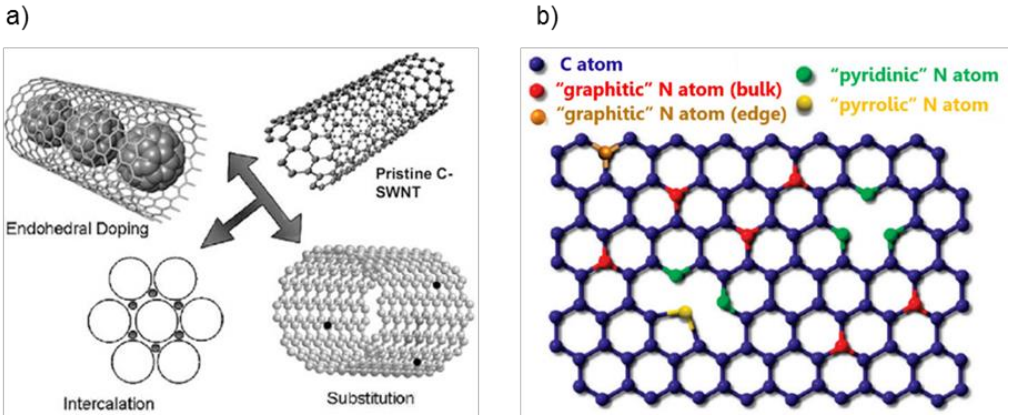

Figure 3. 1 (a) Visualisation of the modification strategies of Single Walled Carbon Nanotubes (SWNTs). (b) Forms of nitrogen-substitution in GNR/graphene monolayers.

Figure 3.2 shows three commonly used methods in the synthesis of carbon nanotubes *via* the top down synthetic methodology. As this volume of work concentrates solely on the use of the bottom up approach, these will only be briefly described. Figure 3.2(a) visualises the Arc Discharge method of the synthesis of carbon nanotubes.[12–14] Here, a direct current arc voltage is applied across two graphitic electrodes, typically in an inert atmosphere. Use of strictly graphitic electrodes generally only facilitates the generation of fullerene soot, with MWNTs

assembling on the cathode. Modification of the anode to include metal catalysts facilitates the generation of SWNTs as soot.[14] The introduction of nitrogen to the atmosphere allows the generation of nitrogen-substitution in the nanotube.

Figure 3.2(b) shows the generation of carbon nanotubes through the method of laser ablation.[15–17] In this method, a graphitic target in vaporised through use of a high powered laser, at elevated temperatures of *circa.* 1200 °C, under a partial vacuum. Control over the quantity and quality of the resulting SWNTs or MWNTs is facilitated though the altering of a number of factors including temperature, laser power, inert gas choice, and pressure. Use of a catalyst is generally required for the generation of SWNTs, which is typically cobalt or nickel. As visualised in Figure 3.2(b), use of a much-cooled "Collector" promotes the "self-assembly" of the nanotubes from the carbon vapours. Addition of a nitrogen precursor to the target facilitates nitrogen-substitution of the resulting nanotubes.

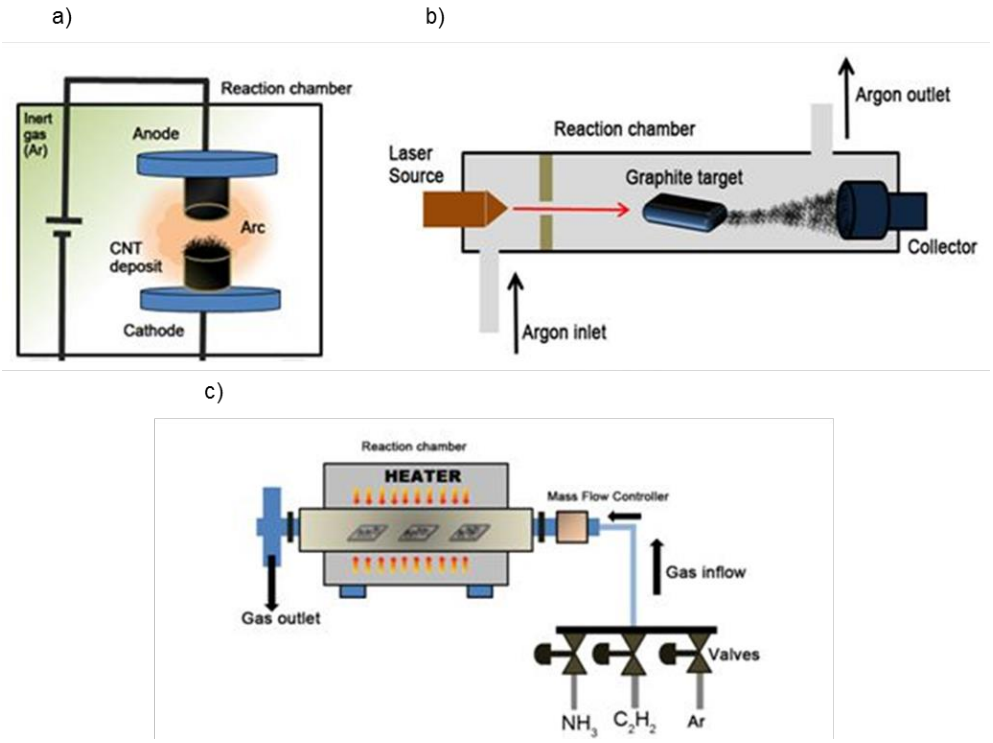

Figure 3. 2 Methods of GNR and N-GNR "top down" synthetic strategies. (a) Arc discharge. (b) Laser ablation. (c) Chemical Vapour Deposition (CVD).

Figure 3.2(c) shows the most commonly used method of nanotube synthesis, Chemical Vapour Deposition (CVD).[18–23] Similarly to the laser ablation method, CVD can produce SWNTs or MWNTs, with SWNTs generally formed at higher temperatures. In CVD, gaseous hydrocarbons are energised through used of a high energy source including plasma,[18] or a

heated coil. A process or carrier gas (often inert) is used to control the concentration of the relevant hydrocarbons, with nitrogen substitution in the resulting nanotube realised through addition of nitrogen precursors. On elevation of the furnace temperature, the gaseous hydrocarbons are broken apart at pre-selected substrate containing nickel, cobalt, or iron catalyst(s). Further to binding, nanotube growth is facilitated. Whilst this is an over-simplification of the process, the large number of CVD techniques towards nanotube synthesis often follow this generalised method. CVD also offers the most promise of the top down methodology towards the successful commercialisation of nanotubes, and GNRs, as it is low cost, and offers growth of the nanotube directly on the substrate.[24]

3.1.2 General Introduction

This chapter will introduce current literature work dealing with the nitrogen-doped graphene nanoribbons (N-GNRs), before introducing the theoretically postulated pyrazine-substituted GNRs. This research area has become increasingly active, driven by the realisation of real-world device fabrication using all-carbon GNRs,[25] instead of their larger graphene counterparts. Due to their small size, a solution-based chemistry approach has allowed a "bottom-up" synthetic methodology to be adopted towards the generation of the pristine N-GNR samples for optoelectronic devices. This heralds an exciting fusion of bench chemistry with high-level chemical physics techniques. Larger PAH systems suffer from poor to non-existent solubility,[26] fuelled by their propensity to stack, the use of smaller molecular fragments as "feedstock" allows circumvention of this problem, with the cyclodehydrogenation and polymerisation steps typically occurring on reactive metallic surfaces without the need for solvent. However, rather strikingly, examples of synthetically accessible precursors in the literature for these systems are sparse. It is for this reason that recent high-impact literature publications have concentrated heavily on the bottom-up synthetic approach, and its modifications.

N-GNRs require meticulous molecular design in order to allow the generation of pristine, fully-cyclised, sp^2 hybridised species. The inclusion of nitrogen atoms into the PAH framework requires careful consideration, as the location of the nitrogen atom may prevent full cyclisation, or restrict the growth of the GNR along a number of axes. For this reason, the design of nitrogen-substituted GNRs has remained limited to-date when compared to the all-carbon versions. Resulting ribbons from polyaromatic architectures have typically followed revisions to a standard single repeating unit, 2,7-dibromophenanthrene, though some other routes do exist and will be discussed later. The 2,7-dibromophenanthrene repeating unit, also discussed in detail later, promises access to intriguing and commercially

desirable nitrogen-substituted GNRs, but to-date has been limited to the inclusion of substituents including pyridine and pyrimidine rings.

As discussed, the construction of GNRs can be achieved *via* a top-down or bottom-up approach. Both methodologies are employed for the generation of nitrogen-substituted GNRs, but it is the bottom-up approach that offers the necessary synthetic control over the position of the nitrogen dopants as required in optoelectronic devices. Precise control of the dopant concentration, and of the dopant position within the GNR from the beginning, allows the full realisation of the "fine-tuning" of the electronic properties of GNRs. This is comparable to the doping of conventional silicon-based semiconductors. The two types of semiconductor are n-type, and p-type. In a p-type semiconductor, there is a large concentration of holes, with a small concentration of electrons, resulting in the hole being the main charge carrier. Conversely, in an n-type semiconductor, there is a large concentration of electrons, resulting in the electron being the charge carrier. Addition of nitrogen to the GNR structure generates an n-type semiconductor.[27] As a general rule, increasing the nitrogen content results in an increase in the GNR's electron mobility values.[28] As the top-down approach cannot achieve the same precise level of dopant concentrations, pyridazine-substitution patterns in N-GNRs are likely to be most accessible *via* the bottom-up approach.

This chapter aims to successfully incorporate a pyridazine ring into an extended 2,7-dibromophenanthrene repeating unit, and to thereby realise the first molecular fragment of this type. This will generate a "chevron-type" GNR,[29] with a smaller width compared to most literature compounds. Whilst pyridazine-substituted systems have been theoretically investigated, no experimental results exist.[30–32] These theoretical systems are discussed in detail within this chapter. A synthetically accessible pyridazine-substituted GNR would prove an interesting route to confirm or contradict these theoretical results. Additionally, a synthetically accessible route towards incorporating pyridazine embedded GNR structures would greatly assist in the development of novel precursor compounds.

3.1.3 Nitrogen-substituted Graphene Nanoribbons

3.1.3.1 On-surface Precursors

Figure 3.3 shows three approaches of note towards nitrogen-substituted PAH-type compounds that may be tailored towards nitrogen-substituted GNRs. These are formed *via* on-surface synthetic reactions or in solution, generating compounds requiring a further cyclodehydrogenation step, or requiring further oligomer growth. The compounds included in Figure 3.3 do not use the 2,7-dibromophenanthrene core system, but are (i) dimers and trimers, or (ii) require numerous synthetic steps in their generation. The lack of a diverse

library of precursors with the ability to be incorporated in the design of future nitrogen-substituted GNRs has significant consequences, and these examples are discussed here to demonstrate the challenges towards novel nitrogen-substituted GNRs.

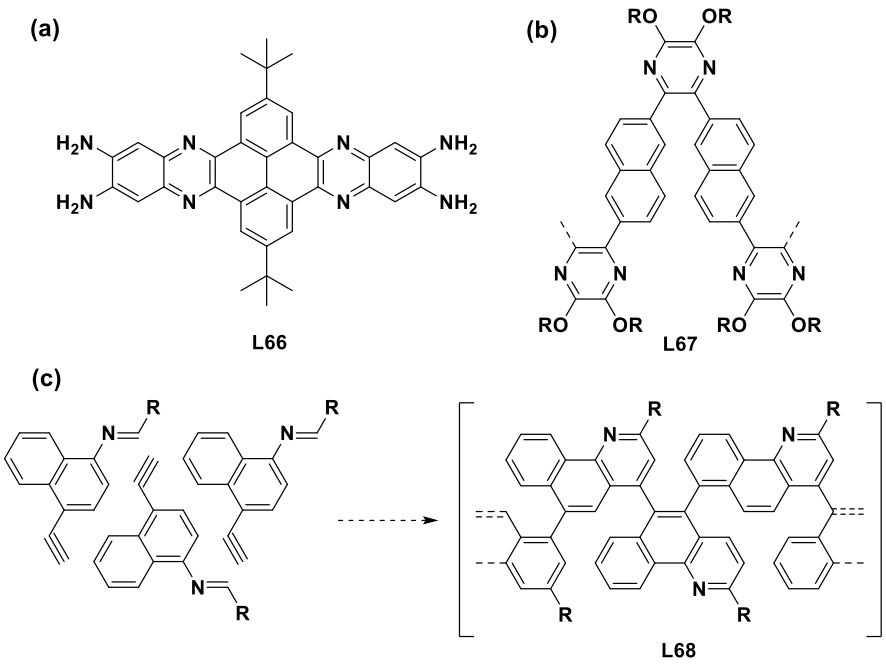

Figure 3. 3 (a)-(c) Literature examples of compounds with as N-GNR molecular fragments.

Figure 3.3(a) shows work carried out by Jiang *et al.*[33] towards the reaction of molecular precursors to form pyrene-fused pyrazaacenes (PPAs), **L66**, on metal surfaces. The synthesis of the PPA here occurs through a diketone located on the pyrene, with an aromatic 1,2,4,5-tetraamine under Schiff base conditions. PPAs generated in solution-based syntheses suffer from extreme insolubility, hindering both their synthesis and their characterisation. The approach taken here was to investigate if the synthesis of PPAs on metal surfaces could be undertaken through the deposition of the precursors, with subsequent annealing. Studies on three metal surfaces, Ag(111), Au(111) and Cu(111), generated significantly different results, with the Ag(111) surface being the only surface capable of carrying out the on-surface synthesis of the desired PPAs. In a "Goldilocks-type" situation, the Au(111) surface proved incapable of successfully anchoring the precursors during the annealing step, while the Cu(111) surface proved too reactive, and led to precursor decomposition during the annealing step.[33] The generation of the PPAs on the Ag(111) surface were then subjected to Scanning Tunnel Microscopy (STM) and X-ray Photoelectron Spectroscopy (XPS). The work concluded with studies of varying ketone and amine concentrations in the deposition step, which resulted in significant differences in dimer, trimer, or oligomer formation. However,

dimer and trimer growth were seen in much greater quantities compared to longer oligomers. Whilst GNR generation was not the goal of this work, the ability to generate long oligomers points towards the ability to generate nitrogen-substituted GNRs in future work if appropriate forcing conditions can be found towards much longer oligomer growth. Here, the nitrogen concentration (dopant concentration) could be precisely controlled, with modification of the structure possible before precursor deposition. Use of pyrazine-derived systems offers a route to nitrogen-substituted GNRs that has yet to be fully realised. However, it is noted here that the linear nature of their construction will mean that those GNRs generated this way will suffer some synthetic limitations.

Figure 3.3(b) reveals another N-GNR precursor, **L67**, once again incorporating pyrazine as the nitrogen dopant precursor. Of significant difference however, here the pyrazine ring is now on the periphery of the GNR rather than central to the GNR's synthesis. It is therefore not used to directly generate the GNR, but rather used as a synthon to incorporate nitrogen atoms into the GNR structure. Reported by Kim *et al.*,[28] this attempt at a novel nitrogen-substituted GNR is achieved through the simple swapping of a single phenyl precursor ring to that of a pyrazine ring. **L67** is synthesised *via* Suzuki cross-coupling reactions between the bromo-substituted pyrazine rings (or phenyl rings) and boronic acid-substituted naphthalene's. The highly solubilising alkoxy groups of the pyrazine or phenyl rings allowed the authors to attempt the cyclodehydrogenation step in a solution-based approach, yielding soluble GNRs for subsequent use. Using different amounts of the phenyl or pyrazine precursors also allowed the generation of GNRs with different nitrogen dopant concentrations. Comparison of three of these systems with varying dopant concentration confirmed previously calculated results, with increasing nitrogen concentration resulting in a large increase in the electron mobility of the nitrogen-substituted GNR. This was estimated *via* the construction of back-gated thin-film transistors (TFTs), with Au source-drain electrodes. Measurements per TFT were repeated ten times, with the carrier mobility calculated from the transfer curve of the source-drain current versus the gate voltage in the well-resolved saturation regime. This effectively demonstrated that the charge transport behaviour of these GNRs is n-type at large dopant concentrations. [28]

Finally, Figure 3.3(c) shows a potential nitrogen-substituted GNR from a polybenzoquinoline-based precursor **L68**. Unlike the other two examples given in Figure 3.3, the N-GNR has yet to be synthetically realised. Developed by Dibble *et al.*,[34] at the time of submission, polybenzoquinolines had not featured as precursors towards GNR, and whilst not realised in the submission, the authors expected to achieve the cyclodehydrogenation step on a reactive metal surface. The benzoquinoline precursor compounds are synthesised (and therefore polymerised) *via* an aza-Diels-Alder (Povarov-type) reaction between aromatic

imines and terminal acetylenes, using $BF_3.OEt_2$ as the Lewis acid catalyst, and chloranil as the sacrificial oxidant. The authors also varied the peripheral substituents, finding this had little impact on the polymerisation step. As these polymers were discovered to have good solubility in organic solvents, NMR and UV-visible studies were carried out, with the polybenzoquinolines demonstrating a broadening and red shifted absorption compared to their "monomer" model compounds. The use of the aza-Diels-Alder step is a novel concept in N-GNR synthesis, and holds much promise, as the authors note the ease of their generation, which is also low cost and follows assured synthetic steps. Whilst these examples are not exhaustive of the research in this area, they do illustrate the importance of developing interesting precursors, and establishing new selective synthetic routes towards their realisation as N-GNRs.

3.1.3.2 Nitrogen-substituted GNRs from 2,7-dibromophenanthrene

The most significant body of work in N-GNR generation has used extended platforms based on the 2,7-dibromophenanthrene repeating unit. Here, the use of the 2,7-dibromophenanthrene core forces the construction of "chevron-type" GNRs,[29] both for all-carbon systems and for those with a degree of nitrogen-substitution. Their synthesis requires the generation of the cyclopentadienone structure from 2,7-dibromophenanthrene-9,10-dione for the further use in a Diels-Alder reaction to form the desired precursor. This method has ignored substitution of the 2,7-dibromophenanthrene core, and of the resulting cyclopentadienone, with modification of the GNR being limited to the acetylene reagent used in the Diels-Alder step. For this reason, modification of literature-based GNRs have only occurred on the periphery of the GNR, on the reverse of the GNR "bay" region (of the 2,7-dibromophenanthrene core).

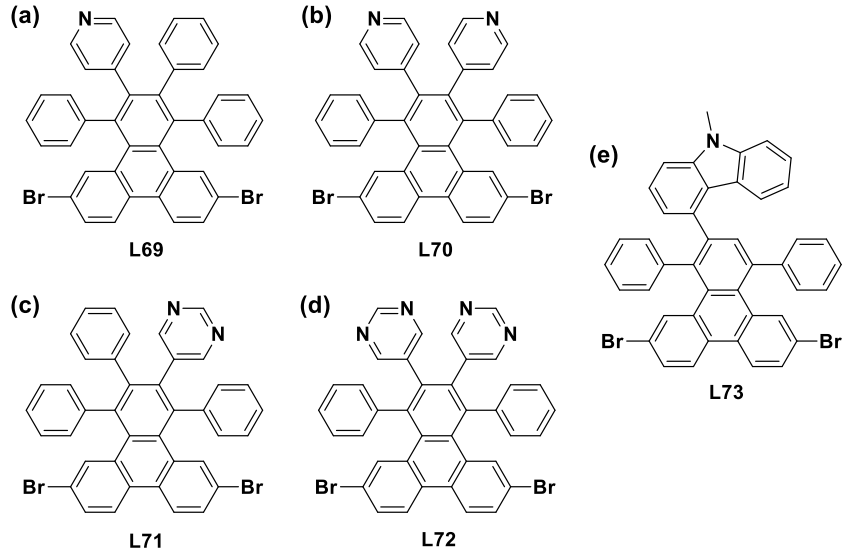

Figure 3. 4 (a)-(e) Literature examples of compounds with established use as nitrogen-substituted GNR molecular fragments derived from a 2,7-dibromophenanthrene core.

Figure 3.4 shows five recently published N-GNR precursors. Figure 3.4(a)-(b) (**L69** and **L70**) are created by placing the pyridine rings into the acetylene reagent used in the Diels-Alder step, whereas Figure 3.4(c)-(d) (**L71** and **L72**) are created using pyrimidine acetylenes. Figure 3.4(e) (**L72**) features an additional literature example, with the inclusion of the methyl-carbazole generating two GNR structures upon annealing.

Work by Cai *et al.*[1] initially produced the first chevron-type all-carbon GNR. Here, 6,11-dibromo-1,2,3,4-tetraphenyltriphenylene was used as the GNR precursor, and following sample deposition on Au(111), two annealing steps were undertaken (Figure 3.5). The first, at 250 °C generates polymer chains of the precursor, through halogen dissociation (in this bromine) at the phenanthrene core, with subsequent coupling of the biradical monomers. A second annealing step, at 440 °C provides sufficient activation energies to initiate cyclodehydrogenation, generating the GNR. As can be seen in Figure 3.5, STM is used to visualise the successful annealing steps of the chevron-type GNRs.

Following the successful synthesis of this chevron-type all-carbon GNR, it was only a matter of time before nitrogen doping was considered, with the first example seen through the work of Bronner *et al.*[35] As shown in Figure 3.4(a)-(b), Bronner and co-authors introduced single nitrogen atoms *via* the substitution of phenyl rings for pyridine rings. The stepwise study, from no nitrogen substitution, to a single pyridine ring, to a second pyridine ring, revealed some fascinating information about the inclusion of nitrogen atoms in chevron-type GNRs. Most significant, Bronner discovered that increasing the nitrogen dopant concentration resulted in little change to the GNR band gap, but the entire band structure was shifted

towards lower energies. This was determined by angle-resolved high-resolution electron energy loss spectroscopy (HREELS), coupled with photoelectron spectroscopy.[35]

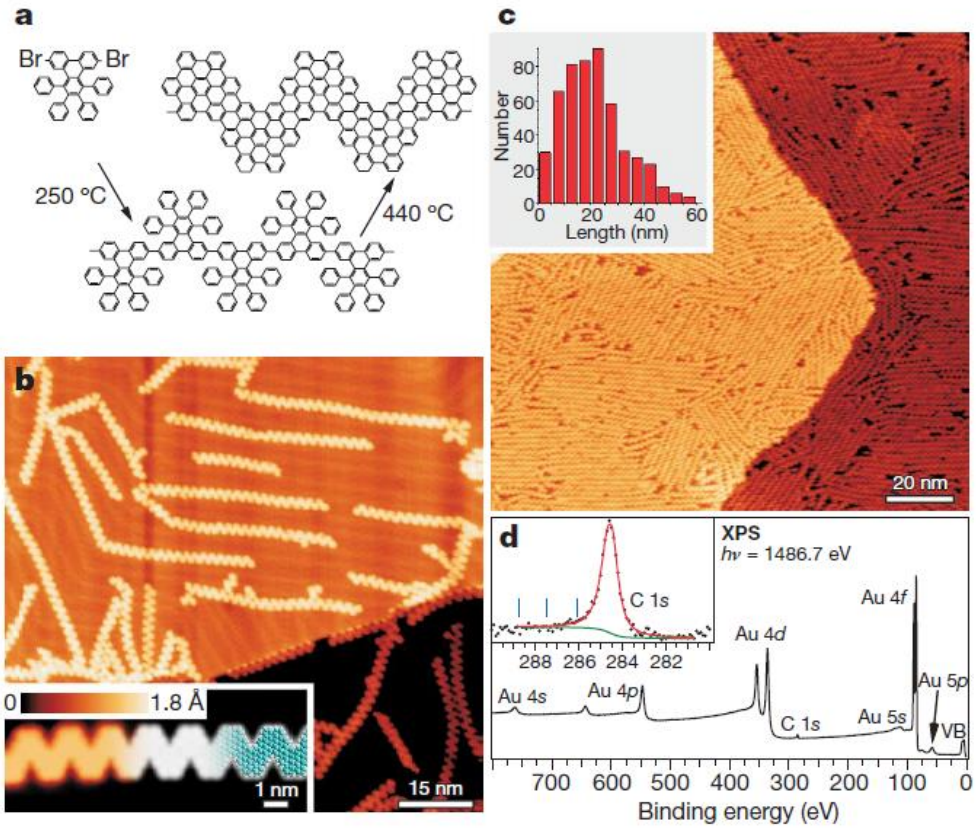

Figure 3. 5 Direct STM imaging, and XPS spectroscopy studies of 6,11-dibromo-1,2,3,4-tetraphenyltriphenylene.[1]

Zhang *et al.*[36] undertook a study of **L70** through STM, in a manner similar to that of Cai *et al.*[1] in Figure 3.5. These STM images demonstrated that nitrogen-substitution of GNRs displayed very different behaviour of the Au surface compared to their all-carbon variants, with the nitrogen doped GNRs no longer growing along the herringbone structure of the Au(111) surface. Instead, their N-GNRs grew in a side-by-side formation, with the vertices of the chevron shape (armchair edge) aligning against each other. Both **L69** and **L70** demonstrated that nitrogen-substitution allowed efficient tuning of the band gap of GNRs *via* dopant concentration and position.

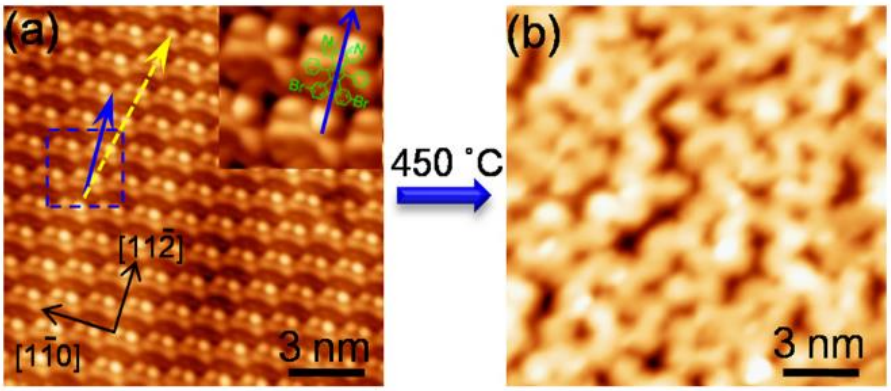

Figure 3. 6 Direct STM imaging of **L70** at high coverage levels, showing dimer/trimer/tetramer formation (b).[36]

Another intriguing conclusion from the work of Zhang *et al.*[36] was that consideration must be given to the level of coverage on the Au surface. Figure 3.6 demonstrates that at high coverage, GNR growth is no longer favoured, but rather dimerisation and trimerisation. Some tetramer growth is also seen. This observation led the authors to conclude that for high quality GNR growth, coverage must remain at the sub-monolayer level. The authors postulate that at high coverage levels, the monomers suffer from restricted diffusion and rotation.[36]

In Figure 3.4(c), **L71** now features a pyrimidyl ring instead of a pyridine ring. In a publication from Vo *et al.*[37] **L71** is used to generate nitrogen-substituted GNRs *via* solution-based synthesis. Uniquely this study uses Yamamoto cross coupling of the molecular precursors in solution rather than surface assisted polymerisation. Further to this, cyclodehydrogenation is achieved through the Scholl reaction. The Scholl reaction is an aromatic coupling reaction utilising a Lewis acid and a protic acid, and can be described between two free arene rings, or as the cyclodehydrogenation step within a larger PAH system. Two competing mechanisms exist; the arenium cation pathway, and the radical cation pathway. On deposition to mica or an Au(111) surface, the GNRs are characterised with STM and Atomic Force Microscopy (AFM), with Raman spectroscopy also used to confirm the chevron-like construction of the nitrogen-doped GNR. Unsurprisingly, this work has not been carried out with the pyridine systems **L69** or **L70**, as it is well-established that the cyclodehydrogenation step is far easier with pyrimidyl systems.[38]

Figure 3.4(d) shows the molecular precursor **L72**.[39] As the unit cell of a GNR is often considered as a two-monomer polymer within the GNR, **L72** is of interest as the nitrogen doping has now increased to eight atoms. This dramatic amount of nitrogen doping provides further insights into the effects of nitrogen-substitution in GNRs, both optoelectronically and

structurally. Further work by Vo *et al.*,[39] reveals that on the generation of 8N (eight nitrogens per unit cell) GNRs, the GNRs self-assemble into ordered metamaterials. Both solution-based synthesis and surface assisted synthetic methods are used, as the authors attempted to understand the driving force behind this self-assembly process. In a development to the work carried out by Zhang *et al.*[36] with **L70**, the 8N GNR **L72** now orders itself in three dimensions. These 3D stacks are generated by van der Waals and π stacking interactions when the GNRs are synthesised in solution.

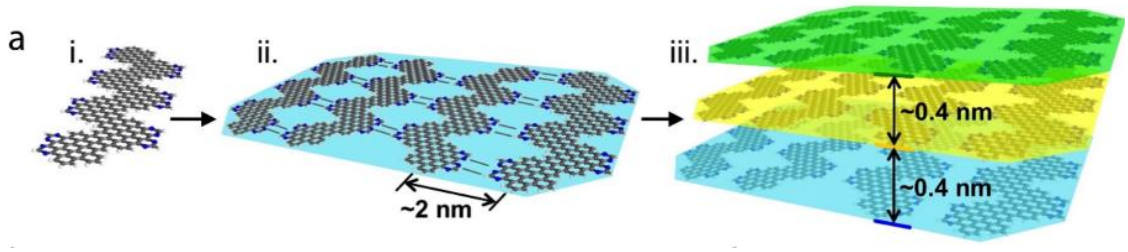

Figure 3. 7 Computational modelling of **L72** showing 2D and 3D distances of self-assembled structures.[39]

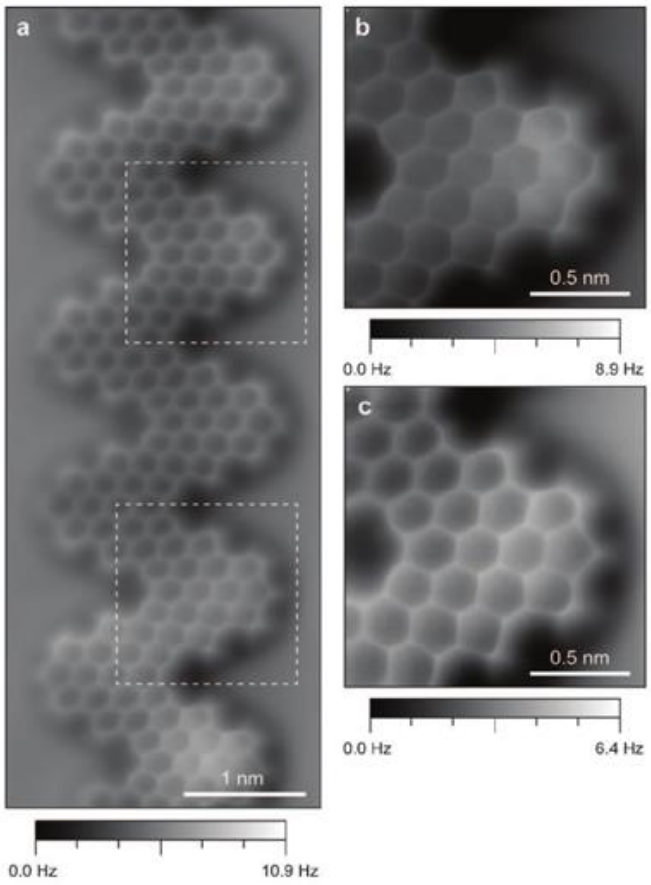

Figure 3. 8 Direct AFM imaging of **L73**, showing carbazole and rearranged phenanthridine ring systems. Reproduced from reference.[40]

Figure 3.7 shows this 3D stacking of the 8N GNRs, with their 3D form being that of a macroscopic crystalline structure. Fascinatingly, the properties of this macroscopic structure are governed by the nanoscale constituents (the GNRs), once again demonstrating the attractive nature of the bottom-up approach to GNR development.

The final monomer precursor in Figure 3.4(e) is **L73**. This work from Marangoni *et al.*,[40] demonstrates the phenomenon of GNR "edge reconstruction". Here, upon successful polymerisation and cyclodehydrogenation, two thermally induced reactions occur. Firstly, a thermally induced homolysis of the methyl-carbazole occurs, generating the unsubstituted carbazole ring system. Secondly, a thermally induced rearrangement occurs with some of the methyl-carbazole edges rearrange to form phenanthridine ring systems. This is of significant interest as the carbazole edges are electron rich, while the rearranged phenanthridine edges are electron deficient. This is the first example in the literature to utilise a single molecular precursor towards hetero-structured GNRs. The authors put forward a postulated reaction mechanism for this rearrangement, with AFM imaging used to distinguish between the two different ring systems (Figure 3.8).[40]

3.1.3.3 Pyridazine-substituted Graphene Nanoribbons

At the time of writing, there are no synthetically accessible pyridazine-substituted GNRs in the literature. However, in the last two years, two publications have undertaken Density Functional Theory (DFT) calculations on the inclusion of pyridazine rings into the GNR structure.[30,31]

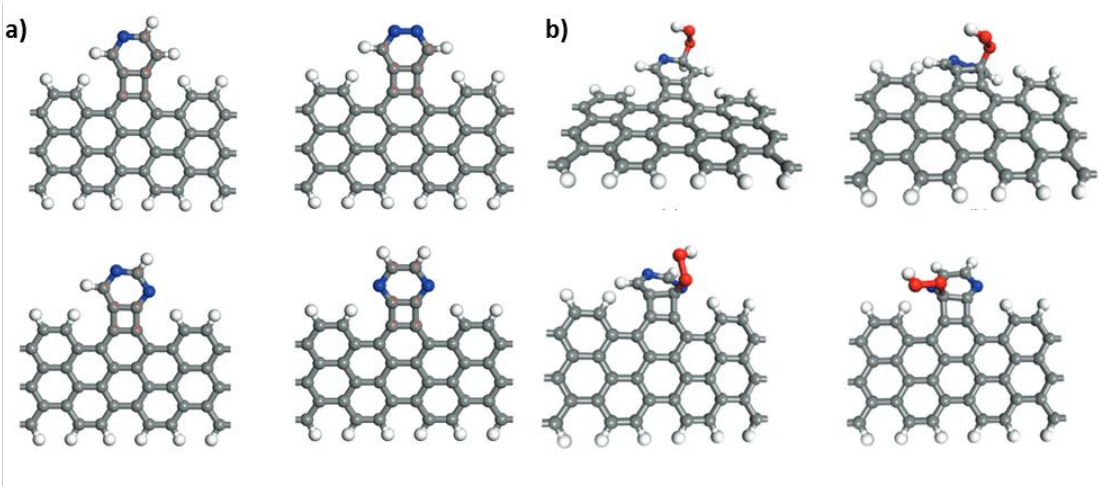

Figure 3. 9 (a) Optimised DFT structures of nitrogen-substituted GNRs. (b) Optimised DFT structures of nitrogen-substituted GNRs showing OOH absorption. Reproduced from reference.[31] N = blue. O = red.

The first of these publications from Zhang *et al.*,[31] utilised DFT calculations of nitrogen-doped GNRs towards the design of metal-free electrocatalysts for the oxygen reduction reaction (ORR). In this study, it was discovered that pyrimidine substitution was the most favourable substitution, offering ORR catalytic activity similar to that of the model Pt-based catalysts. Whilst this study only briefly studied the pyridazine ring substitution, it was the first study to it.

Figure 3.9(a) shows the optimised GNR structures, while Figure 3.9(b) demonstrates OOH absorption. The authors note that the pyridazine structure is unique among those calculated, as the C atom with the largest positive charge is considered to be the catalytic site. In all systems evaluated, this C atom was found to be adjacent to the N atom, with the exception of the pyridazine ring system. With the pyridazine ring, the C atom showing catalytic activity is β to one of the N atoms.

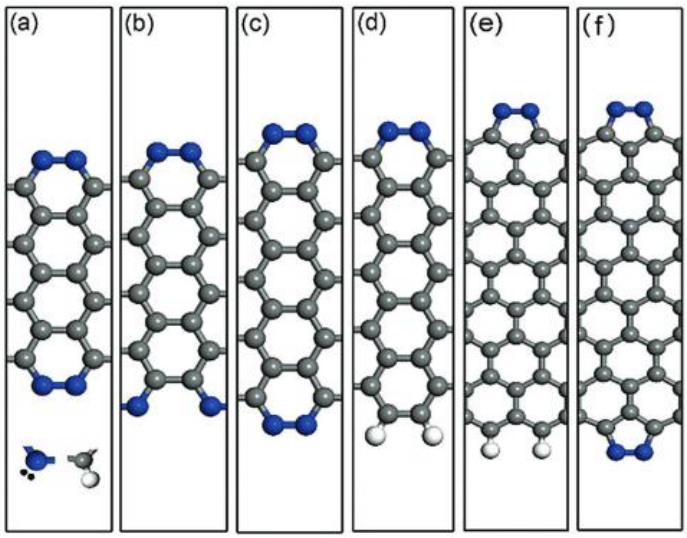

Figure 3. 10 (a) Optimised DFT structures of pyridazine- and pyrazole-substituted GNRs.[30]

Of great interest towards pyridazine-substituted GNRs is the work of Liu *et al*.[31] Here, DFT calculations are used to examine the nitrogen-substituted GNRs towards their candidacy for nanowires in molecular integrated circuits (MICs). Unlike the previous study of Zhang *et al.*,[31] the pyridazine ring structures here are of the greatest interest. Strikingly, inclusion of a pyrazine ring into the GNR structure dramatically changes the electronic properties of the GNR versus inclusion of a five membered pyrazole ring. With pyridazine-substitution, delocalised bands are introduced near the Fermi level, with a subsequent raising of the Fermi level introducing metallic electronic structure. For those pyridazine-substituted GNRs of a width of n=3p+2, perfectly linear I–V characteristics are observed. These characteristics hint

heavily that the pyridazine-substituted GNRs may be used as electrodes and nanowires in molectronics. The authors also note the benefit of the planar structure of these GNRs, making them an attractive alternative to the tubular nanotubes currently investigated towards MICs, as the tube-like structure of the nanotubes result in cross connections; a fate not suffered in planar materials. Figure 3.10 shows the pyridazine-substituted GNRs used in the authors' calculations.

As alluded to earlier, the bottleneck in the generation of these new systems are bench chemistry processes. A large number of research groups are active in the field of on-surface polymerisation chemistry. Draper *et al.* pioneered the inclusion of nitrogen atoms into large polyaromatic and PAH systems, and are one of the few research groups capable of overcoming this bottleneck towards greater diversification of nitrogen-substituted GNRs. This chapter is the first of many attempts at this diversification process with regard to pyridazine systems, with the Draper research group already making significant progress in this field with cyclotrimerised symmetric and asymmetric pyridine and pyrimidine polyphenylenes.[41] It is hoped this work will inform the future design of nitrogen- and pyrazine-substituted GNRs.

3.2 Results & Discussion

As already discussed, 2,7-dibromophenanthrene-9,10-dione, **81**, has become the formative unit from which to build increasingly elaborate all-carbon, and heteroatom graphene nanoribbons (GNRs). For this reason, **81** was chosen as an ideal candidate to begin a bottom-up approach to pyridazine-substituted GNRs. To achieve the desired narrow width of the postulated pyridazine-substituted GNR, the smallest pyridazine-containing PAH molecule must first be designed. A thorough literature review revealed only large polyaromatic and PAH-type molecules containing pyridazine rings. These are unsuitable due to their size, or an inability to incorporate the desired dibromophenanthrene "core" unit for on-surface polymer formation. A retrosynthetic analysis was carried out to determine if pyridazine could be incorporated into a hexaphenylbenzene-like fragment, with analysis showing the possible generation of the dibromophenanthrene core, combined with a diphenyl-substituted phthalazine system. The resulting target molecule, 6,11-dibromo-1,4-diphenyldibenzo[f,h]phthalazine, **78**, is shown in Scheme 3.1.

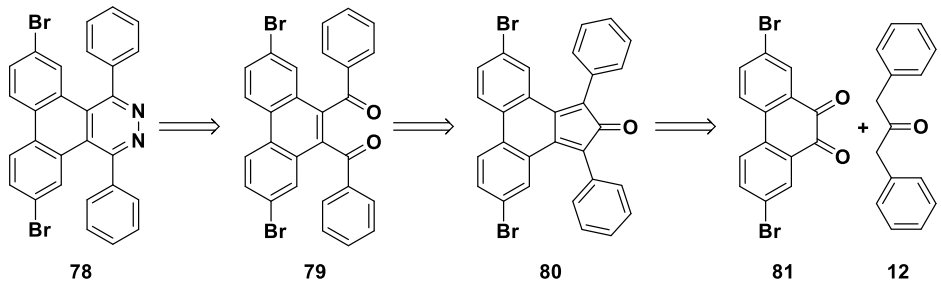

Scheme 3. 1 Retrosynthesis of 6,11-dibromo-1,4-diphenyldibenzo[f,h]phthalazine, **78**.

On further review of the literature, a synthetic preparation was available for the cyclopentadienone intermediate 5,10-dibromo-1,3-diphenyl-2H-cyclopenta[l]phenanthren-2-one, **80**,[42] but not for the diketone intermediate (2,7-dibromophenanthrene-9,10-diyl)bis(phenylmethanone), **79**. A similar reaction mechanism for this cyclopentadienone ring-opening is discussed in detail in Chapter 1. The Pauson-Khand reaction, utilising a [2+2+1] cycloaddition between an alkyne, an alkene, and CO was not undertaken due to the inability to control the stereochemistry of the resulting stereoisomers, and the necessary second oxidation of the α,β-cyclopentenone to the desired cyclopentadienone. The remaining step, a double Schiff-type base condensation with hydrazine monohydrate to generate **78** was also not found in the literature, but could be carried out in a similar procedure to those systems with the same di-carbonyl structure. Thus, **78** is found to be a novel molecule incorporating the desired features towards the first experimentally generated pyridazine-substituted GNR.

3.2.1 Synthesis & Structural Characterisation of 78

The synthesis of **81** was achieved through the bromination of commercially available phenanthrene-9,10-dione with N-Bromosuccinimide in concentrated H_2SO_4 without synthetic difficulty.[37] However, the next synthetic step, the generation of the cyclopentadienone intermediate **80** *via* reaction with 1,3-diphenylpropan-2-one, **12**, proved far more challenging. Several synthetic challenges were found. Initial methods included those of Alameddine *et al*.,[42] through the use of KOH in refluxing MeOH, which were found to generate the desired product **80** as a green solid, but in low yield and with significant side product formation. Purification attempts to obtain an analytically pure sample of **80** proved impossible across a significant range of solvents utilised as the mobile phase in silica-based column chromatography.

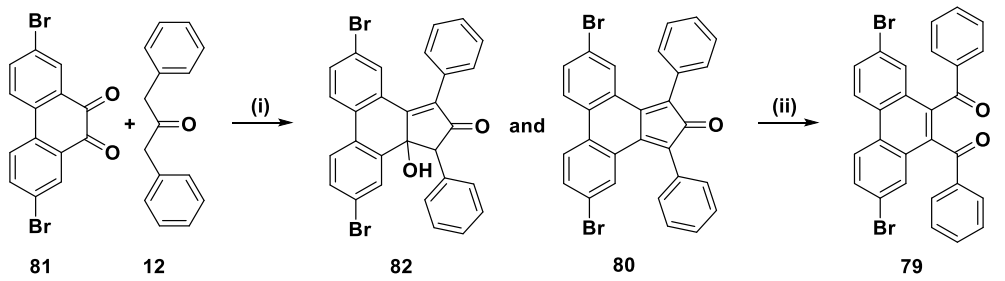

Scheme 3. 2 Synthesis of **79**. (i) piperidine, EtOH, rt, 16 h. (ii) xylenes, 140 °C, 16 h, 30 %.

To resolve this issue, attempts were made to isolate the single hydroxyl product, 5,10-dibromo-11b-hydroxy-1,3-diphenyl-1,11b-dihydro-2H-cyclopenta[l]phenanthren-2-one, **82**. This product was assumed to have decreased solubility in the MeOH or EtOH reaction solvent, and precipitation with hexanes would potentially allow its segregation from any side products. Review of the reaction conditions led to the substitution of KOH with the softer base piperidine, and the removal of a heat source, allowing the reaction to proceed at ambient temperature. This method successfully generated the single hydroxyl product **82**, according to analysis with high resolution mass spectrometry, but on attempts to isolate the product, the green colour of the cyclopentadienone intermediate **80** was also found. Due to the mixed nature of the products, both products were evident in the NMR spectra in similar ratios. However, the impurities and side products formed in the reaction were seemingly removed through precipitation of the **80**/**82** mixture from acetone with hexanes as hoped.

As the next reaction step would require the generation of the cyclopentadienone intermediate, it was decided to attempt the synthesis of the diketone intermediate **79** with the mixed product sample. The product mixture **80**/**82** was dissolved in pre-dried xylenes, with neutral Al_2O_3 as a dehydrating agent, and refluxed in air overnight. The use of this neutral Al_2O_3 as a dehydrating agent, and a suggested reaction mechanism for this cyclopentadienone ring-opening, are discussed in detail in Chapter 1. Following a standard aqueous work-up using CH_2Cl_2 as the organic layer, silica-based column chromatography proved successful in allowing the isolation of an analytically pure sample of the diketone intermediate **79** (Scheme 3.2). Using a 1:1 CH_2Cl_2:petroleum ether solvent system as the mobile phase, **79** was eluted as a pale yellow solid (30 %).

79 was structurally characterised by HRMS, multinuclear NMR studies, and through the study of the ATR-FTIR (See Chapter 5, Experimental). The electrospray ionisation mass spectrum shows a peak at *m/z* = 542.9585 corresponding to $[M+H]^+$. The calculated value is 542.9589 for $[C_{28}H_{17}Br_2O_2]^+$. Multinuclear NMR studies were carried out on **79**, with the ^1H NMR spectrum in $CDCl_3$ shown in Figure 3.11 (with $^{13}C\{^1H\}$ inset).

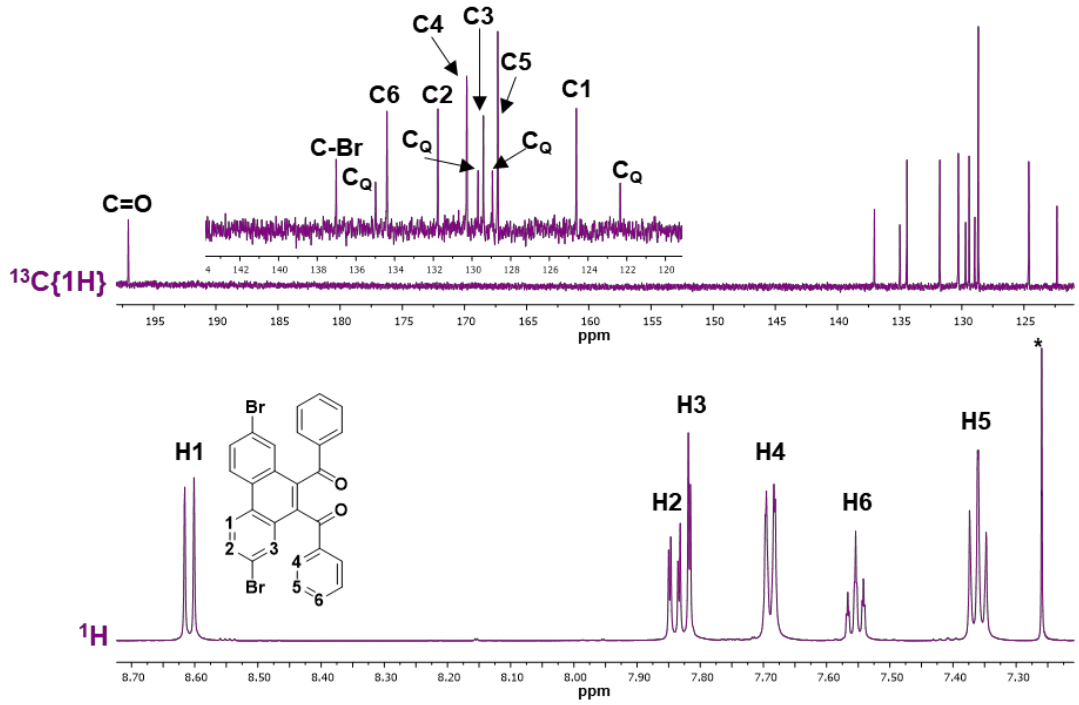

Figure 3. 11 $^{13}C\{^1H\}$ and ^1H NMR spectra of **79**. Zoomed region inset. ($CDCl_3$. 400 MHz for ^1H, 100 MHz for $^{13}C\{^1H\}$. RT). C_Q = quaternary carbons.

Analysis of the ^1H NMR of **79** reveals two patterns common in PAH molecules of this kind. The first of these patterns is in the dibromophenanthrene PAH-core. H1-H3 appear downfield in the spectrum, with H1 being most deshielded at *δ* 8.63 ppm. H2 appears as a dd at δ 7.86 ppm, with the final proton signal in the dibromophenanthrene PAH-core, H3, appearing as a pseudo-singlet at δ 7.86 ppm. The second pattern, that of the free phenyl proton signals follow a more distinct pattern. The three phenyl signals follow an *o*, *p*, *m* sequence found in similar PAH-type structures in the literature, and are characteristic of shifts for aromatic rings of this kind. The three phenyl signals, H4-H6 appear upfield with regards to those signals of the dibromophenanthrene PAH-core, at δ 7.72, 7.38, and 7.58 ppm respectively. Each signal in **79** is confirmed with comparison to similar systems in the literature, and with the use of HSQC and HMBC spectra collected as part of the NMR analysis. The distinctive carbonyl signal expected at a highly downfield value is confirmed at δ 197 ppm, in the $^{13}C\{^1H\}$ spectrum.

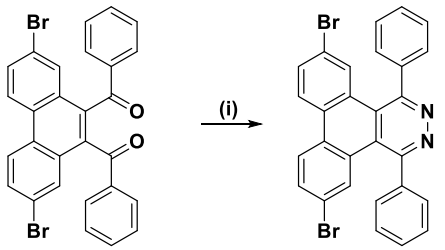

79 78

Scheme 3. 3 Synthesis of **78**. KOH, EtOH, $N_2H_4.H_2O$, 80 °C, 4 h, 85 %.

On the successful generation of the diketone intermediate **79**, attention turned to the synthesis of the novel pyridazine-containing molecule, **78**. Commonly, Schiff base condensation reactions typically use a strong base to initiate the reaction process through deprotonation of one of the hydrazine nitrogen's. Thus, **79** was added to a mixture of hydrazine monohydrate in refluxing EtOH, followed by the careful and dropwise addition of an ethanolic solution of KOH. The reaction mixture was then left at reflux overnight, followed upon cooling by an aqueous work-up. In order to obtain an analytically pure sample of **78** (Scheme 3.3), column chromatography was carried out using a mobile phase of 95:5 CH_2Cl_2:MeOH, eluting the product as a pale yellow solid (85 %).

78 was structurally characterised by HRMS, multinuclear NMR studies, and the ATR-FTIR (See Chapter 5, Experimental). The electrospray ionisation mass spectrum shows a peak at *m/z* = 538.9767 corresponding to $[M+H]^+$. The calculated value is 538.9753 for $[C_{28}H_{17}Br_2N_2]^+$. Multinuclear NMR studies were carried out on **78**, with the ^1H NMR spectrum in $CDCl_3$ shown in Figure 3.12.

Analysis of the ^1H NMR of **78** reveals the same two patterns common in PAH molecules found in **79**. However, in the first pattern, there has been an exchange between H2 and H3 when compared to that of **79**. Now, H3 appears significantly downfield in comparison to H2, appearing at δ 7.72 ppm, again as a pseudo-singlet. H1 is shifted upfield with respect to its corresponding signal in **79**, at δ 8.41 ppm. H2 remains essentially unchanged between the two molecules at δ 7.78 ppm. Due to the overlapping signals of H5 and H6, the use of the HSQC is required to determine the second pattern, that of the *o*, *p*, *m* sequence, with the spectrum proving **78** maintains this sequence, with H4-H6 appearing at δ 7.71, 7.56, and 7.60 ppm respectively. Similarly to **79**, each signal is confirmed *via* comparison to similar systems, and with the use of HSQC and HMBC spectra collected as part of the NMR analysis. The definitive absence of the carbonyl peak of **79** is shown in the inset of Figure 3.12, showing values up to δ 200 ppm in the $^{13}C\{^1H\}$ spectrum.

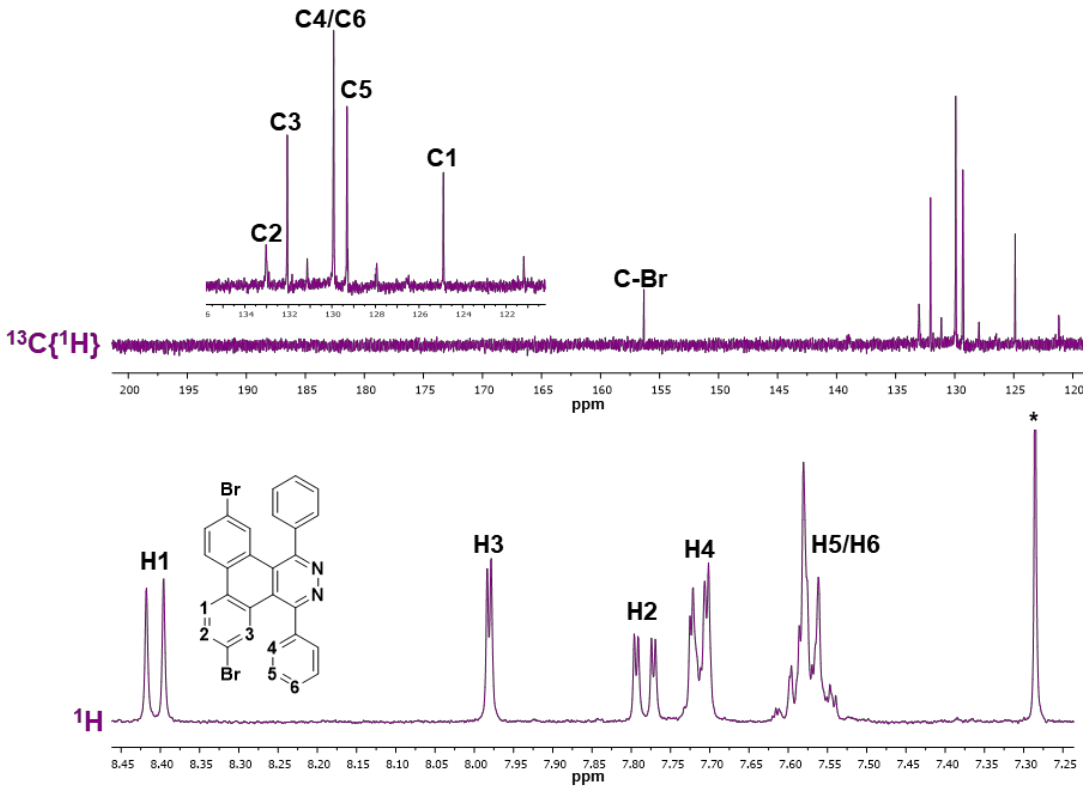

Figure 3. 12 $^{13}C\{^{1}H\}$ and ^{1}H NMR spectra of **78**. Zoomed region inset. ($CDCl_3$. 400 MHz for ^{1}H, 100 MHz for $^{13}C\{^{1}H\}$. RT). Unlabelled peaks in the $^{13}C\{^{1}H\}$ spectra are quaternary carbons.

3.2.2 Thermal Analysis of 1

To estimate the thermal stability of **78** as a molecular fragment towards on-surface reactions and analysis, a thermogravimetric analysis (TGA) plot was recorded. The compound **78** was added to a pre-weighed ceramic crucible, and its mass was recorded. Both mass measurements were undertaken in the furnace. The crucible was heated to 30 °C and held for one minute. Following this stage, the crucible was heated to 120 °C at a rate of 10 °C per minute, and was held at this temperature for 30 minutes to allow for the evaporation of any remaining high boiling-point solvents. On completion of this isothermal step, the crucible was heated to 700 °C at a rate of 10 °C per minute, before cooling to ambient temperature. The cooling rate was not controlled. All heating was carried out under a constant stream of N_2 gas.

Analysis of the TGA plot reveals **78** undergoes thermal decomposition at 380 °C (Figure 3.13), with the thermal stability of the bulk powder showing resistance until 400 °C. This dramatic mass loss is likely to be from product evaporation. As the system is not under vacuum, and similar PAH-type compounds demonstrate melting points at these temperatures

at ambient pressure, the probable collapse of the pyridazine ring structure is likely for this step. As most on-surface cyclodehydrogenation steps occur between temperatures of 350-400 °C, this gave cause for concern. However, as the reactivity of the surface may assist in the cyclodehydrogenation step, through lowering of the activation energy of this process, it was determined that on-surface work should be carried out to investigate.

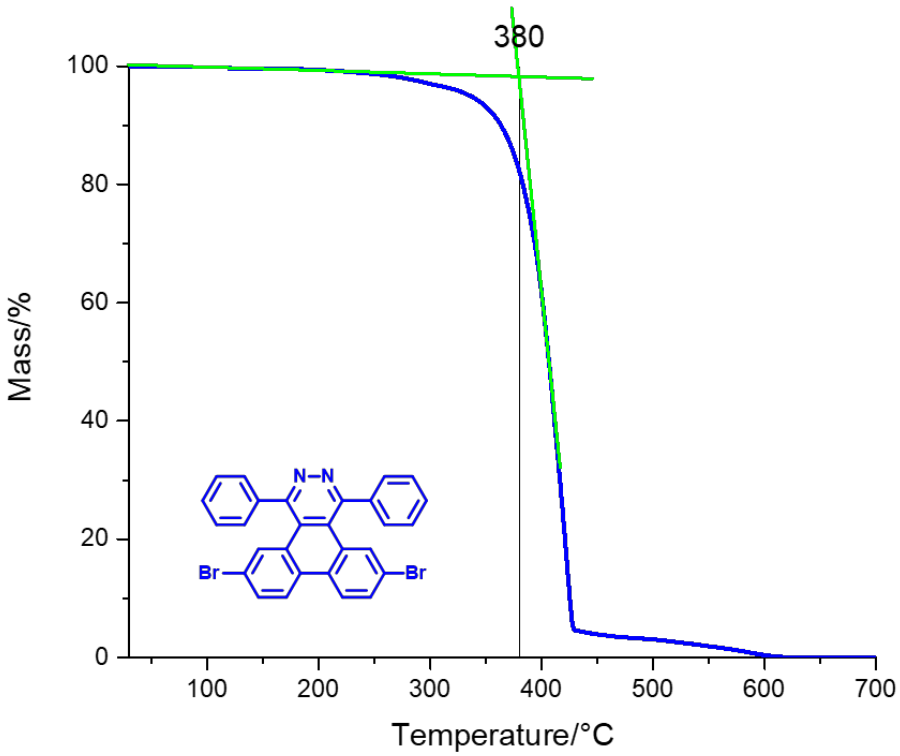

Figure 3. 13 Thermogravimetric analysis of **78**, showing mass change (y-axis) against temperature (x-axis).

3.2.3 On-surface Behaviour of 78

PAH-type fragments behave with some regularity when deposited on reactive (111) surfaces. As **78** is the first pyridazine-substituted system, a change in this regular behaviour was not unexpected. Analysis of the observed behaviour was to be carried out *via* a Scanning Tunnelling Microscope (STM) technique, on an Au(111) surface. The expected behaviour of **78** on an Au(111) surface is visually summarised in Figure 3.14.

Upon deposition to the Au surface at room temperature, two scenarios are likely. At ambient temperature, some random disorder is expected in the monolayer of **78** formed on the Au(111) surface. It is expected that there may exist a thermal barrier to the formation of ordered self-assembled structures such as chains or islands of **78**. However, as seen in other work with

other dibromophenanthrene PAH-core fragments, some self-assembly may occur at high coverage levels.[36] As pyridazine-substituted GNR fragments have to-date remained a purely computational research endeavour, the nature of these self-assembled structures can only be postulated here. In Figure 3.14, the possible self-assembly of **78** at ambient temperature is visually demonstrated. Due to repulsive effects from the lone pairs of the iminic nitrogens of the pyridazine ring, it is assumed that the self-assembly structure will result in an AAA-type pattern chain, with the pyridazine ring pointing "into" the dibromophenanthrene PAH-core. A further hypothesis is that due to the steric demands of the free phenyls, an inversion of this AAA pattern to BBB will result in parallel chains.

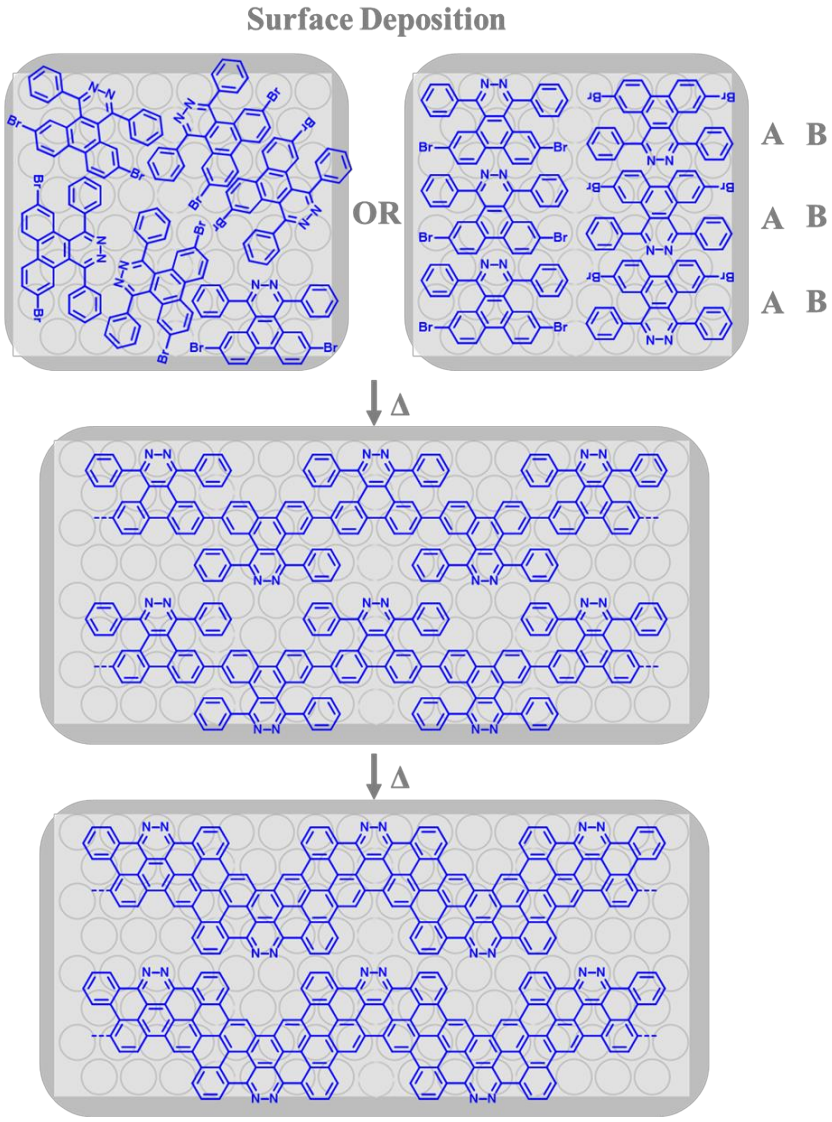

Figure 3. 14 Visual representation of surface deposition of **78**, and subsequent polymerisation and cyclodehydrogenation steps on Au(111) surface.

Upon the successful deposition of **78** to the Au(111) surface, the surface is heated (hereafter referred to as annealed) to approximately 150-200 °C to generate the reactive radical species through halogen-bond cleavage necessary for polymerisation to occur. In the self-assembled pattern version of the monolayer, the reactive positions are already in close contact, aiding the polymerisation step.

Following the successful polymerisation step, further annealing to increased temperatures of > 300 °C would allow the desired cyclodehydrogenation step to occur. This is assumed to be a facile step, albeit at elevated temperatures, due to the reactive nature of the surface, and the polymer's forced ABAB alignment of the necessary bond positions. Should each of these steps occur in succession as expected, the first pyridazine-substituted GNR will have been successfully generated. However, as thermal analysis of **78** reveals the pyridazine ring to be unstable at these high temperatures, careful examination of the generated structures at each annealing step will be carried out *via* STM.

The on-surface work was carried through collaboration with Dr. Shi-Xia Liu of the University of Bern in Switzerland. Sample preparation and STM imaging was carried out by Dr. Shiyong Wang, supervised by Dr. Pascal Ruffieux, and Prof. Roman Fasel. A commercial low-temperature STM (Scienta Omicron) was used for sample preparation and characterisation *in situ* under ultra-high vacuum conditions with a base pressure below 1×10^{-10} mbar. The Au(111) single crystal was cleaned by standard argon sputtering and annealing cycles. The molecules were thermally evaporated from quartz crucibles to Au(111) held at room temperature. The sample was annealed to 200 °C and 350 °C to activate dehalogenation and cyclodehydrogenation reactions. All the STM images were taken at constant current mode.

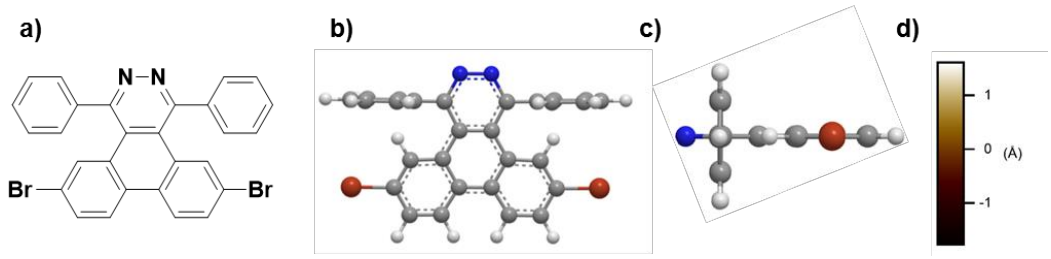

Figure 3. 15 (a)-(c) Molecular representations of **78**. (a) ChemDraw, and (b)-(c) Chem3D. (d) Representative example of STM tip distance to the surface in Ångström (Å).

Figure 3.15 shows molecular representations of **78**, demonstrating the 90° angle from planarity of the free phenyl rings in Figure 3.15(c). Figure 3.15(d) shows the STM tip distance

from the surface, and is shown here in Ångström (Å). The observed behaviour of **78** is now discussed in detail through a selection of STM images, along with visual aids.

Figure 3.16(a-c) demonstrates the initial STM scans taken at ambient temperature, further to sample deposition. In the increasing resolution, it is immediately apparent that a single pattern type dominates the surface monolayer. Figure 3.16(c) reveals that this pattern is of the AAA/BBB pattern postulated earlier, with the free phenyl rings of **78** pointing perpendicular to the surface. This is revealed by the repeating bright spots of the free phenyl rings of **78** visible in STM images of greater resolution. On careful inspection of Figure 3.16(c), the pattern AAA/BBB does not hold true for the entire self-assembled structure. Some patterns run AAA/AAA, or *vice versa* in patterns of BBB. For the purpose of this discussion, this self-assembled structure will be referred hereafter as the "packed structure".

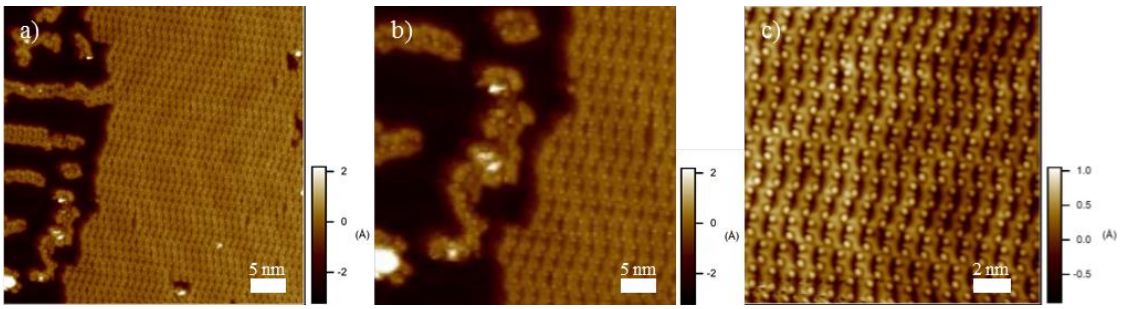

Figure 3. 16 (a)-(c) STM images of the monolayer of **78** on an Au(111) surface.

Visualisation of these patterns is further shown in Figure 3.17. Here, further investigation of Figure 3.17(a) reveals a random orientation of **78** at the edge of the packed structure. The dominance of the packed structure suggests that the assumed thermal barrier to the formation of this structure is of little consequence. This orientation is favoured as molecular units of **78** are now "lined-up" for the next polymerisation step.

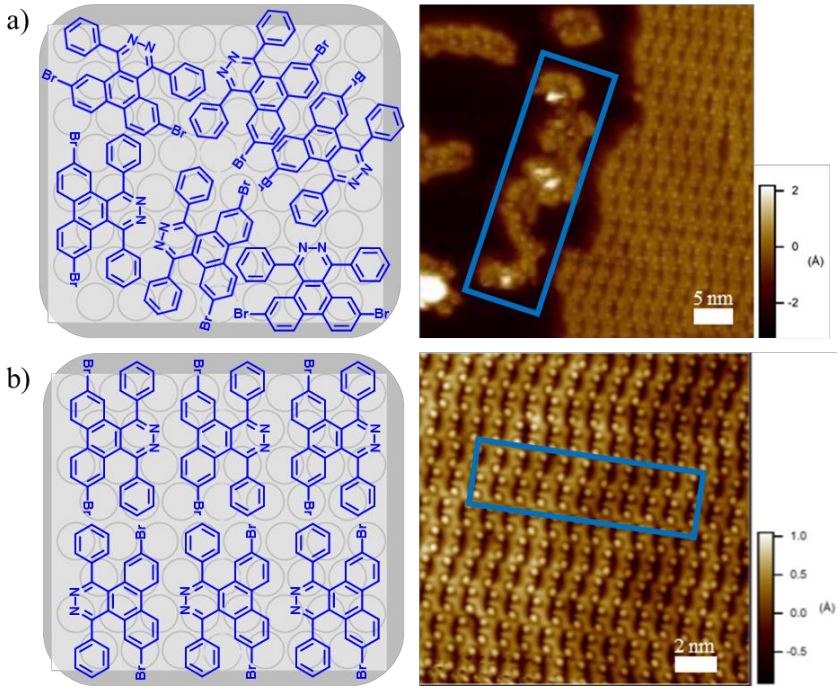

Figure 3. 17 (a)-(b) Visual representations of the proposed structures of **78** on Au(111), and their corresponding STM images.

On annealing the surface to 200 °C for twenty minutes, further STM scans reveal a much-changed surface pattern. As shown in Figure 3.18, the self-assembled packed structure is now completely replaced by a chain-like pattern. Increased resolution in Figure 3.18(c) demonstrates that the annealing process has indeed initiated a successful polymerisation of the molecular units of **78** on the surface.

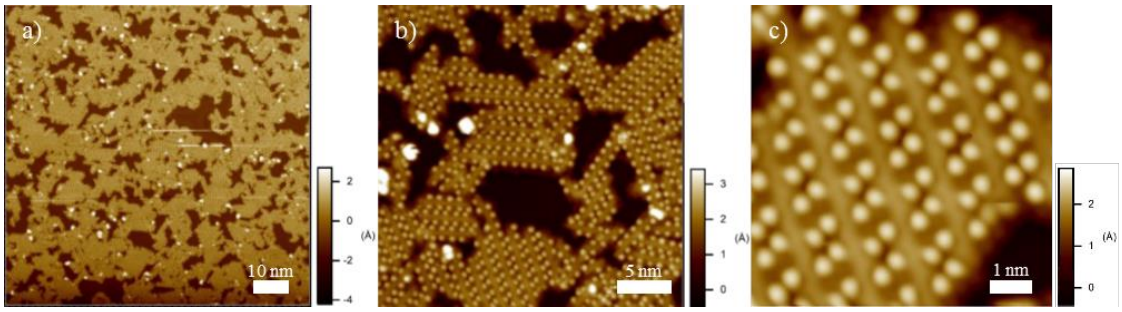

Figure 3. 18 (a)-(c) STM images of the self-assembled polymers of **78** on an Au(111) surface.

For the purpose of this discussion, this polymerisation structure will be referred hereafter as the "chain structure". As expected, the annealing temperature of 200 °C, coupled with the short annealing time, has not provided sufficient energy to initiate the cyclodehydrogenation

step. This is evidenced by the retention of the bright spots in the STM image of the free phenyl rings of **78**, pointing perpendicular from the Au surface. This brightness is demonstrated in Figure 3.15(d), where the orientation of the free phenyl rings results in an increased STM tip distance to the surface. In Figure 3.18(c), careful inspection also reveals the "void" between the individual chains of **78**. In Figure 3.18(a)-(b), it can be seen that the individual chains still attempt to generate a self-assembled structure, with Figure 3.18(b) most clearly revealing "pockets" or "islands" of these self-assembled chains. Visualisation of these patterns is further shown in Figure 3.19. On the successful generation of the polymer chains of **78**, further annealing was undertaken to investigate if the successful surface-assisted cyclodehydrogenation could reveal the first pyridazine-substituted GNR. On annealing to 350 °C for twenty minutes, further STM scans reveal once again a much-changed surface pattern.

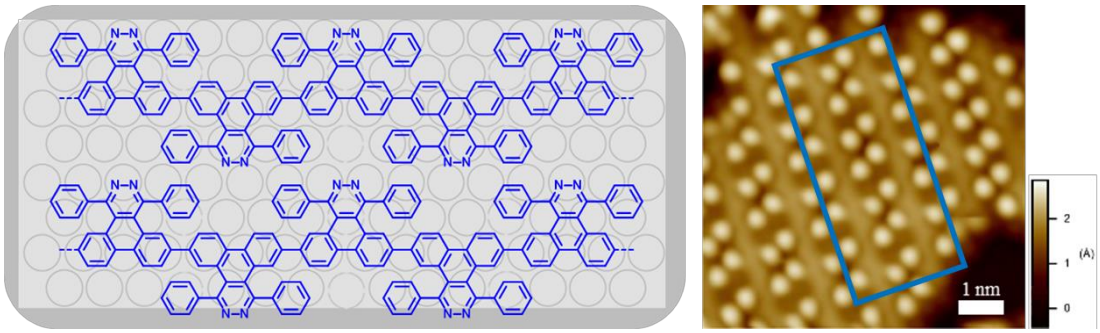

Figure 3. 19 Visual representations of polymer chains of **78** on an Au(111) surface, and a corresponding STM image.

In Figure 3.20(a), it is apparent that the cyclodehydrogenation step has either (a) partially worked, or (b) has not worked, and a further reaction step has taken place. Visualisation is expected to be somewhat hindered here, due to the loss of the regular bright spots of the free phenyl rings of **78**, which are now part of the planar and fully hybridised GNR. Increased resolution in Figure 3.20(b) reveals these spots once again, heralding that if the cyclodehydrogenation step has worked, it has only worked in a partial manner. If option (a) is considered, that only partial cyclodehydrogenation has occurred, further annealing may be possible to "force" the process to occur across the polymer chains. To investigate this, further annealing to 400 °C for twenty minutes was undertaken, with subsequent STM images collected. These images are shown in Figure 3.20(c) and (d). On inspection of these images, it is clear that the effort to force the cyclodehydrogenation step has not been successful. Bright spots of the free phenyl rings are still visible, but appear now with an increased irregularity indicating that other reaction processes may have occurred at this elevated temperature. This

is confirmed through analysis of Figure 3.20(d), which provides the resolution required to determine that the free phenyls are now pointing at odd angles to the phenanthrene-core.

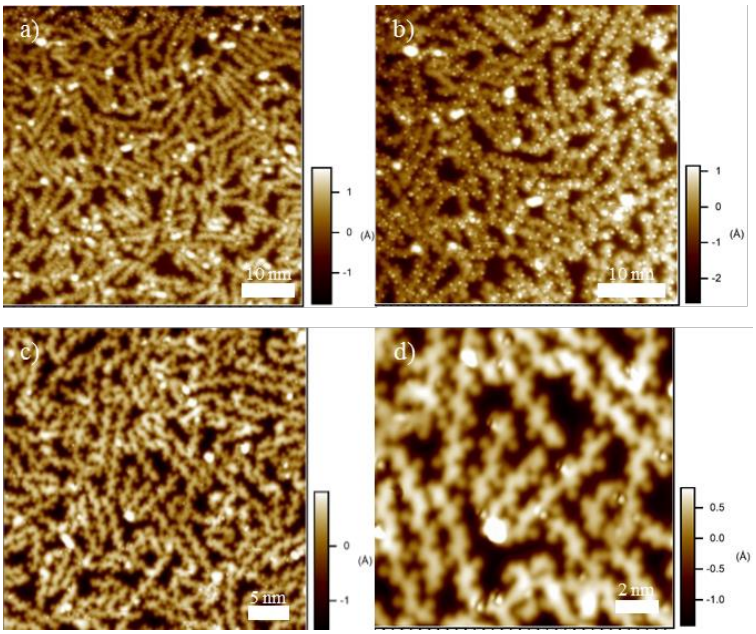

Figure 3. 20 (a)-(b) STM images of **78** on an Au(111) surface further to annealing at 350 °C. (c)-(d) STM images of **78** on an Au(111) surface further to annealing at 400 °C.

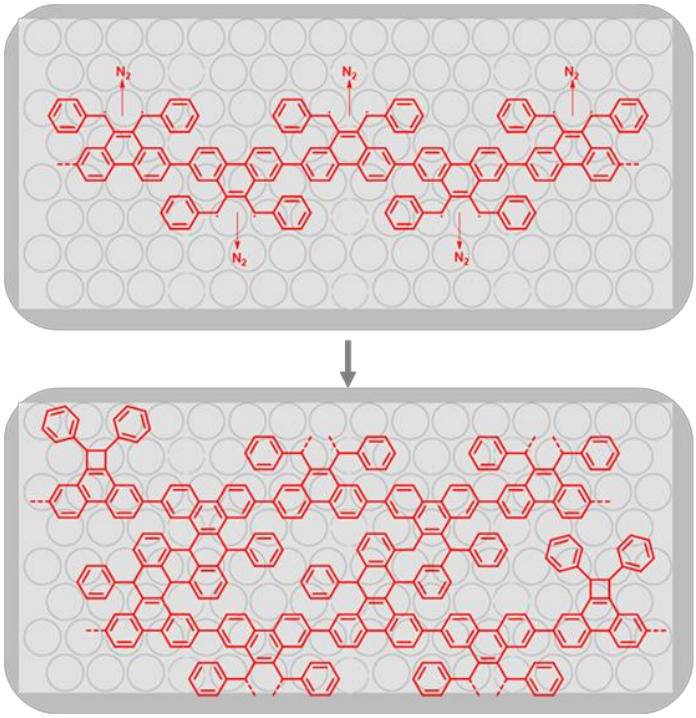

Figure 3. 21 Visual representation of on-surface loss of N_2, and hypothesised subsequent bond formation and ring fusions of **78** on an Au(111) surface.

The most logical explanation to this observation is through the collapse of the pyridazine ring, predicted by the TGA results, allowing the phenyls to now point out of the expected axis. This almost certainly indicates the generation of free N_2 from the collapse of the pyridazine ring; a process which would generate two radicals in the remaining surface-bound structure. Due to the reactive nature of the radical atoms, the reactive (111) surface, and the elevated temperature, rapid fusion of the edges of the polymer chains most likely occurs in a random fashion. Some hypothesised structures from this process are illustrated in Figure 3.21.

Whilst the ultimate goal of this work was not realised, the results of this work is very exciting. For the first time, the successful polymerisation of a pyridazine-containing N-GNR has been realised on a reactive surface, with data obtained suggesting the potential differences in reactivity between that of pyridazine *versus* other N-containing aromatics. The difference in reactivity may present an opportunity towards the ORR discussed earlier by Zhang *et al*.[31] Further work will need to be carried out to confirm if this risk is related to the annealing temperature, or the surface reactivity. These preliminary studies indicate that the pyridazine ring is stable in the polymerisation step, despite the abundance of radicals generated in this process. There is therefore an opportunity to repeat this work with **78** with a surface of greater reactivity, but a significantly lower annealing temperature.[43] A second option may be through the Yamamoto-type coupling and Scholl reaction used by Vo *et al.*,[37] generating the pyridazine GNRs in solution. Yamamoto coupling is a cross coupling reaction between two halogenated arene systems, utilising a $Ni(cod)_2$ catalyst. These GNRs may then be deposited to mica or the Au(111) surface for visualisation studies. This work is ongoing, may then lead to the successful realisation of pyridazine-substituted GNRs.

It is evident that N-GNRs still have a significant role to play in the device-based application of graphene-like systems. However, to realise their large-scale use, the "bottom-up" synthetic strategies must be strictly controlled to allow the substantial production of identical GNR frameworks, through control of ribbon length, control of potential side reactions, and their subsequent removal from the reaction surface. Methods envisaged to resolve these requirements include that of Chen *et al*.,[44] which uses chemical vapour deposition (CVD) to generate large-area GNR films which can be transferred onto a variety of substrates towards device fabrication.

3.3 Conclusions & Future Work

In addition to the above work, proposed modification of alternative metal surfaces, needing lower annealing temperatures, opportunities also remain to rapidly increase the number of nitrogen-substituted PAH-type compounds for on-surface studies. As summarised earlier,

pyrimidine- and pyridine-substituted systems currently exist in the literature. However, the design of these systems currently only allows for nitrogen-substitution at only one edge of the chevron-type GNR framework. Through the use of systems based on the dibromophenanthrene-core system, one edge is immediately precluded from nitrogen-substitution.

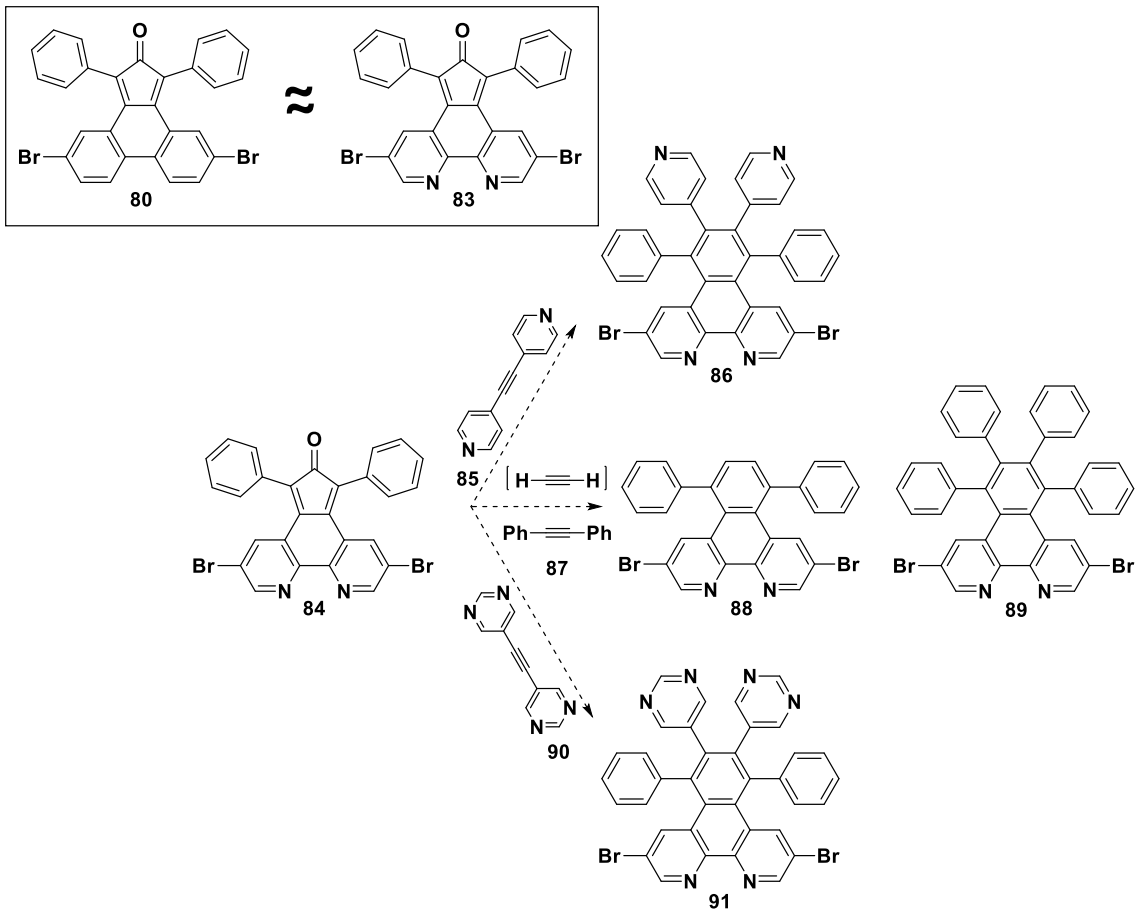

Scheme 3. 4 Future work utilising the dibromophenanthroline-core system **83**, modelled on **80**. Reactions shown indicate routes to products with a range of N-substitution.

Scheme 3.4 demonstrates that an exchange for this dibromophenanthrene-core system to that of a 1,10-phenanthroline-core system would facilitate nitrogen-substitution on the two edges of the GNR, including into the "bay" edge of the chevron-type GNR. As all of the acetylene-derived reagents found in Scheme 3.4 are known, the generation of the dibromo 1,10-phenanthroline cyclopentadienone product **84**, is the one significant synthetic challenge. By comparison with **78**, the pre-fused phenanthroline three-ring system would not be expected to affect the self-assembly of a similar packed structured monolayer. Therefore, only the wet

chemistry approach to the synthesis of **84** remains to be tackled. This initial work is not discussed in this thesis, but attempts to overcome this solubility issue are ongoing.

The demonstrated successful polymerisation step of the pyridazine-substituted PAH may be considered the most challenging of the required steps in the formation of GNRs, as it requires a large-scale on-surface movement and reorganisation of the monomers into the polymer chains. The cyclodehydrogenation step, in comparison, simply requires the correct surface reactivity and annealing temperature.

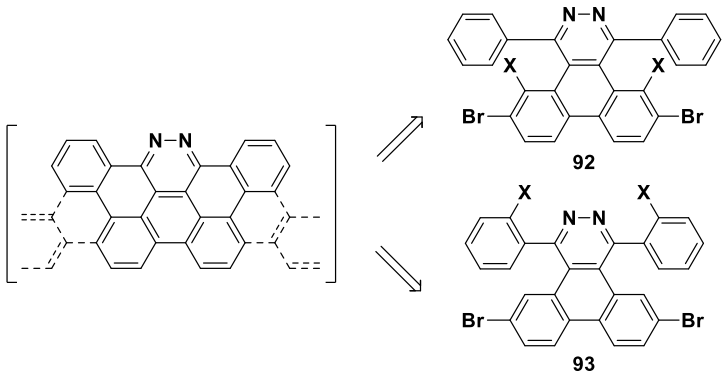

Scheme 3. 5 Retrosynthesis of the postulated GNR of **78** showing two low temperature halogen-assisted cyclodehydrogenation routes.

Scheme 3.5 shows a retrosynthetic analysis of the on-surface pyridazine nanoribbon, demonstrating two novel compounds that may allow the realisation of the cyclodehydrogenation step without collapse of the pyridazine ring. Halogen substitution is used in a number of solution-based cyclodehydrogenation processes. In these examples, the loss of the halogen through chemical means or through photoactivation, generates a radical capable of assisting in the cyclodehydrogenation step. Often, these halogen atoms are Cl or F, as Br or I substitution may exist elsewhere in the compound for further reactive use. **92** serves as an example of halogen-substitution at the 1- and 8-positions of the phenanthrene core. In reality, the synthesis of **92** represents considerable challenges, as the necessary bromination of the 2- and 7-positions is also required for nanoribbon growth. **93** may prove to be a synthetically more accessible variant of this retrosynthetic analysis, with the halo-functionality on the free phenyls. This is likely achieved *via* the monoketone precursor, before the generation of the necessary cyclopentadienone intermediate. Substitution of these positions with bromine may allow the cyclodehydrogenation step to occur simultaneously with the polymerisation step. However, a simple thought experiment immediately indicates that a competing polymerisation step between these positions is now viable, thus interfering

with the generation of the expected GNRs. Another strategy may be through surface deposition, polymerisation, and then a photoactivated cyclodehydrogenation step. This work remains unrealised, but may offer new routes to pyridazine-substituted GNRs in the future.

In conclusion, the solution-based synthesis of the first dibromophenanthrene-pyridazine PAH-type compound was successfully completed. The target molecule, **78**, was deposited on pre-cleaned Au(111), where it self-assembled into a desirable packed structure, with low temperature annealing generating a successful polymerisation of **78** into self-assembled chains. This appears to be the first successful on-surface polymerisation of pyridazine-substituted PAH molecules. However, on further annealing at high temperatures, the pyridazine ring appears to degrade *via* liberation of N_2, with the resulting radical species resulting in rapid, and random, bond formation and ring fusion. This ring fusion results in randomised nanoribbons unsuitable for further study. This work will inform the design of future pyridazine-substituted PAH molecules, and the design of on-surface cyclodehydrogenation steps for these systems in the future.

3.4 References

1 J. Cai, P. Ruffieux, R. Jaafar, M. Bieri, T. Braun, S. Blankenburg, M. Muoth, A. P. Seitsonen, M. Saleh, X. Feng, K. Müllen and R. Fasel, *Nature*, 2010, **466**, 470.

2 V. Barone, O. Hod and G. E. Scuseria, *Nano Lett.*, 2006, **6**, 2748–2754.

3 Y.-W. Son, M. L. Cohen and S. G. Louie, *Nature*, 2006, **444**, 347.

4 K. Wakabayashi, *Phys. Rev. B*, 2001, **64**, 125428.

5 M. A. Rafiee, W. Lu, A. V Thomas, A. Zandiatashbar, J. Rafiee, J. M. Tour and N. A. Koratkar, *ACS Nano*, 2010, **4**, 7415–7420.

6 M. Pumera, *Energy Environ. Sci.*, 2011, **4**, 668–674.

7 C. Xu, B. Xu, Y. Gu, Z. Xiong, J. Sun and X. S. Zhao, *Energy Environ. Sci.*, 2013, **6**, 1388–1414.

8 M. C. Paiva, W. Xu, M. Fernanda Proença, R. M. Novais, E. Lægsgaard and F. Besenbacher, *Nano Lett.*, 2010, **10**, 1764–1768.

9 M. Terrones, *ACS Nano*, 2010, **4**, 1775–1781.

10 J. Wang, L. Ma, Q. Yuan, L. Zhu and F. Ding, *Angew. Chemie Int. Ed.*, 2011, **50**, 8041–8045.

11 A. V Talyzin, S. Luzan, I. V Anoshkin, A. G. Nasibulin, H. Jiang, E. I. Kauppinen, V. M. Mikoushkin, V. V Shnitov, D. E. Marchenko and D. Noréus, *ACS Nano*, 2011, **5**, 5132–5140.

12 J. L. Hutchison, N. A. Kiselev, E. P. Krinichnaya, A. V Krestinin, R. O. Loutfy, A. P. Morawsky, V. E. Muradyan, E. D. Obraztsova, J. Sloan, S. V Terekhov and D. N. Zakharov, *Carbon.*, 2001, **39**, 761–770.

13 C. Journet, W. K. Maser, P. Bernier, A. Loiseau, M. L. de la Chapelle, S. Lefrant, P. Deniard, R. Lee and J. E. Fischer, *Nature*, 1997, **388**, 756.

14 D. S. Bethune, C. H. Kiang, M. S. de Vries, G. Gorman, R. Savoy, J. Vazquez and R. Beyers, *Nature*, 1993, **363**, 605.

15 M. Yudasaka, T. Komatsu, T. Ichihashi and S. Iijima, *Chem. Phys. Lett.*, 1997, **278**, 102–106.

16 M. Yudasaka, R. Yamada, N. Sensui, T. Wilkins, T. Ichihashi and S. Iijima, *J. Phys. Chem. B*, 1999, **103**, 6224–6229.

17 A. M. Morales and C. M. Lieber, *Science*, 1998, **279**, 208–211.

18 M. Chhowalla, K. B. K. Teo, C. Ducati, N. L. Rupesinghe, G. A. J. Amaratunga, A. C. Ferrari, D. Roy, J. Robertson and W. I. Milne, *J. Appl. Phys.*, 2001, **90**, 5308–5317.

19 M. Cantoro, S. Hofmann, S. Pisana, V. Scardaci, A. Parvez, C. Ducati, A. C. Ferrari, A. M. Blackburn, K.-Y. Wang and J. Robertson, *Nano Lett.*, 2006, **6**, 1107–1112.

20 S. Huang, M. Woodson, R. Smalley and J. Liu, *Nano Lett.*, 2004, **4**, 1025–1028.

21 J. K. W. Sandler, J. E. Kirk, I. A. Kinloch, M. S. P. Shaffer and A. H. Windle, *Polymer*, 2003, **44**, 5893–5899.

22 A. M. Cassell, J. A. Raymakers, J. Kong and H. Dai, *J. Phys. Chem. B*, 1999, **103**, 6484–6492.

23 J.-F. Colomer, C. Stephan, S. Lefrant, G. Van Tendeloo, I. Willems, Z. Kónya, A. Fonseca, C. Laurent and J. B. Nagy, *Chem. Phys. Lett.*, 2000, **317**, 83–89.

24 K. Gong, F. Du, Z. Xia, M. Durstock and L. Dai, *Science*, 2009, **323**, 760–764.

25 Z. J. Qi, J. A. Rodríguez-Manzo, A. R. Botello-Méndez, S. J. Hong, E. A. Stach, Y. W. Park, J.-C. Charlier, M. Drndić and A. T. C. Johnson, *Nano Lett.*, 2014, **14**, 4238–4244.

26 L. T. Scott, *Chem. Soc. Rev.*, 2015, **44**, 6464–6471.

27 J. Cai, C. A. Pignedoli, L. Talirz, P. Ruffieux, H. Söde, L. Liang, V. Meunier, R. Berger, R. Li, X. Feng, K. Müllen and R. Fasel, *Nat. Nanotechnol.*, 2014, **9**, 896.

28 K. T. Kim, J. W. Lee and W. H. Jo, *Macromol. Chem. Phys.*, 2013, **214**, 2768–2773.

29 R. Denk, A. Lodi-Rizzini, S. Wang, M. Hohage, P. Zeppenfeld, J. Cai, R. Fasel, P. Ruffieux, R. F. J. Berger, Z. Chen, A. Narita, X. Feng, K. Mullen, R. Biagi, V. De Renzi, D. Prezzi, A. Ruini and A. Ferretti, *Nanoscale*, 2017, **9**, 18326–18333.

30 L. Liu, X.-F. Li, Q. Yan, Q.-K. Li, X.-H. Zhang, M. Deng, Q. Qiu and Y. Luo, *Phys. Chem. Chem. Phys.*, 2017, **19**, 44–48.

31 H. Zhang, J. Zhao and Q. Cai, *Phys. Chem. Chem. Phys.*, 2016, **18**, 5040–5047.

32 F. J. Martin-Martinez, S. Fias, G. Van Lier, F. De Proft and P. Geerlings, *Phys. Chem. Chem. Phys.*, 2013, **15**, 12637–12647.

33 L. Jiang, A. C. Papageorgiou, S. C. Oh, Ö. Sağlam, J. Reichert, D. A. Duncan, Y.-Q. Zhang, F. Klappenberger, Y. Guo, F. Allegretti, S. More, R. Bhosale, A. Mateo-Alonso and J. V Barth, *ACS Nano*, 2016, **10**, 1033–1041.

34 D. J. Dibble, Y. S. Park, A. Mazaheripour, M. J. Umerani, J. W. Ziller and A. A. Gorodetsky, *Angew. Chemie Int. Ed.*, 2015, **54**, 5883–5887.

35 C. Bronner, S. Stremlau, M. Gille, F. Brauße, A. Haase, S. Hecht and P. Tegeder, *Angew. Chemie Int. Ed.*, 2013, **52**, 4422–4425.

36 Y. Zhang, Y. Zhang, G. Li, J. Lu, X. Lin, S. Du, R. Berger, X. Feng, K. Müllen and H.-J. Gao, *Appl. Phys. Lett.*, 2014, **105**, 23101.

37 T. H. Vo, M. Shekhirev, D. A. Kunkel, F. Orange, M. J.-F. Guinel, A. Enders and A. Sinitskii, *Chem. Commun.*, 2014, **50**, 4172–4174.

38 C. Delaney, G. M. Ó Máille, B. Twamley and S. M. Draper, *Org. Lett.*, 2016, **18**, 88–91.

39 T. H. Vo, U. G. E. Perera, M. Shekhirev, M. Mehdi Pour, D. A. Kunkel, H. Lu, A. Gruverman, E. Sutter, M. Cotlet, D. Nykypanchuk, P. Zahl, A. Enders, A. Sinitskii and P. Sutter, *Nano Lett.*, 2015, **15**, 5770–5777.

40 T. Marangoni, D. Haberer, D. J. Rizzo, R. R. Cloke and F. R. Fischer, *Chem. – Eur. J.*, 2016, **22**, 13037–13040.

41 L. P. Wijesinghe, B. S. Lankage, G. M. O. Maille, S. D. Perera, D. Nolan, L. Wang and S. M. Draper, *Chem. Commun.*, 2014, **50**, 10637–10640.

42 B. Alameddine, R. S. Anju, F. Al-Sagheer and T. A. Jenny, *New J. Chem.*, 2016, **40**, 10363–10370.

43 J. D. Teeter, P. S. Costa, M. Mehdi Pour, D. P. Miller, E. Zurek, A. Enders and A. Sinitskii, *Chem. Commun.*, 2017, **53**, 8463–8466.

44 Z. Chen, W. Zhang, C.-A. Palma, A. Lodi Rizzini, B. Liu, A. Abbas, N. Richter, L. Martini, X.-Y. Wang, N. Cavani, H. Lu, N. Mishra, C. Coletti, R. Berger, F.

Klappenberger, M. Kläui, A. Candini, M. Affronte, C. Zhou, V. De Renzi, U. del Pennino, J. V. Barth, H. J. Räder, A. Narita, X. Feng and K. Müllen, *J. Am. Chem. Soc.*, 2016, **138**, 15488–15496.

Chapter 4

Extended Phenanthrene Systems as Donor-Acceptor-Donor Compounds for Optoelectronic Applications

4 Introduction

4.1.1 General Introduction

With the constant drive for smaller, thinner and lighter optoelectronic devices, the term Organic Light Emitting Diode (OLED) has become ubiquitous with "smart" devices. However, despite being developed by the Eastman Kodak company in the 1980's,[1] OLED containing devices have only recently made the move from those larger display technologies like high definition TVs, to smaller and increasingly difficult to produce smartphones and tablets.

An OLED at its simplest form is a LED device utilising an organic molecule-based emissive electroluminescent layer.[2] This layer, acting as an organic semiconductor, is sandwiched between two electrodes, and becomes emissive on electrical conduction through the layer.[2] As OLED technology is one of the most active research areas in synthetic and physical chemistry, the nomenclature surrounding different sub-technologies of OLED research has become confusing. Some abbreviations include PHOLED (phosphorescent OLED),[3] AMOLED (active-matrix OLED),[4] PMOLED (passive-matrix OLED),[5] P-OLED (polymer OLED),[6] WOLED (white OLED),[7] and SM-OLED (small molecule OLED). For the purposes of this chapter, the term OLED will be used to refer to the over-arching term of SM-OLED, as with the exception of polymer-based systems, small molecules constitute most of the OLED emissive layers.

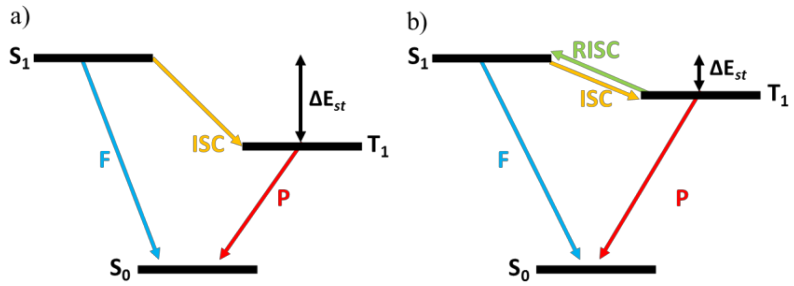

Figure 4. 1 Simplified Jablonski diagrams showing the fate of excited states; (a) large, and (b) small, ΔE_{st} values. F = fluorescence. P = phosphorescence. ISC = intersystem crossing. RISC = reverse intersystem crossing.

Despite their use in several commercial devices, the use of transition metal-based phosphorescent organic light emitting diodes (PHOLEDS) has become a topic of increasing cost concern to device manufactures, because of their reliance on expensive precious metals like Ir or Pt,[7,8] among the most expensive of all the elements. From 2012 onwards, the field

of thermally assisted delayed fluorescence (TADF) has been touted as a solution to address this problem.[9–11] This promises systems capable of "metal-like" OLED performance using strictly organic components. Developed by Adachi *et al.*,[12] TADF is a recent literature term for "E-type" fluorescence *i.e.* thermal repopulation of the S_1 state from the first triplet excited state (T_1).[13]

Figure 4.1 shows two simplified Jablonski diagrams. Figure 4.1(a) demonstrates the S_0, S_1 and T_1 states for a simplified organic chromophore. Here, luminesce from the S_1 state will result in fluorescence, with luminescence from the T_1 state resulting in phosphorescence. It is noted that intersystem crossing (ISC) from S_1 to T_1 is spin-forbidden and will not occur readily without the presence of a heavy atom to induce enhancement of spin-orbit coupling. This arrangement is a consequence of the HOMO and LUMO orbitals overlapping to a great degree, resulting in a large difference between the S_1 and T_1 energies (ΔE_{st}).[14] However, Figure 4.1(b) demonstrates a significant reduction in ΔE_{st}, facilitating ISC and more importantly, thermal upconversion or reverse intersystem crossing (RISC). A common method to achieve this reduction in ΔE_{st} is through the effective charge separation of the HOMO and LUMO energies to different components within a single molecule. This is discussed in greater detail shortly. TADF can therefore be summarised as delayed fluorescence following a simplified pathway of $S_0 \rightarrow S_1 \rightarrow T_1 \rightarrow S_1 \rightarrow S_0$.

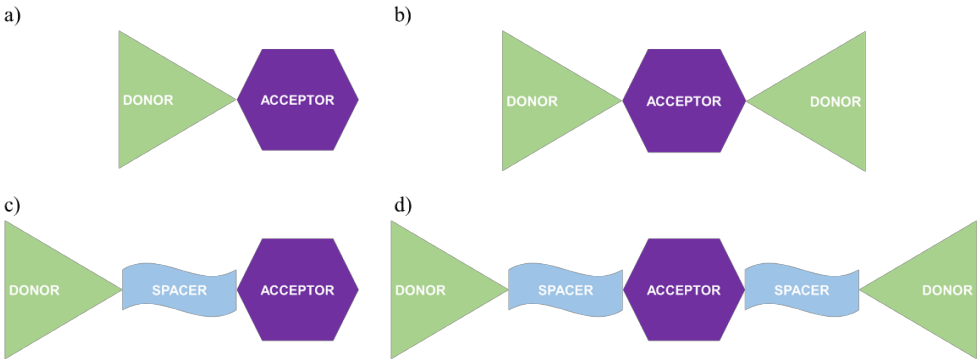

Figure 4. 2 (a) Donor-Acceptor compound. (b) Donor-Acceptor-Donor compound. (c) Donor-π-Acceptor compound. (d) Donor-π-Acceptor-π-Donor compound.

As mentioned, a popular method to achieve TADF behaviour is through the careful design of organic compounds into distinct donor and acceptor components. Figure 4.2 visualises four types of donor and acceptor compounds. Type-A is a Donor-Acceptor compound (D-A); Type-B is a Donor-Acceptor-Donor compound (D-A-D); Type-C is a Donor-π-Acceptor compound (D-π-A); Type-D is a Donor-π-Acceptor-π-Donor (D-π-A-π-D). Unfortunately, in

the literature, D-A-D and D-π-A-π-D are often used interchangeably. For the purposes of this work, D-A-D will be used to describe D-π-A-π-D systems unless otherwise specified, as systems with the π spacer feature increasingly in the literature. Often this π spacer is a single phenyl ring, or a conjugated bond in the form of an alkene or alkyne linker. This π spacer has been found to be beneficial in many systems, effectively lowering the ΔE_{st}, and increasing the S1 → T1 efficiency.[15] There are several factors one must consider throughout the design process of organic compounds for TADF-type OLED applications. These include, but are not limited to, fluorescence rate (k*f*), TADF lifetime, and photoluminescence quantum yield (Φ). This introduction will concentrate on materials considered as TADF materials, as a method towards describing the photophysical (and electrochemical) properties of D-A-D type compounds. However, the use of D-A-D compounds reaches beyond their single use as OLED electroluminescent layers, with several examples given as part of this literature review.

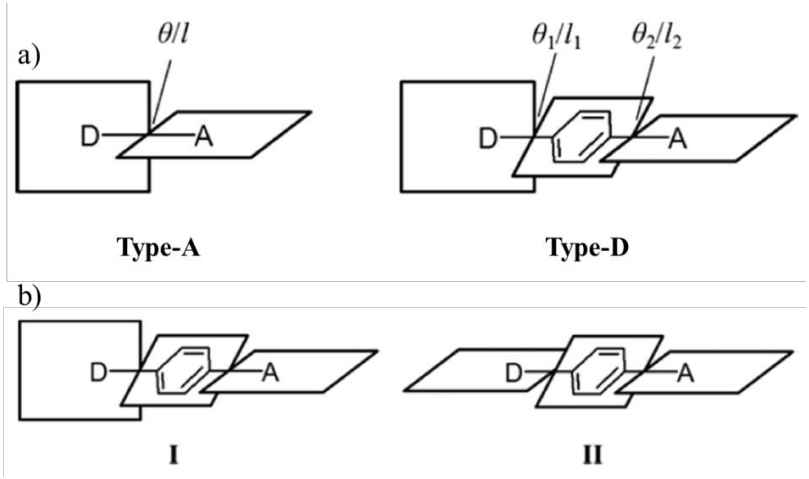

Figure 4. 3 (a) Donor-Acceptor compound showing large dihedral angle; Donor-π-Acceptor compound showing reduced dihedral angle. (b) Twisted and planar Donor-π-Acceptor compounds.[15]

Figure 4.3(a) demonstrates representative examples of Type-A and Type-D compounds. Type-A compounds, without a π spacer, are often constructed so that there exists a large dihedral angle between the donor and acceptor components.[16] This is once again to achieve effective charge separation between the HOMO and LUMO orbitals. However, in Type-D compounds, with the π spacer, the requirement for such a large dihedral angle is less strict, with the increased separation distance between the HOMO and LUMO orbitals facilitating a lowering of ΔE_{st}.[15] Figure 4.3(b) further demonstrates that in these D-A-D systems, both the donor and acceptor components may be planar with respect to each other, or exist in a twisted

conformation. As TADF materials require charge separation of the HOMO and LUMO energies, the goal of the construction of TADF compounds is to induce an intramolecular charge transfer (ICT) transition, through careful synthetic design.[17–19] Figure 4.4 visualises the D-A-D ICT transition, from the donor component (or donor antennae), to the acceptor core.

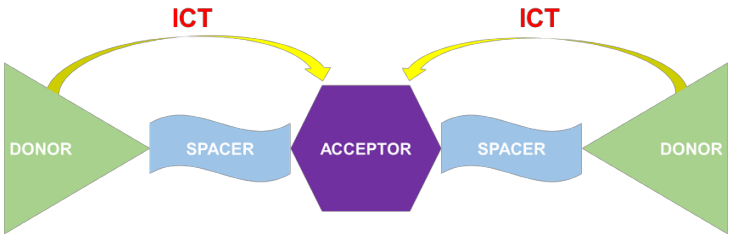

Figure 4. 4 ICT transitions from the donor component to the acceptor component of a Donor-π-Acceptor-π-Donor compound. ICT = intramolecular charge transfer.

Despite being an active research area, there are currently only a small number of readily modifiable donors and/or acceptor components in the literature. These will be discussed in detail shortly. Therefore, there exists an opportunity to increase the number of structures capable of acting as either donor, or acceptor components, towards TADF applications in OLED technology and other optoelectronic technologies.

This chapter will deal exclusively with the design and synthesis of novel extended phenanthrene-pyridazine systems as compounds suitable towards for their eventual incorporation into OLED device architectures. The use of phenanthrene systems as TADF materials towards OLED devices remains low in the literature, and thus offers an opportunity to rapidly generate a diverse library of novel compounds for further testing. This chapter will introduce the first phenanthrene-pyridazine hybrid compounds, constructed *via* a Donor-π-Acceptor-π-Donor (D-A-D) arrangement, utilising common organic chromophore structures as the donor antennae, with the phenanthrene-pyridazine acting as the compound's novel acceptor. The following sections will detail a literature review of systems used as D-A-D materials, and other technologies. The synthetic design of the structures detailed in this chapter lend them towards an emerging field of great interest in optoelectronic research, and will be discussed in detail.

4.1.2 Organic Donor-Acceptor-Donor Compounds

There is a growing research interest in D-A-D compounds of a strictly organic nature. This is undoubtedly due to their lower cost compared to those systems containing transition metals. The fixed coordination environment of valent metals also restricts the molecular design of these transition metal-based systems; a problem not found in the synthesis of organic compounds.

In the literature, there are two categories of D-A-D compounds may be categorised. Chart 4.1 demonstrates two examples of the former. The first system, featuring higher functionalisation of the simplest system, 2,6-bis(4-(diphenylamino)phenyl)anthracene-9,10-dione, **L74**, is a D-A-D compound featuring triphenylamine-type donor components, with an anthracene-9,10-dione acceptor component. The work, published by Zhang *et al.*,[15] attempted to design molecules capable of red-type fluorescence. As noted by the authors, for effective TADF molecules, a small energy difference between the singlet and triplet excited states (ΔE_{st}) is a fundamental requirement. Here, the authors synthesise Type-D compounds, and find that the inclusion of the phenyl bridge facilitates a lowering of the ΔE_{st}, as a direct result of creating effective charge separation between the donor and acceptor components. In each of the structures generated, the HOMO is located on the amine donor, with the LUMO energy situated in the anthracene-9,10-dione acceptor. Yellow/red TADF was observed for all compounds.

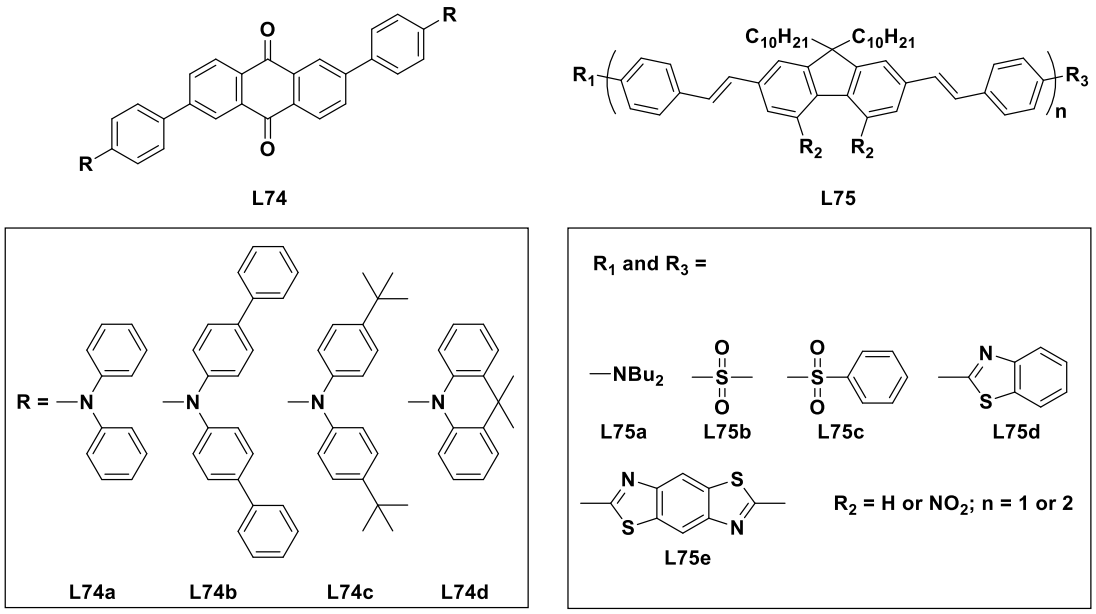

Chart 4. 1 Examples of Donor-Acceptor-Donor compounds.

The second system, **L75**, in Chart 4.1, derived from a fluorene core system, is work reported by Yao *et al.*,[20] towards two-photon fluorescence imaging of cells. Here, the fluorene component acts as both the π-bridge, and bearer of the acceptor groups (in this case nitro-substitution). Both amine-type, and sulfone-type donors were used in this work, including triphenylamine and thiazole ring systems. Common in many systems is the use of long chains to control solubility, with this work using long aliphatic chains to control the hydrophilicity/hydrophobicity interactions of the in-cell probes. The use of the D-A-D structure *versus* that of either the respective D-A or D-D analogues improved the two-photon absorptivity.

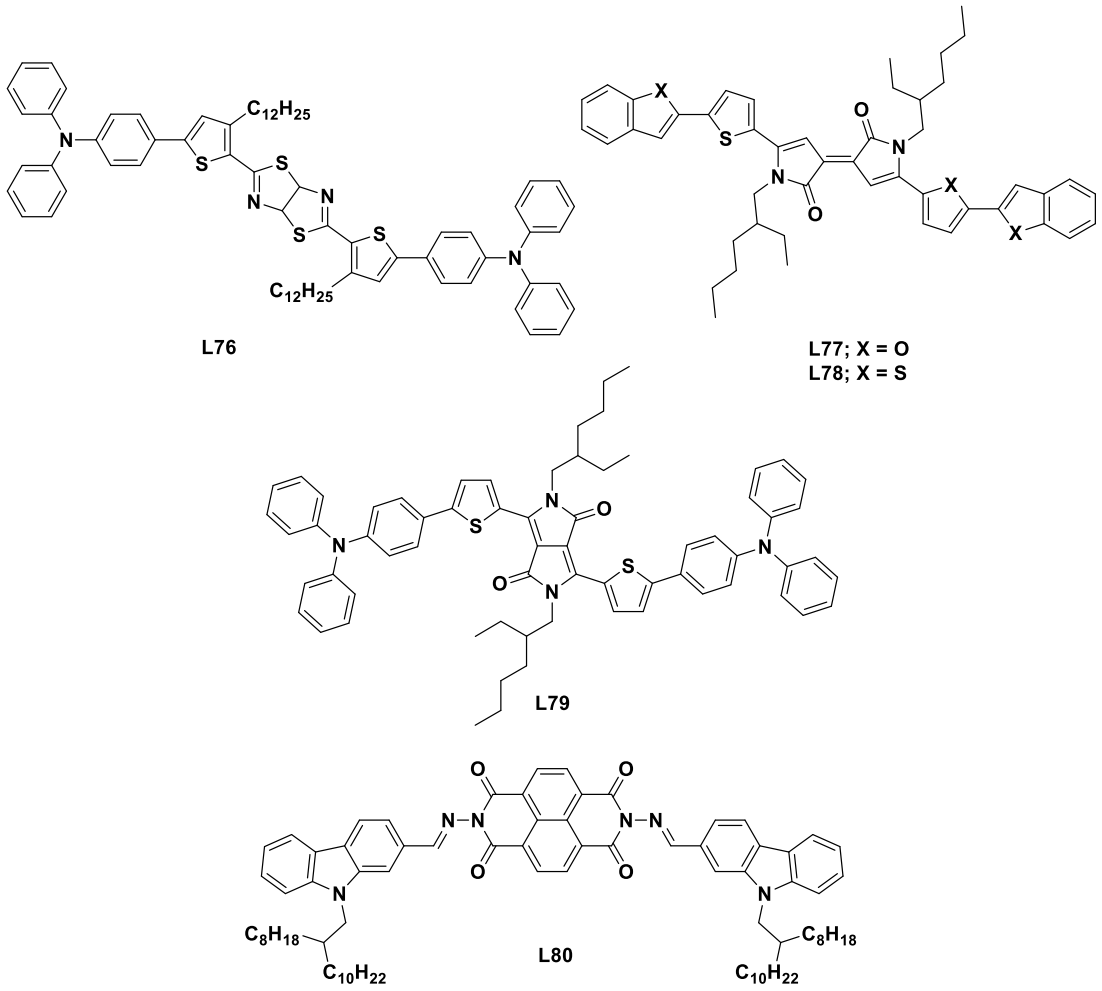

Chart 4. 2 Examples of Donor-Acceptor-Donor compounds based on Pechmann dyes, or napthalimide.

The use of heterocyclic ring systems as the donor components should be immediately apparent, with N- or S-containing ring systems often used, as seen by the work of Zhang and

Yao earlier. However, these systems may also be used within the acceptor component of the D-A-D system. Chart 4.2 shows three systems in the literature using N- and S-heterocycles within both their donor and acceptor components. The first system, **L76**, developed by Shi *et al.*,[21] is a solution processable D-A-D compound for inclusion in an organic solar cell. Built upon a thiazolothiazole core system, the inclusion of this electron withdrawing N- and S-containing heterocycle acts as an efficient acceptor component. Here, triphenylamine is used as the donor component, with the alkyl-chain substituted thiophene acting as the spacer (Type-D). While the work is preliminary, the inclusion of the thiazolothiazole acceptor system facilitated the **L76** system achieving power conversion efficiencies (PCEs) among the highest reported (at time of publication) for organic small molecule solar cells (OSCs). The second and third systems, **L77** and **L78**, developed by Z. Cai *et al.*,[22] use a Pechmann dye as the electron withdrawing acceptor core for the two system's inclusion into organic field-effect transistors (OFETs). The inclusion of benzothiophene donors in **L77**, and benzofuran donors in **L78**, give different hole mobility values when constructed into thin film OFETS. **L78** shows high hole mobility values while **L77** shows poor hole mobility values, with the authors citing poor thin film morphology and low molecular ordering as potential reasons for this difference. Of note here, whilst systems already presented contain the HOMO and LUMO on the respective donor or acceptor components of the molecules, **L77** and **L78** feature both the HOMO and LUMO orbitals across the Pechmann dye, with the donor components not contributing greatly. However, the authors conclude that this may be modified through the appropriate selection of new electron donor components.

The fourth system, **L79,** developed by Y. Cai *et al.*,[23] may be considered as a hybrid of compounds **L76**, and **L77**/**L78**, as it uses a triphenylamine-thiophene donor, but with a Pechmann dye acceptor core. The authors synthesised **L79** as a D-A-D compound towards photoacoustic imaging (PAI) guided photodynamic/photothermal synergistic therapy. When **L79** is formed into nanoparticles and injected *in vivo*, laser irradiation generates reactive singlet oxygen for photodynamic therapy. The final system in Chart 4.2 is **L80**, developed by Zhuang *et al.*,[24] using an napththalimide acceptor and two carbazole donors. Long alkyl chains are used to increase the solubility of the system in common organic solvents. Here, the design of the compound in a D-A-D arrangement allows the study of D-A-D systems towards organic-based specific memory devices, a rarity as noted by the authors. Here, the HOMO orbital is situated on one of the donor carbazole moieties, with the LUMO orbital situated on the napthalimide core system. When formed as a thin film, and subjected to a bias sweep of negative voltage, a **L80**/Al sandwich complex can be switched "ON", with retention of this ON-state for six minutes. This is considered as "volatile" memory, which is a computer-type memory lost immediately or rapidly on loss of power. It should be immediately apparent that

from the limited number of systems described, D-A-D compounds find use in a diverse range of research fields.

Synthetic access to acceptor components is dominated by the inclusion of pyrazine ring structures. This is undoubtedly due to (a) the ease of their synthesis, formed from the double Schiff base condensation of an ortho diamine and an ortho dione, and (b) their electron withdrawing nature. Chart 4.3 demonstrates three systems, **L81**,[25] **L82**,[26] and **L83**.[26] Developed by Data[25] and Okazaki[26] *et al*., these systems are capable of efficient TADF behaviour, showing high external efficiencies when constructed into OLED devices. The inclusion of the phenothiazine ring structure in **L82** and **L83** generates mechanochromic luminescent behaviour, where reversible luminescence colour changes are seen in response to external mechanical stimuli (grinding, temperature, electric field, *etc.*). The authors report this phenomenon as due to the different conformations possible of the phenothiazine ring structure ("quasi-equatorial" and "quasi-axial").

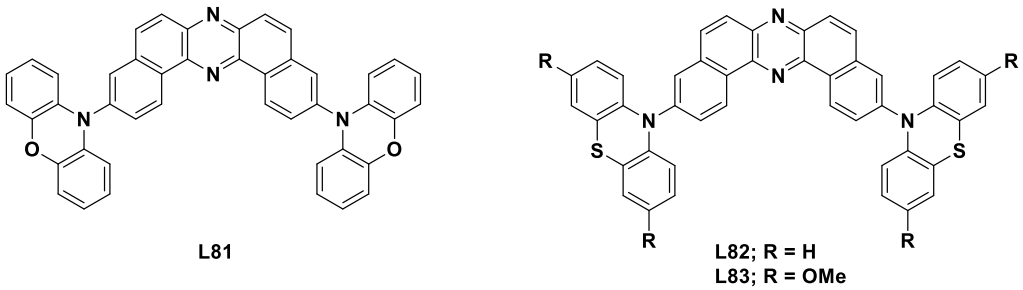

Chart 4. 3 Examples of Donor-Acceptor-Donor compounds derived from a pyrazine core.

4.1.3 D-A-D Compounds as NIR Emitters

The compounds of Chart 4.4 display green to red and near infrared (NIR) emission in both the solution state, and when constructed into OLED devices. D-A-D compounds are coveted as NIR emitters, and their generation is an increasingly active research area. The first two compounds, **L84**, and **L85**, developed by Qian *et al.*,[27] utilise the common triphenylamine donor component, with an acceptor component constructed from a pyrazine ring and a 1,2,5-thiadiazole ring. Here, the authors report efficient and radiant NIR emission from both compounds when assembled into an OLED device using AlQ_3 as chosen host. Both compounds were thermally stable, and were assembled into the OLED device *via* vapour deposition. **L84**, featuring no substitution to the pyrazine ring, showed a single NIR emission at 752 nm.

As visualised in Chart 4.4, the 1,2,5-thiadiazole ring system is a popular choice for the generation of compounds capable of NIR emission. The third system in Chart 4.4, replacing the aforementioned pyrazine ring with a second thiadiazole ring, **L86**, generated a system capable of NIR emission >1000 nm, once again using triphenylamine donor components. Developed by Qian *et al.*,[28] **L86** gives NIR emission beyond 1000 nm in both solution state (CH_2Cl_2), and when constructed into thin films. This emission is maintained when **L86** is assembled into an OLED device, again through the method of vapour deposition. The OLED is non-doped.

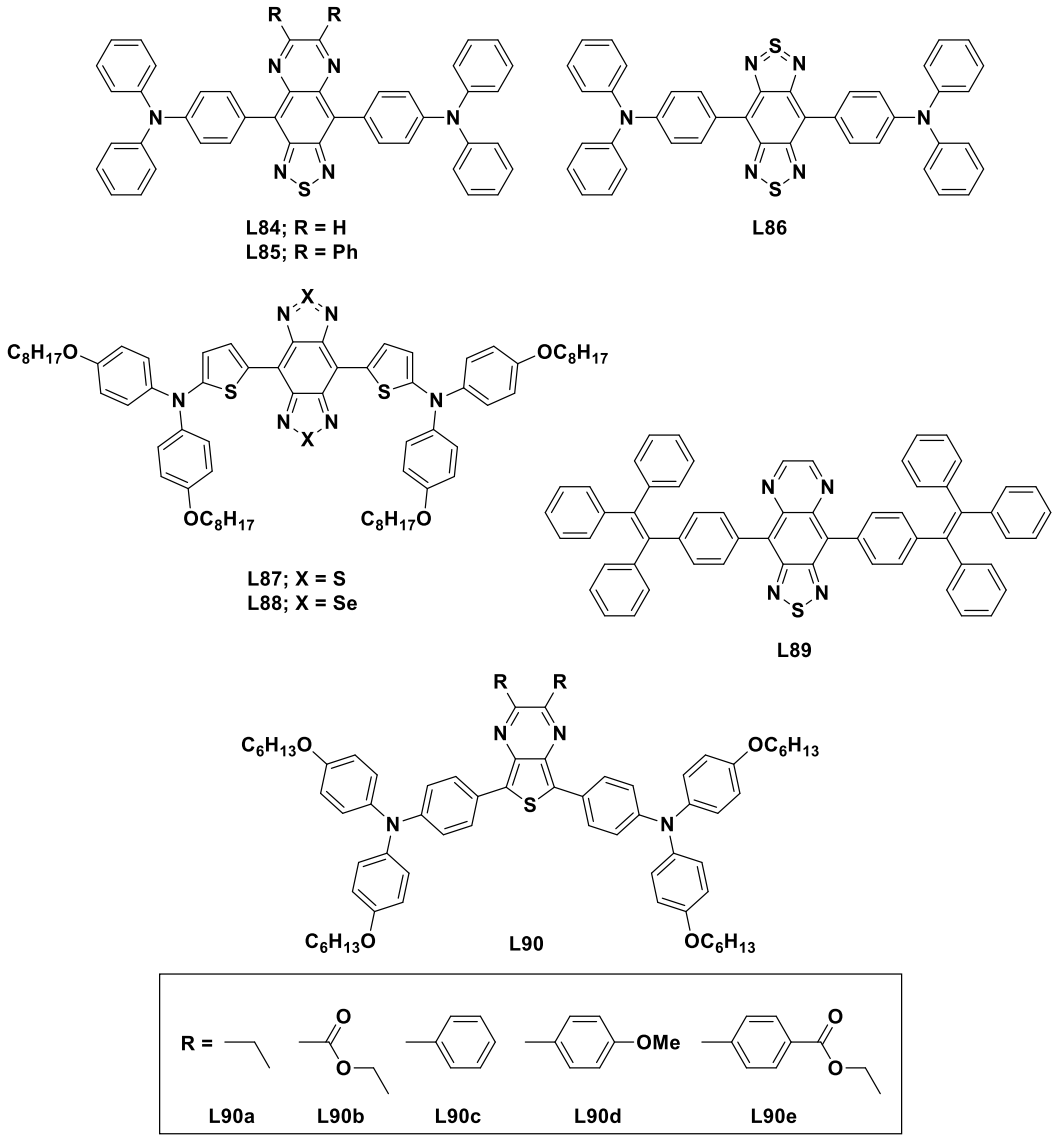

Chart 4. 4 Examples of Donor-Acceptor-Donor compounds as NIR emitters.

Compounds four and five in Chart 4.4, **L87** and **L88**, again developed by Qian *et al.*,[29] feature a similar D-A-D architecture to earlier systems, with an aryl amine donor component.

However, unlike earlier systems, the π-bridge is not a phenyl ring, but a thiophene ring. The bis-benzothiadiazole ring system also demonstrates synthetic modification, with **L87** featuring the standard bis-benzothiadiazole ring, but **L88** demonstrating replacement of the sulfur of the thiadiazole ring with Selenium. The substitution of S with Se lowers the band gap of the compound, while also causing a red shift in the photoluminescence. **L88**, exhibits an emission at 1485 nm in CH_2Cl_2. However, undoped OLEDs were not realised by the authors, with doping required to facilitate NIR OLED devices capable of emission at 1050 nm.

Compound six, **L89**, developed by Du *et al.*,[30] once again uses the combination of the pyrazine-thiadiazole ring system as the acceptor component, but without the typical aryl amine donor. **L89** utilises the rigid tetraphenylethene (TPE) donor system. The use of the tetraphenylethene donor here was deliberate, as there is an aggregation-induced emission enhancement (AIEE) which reduces π-π stacking. Similar to previous system, **L89** is also an NIR emitter. The authors assembled doped and non-doped OLED systems, with results suggesting that systems capable of AIEE are suitable for non-doped OLED devices in the future.

The final systems in Chart 4.4, **L-90** – **L90e**, developed by McNamara *et al.*,[31] feature an aryl amine donor, with a thiophene-pyrazine core ring system (thienopyrazines) as the acceptor component of the D-A-D architecture. Whilst not developed with a specific device application, all compounds show NIR emission in solution and as thin films. Substitution of the pyrazine ring offers an opportunity to control the absorption and emission wavelength maxima through optical band gap control moving from simple alkyl functionality towards the ethyl ester functionality. Through increasing the electron withdrawing nature of the pyrazine ring, the ICT is facilitated in a more complete manner. The authors also note the effect of bond angle change between the donor and acceptor rings on the Stokes shift of the systems.

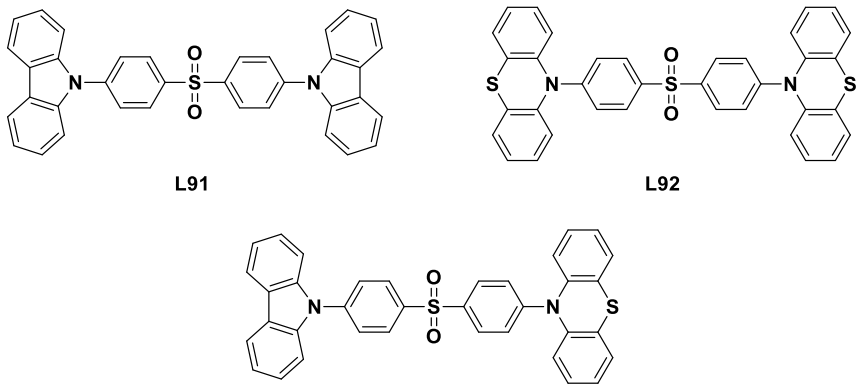

Chart 4. 5 Examples of symmetric and asymmetric Donor-Acceptor-Donor compounds.

While D-A-D systems are nearly always constructed using a single acceptor, and two donors of the exact same structure, recent work is revealing interesting results through the construction of D-A-D' systems, where the second donor is often similar but not the same as the first one. Chart 4.5 shows three systems. **L91** and **L92** are symmetrical D-A-D systems, with **L93** an asymmetrical D-A-D' system. Studied by Aydemir *et al.*,[32] all three systems feature a diphenyl-sulfone core acceptor component. Of great interest is the D-A-D' system **L93**, as it is dual emissive, suggesting that future OLED systems may be designed with broad emission. In this system, the authors report no evidence of charge transfer between the two different donor components, which is attributed to the perpendicular nature (orthogonality) of the D-A and A-D' components.

4.1.4 Pyridazine-based Donor-Acceptor-Donor Compounds

Pyridazine ring systems in the literature as acceptor components in D-A-D architectures are rare. Chart 4.6 shows some of the known systems, but which do not feature the synthetic diversity of other D-A-D systems.

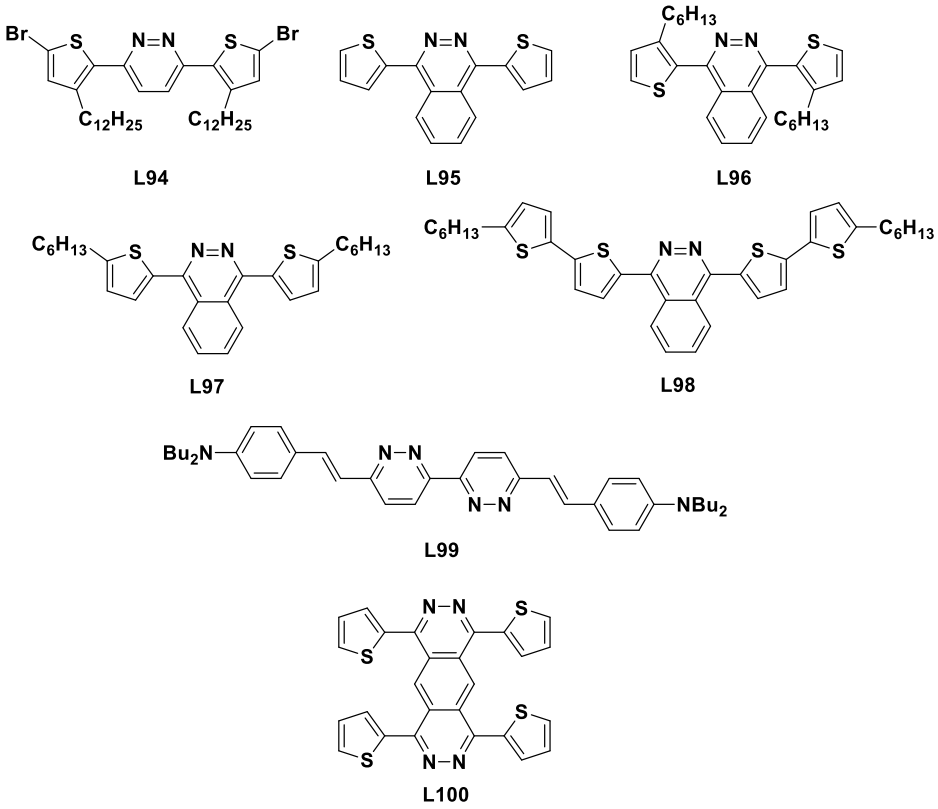

Chart 4. 6 Examples of pyridazine-containing Donor-Acceptor-Donor compounds.

The first pyridazine system constructed into a D-A-D type architecture appears to be **L94**, developed by Yasuda *et al*.[33] Consisting of a pyridazine acceptor, and thiophene rings as the respective donors**, L94** was polymerised into polymer chains. Electrochromism of the polymers was observed through electrochemical measurements of thin films, and demonstrated a carrier mobility of 3 x 10^{-3} cm^2 V^{-1} s^{-1} when used as a p-type semiconductor in a field-effect transistor. The next four systems in Chart 4.6 (**L95**, **L96**, **L97**, and **L98**) were synthesised by Su *et al.*,[34] and are small monomer D-A-D systems featuring thiophene donors and pyridazine acceptor components. Here, the authors changed the position of the side chains and found this resulted in significant changes to the optoelectronic properties of the systems. **L98**, featuring a double thiophene donor "unit", features much stronger fluorescent emission than **L96** or **L97**.

The sixth system in Chart 4.6 is **L99**, a D-A-D compound featuring two pyridazine rings as the system's acceptor component. Developed by Lincker *et al*.,[35] the compound was studied and revealed fluorescent luminescence and significant solvatochromism. Construction into an OLED device generates a green-emitting system, with an external quantum efficiency of 4%. The final system in Chart 4.6 is **L100**, developed by Liu *et al.*,[36] is a H-shaped compound featuring an azaanthracene core of two pyridazine rings. The system was studied and revealed n-type character, with the authors suggesting their system as a good candidate for organic electronic devices. As can be seen, the use of pyridazine ring structures in the literature is limited, with no system yet reporting TADF emission.

4.1.5 Phenanthrene-based Donor-Acceptor-Donor Compounds

There are several D-A-D systems in the literature utilising the phenanthrene ring system. However, these examples are very recent, and are growing in importance.

Chart 4.7 shows a number of systems derived from a phenanthrene core ring system. Immediately apparent, is that in nearly all cases, synthetic "inclusion" of the phenanthrene ring is exclusively paired with a pyrazine ring. The inclusion of the aforementioned thiadiazole ring is also very common. Condensation of phenanthrene-9,10-dione with an ortho di-amine is the synthetic preparation of choice here in all cases. The first system in Chart 4.7 is **L101**, developed by Li *et al.*,[37] and demonstrates the inclusion of a phenanthrene ring system into a conjugated polymer. Of interest here, is that the phenanthrene ring system only has a small influence on the charge carrier transport of the polymer. However, despite this, the authors report a photoresponsivity of the phenanthrene-containing polymer of 400 A/W, which exceeds single-crystal silicon-based organic phototransistors. The second to fifth systems in Chart 4.7, **L102**, **L103**, **L104**, and **L105** developed by Kato et al.,[38] are not strictly

D-A-D compounds, but are constructed in a similar fashion, and are therefore included in this review. The phenanthrene ring system offers the possibility of increasing the π-conjugation. This is also seen through inclusion of the acetylene linker in **L102** and **L103** *versus* **L104** and **L105**. These compounds showed light absorption up to 750 nm, and were investigated towards their self-assembled clusters on varying the alkoxy groups. The sixth system in Chart 4.7, **L106**, developed as part of work described earlier by Qian *et al.*,[27] is an NIR emitter for OLEDs. The inclusion of the phenanthrene ring system here *versus* earlier systems, generates an expected red shift in the emission to longer wavelengths.

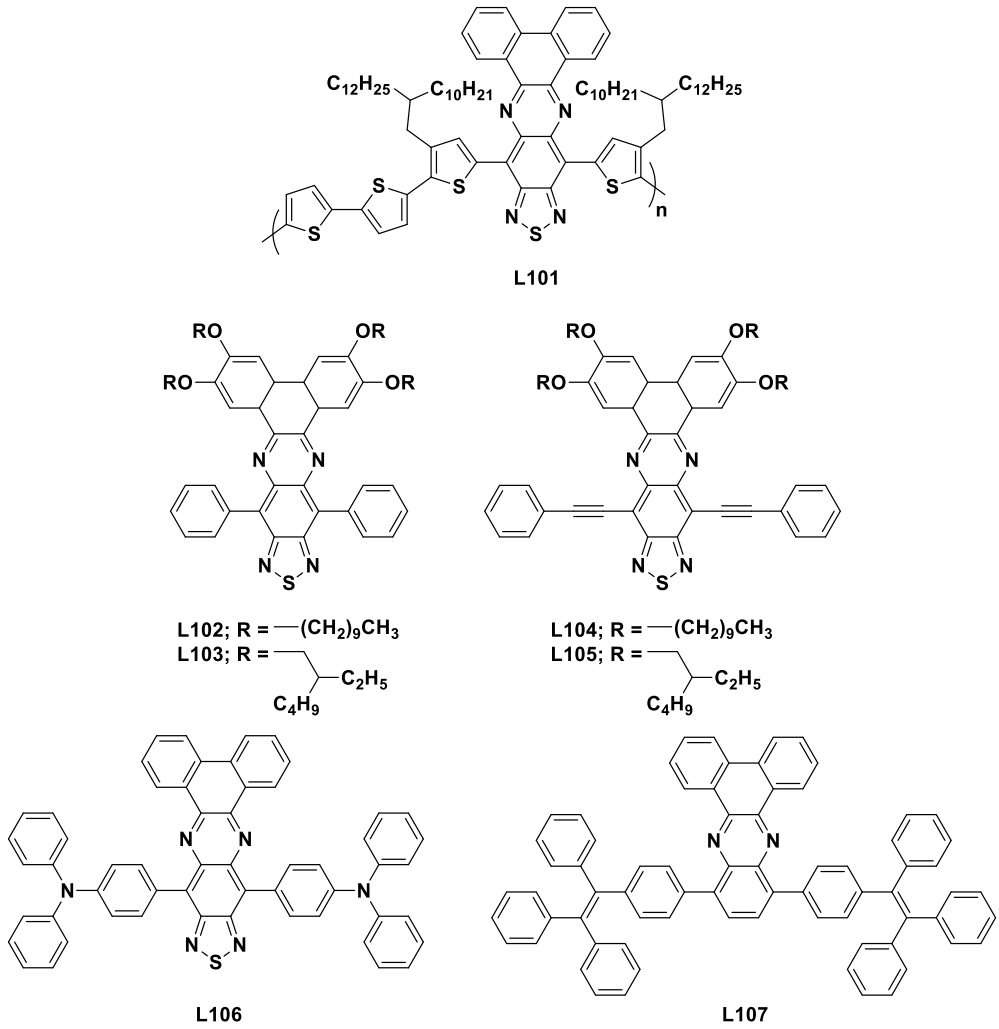

Chart 4. 7 Examples of phenanthrene-containing Donor-Acceptor-Donor compounds.

The final system in Chart 4.7, **L107**, may be considered a simpler system to **L106**, *i.e.* without the thiadiazole ring. Here, **L107** uses the tetraphenylethene (TPE) moiety as the respective donors within the D-A-D architecture. Developed by Ekbote *et al.*,[39] the TPE donor was once again chosen towards aggregation-induced emission enhancement (AIEE). The authors report

strong ICT transitions from the TPE donors to the phenanthrene-pyridazine acceptor core, with AIEE emission dominating at higher water concentrations. Further to these results, mechanochromic behaviour was observed *via* powder X-ray diffraction (XRD), revealing that a morphological change from crystalline to amorphous is responsible for this mechanochromic phenomenon.

Whilst Chart 4.7 demonstrates D-A-D structures (or similar) where the donors are synthetically accessed "away" from the phenanthrene ring system, there are several examples of D-A-D architectures where the donors are substituted directly to the phenanthrene ring system. Chart 4.8 shows four examples of this type of system, once again featuring the pyrazine ring common to phenanthrene systems.

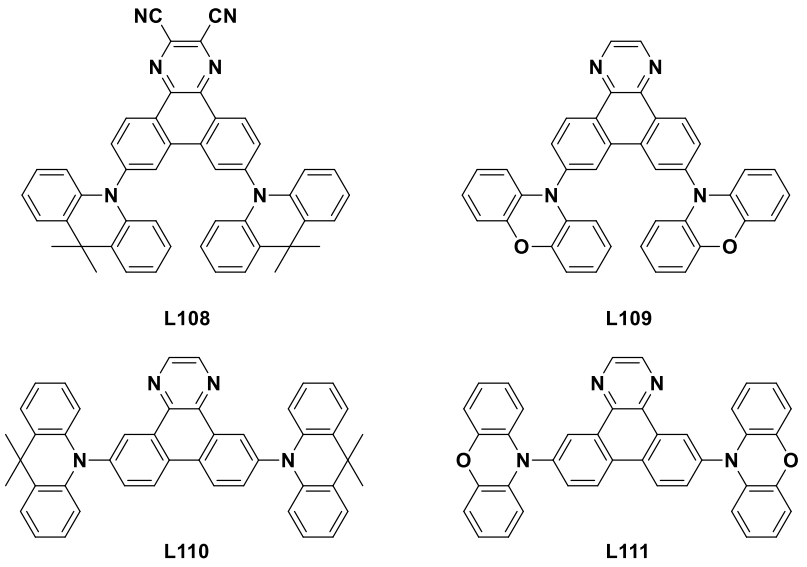

Chart 4. 8 Examples of phenanthrene-containing Donor-Acceptor-Donor compounds.

The first system in Chart 4.8, **L108**, was developed by Wang et al.,[40] and features a D-A-D architecture using an acridine donor at the 3- and 6-positions of the phenanthrene ring system. The acridine donor is chosen for its large steric hindrance and dihedral angles, with the authors reporting very low ΔE_{st} values. As a result, the authors fabricate an OLED, finding the acridine donors suitable towards the generation of long-wavelength TADF materials.

The second, third, and fourth systems in Chart 4.8, **L107** – **L111**, developed by Takahashi *et al.*,[41] feature another system showing substitution of the 3- and 6-positions of the phenanthrene ring system (**L109**), and two systems showing substitution at the 2- and 7-positions (**L110** and **L111**). All of the generated systems are luminescent, and have very small ΔE_{st} values. In codeposited thin films, TADF behaviour is seen. The phenoxazine systems

L109 and **L111** give green emission when fabricated into an OLED device, with external electroluminescent quantum efficiencies of approximately 12 %.

4.1.6 Proposed Phenanthrene-Pyridazine Donor-Acceptor-Donor Compounds

Whilst not exhaustive, this literature review demonstrates the lack of novel donor or acceptor components in the literature, with systems often relying on small modifications of common components to achieve positive contributions towards eventual commercialisation. This is a significant bottleneck, which could be overcome through the synthetic design of new donor or acceptor components, which themselves may be modified or functionalised.

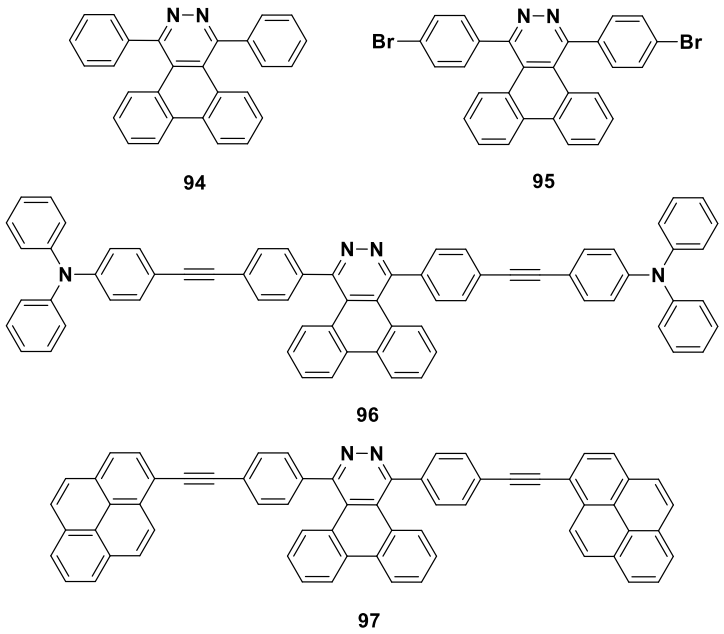

Chart 4. 9 Proposed phenanthrene-pyridazine compounds for this study.

The purpose of this work is to demonstrate the synthetic access to a new acceptor component, with potential to rapidly generate a diverse library of D-A-D architectures with common donor components. It is hoped that the synthetic design of these compounds will facilitate TADF behaviour in these compounds, with the potential for mechanochromic behaviour also possible. This chapter will introduce the first phenanthrene-pyridazine hybrid compounds, constructed *via* a Donor-π-Acceptor-π-Donor (D-A-D) arrangement, utilising common organic chromophore structures as the donor antennae, with the phenanthrene-pyridazine acting as the compound's novel acceptor. Chart 4.9 shows these target compounds.

With the pyridazine ring embedded into the extended phenanthrene core system, it is hoped that this novel acceptor component will facilitate strong ICT transitions from two common electron donor components, triphenylamine (in compound **96**), and pyrene (in compound **97**). The basic system, **94**, will act as a model system. The inclusion of an acetylene spacer will allow the study of the D-π-A-π-D architecture. As the acetylene spacer is less common in literature examples, this will allow the study of the effect of increased π-conjugation between the donor and acceptor components. This study hopes to reveal if a pyridazine ring-containing PAH acceptor component is worthy of extensive future research interest, towards its potential inclusion in next generation devices. As there are no directly comparable analogues, this study is the first attempt to understand the optoelectronic properties of this compound type.

The attempted syntheses, structural characterisation, and electrochemical and photophysical investigations of these systems are detailed, along with a comprehensive future work.

4.2 Results & Discussion

99 is the dibrominated form of **12** used in previous chapters, while **103** makes a unique change to the more common bromo substitution of the phenanthrene ring. Due to issues of solubility and low yield with the cyclopentadienone system **80**, synthetic access at these positions was not considered for this work.

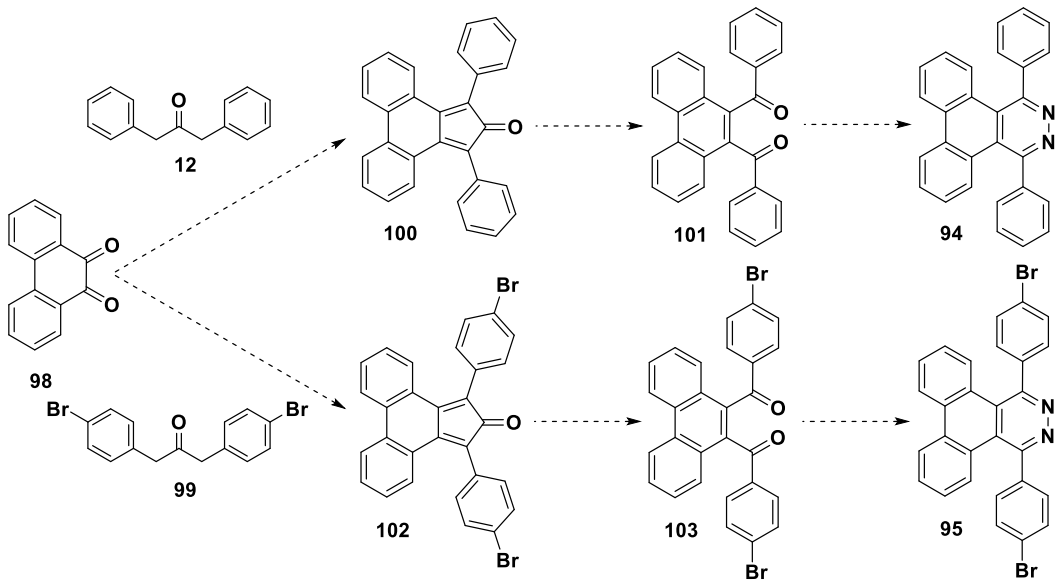

Scheme 4. 1 Proposed synthetic routes to **94** and **95**.

Scheme 4.1 demonstrates the proposed synthetic preparations to the desired systems **94** and **95**. The ring opening step to **101** and **103** was assumed to be completed in a similar fashion to the ring opening step towards **79**, with hydrazine hydrate once again being used to generate the desired pyridazine ring. Inclusion of the necessary para-bromination is achieved *via* the monoketone step, **99**. The synthetic steps, and difficulties encountered, are included in the proceeding sections.

4.2.1 Synthesis & Structural Characterisation of 94 and 95

4.2.2 Synthesis of 94 and 95

1,3-diphenyl-2H-cyclopenta[l]phenanthren-2-one, **100**, was readily generated following a modified literature preparation, and used without further purification.[42] However, the reaction time of 15 minutes was extended to 45 minutes. The Knoevenagel reaction here between phenanthrene-9,10-dione **98** and 1,3-diphenylpropan-2-one **12** appears unable to proceed at ambient temperatures, with refluxing MeOH required.

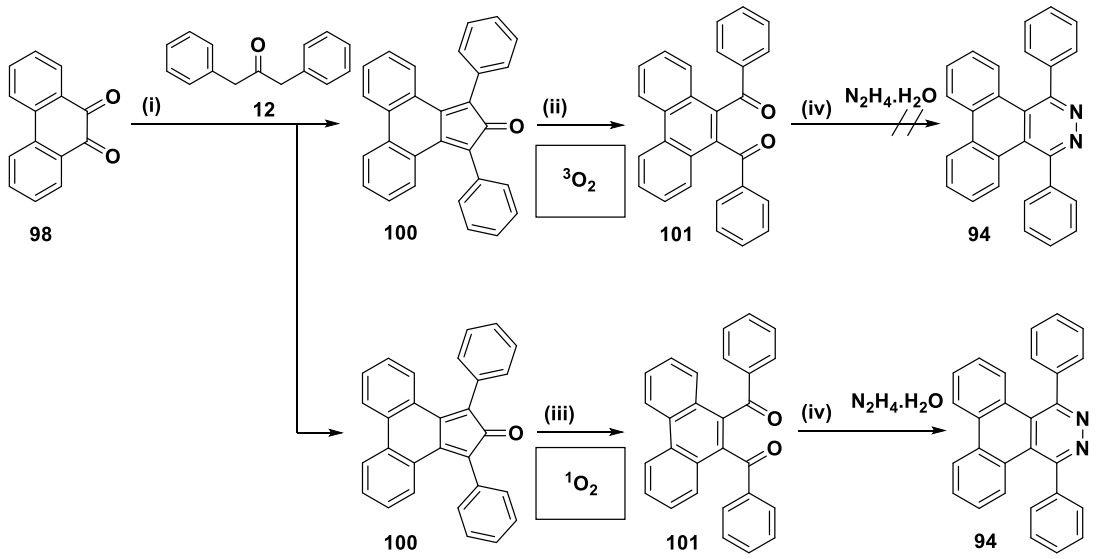

Scheme 4. 2 Attempted, and successful syntheses towards **94**. (i) MeOH, KOH, RT, 16 h, 58 %. (ii) Chlorobenzene, 130 °C, 16 h. (iii) Chloramine T hydrate, H_2O_2, MeOH, CH_2Cl_2, Δ, 1 h, 27 %. (iv) EtOH, KOH, 80 °C, 4 h, 84 %.

The ring opening step of **100** towards phenanthrene-9,10-diylbis(phenylmethanone) **101**, was attempted in air in refluxing chlorobenzene. Following overnight reaction, the deep opaque green colour was replaced with a bright transparent yellow colour. However, following the removal of the chlorobenzene solvent *in vacuo*, a significant number of impurities were

observed *via* Thin Layer Chromatography (TLC). As **101** was expected to be an off-white solid, the bright yellow colour was assumed to be an impurity formed in the ring opening step, but remains unidentified. Significant attempts were made towards the removal of this impurity *via* silica-based column chromatography but these proved unsuccessful. An attempt was made to generate the pyridazine product, 1,4-diphenyldibenzo[f,h]phthalazine, **94**, directly, using hydrazine hydrate (50-60 % in H_2O), with a successful generation of the product being reported over the two steps. However, the impurity appeared to react with the hydrazine hydrate, greatly increasing the number of impurities observed *via* TLC. Attempts to precipitate and recrystallise the product were unsuccessful.

As the air-mediated ring opening step is achieved through the radical addition of $^3O_2$, it was postulated that the bright yellow impurity may be an incomplete reaction product of **100** to **101**. For that reason, the ring opening step was attempted with the use of the highly reactive $^1O_2$, generated *via* the literature method of Evans *et al*.[43] In this reaction, singlet oxygen is generated from the oxidation of H_2O_2 by chloramine T hydrate. On addition of H_2O_2 to a solution of **100** and chloramine T hydrate in a mixed solvent of CH_2Cl_2:MeOH, the deep opaque green colour of **100** was seen to sluggishly change to yellow/orange. Addition of heat to the reaction vessel (*via* use of a heat gun), was enough to force the reaction to completion. Stirring at ambient temperature for a further hour facilitated a colour change from yellow/orange to off-white. Analysis by TLC confirmed the absence of the bright yellow product previously seen with the air-mediated attempt. Silica column chromatography yielded **100** as an off-white solid in good yield (Scheme 4.2). The generation of the pyridazine ring product **94** was attempted once again *via* the use of hydrazine hydrate. This attempt was successful, with the precipitation from diethyl ether yielding an analytically pure sample for further study. These steps are summarised in Scheme 4.2. These products are characterised by high resolution mass spectrometry studies (HRMS), with this data summarised in Table 4.1.

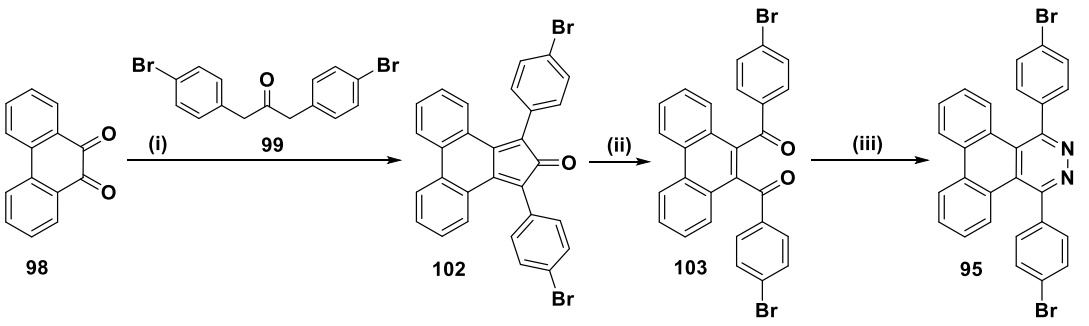

Scheme 4. 3 Synthesis of **95**. (i) MeOH, KOH, RT, 16 h, 54 %. (ii) Chlorobenzene, 130 °C, 16 h, 61 %. (iii) EtOH, KOH, 80 °C, 4 h, 93 %.

Generation of the di-brominated cyclopentadienone product 1,3-bis(4-bromophenyl)-2H-cyclopenta[l]phenanthren-2-one, **102**, was achieved following the synthetic preparation of **100**, but using the di-brominated monoketone precursor 1,3-bis(4-bromophenyl)propan-2-one, **99**.[44] Despite difficulties with the air-mediated ring opening of **100**, attempts were made here with **102** in refluxing chlorobenzene. After removal of the chlorobenzene solvent, a bright yellow impurity was found *via* TLC. However, due to differences in solubility between **101** and **103**, attributed to the di-brominated substitution of **103**, precipitation from diethyl ether yielded an analytically pure sample of **103** for further synthesis. The bright yellow impurity was soluble in the ether solvent, and this may dispute earlier assumptions that the yellow impurity resulted from the incomplete ring opening. Attempts to purify and identify the yellow impurity by NMR and mass spectrometry were unsuccessful. The successful generation of the pyridazine ring product 1,4-bis(4-bromophenyl)dibenzo[f,h]phthalazine, **95**, was achieved once again from the reaction of **103** with hydrazine hydrate (Scheme 4.3). These products are characterised by HRMS, with the data summarised in Table 4.1.

Table 4. 1 High resolution mass spectrometry analysis of **101**, **94**, **103**, and **95**. (ESI, CH_2Cl_2)

Compound	Molecular Formula	Calculated Mass $[M+H]^+$	m/z
101	$C_{28}H_{18}O_2$	387.1385	409.1202 [M+Na]
94	$C_{28}H_{18}N_2$	383.1548	383.1538
103	$C_{28}H_{16}Br_2O_2$	542.9595	564.9423 [M+Na]
95	$C_{28}H_{16}Br_2N_2$	538.9758	538.9757

4.2.3 Multinuclear NMR Analysis of 94

As **101** is already present in the literature, it's full NMR characterisation will not be included here. However, while **94** also has literature references, no NMR characterisation was found, and as such, **94** was spectroscopically characterised by multinuclear NMR studies, and the ATR-FTIR as part of this work (See Chapter 5, Experimental). The ^1H and $^{13}C\{^1H\}$ NMR spectra in $CDCl_3$ are shown in Figure 4.5. The symmetrical structure of **94** aids in the assignment of the respective ^1H and $^{13}C\{^1H\}$ signals. However, due to the small number of signals, selective 1D TOCSY experiments were required to fully assign the spectra (Figure 4.6). The four phenanthrene signals are clearly visible in the ^1H spectrum, as two doublets, and two triplets. The most downfield signal corresponding to H1 is observed at δ 8.61 ppm. The phenanthrene proton signals follow a pattern of H1, H4, H3, and H2, with the free phenyl proton signals once again following the *o*, *m*, *p* sequence. As the pyridazine ring is electron

deficient, the signals of the free phenyl act in a similar manner as to that of an electron withdrawing substituent. Due to the highly symmetrical nature of **94**, the HSQC (Figure 4.7(a)) facilitated the successful assignment of the $^{13}C\{^{1}H\}$ spectrum (Figure 4.5). However, this high symmetry also resulted in the HMBC spectrum being of little use (Figure 4.7(b)).

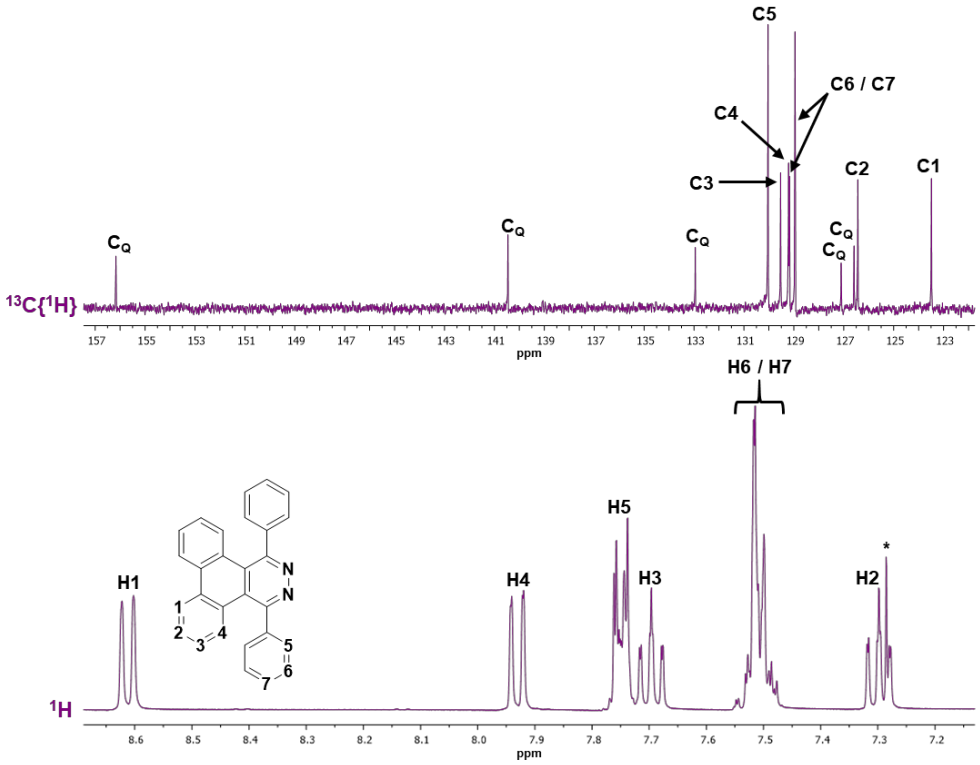

Figure 4. 5 $^{13}C\{^{1}H\}$ and ^{1}H NMR spectra of **94**. ($CDCl_3$. 400 MHz for ^{1}H, 100 MHz for $^{13}C\{^{1}H\}$. RT). C_Q = quaternary carbons.

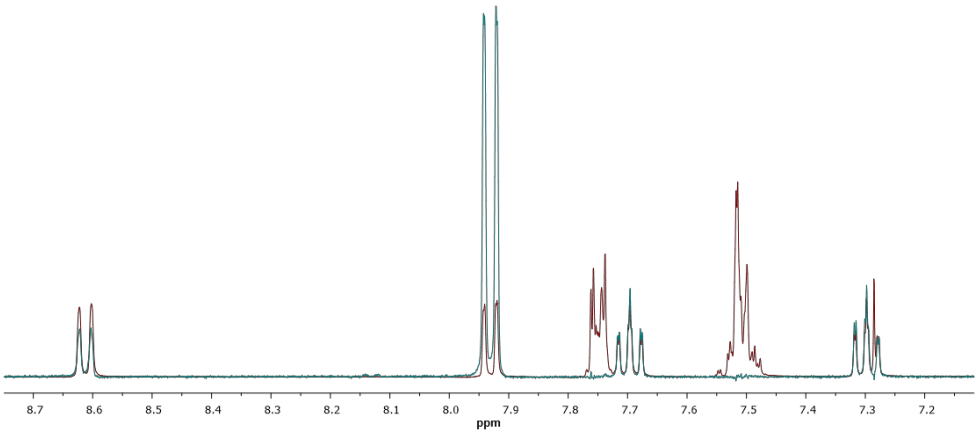

Figure 4. 6 Selective 1D TOCSY experiments revealing the spin systems of **94**, with full aromatic ^{1}H region (maroon spectrum). ($CDCl_3$. 400 MHz for ^{1}H. RT)

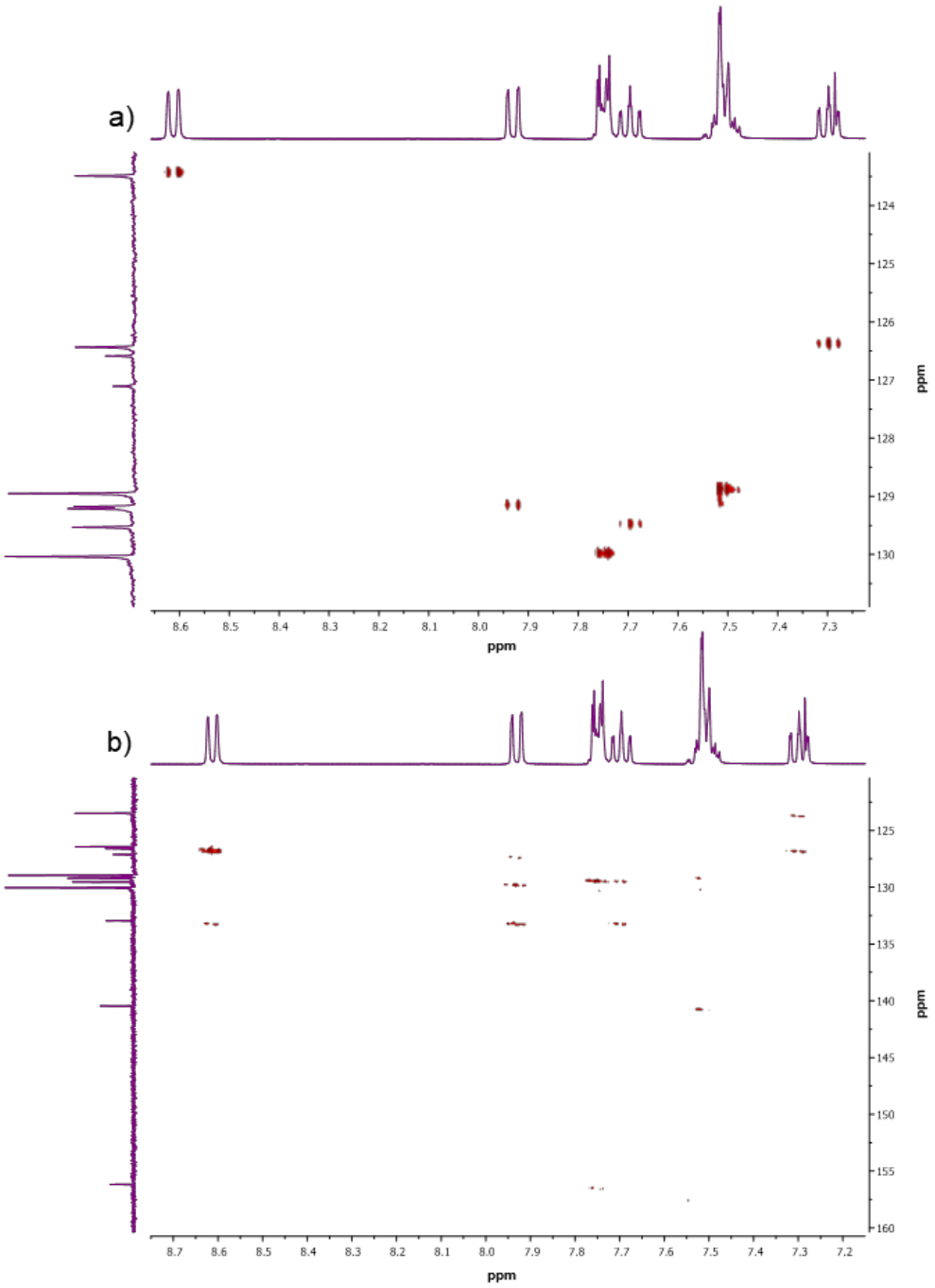

Figure 4. 7 (a) HSQC spectrum of **94** showing the direct ^{1}H and $^{13}C\{^{1}H\}$ signal correlations. (b) HMBC spectrum of **94** showing long range ^{1}H and $^{13}C\{^{1}H\}$ signal correlations ($CDCl_3$. 400 MHz for ^{1}H, 100 MHz for $^{13}C\{^{1}H\}$. RT)

4.2.4 Multinuclear NMR Analysis of 103

The diketone-dibromo precursor **103** is a novel compound, and as such, it was spectroscopically characterised by multinuclear NMR studies, and the ATR-FTIR (See Chapter 5, Experimental). The ^{1}H and $^{13}C\{^{1}H\}$ NMR spectra in $CDCl_3$ are shown in Figure

4.8. The symmetrical structure of **103** aids in the assignment of the respective ^{1}H and $^{13}C\{^{1}H\}$ signals. However, due to an even smaller number of signals, from the para-bromo substitution, selective 1D TOCSY experiments were again required to fully assign the spectra (Figure 4.9).

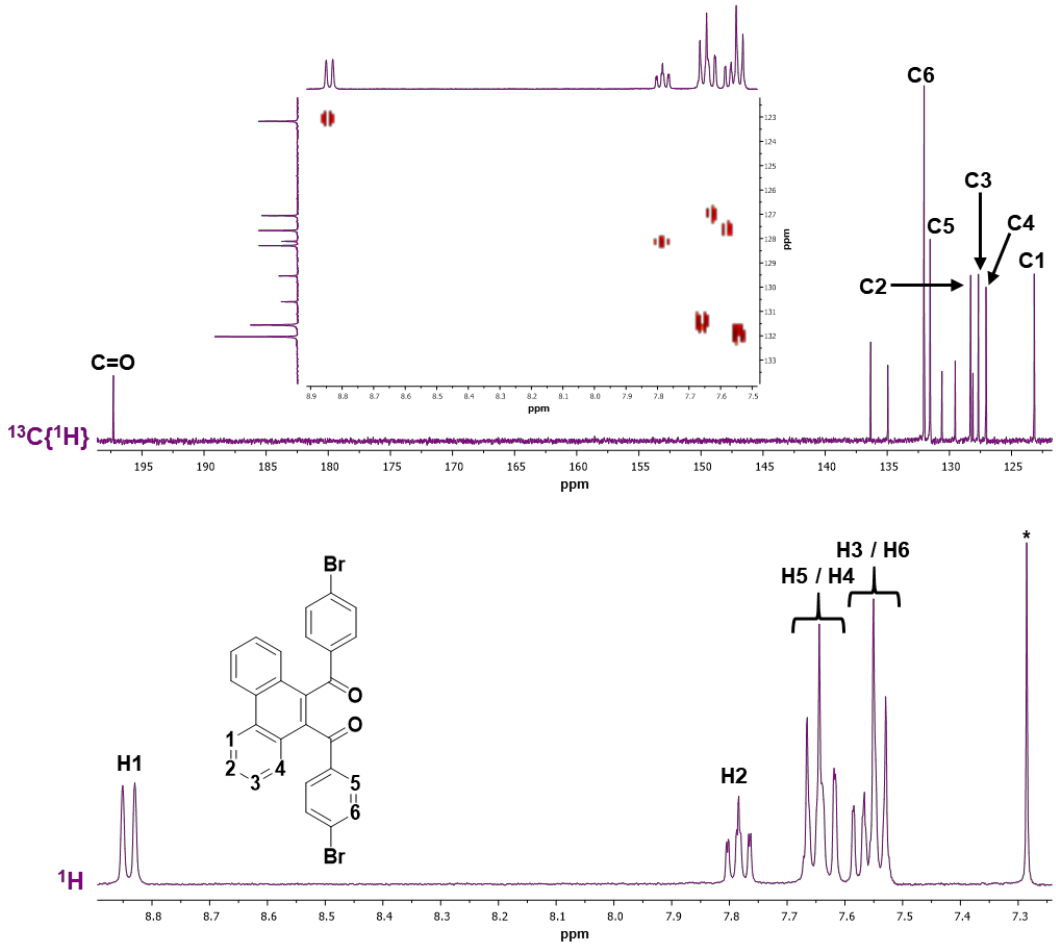

Figure 4. 8 $^{13}C\{^{1}H\}$ and ^{1}H NMR spectra of **103**. HSQC inset. ($CDCl_3$. 400 MHz for ^{1}H, 100 MHz for $^{13}C\{^{1}H\}$. RT). Unlabelled peaks in the $^{13}C\{^{1}H\}$ spectrum are quaternary carbons.

The four phenanthrene signals are no longer clearly visible in the ^{1}H spectrum, with only the signals for H1 and H2 readily distinguishable. The most downfield signal corresponding to H1 is observed at δ 8.84 ppm. H2, appearing at δ 7.30 ppm for **94**, appears at a downfield shift of δ 7.78 ppm. The free phenyl proton signals, expected as two doublet signals, overlap with the phenanthrene ring signals in the ^{1}H spectrum. Due to the highly symmetrical nature of **103**, the HSQC (Figure 4.8) facilitated the successful assignment of the $^{13}C\{^{1}H\}$ spectrum (Figure 4.8).

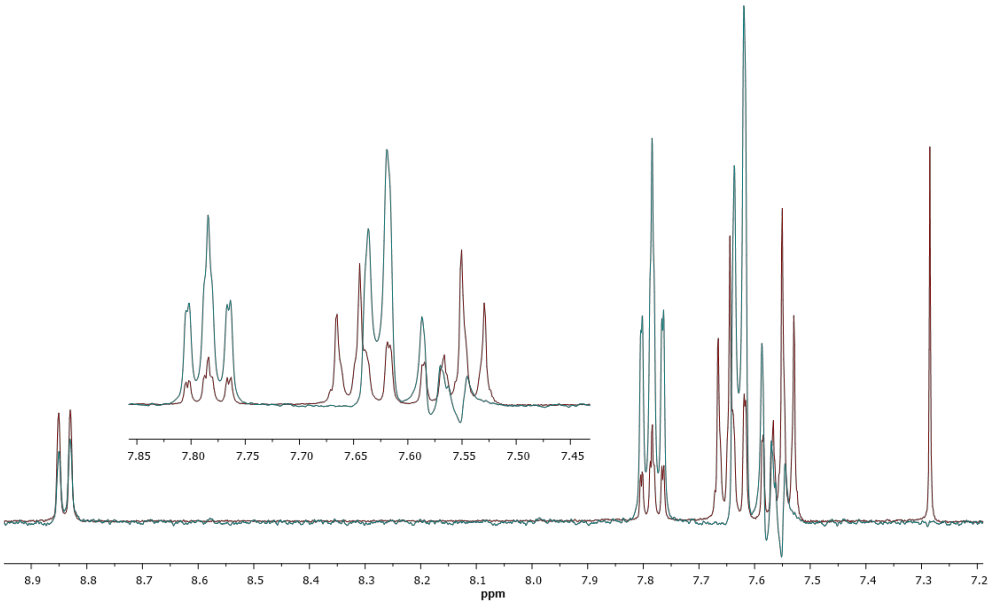

Figure 4. 9 Selective 1D TOCSY experiments revealing the spin systems of **103**, with full aromatic ^{1}H region (maroon spectrum). ($CDCl_3$. 400 MHz for ^{1}H. RT)

4.2.5 Multinuclear NMR Analysis of 95

The dibromo-pyridazine compound **95** is also a novel compound, and as such, it was spectroscopically characterised by multinuclear NMR studies, and the ATR-FTIR (See Chapter 5, Experimental). The ^{1}H and $^{13}C\{^{1}H\}$ NMR spectra in $CDCl_3$ are shown in Figure 4.10. The symmetrical structure of **95** aids in the assignment of the respective ^{1}H and $^{13}C\{^{1}H\}$ signals (Figure 4.10). The four phenanthrene proton signals are well resolved, and confirmed through use of a selective 1D TOCSY experiment (Figure 4.11). The most downfield signal corresponding to H1 is observed at δ 8.63 ppm. Similarly to **94**, the signal corresponding to H2, appears once again at δ 7.37 ppm. The free phenyl proton signals, expected as two doublet signals, appear as one large singlet. Use of the integration value, and the low number of signals in the spectrum confirm their overlapped nature. Use of the HSQC (Figure 4.10, inset) also facilitates conformation of this overlapping. The HSQC spectrum also facilitated the successful assignment of the $^{13}C\{^{1}H\}$ spectrum (Figure 4.10).

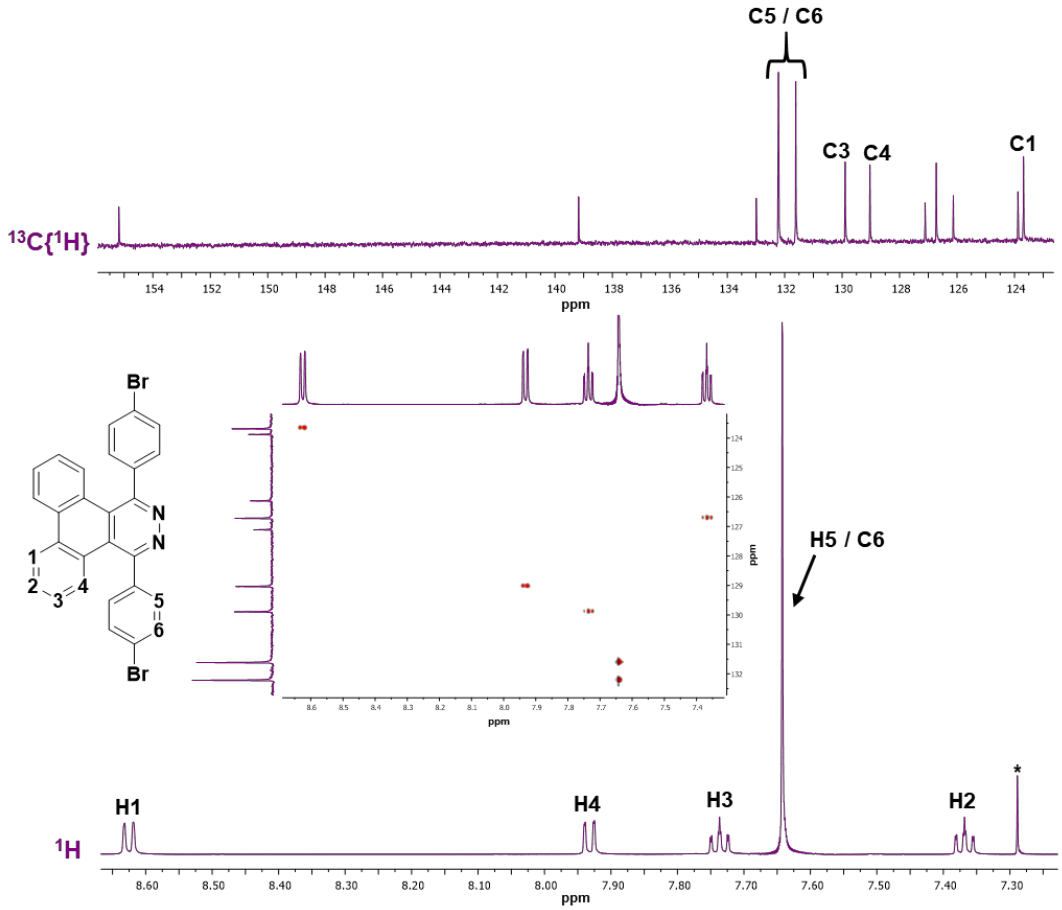

Figure 4. 10 $^{13}C\{^{1}H\}$ and ^{1}H NMR spectra of **95**. HSQC inset. ($CDCl_3$. 400 MHz for ^{1}H, 100 MHz for $^{13}C\{^{1}H\}$. RT). Unlabelled peaks in the $^{13}C\{^{1}H\}$ spectrum are quaternary carbons.

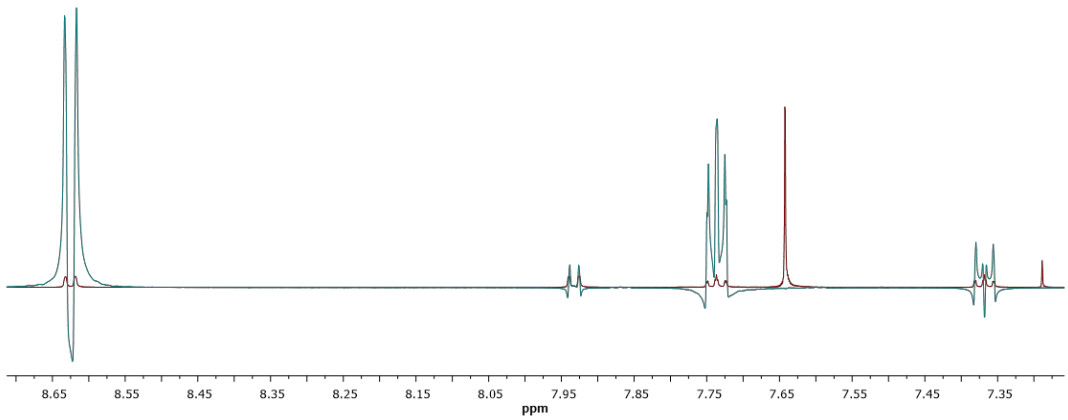

Figure 4. 11 Selective 1D TOCSY experiments revealing the spin systems of **95**, with full aromatic ^{1}H region (maroon spectrum). ($CDCl_3$. 400 MHz for ^{1}H. RT)

4.2.6 Synthesis & Structural Characterisation of 96 and 97

4.2.7 Attempted Syntheses of 96 and 97

Further to the successful synthesis of **95**, the syntheses of two Donor-Acceptor-Donor compounds were undertaken. As the phenanthrene-pyridazine product **95** is substituted at the para-positions of the free phenyl rings, the simplest method of modification (addition of the respective donor compound) to these positions was *via* cross-coupling reactions. Two donors were chosen to study these novel systems, the common triphenylamine system, 4-ethynyl-N,N-diphenylaniline, **105**, and the less common pyrene system, 1-ethynylpyrene, **106**. Scheme 4.4 shows the successful Sonogashira cross coupling reactions of **95** and **106**, and the unsuccessful synthesis of **96**.

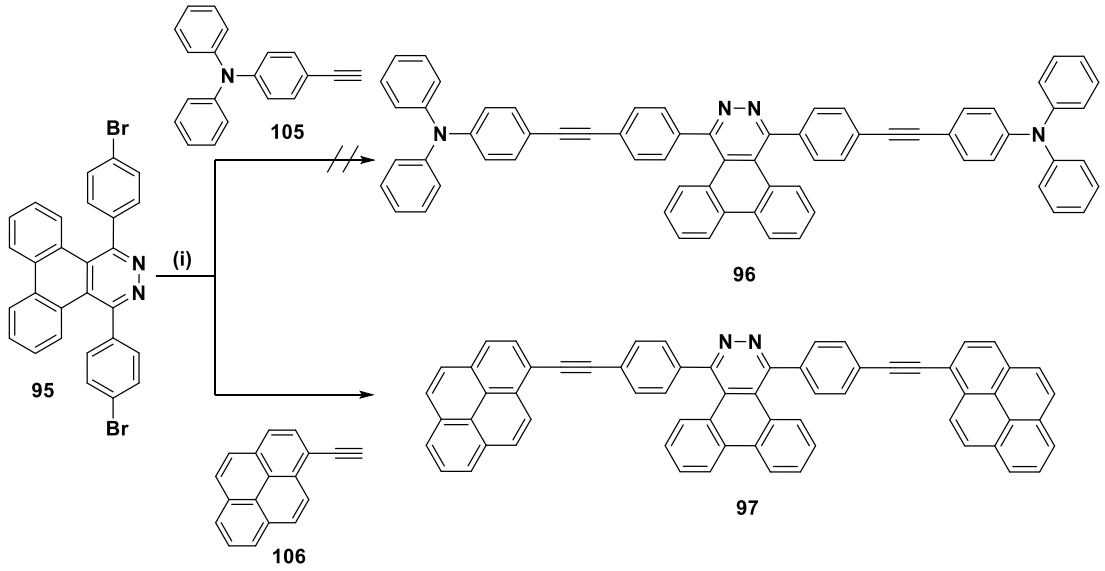

Scheme 4. 4 Attempted syntheses towards **96** and **97**. (i) $Pd(PPh_3)_4$, PPh_3, CuI, DMF, triethylamine, 80 °C, 16 h, Ar. Yield of **97** = 7 %.

Despite confirmation of the successful synthesis of the di-triphenylamine product **96** by HRMS (Table 4.2), efforts to purify the crude reaction mixture by a number of column chromatography methods failed. This was compounded by the apparent decomposition of the product using a simple 2D TLC stability study. Here, a normal TLC run is undertaken, before the TLC plate is allowed dry and turned 90°. The TLC plate is then allowed run once more, with diagonal spots revealing unstable compounds. On repeat of the experiment, a similar issue was found, with the highly luminescent material unable to be sufficiently purified.

The di-ethynylpyrene product however, **97**, was successfully synthesised and characterised by HRMS and multinuclear NMR studies (Table 4.2). Despite using a copper-free Sonogashira cross coupling methodology, and significant care being taken to removal O_2 from the reaction mixture *via* the freeze-pump-thaw method, considerable amounts of the respective homocoupled (Glaser coupled) products were found after each reaction.[45] Use of silica-based column chromatography, using $CHCl_3$ → 50:50 $CHCl_3$:EtOAc as the mobile phase, yielded **97** with a small amount of impurities. No gradient was used. Precipitation from diethyl ether allowed the collection of a pure sample for photophysical, electrochemical, and thermal stability studies.

Table 4. 2 High resolution mass spectrometry analysis of **96** and **97**. (ESI, CH_2Cl_2)

Compound	Molecular Formula	Calculated Mass $[M+H]^+$	m/z
96	$C_{68}H_{44}N_4$	917.3644	916.3599 [M][a]
97	$C_{64}H_{34}N_2$	831.2800	831.2769

[a] MALDI-TOF

4.2.8 Multinuclear NMR Analysis of 97

The di-ethynylpyrene product **97** is the first D-π-A-π-D architecture, comprising a pyrene donor, a phenanthrene-pyridazine acceptor, with ethynyl π-spacers. As such, it was spectroscopically characterised by multinuclear NMR studies, and the ATR-FTIR (See Chapter 5, Experimental). The ^1H and $^{13}C\{^1H\}$ NMR spectra in $CDCl_3$ are shown in Figure 4.12. As pyrene signals are notoriously difficult to assign, due to the high overlap of its respective proton signals, the symmetrical structure of **97** did not necessarily aid the assignment of the respective ^1H and $^{13}C\{^1H\}$ signals of the total compound. Despite the good resolution of the ^1H spectrum, the four phenanthrene proton signals are not well resolved, and are confirmed through use of a number of selective 1D TOCSY experiments (Figure 4.13). The most downfield signal is observed at δ 8.75 ppm, and is pyrene-based. The signal corresponding to H1 is observed at δ 8.67 ppm. The signal corresponding to H2, appears at δ 7.41 ppm, with H3 appearing at δ 7.77 ppm. The free phenyl proton signals, expected as two doublet signals, appear as one large singlet at δ 7.88 ppm. Use of the integration value is once again used to confirm their overlapped nature. Use of the HSQC (Figure 4.14) also facilitates conformation of this overlapping, and allowed the successful assignment of the $^{13}C\{^1H\}$ spectrum (Figure 4.12). The two spin system of the pyrene ring coupled to the acetylene linker

is identified through use of the HMBC, with a selective 1D TOCSY experiment revealing the second signal (Figure 4.13)

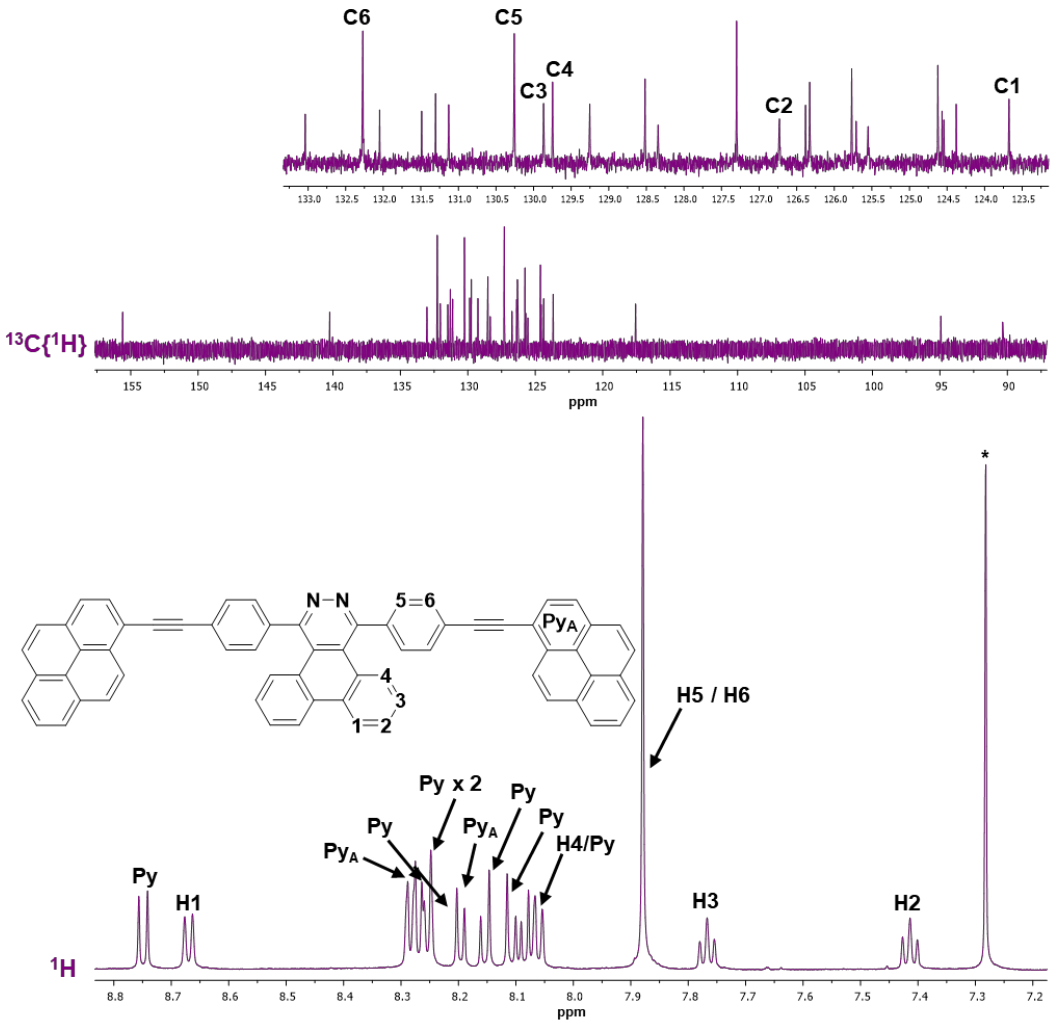

Figure 4. 12 $^{13}C\{^{1}H\}$ and ^{1}H NMR spectra of **97**. Zoomed region inset. ($CDCl_3$. 400 MHz for ^{1}H, 100 MHz for $^{13}C\{^{1}H\}$. RT). Unlabelled peaks in the $^{13}C\{^{1}H\}$ spectra are quaternary carbons.

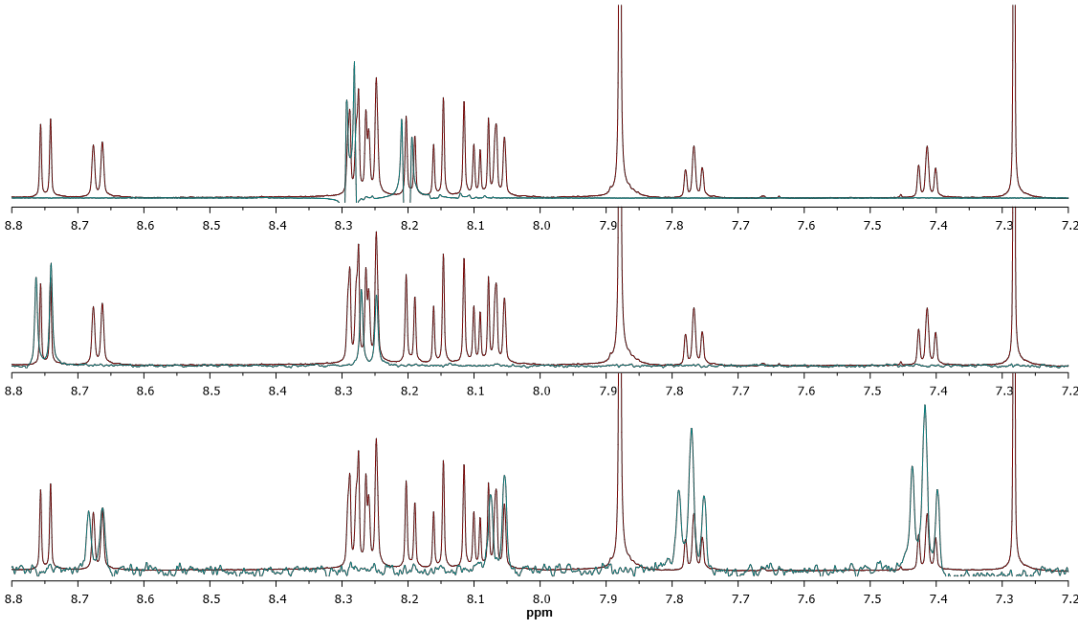

Figure 4. 13 Selective 1D TOCSY experiments (green) revealing the spin systems of **97**, with full aromatic ^{1}H region (maroon spectrum). ($CDCl_3$. 400 MHz for ^{1}H. RT)

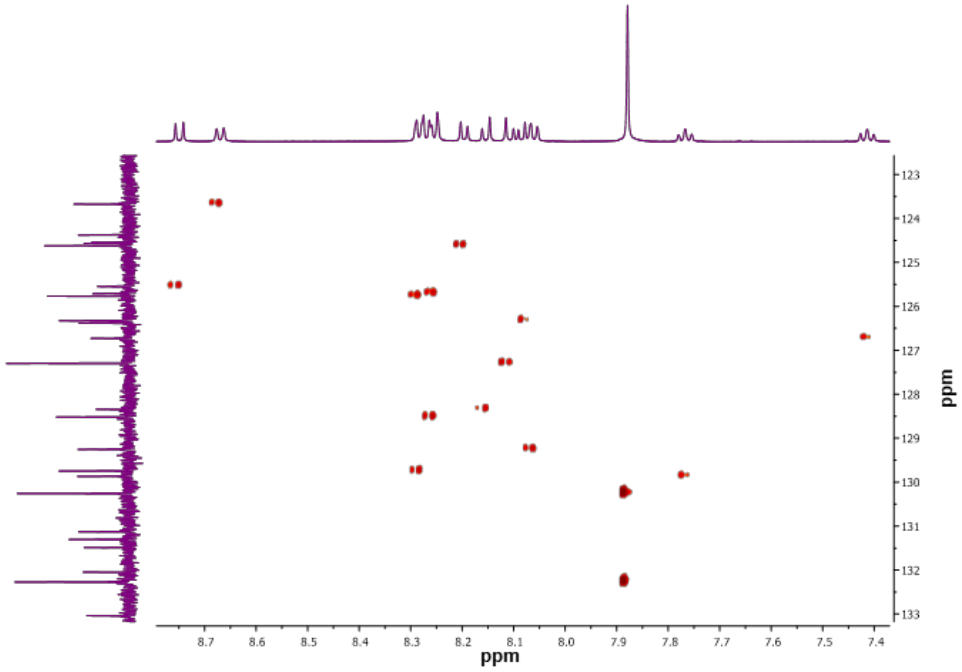

Figure 4. 14 HSQC spectrum of **97** showing the direct ^{1}H and $^{13}C\{^{1}H\}$ signal correlations. ($CDCl_3$. 400 MHz for ^{1}H, 100 MHz for $^{13}C\{^{1}H\}$. RT)

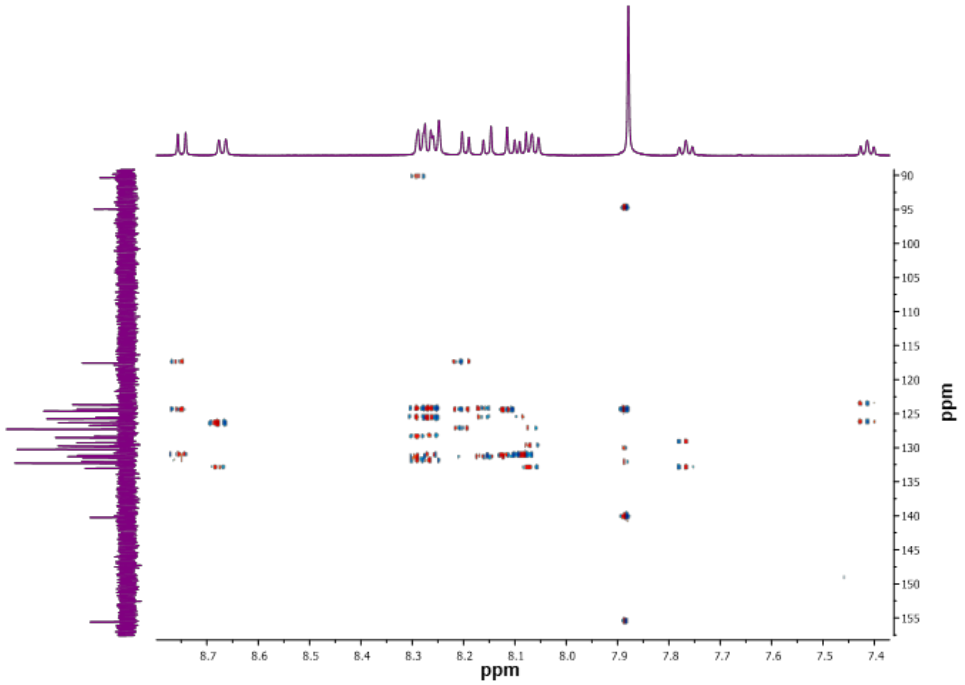

Figure 4. 15 HMBC spectrum of **97** showing the long range ^{1}H and $^{13}C\{^{1}H\}$ signal correlations. ($CDCl_3$. 400 MHz for ^{1}H, 100 MHz for $^{13}C\{^{1}H\}$. RT)

4.3 Electrochemical Investigations of 94 and 97

Cyclic Voltammetry (CV) studies were carried out on $1x10^{-4}$ M solutions of **94** and **97**, in CH_2Cl_2 (0.1 M nBu_4NPF_6). CV studies at concentrations of 1mM solutions did not give satisfactory resolution of the voltammogram. Cyclic voltammograms were recorded using an Ag/AgCl reference electrode, a Pt wire counter electrode, and a glassy carbon working electrode.

Figure 4.16(a)-(b) shows the oxidative and reductive cyclic voltammograms of **94** and **97**. The oxidation of **94** is irreversible at +1.94 V, with a similar value observed for **97** at +1.95 V. This suggests the HOMO of **94** and **97** is localised in the phenanthrene ring system, yet localisation of the HOMO on the pyrene moieties for **97** cannot be ruled out, as not enough information is gained by the relatively crude nature of the CV experiment. The reductive cyclic voltammogram for **94** show a single reversible process at -1.76 V. This is postulated as a one electron reduction to the central pyridazine ring of **94**. This would suggest the LUMO of **94** is localised across the central pyridazine ring, as well as the phenanthrene ring system. Table 4.3 summarises the electrochemical data of each compound. The reductive cyclic voltammogram of **97** appears less resolved, and does not yield sufficient information about the processes occurring at the LUMO energy of **97**.

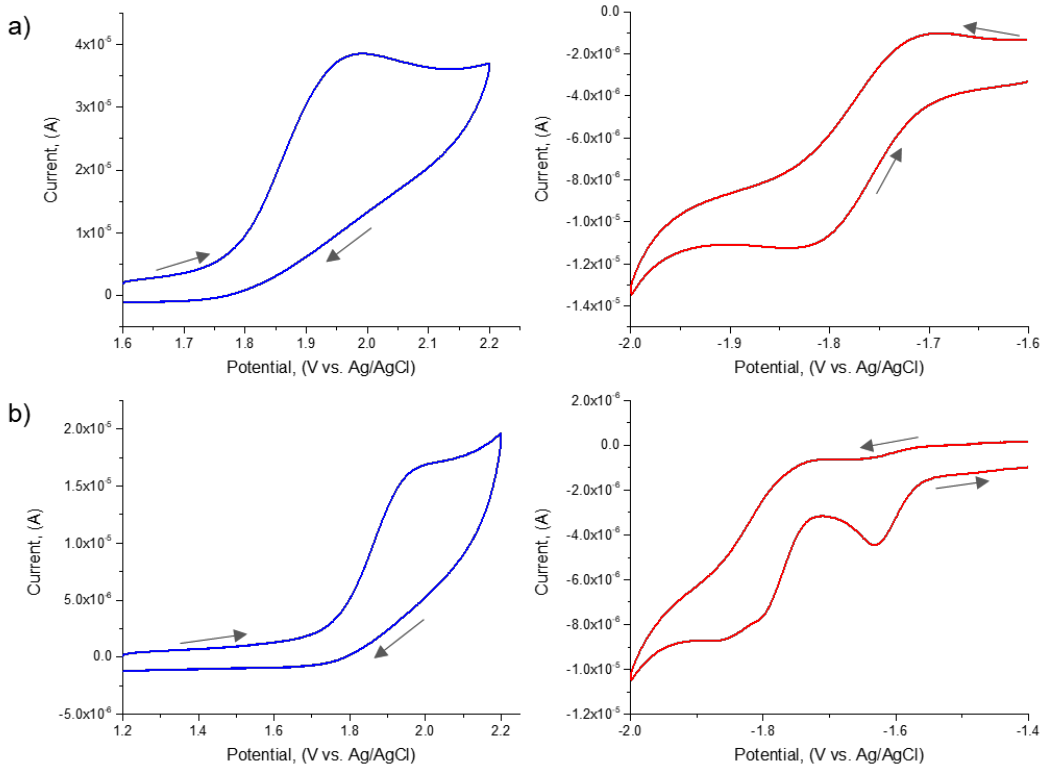

Figure 4. 16 (a) Oxidative (blue) and reductive (red) cyclic voltammograms of **94**. (b) Oxidative (blue) and reductive (red) cyclic voltammograms of **97**. CH_2Cl_2 and 0.1 M $TBAPF_6$. Scan rate = 0.1 V/s.

Table 4. 3 Electrochemical data for **94** and **97** (CH_2Cl_2. 0.1 M $TBAPF_6$. Scan rate = 0.1 V/s.). Samples prepared in air and purged with N_2 for 10 mins and for the duration of measurement.

Compound	**Oxidation**	**Reduction**
	E_{pc}/V	**$E_{1/2}$/V, [ΔE_p/mV]**
94	+1.94	-1.76 [110]
97	+1.95	-1.63 [E_{pa}], -1.87 [E_{pa}]

4.4 Photophysical Investigations of 94 and 97

4.4.1 UV-visible Absorption Spectra of 94 and 97

The UV-visible absorption spectra of **94** and **97** are shown in Figures 4.17 and 4.18, with data summarised in Table 4.4.

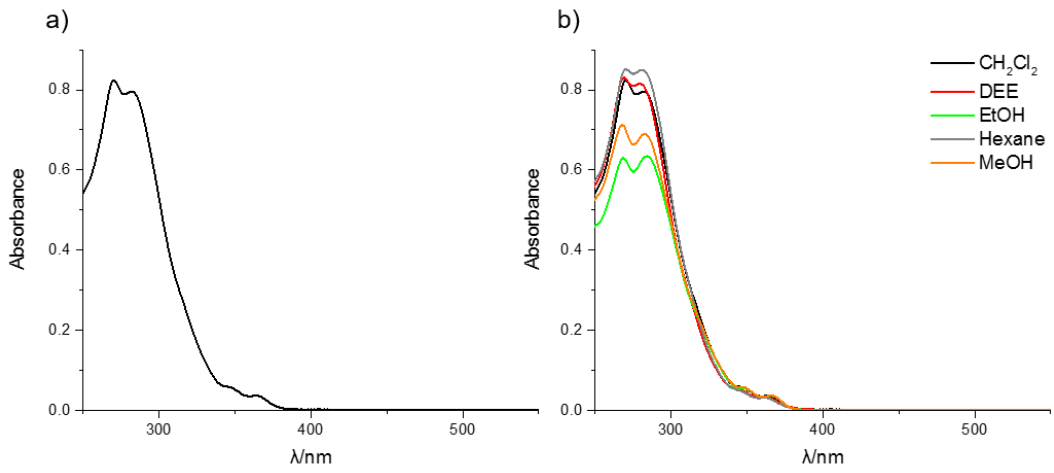

Figure 4. 17 (a) UV-visible absorption spectra of **94** in CH_2Cl_2 (10^{-5} M). (b) Solvatochromism studies (UV-visible absorption spectra) of **94** in CH_2Cl_2, DEE, EtOH, Hexane, and MeOH (10^{-5} M). DEE = Diethyl ether.

Four absorptions are seen for **94** (Figure 4.17(a)), with the two strongest absorptions occurring at λ_{abs} = 270 nm and λ_{abs} = 282 nm. These high energy absorptions are assigned to the π-π* transitions within the phenanthrene ring system, and the pendant phenyl rings. The much weaker bands at λ_{abs} = 345 nm and λ_{abs} = 365 nm, and are also assigned as π-π* transitions.

Solvatochromism studies were performed for **94**, with the respective UV-visible profiles given in Figure 4.17(b). Solvents chosen were CH_2Cl_2, EtOH, MeOH, diethyl ether (DEE), and hexane. Maintaining a concentration of 10^{-5} M for all solutions, no significant change was seen for the peak emission wavelength, indicating that the ground state energy of **94** is unaffected by the solvent polarity.

The absorption spectra of **97** (Figure 4.18(a)) show distinctive ethynylpyrene-based transitions at λ_{abs} = 380 nm and λ_{abs} = 400 nm. These are assigned as π-π* transitions within the pyrene rings. Further higher energy transitions are observed at λ_{abs} = 273 nm and λ_{abs} = 285 nm, and are assigned to the π-π* transitions within the phenanthrene ring system, and the pendant phenyl rings.

Unlike for **94**, solvatochromism studies (Figure 4.18(b)) revealed a significant change in the ground state energy for **97** in MeOH. Solvents chosen were CH_2Cl_2, EtOH, MeOH, diethyl ether (DEE), THF, and Cyclohexane, whilst maintaining a concentration of 10^{-5} M for all solutions.

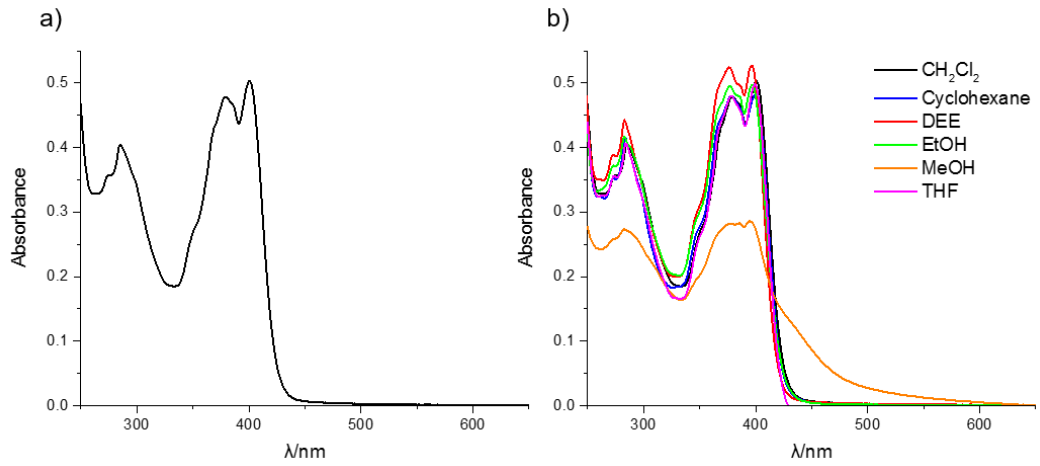

Figure 4. 18 (a) UV-visible absorption spectra of **97** in CH_2Cl_2 (10^{-5} M). (b) Solvatochromism studies (UV-visible absorption spectra) of **97** in CH_2Cl_2, Cyclohexane, DEE, EtOH, MeOH, and THF (10^{-5} M). DEE = Diethyl ether.

Table 4.4 UV-visible spectral data for compounds **94** and **97** in CH_2Cl_2 at RT (10^{-5} M).

Compound	**λ_{abs}/nm** **[ϵ x 10^4/M^{-1} cm^{-1}]**
94	270 [8.20], 282 [7.96], 345 [0.58], 365 [0.36]
97	273 [3.56], 285 [4.04], 380 [4.81], 400 [5.04]

4.4.2 Emission Studies of 97

As compound **94** is non-emissive, no emission studies were carried out. However, **97** is emissive on excitation at λ_{ex} = 400 nm, and the steady state emission profiles in a number of solvents were recorded (Figure 4.19(a)). Upon excitation at this wavelength, a single broad emission band is observed at λ_{em} = 485 nm in CH_2Cl_2 (black line). Due to the significant change in the absorption profile for **97** in solvatochromism studies, further emission-based solvatochromism studies were performed for **97**, with the respective profiles given in Figure 4.19(a). Solvents chosen were CH_2Cl_2, MeOH, EtOH, Cyclohexane, DEE, and THF. Maintaining a concentration of 10^{-5} M for all solutions, a red shift in the emission maximum was observed on use of high polarity solvents. Whilst use of CH_2Cl_2 resulted in an emission at λ_{em} = 485 nm, EtOH gave a red shifted emission of λ_{em} = 505 nm, with MeOH giving a red shifted emission of λ_{em} = 525 nm. This solvatochromic behaviour was used as the first characteristic to tentatively assign the emission of **97** as charge transfer in nature, which is a required characteristic for D-A-D behaviour. Broad and featureless emission profiles are seen

for a large number of fully-organic TADF compounds in the literature.[25,46–48] As the emission profiles of **97** are broad and featureless in all of the solvents studied as part of the solvatochromism studies (Figure 4.19), this lent further credibility to the emission being of charge transfer character in nature.

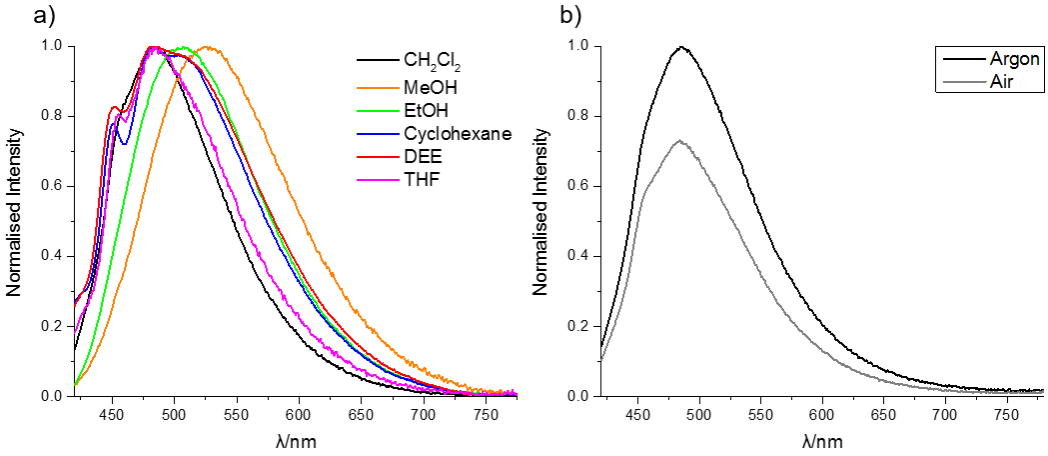

Figure 4. 19 (a) Solvatochromism studies (normalised emission spectra) of **97** in CH_2Cl_2, MeOH, EtOH, Cyclohexane, DEE, and THF. (10^{-5} M). DEE = Diethyl ether. (b) Degassing studies (emission spectra) of **97** in CH_2Cl_2 in air and Ar. Degassed *via* three cycles of freeze-pump-thaw. (10^{-5} M).

As **97** was designed towards investigation of phenanthrene-pyridazine as acceptor components in TADF materials, further study of the emission intensity of **97** in air *versus* Ar were undertaken. As TADF materials access the triplet state of a molecule, before thermal repopulation of the singlet state for fluorescence, any oxygen present has the potential to interact with the triplet state, quenching the molecules luminescence.[49] Figure 4.19(b) clearly demonstrates the effect of atmospheric oxygen on the fluorescence intensity of **97**, reducing the intensity by approximately 25 %. Due to the correspondingly high energy value of the emission wavelength, phosphorescence is not expected to occur in **97** at room temperature.[49] This decrease in emission intensity further points to the emission of **97** being of charge transfer character. However, due to the presence of pyrene within the molecular structure of **97**, generation of the pyrene-pyrene excimer (excited dimer pair)[50] could not be ruled out. The pyrene excimer is known to emit as a broad and featureless band,[50] with the λ_{max} of the excimer also being sensitive to changes in solvent polarity.[51] This inevitably complicates the discernment of charge transfer and TADF behaviour in systems with pyrene within the molecule structure. Dilution studies offer a simple solution to this problem, with the excimer expected to form in high concentrations (often referred to as saturation studies in the

literature), and not be present in very dilute concentrations. As the excimer can form as part of a static or dynamic process, the high dilution studies dramatically reduce intermolecular interactions.

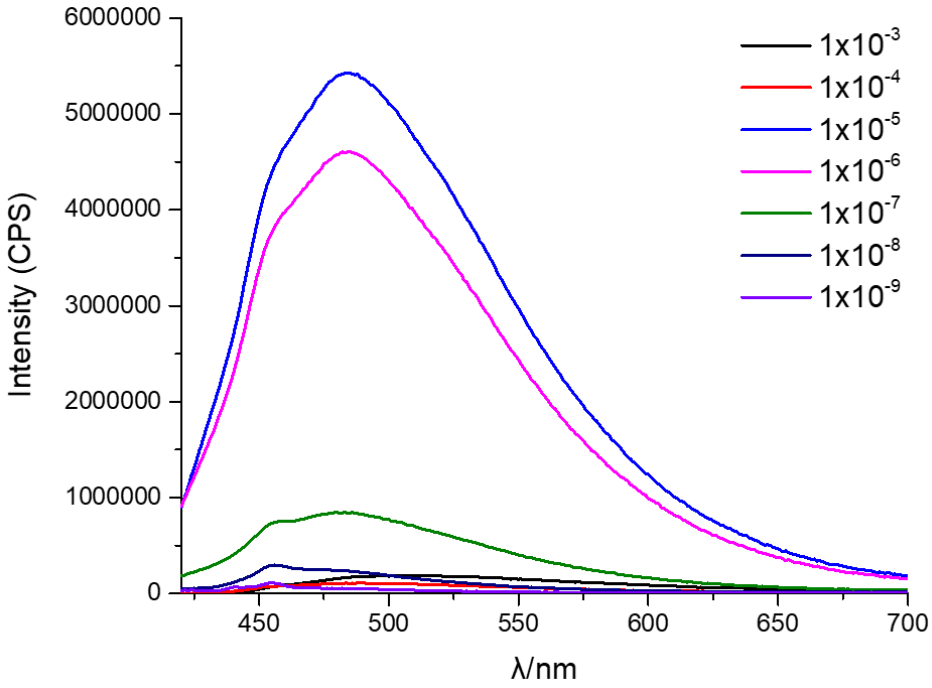

Figure 4. 20 Dilution studies of **97** in CH_2Cl_2 (λ_{ex} = 400 nm).

In an attempt to discern if the pyrene-pyrene excimer contributed to the emission profile of **97**, dilution studies were carried out ranging from a concentration of $1x10^{-3}$ M to $1x10^{-9}$ M (Figures 4.20 and 4.21). Figure 4.20 shows the effect of concentration of the emission intensity of **97**. Very concentrated and very dilute samples show almost no luminescence, with the middle concentration values of $1x10^{-5}$ and $1x10^{-6}$ M showing the expected fluorescence of the previous solvatochromic studies. This can be easily explained through reabsorption factors at the higher concentrations, and insufficient amounts of the compound at much lower concentrations. However, when the emission profiles are normalised and plotted together, a much different picture emerges (Figure 4.21).

Figure 4.21(a) shows an overlay of the emission profiles of **97** at the different concentration values, normalised to 1. The concentration dependence of the peak at λ_{em} = 485 nm is immediately apparent, with the large and featureless band constricting in size dramatically going from high concentrations to the much lower concentrations. Figure 4.21(b) features the same information but in a "waterfall" construction, which clearly visualises the stepwise reduction of the peak's width as the concentration is lowered. In the original solvatochromism

studies (Figure 4.19(a)), a faint shoulder at λ_{em} = 455 nm is seen in the CH_2Cl_2 sample. In the dilution studies, this shoulder becomes increasingly prominent as the concentrations of **97** are lowered, before becoming the λ_{max} for **97** once a concentration value of $1x10^{-8}$ M is reached. These dilution studies indicate that a pyrene-pyrene excimer is responsible for a significant proportion of the compound's emission profile at the standard studied concentration of $1x10^{-5}$ M.

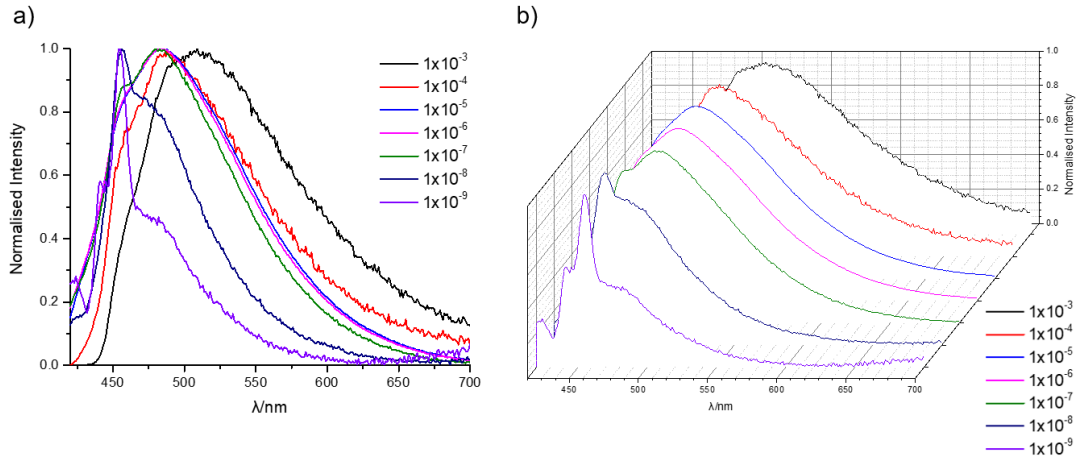

Figure 4. 21 (a)-(b) Dilution studies (normalised intensity) of **97** in CH_2Cl_2 (λ_{ex} = 400 nm).

As the emission profile of **97** shows characteristics of both TADF charge transfer character, and the pyrene-pyrene excimer, further attempts to reveal the true nature of the emissive behaviour were undertaken through emission quantum yield, and the excited state lifetime measurements. As a TADF charge transfer transition and a pyrene-pyrene excimer would be expected to have different quantum yields and lifetime values, it was hoped that these studies would be capable of confirming that both processes were occurring for **97**. The pyrene excimer is expected to have a large emission quantum yield.[52]

The fluorescence quantum yield was measured using the single-point relative method, using quinine sulfate as the reference, in CH_2Cl_2 at RT. The single-point method was utilised through calculation of the integrated emission intensities of both **97** and quinine sulfate, measured on the same instrument, with identical entrance and exit slit values. Optically dilute samples (Abs = ~0.1) of both **97** and quinine sulfate were prepared. The quantum yield of **97** *via* the single-point method was calculated and is included in Table 4.5.

Attempts to collect the excited state lifetime of **97** in air and N_2 were unsuccessful. Data fitting using a number of exponential decays did not give meaningful values for further study or comparison.

Table 4. 4 Emission data for **97** in CH_2Cl_2 at RT (10^{-5} M).

Compound	λ_{em}/nm	τ/ns (λ_{ex}/nm; λ_{em}/nm)	Φ
97	485 (CH2Cl2), 505 (EtOH), 525 (MeOH)	-- / --	0.02 (Ar), 0.008 (air)

Analysis of all of the results together reveals conflicting data. As no excited state lifetimes could be contained, the low emission quantum yield would indicate that the pyrene excimer is not the dominant emissive process for **97**. However, the dilution studies indicate the opposite, with the emission band appearing to be very dependent on concentration, suggesting a significant excimer contribution. As the solvatochromism studies yield the same results for both TADF charge transfer, and pyrene-pyrene excimer emission processes, further studies are therefore necessary to assign if **97** is capable of TADF behaviour, or if the pyrene-pyrene excimer renders this structural design problematic going forward. While a number of publications deliberately attempt to prevent excimer formation, recent work by Mallesham *et al.*, reveals a dramatic increase in the electron and hole mobility values of TADF materials when pyrene excimers are formed within a thin film.[53] This demonstrates that there is a significant opportunity to include pyrene within future TADF compounds, with this work being the first study to utilise pyrene in a D-A-D structure with a novel pyridazine acceptor component.

4.5 Thermal Analysis of 94 and 97

To estimate the thermal stability of phenanthrene-pyridazine ring systems as acceptors for TADF materials, a thermogravimetric analysis (TGA) plot was recorded for both **94** and **97**. The first compound, **94**, was added to a pre-weighed ceramic crucible, and its mass was recorded. Both mass measurements were undertaken in the furnace. The crucible was heated to 30 °C and held for one minute. Following this stage, the crucible was heated to 120 °C at a rate of 10 °C per minute, and was held at this temperature for 60 minutes to allow for the evaporation of any remaining high boiling-point solvents. On completion of this isothermal step, the crucible was heated to 800 °C at a rate of 10 °C per minute, before cooling to ambient temperature. The cooling rate was not controlled. All heating was carried out under a constant stream of N_2 gas.

Analysis of the TGA plot reveals **94** undergoes thermal decomposition at 350 °C. This dramatic mass loss is likely to be from product evaporation. As the system is not under

vacuum, and similar PAH-type compounds demonstrate melting points at these temperatures at ambient pressure, the probable collapse of the pyridazine ring structure is postulated here for the rapid decomposition of **94**, before evaporation of the remaining PAH compounds. This was expected further to similar results seen for **78**. The thermal stability of **94** of 350 °C means that these compounds may find use as acceptor components in TADF materials (Figure 4.22).

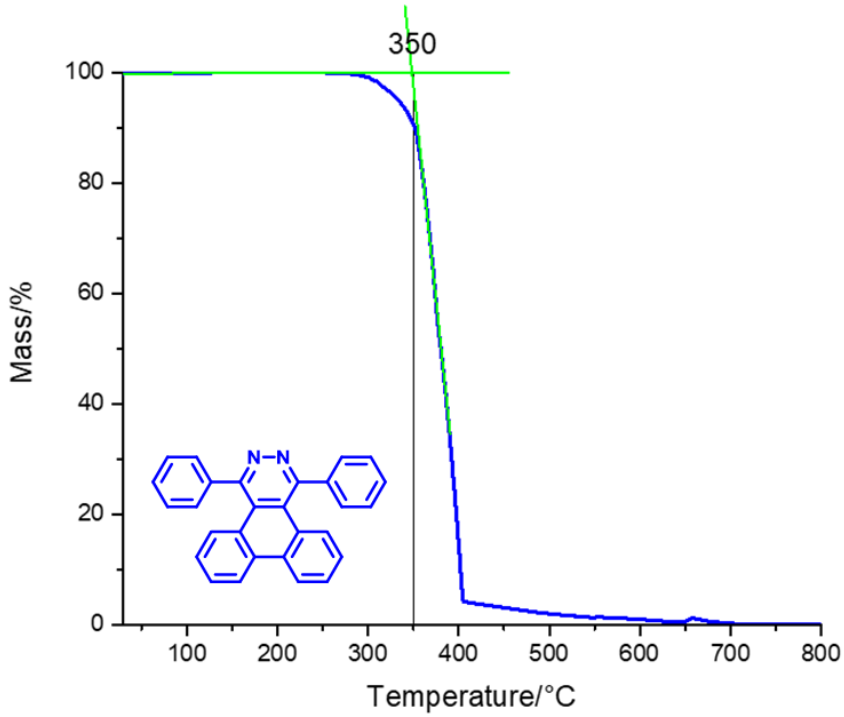

Figure 4. 22 Thermogravimetric analysis of **94**, showing mass change (y-axis) against temperature (x-axis).

With the thermal stability of **94** now known, attention turned to the TGA plot of the di-pyrene compound **97**. Following the same procedure as for **94**, the TGA plot was recorded and is shown in Figure 4.23. Unlike the plot for **94**, there is no single decomposition step. Instead, there is only a 14 % mass loss of the total sample to 850 °C. In Figure 4.21, four lines visualise steps in the TGA plot. The first, at 125 °C, is a small mass loss, expected from the loss of high boiling point solvents at the isothermal. At 210 °C, there has only been a 1 % mass change. As **94** had shown thermal stability to 350 °C, this is not expected to be that of the collapse of the central pyridazine ring. At 420 °C, there has been a total mass change of 3 %. Again, this is not considered to involve collapse of the pyridazine ring, as the total nitrogen content of **97** is 3.37 %. Accounting for solvent loss, and experimental error, it is much more likely that the collapse of the pyridazine ring occurs between 420 °C and 650 °C. At 650 °C,

there has been a total mass change of 10 %. Further analysis will be required to determine the exact thermal stability of **97**, with this initial work suggesting it is >420 °C.

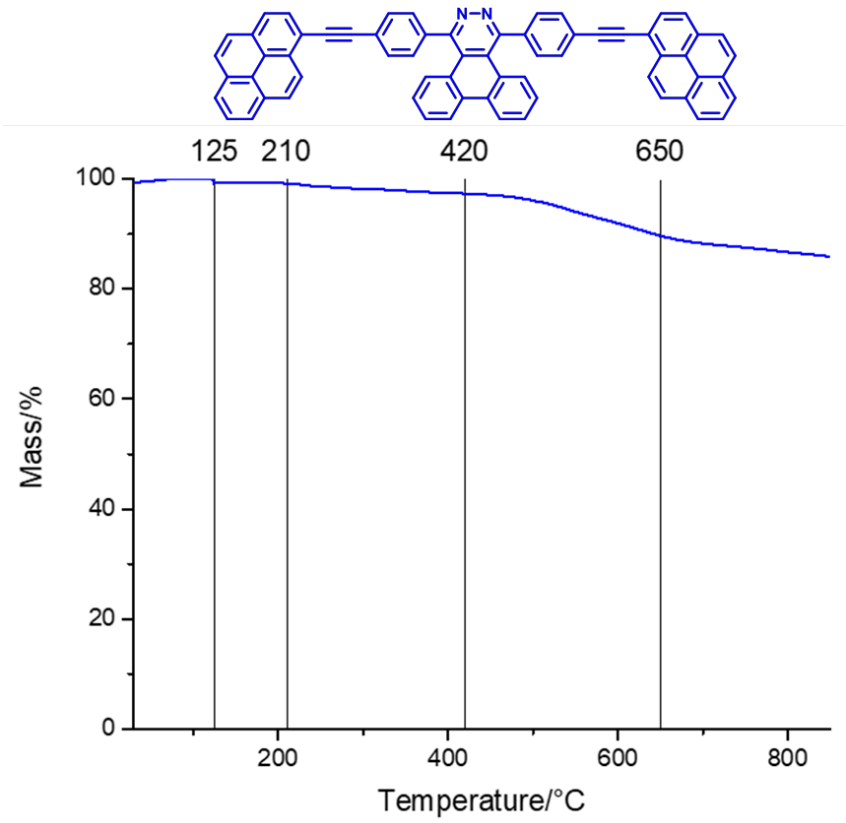

Figure 4. 23 Thermogravimetric analysis of **97**, showing mass change (y-axis) against temperature (x-axis).

4.6 Conclusions & Future Work

Whilst the triphenylamine donor compound **96** could not be realised as part of this work, further to the successful generation of the first Donor-Acceptor-Donor compounds featuring a phenanthrene-pyridazine acceptor core, an opportunity now exists to rapidly generate a diverse library of similar compounds. These compounds may find use across a number of optoelectronic fields, including those of OLED materials,[54] DSSC antennae,[55] and organic memory devices.[56] As **95** was designed as a "gateway" compound, offering numerous synthetic preparations towards this diverse compound library, the modification of the core di-bromo phenanthrene-pyridazine structure **95** will allow for the immediate generation of novel compounds of a similar structure to **96** and **97**, but without the alkyne spacer group.

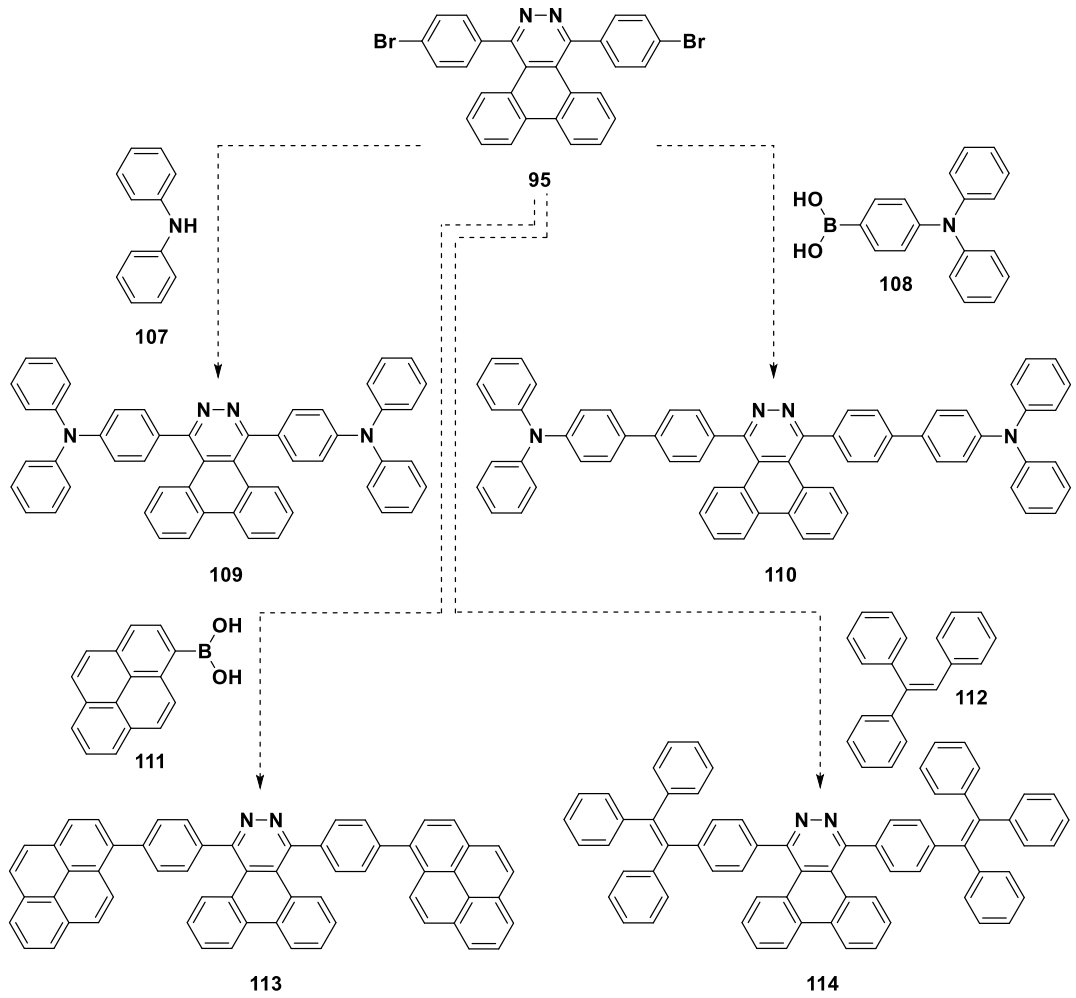

Scheme 4. 5 Potential D-A-D compounds for further study from the "gateway" precursor **95**.

Scheme 4.5 shows some ongoing work towards a number of these modified alkyne-free systems. The first of these target compounds is 4,4'-(dibenzo[f,h]phthalazine-1,4-diyl)bis(N,N-diphenylaniline), **109**. As the precursor **95** features two bromo-substituted sites, a double Buchwald-Hartwig amination reaction with two equivalents of diphenylamine (**107**) would facilitate the generation of **109**. Here, the triphenylamine component of the structure is formed from the free-phenyl of the precursor, offering an opportunity to study the effect of the close proximity of the donor and acceptor components. Further to this, the generation of the second target, 4',4'''-(dibenzo[f,h]phthalazine-1,4-diyl)bis(N,N-diphenyl-[1,1'-biphenyl]-4-amine), **110**, featuring a phenyl bridge between the triphenylamine donor and phenanthrene-pyridazine acceptor, would allow study of the effect of decreasing the proximity of the donor and acceptor components. **10** may be generated through Suzuki cross coupling of **95** with two equivalents of (4-(diphenylamino)phenyl)boronic acid, **108**. The third target, 1,4-bis(4-(pyren-1-yl)phenyl)dibenzo[f,h]phthalazine, **113**, may also be generated *via* a double Suzuki cross coupling reaction, this time with the pyrene precursor,

pyren-1-ylboronic acid, **111**. Generation of **110** and **113** allows further study on the effect of replacing the alkyne spacer with that of a phenyl bridge. The final target in Scheme 4.5 is 1,4-bis(4-(1,2,2-triphenylvinyl)phenyl)dibenzo[f,h]phthalazine, **114**, and features the tetraphenylethene donor common to many literature-based structures. The generation of **114** may be facilitated through a Heck cross coupling reaction with the commercially available ethene-1,1,2-triyltribenzene, **112**. Similar to **109**, the construction of the tetraphenylethene donor is formed *via* inclusion of the free phenyl from the reaction precursor **95**. However, synthetic preparations exist towards the generation of the mono-brominated tetraphenylethene compound, (2-(4-bromophenyl)ethene-1,1,2-triyl)tribenzene. This may then be converted to its respective boronic acid, suitable for a Suzuki cross coupling reaction to **95**, generating a further target featuring the single phenyl bridge.

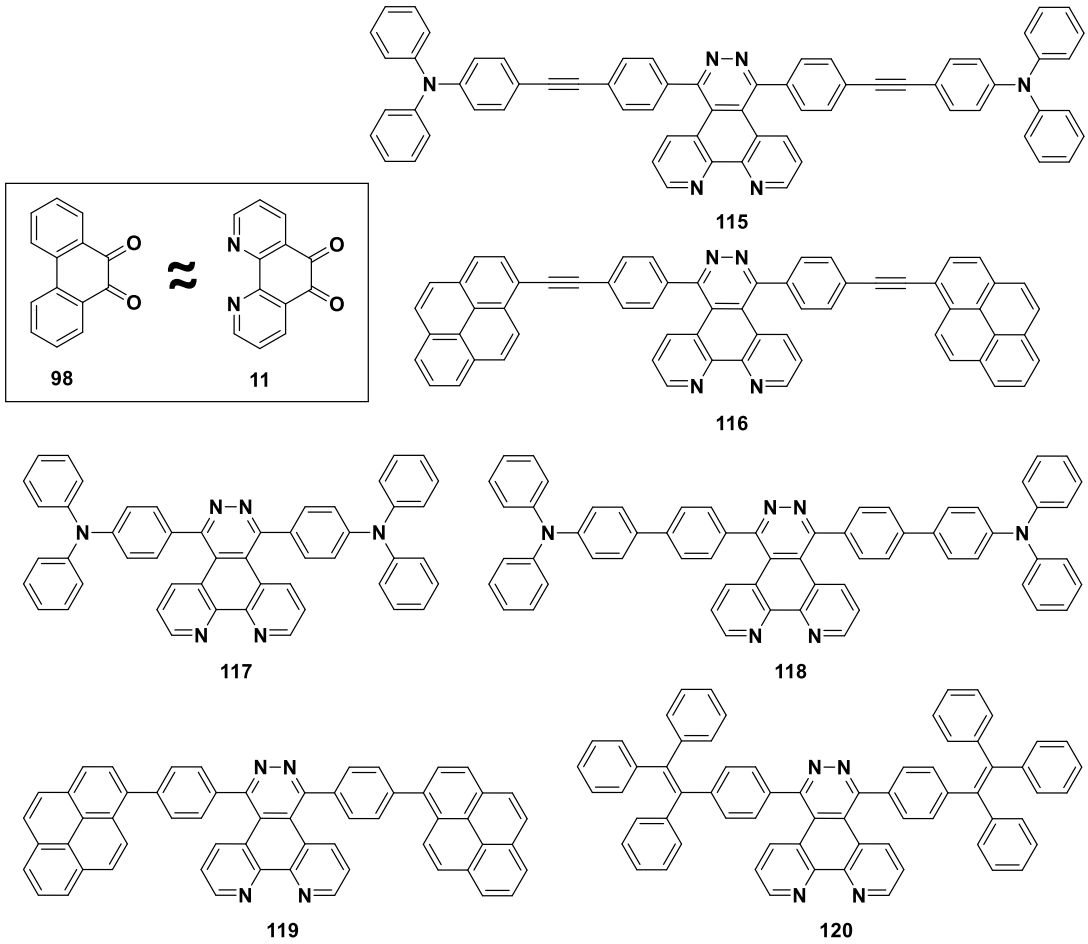

Chart 4. 10 Potential D-A-D compounds for further study from the phenanthroline dione **11**.

Analysis of the literature revealed work by some authors towards the generation of Donor-Acceptor-Donor compounds containing the 1,10-phenanthroline ring system in place of either the phenanthrene or fluoranthene ring systems.[57,58] The introduction of the two iminic nitrogens increases the electron withdrawing character of the ring system *versus* those ring

systems above, and may facilitate a lowering of the LUMO energy of the acceptor core system. There is a large dominance in the literature of donor systems, both novel and synthetically modified versions of well-known structures, with the acceptor systems often chosen as the "static" component of the D-A-D structure. Chart 4.10 demonstrates the conversion of the above mentioned phenanthrene targets, to their phenanthroline analogues. This is achieved through substitution of the phenanthrene-9,10-dione **98** to the corresponding 1,10-phenanthroline-5,6-dione **11**.

In theory, this substitution appears quite facile, but has been found to be synthetically challenging. However, attempts are now ongoing towards the synthesis of the alkyne bridged D-A-D compounds, **115**, and **116**; the triphenylamine donor compounds, **117**, and **118**; the pyrene donor compound, **119**; and the tetraphenylethene donor compound, **120**.

In conclusion, the optimised generation of two phenanthrene-pyridazine hybrid compounds **94** and **95** are presented. The di-brominated cyclopentadienone compound **102** was successfully ring opened to **103** in air in refluxing chlorobenzenes, with precipitation from diethyl ether generating an analytically pure sample for further reaction with hydrazine hydrate. The attempted ring opening of the non-brominated cyclopentadienone analogue **100** in air yielded significant impurities which could not be removed under exhaustive column chromatography conditions. Attempts to generate the pyridazine compound **94** directly failed to allow the removal of the impurities. The successful ring opening of **100** to **101** was achieved *via* the singlet oxygen method of Evans *et al*,[43] before the successful pyridazine ring formation reaction with hydrazine hydrate. The successful generation of the ethynyl-pyrene D-A-D compounds **97** was achieved *via* a Sonogashira cross coupling reaction with $Pd(PPh_3)_4$ in a mixed solvent system of DMF and triethylamine. **97** was structurally characterised through HRMS, IR, and multinuclear NMR studies. Extensive photophysical and electrochemical measurements were collected for **94** and **97**. The thermal stability of the compounds was also collected *via* Thermogravimetric Analysis (TGA).

4.7 References

1 J. C. Deaton, S. C. Switalski, D. Y. Kondakov, R. H. Young, T. D. Pawlik, D. J. Giesen, S. B. Harkins, A. J. M. Miller, S. F. Mickenberg and J. C. Peters, *J. Am. Chem. Soc.*, 2010, **132**, 9499–9508.

2 J. Shinar and R. Shinar, *J. Phys. D. Appl. Phys.*, 2008, **41**, 133001.

3 H.-H. Chang, W.-S. Tsai, C.-P. Chang, N.-P. Chen, K.-T. Wong, W.-Y. Hung and S.-W.

Chen, *Org. Electron.*, 2011, **12**, 2025–2032.

4 Y. Nakajima, T. Takei, Y. Fujisaki, H. Fukagawa, M. Suzuki, G. Motomura, H. Sato, T. Yamamoto and S. Tokito, *J. Soc. Inf. Disp.*, 2011, **19**, 94–99.

5 Y. G. Lee, H.-N. Lee, S. K. Kang, T. S. Oh, S. Lee and K. H. Koh, *Appl. Phys. Lett.*, 2006, **89**, 183515.

6 C. Sekine, Y. Tsubata, T. Yamada, M. Kitano and S. Doi, *Sci. Technol. Adv. Mater.*, 2014, **15**, 34203.

7 J. Zhang, F. Zhao, X. Zhu, W.-K. Wong, D. Ma and W.-Y. Wong, *J. Mater. Chem.*, 2012, **22**, 16448–16457.

8 J. Lee, H.-F. Chen, T. Batagoda, C. Coburn, P. I. Djurovich, M. E. Thompson and S. R. Forrest, *Nat Mater*, 2016, **15**, 92–98.

9 G. Méhes, H. Nomura, Q. Zhang, T. Nakagawa and C. Adachi, *Angew. Chemie Int. Ed.*, 2012, **51**, 11311–11315.

10 H. Tanaka, K. Shizu, H. Miyazaki and C. Adachi, *Chem. Commun.*, 2012, **48**, 11392–11394.

11 T. Nakagawa, S.-Y. Ku, K.-T. Wong and C. Adachi, *Chem. Commun.*, 2012, **48**, 9580–9582.

12 Z. Yang, Z. Mao, Z. Xie, Y. Zhang, S. Liu, J. Zhao, J. Xu, Z. Chi and M. P. Aldred, *Chem. Soc. Rev.*, 2017, **46**, 915–1016.

13 IUPAC, *Blackwell Sci. Publ. Oxford*, 2014, 1670.

14 T. Chen, L. Zheng, J. Yuan, Z. An, R. Chen, Y. Tao, H. Li, X. Xie and W. Huang, *Sci. Rep.*, 2015, **5**, 10923.

15 Q. Zhang, H. Kuwabara, W. J. Potscavage, S. Huang, Y. Hatae, T. Shibata and C. Adachi, *J. Am. Chem. Soc.*, 2014, **136**, 18070–18081.

16 I. S. Park, H. Komiyama and T. Yasuda, *Chem. Sci.*, 2017, **8**, 953–960.

17 J. S. Ward, R. S. Nobuyasu, A. S. Batsanov, P. Data, A. P. Monkman, F. B. Dias and M. R. Bryce, *Chem. Commun.*, 2016, **52**, 2612–2615.

18 H. Tanaka, K. Shizu, H. Nakanotani and C. Adachi, *Chem. Mater.*, 2013, **25**, 3766–3771.

19 V. Jankus, P. Data, D. Graves, C. McGuinness, J. Santos, M. R. Bryce, F. B. Dias and A. P. Monkman, *Adv. Funct. Mater.*, 2014, **24**, 6178–6186.

20 S. Yao, H.-Y. Ahn, X. Wang, J. Fu, E. W. Van Stryland, D. J. Hagan and K. D. Belfield, *J. Org. Chem.*, 2010, **75**, 3965–3974.

21 Q. Shi, P. Cheng, Y. Li and X. Zhan, *Adv. Energy Mater.*, 2012, **2**, 63–67.

22 Z. Cai, Y. Guo, S. Yang, Q. Peng, H. Luo, Z. Liu, G. Zhang, Y. Liu and D. Zhang, *Chem. Mater.*, 2013, **25**, 471–478.

23 Y. Cai, P. Liang, Q. Tang, X. Yang, W. Si, W. Huang, Q. Zhang and X. Dong, *ACS Nano*, 2017, **11**, 1054–1063.

24 H. Zhuang, Q. Zhou, Y. Li, Q. Zhang, H. Li, Q. Xu, N. Li, J. Lu and L. Wang, *ACS Appl. Mater. Interfaces*, 2014, **6**, 94–100.

25 P. Data, P. Pander, M. Okazaki, Y. Takeda, S. Minakata and A. P. Monkman, *Angew. Chemie Int. Ed.*, 2016, **55**, 5739–5744.

26 M. Okazaki, Y. Takeda, P. Data, P. Pander, H. Higginbotham, A. P. Monkman and S. Minakata, *Chem. Sci.*, 2017, **8**, 2677–2686.

27 G. Qian, Z. Zhong, M. Luo, D. Yu, Z. Zhang, D. Ma and Z. Y. Wang, *J. Phys. Chem. C*, 2009, **113**, 1589–1595.

28 G. Qian, Z. Zhong, M. Luo, D. Yu, Z. Zhang, Z. Y. Wang and D. Ma, *Adv. Mater.*, 2009, **21**, 111–116.

29 G. Qian, B. Dai, M. Luo, D. Yu, J. Zhan, Z. Zhang, D. Ma and Z. Y. Wang, *Chem. Mater.*, 2008, **20**, 6208–6216.

30 X. Du, J. Qi, Z. Zhang, D. Ma and Z. Y. Wang, *Chem. Mater.*, 2012, **24**, 2178–2185.

31 L. E. McNamara, N. Liyanage, A. Peddapuram, J. S. Murphy, J. H. Delcamp and N. I. Hammer, *J. Org. Chem.*, 2016, **81**, 32–42.

32 M. Aydemir, S. Xu, C. Chen, M. R. Bryce, Z. Chi and A. P. Monkman, *J. Phys. Chem. C*, 2017, **121**, 17764–17772.

33 T. Yasuda, Y. Sakai, S. Aramaki and T. Yamamoto, *Chem. Mater.*, 2005, **17**, 6060–6068.

34 Y. Su, W. Xu, F. Qiu, D. Wu, P. Liu, M. Xue and F. Zhang, *Chinese J. Chem.*, 2013, **31**, 1397–1403.

35 F. Lincker, D. Kreher, A.-J. Attias, J. Do, E. Kim, P. Hapiot, N. Lemaître, B. Geffroy, G. Ulrich and R. Ziessel, *Inorg. Chem.*, 2010, **49**, 3991–4001.

36 Y. Liu, F. Zhang, C. He, D. Wu, X. Zhuang, M. Xue, Y. Liu and X. Feng, *Chem. Commun.*, 2012, **48**, 4166–4168.

37 M. Li, C. An, T. Marszalek, X. Guo, Y.-Z. Long, H. Yin, C. Gu, M. Baumgarten, W. Pisula and K. Müllen, *Chem. Mater.*, 2015, **27**, 2218–2223.

38 S. Kato, K. Watanabe, M. Tamura, M. Ueno, M. Nitani, Y. Ie, Y. Aso, T. Yamanobe, H.

Uehara and Y. Nakamura, *J. Org. Chem.*, 2017, **82**, 3132–3143.

39 A. Ekbote, T. Jadhav and R. Misra, *New J. Chem.*, 2017, **41**, 9346–9353.

40 S. Wang, Z. Cheng, X. Song, X. Yan, K. Ye, Y. Liu, G. Yang and Y. Wang, *ACS Appl. Mater. Interfaces*, 2017, **9**, 9892–9901.

41 T. Takahashi, K. Shizu, T. Yasuda, K. Togashi and C. Adachi, *Sci. Technol. Adv. Mater.*, 2014, **15**, 34202.

42 G. Y. Wooi and J. M. White, *Org. Biomol. Chem.*, 2005, **3**, 972–974.

43 D. F. Evans and M. W. Upton, *J. Chem. Soc., Dalt. Trans.*, 1985, 1141–1145.

44 B. Alameddine, R. S. Anju, F. Al-Sagheer and T. A. Jenny, *New J. Chem.*, 2016, **40**, 10363–10370.

45 A. C. Benniston, A. Harriman, D. J. Lawrie and S. A. Rostron, *Eur. J. Org. Chem.*, 2004, **2004**, 2272–2276.

46 M. L. Daly, C. A. DeRosa, C. Kerr, W. A. Morris and C. L. Fraser, *RSC Adv.*, 2016, **6**, 81631–81635.

47 L. Q. Yan, Z. N. Kong, Y. Xia and Z. J. Qi, *New J. Chem.*, 2016, **40**, 7061–7067.

48 Q. Zhang, B. Li, S. Huang, H. Nomura, H. Tanaka and C. Adachi, *Nat. Photonics*, 2014, **8**, 326.

49 F. B. Dias, T. J. Penfold and A. P. Monkman, *Methods Appl. Fluoresc.*, 2017, **5**, 12001.

50 J. B. Birks, D. J. Dyson, and I. H. Munro, *Proc. R. Soc. London A Math. Phys. Eng. Sci.*, 1963, **275**, 575–588.

51 L. P. K. and P. Edamana, *Chem. – Eur. J.*, **17**, 8609–8617.

52 C. D. Geddes and J. R. Lakowicz, *Advanced Concepts in Fluorescence Sensing*, 2005.

53 G. Mallesham, C. Swetha, S. Niveditha, M. E. Mohanty, N. J. Babu, A. Kumar, K. Bhanuprakash and V. J. Rao, *J. Mater. Chem. C*, 2015, **3**, 1208–1224.

54 Y. Seino, S. Inomata, H. Sasabe, Y.-J. Pu and J. Kido, *Adv. Mater.*, 2016, **28**, 2638–2643.

55 K. Shankar, J. Bandara, M. Paulose, H. Wietasch, O. K. Varghese, G. K. Mor, T. J. LaTempa, M. Thelakkat and C. A. Grimes, *Nano Lett.*, 2008, **8**, 1654–1659.

56 M.-Y. Leung, S. Y.-L. Leung, D. Wu, T. Yu and V. W.-W. Yam, *Chem. - Eur. J.*, 2016, **22**, 14013–14021.

57 B. Hu, S.-J. Fu, F. Xu, T. Tao, H.-Y. Zhu, K.-S. Cao, W. Huang and X.-Z. You, *J. Org. Chem.*, 2011, **76**, 4444–4456.

58 T. Shigehiro, S. Yagi, T. Maeda, H. Nakazumi, H. Fujiwara and Y. Sakurai, *Tet. Lett.*, 2014, **55**, 5195–5198.

Chapter 5

Experimental

5.1 Technical Information

Unless otherwise stated all reactions were carried out in a nitrogen atmosphere. Separations were undertaken in air. All chemicals were obtained from commercial sources and were used without further purification unless otherwise stated. Solvents were dried using appropriate drying agents, and distilled under a nitrogen atmosphere. Flash chromatography was performed using silica gel 60 (Sigma Aldrich/Merck), particle size 0.04-0.063 mm, or aluminium oxide (Fluka), as the respective stationary phase.

Microwave reactions were carried out in a CEM Discover S-Class Single Mode Microwave reactor under pressure, using specialised sealed "snap-cap" vials.

IR spectra (recorded in cm^{-1}) were recorded in solid form neat on a PerkinElmer Spectrum 100 FTIR spectrometer fitted with a Universal ATR accessory.

Melting points are given uncorrected using a Griffin melting point apparatus.

Electrospray mass spectra were recorded on a micromass LCT electrospray mass spectrometer. Accurate MS were referenced against leucine enkephalin (555.6 g mol-1) or [Glu1]-Fibrinopeptide B (1570.6 g mol-1) and were reported within 5 ppm. MALDI-TOF mass spectra were recorded on a Waters MALDI-QTOF Premier Spectrometer using an α-cyano-4-hydroxy cinnamic acid matrix. All samples were dissolved in methanol, methylene chloride, or acetonitrile unless otherwise stated.

Nuclear magnetic resonance spectra were with (i) a Bruker Avance DPX-400 MHz spectrometer operating at 400.13 MHz for ^{1}H, 100.6 MHz for ^{13}C, or (ii) a Bruker Avance II 600 NMR spectrometer operating at 600.13 MHz for ^{1}H and 150.9 MHz for ^{13}C. The signals for ^{1}H and ^{13}C were referenced to the solvent. ^{13}C NMR spectra were proton decoupled. Chemical shifts (δ) are reported in ppm, and coupling constants (J) in Hertz. "C_Q" is used to refer to quaternary carbons. Following literature precedent, these are not typically assigned. Where the resolution of a signal is not clear, and does not display a clear splitting pattern, the peak is designated as a pseudo-signal to the closest common splitting pattern (ψ). All photophysical studies were carried out with solutions contained using 1x1 cm^2 quartz cells in HPLC grade solvents.

The single-crystal analysis was performed by Dr. Brendan Twamley in Trinity College Dublin with a Brüker SMART APEX CCD diffractometer using graphite monochromated Mo-Kα (λ=0.71073Å) radiation at the temperatures given in tables. Data reduction was performed using SAINT. Intensities were corrected for Lorentz and polarisation effects and for absorption by SADABS. Space groups were determined from systematic absences and checked for higher symmetry. The structures were solved by direct methods using SHELXS

and refined on F^2 using all data by full-matrix least-squares procedures with SHELX-97. All non-hydrogen atoms were refined with anisotropic displacement parameters. Hydrogen atoms were included in calculated positions with isotropic displacement parameters 1.3 times the isotropic equivalent of their carrier carbons. Absolute structure determinations were based on the Flack parameter. The functions minimised were $\Sigma w(Fo^2 - Fc^2)$, with $w=[\sigma^2(Fo^2) + (aP)^2 + bP]^{-1}$, where $P= [max(Fo)^2 + 2Fc^2]/3$. In all cases, final Fourier syntheses showed no significant residual electron density in chemically sensible positions. The SQUEEZE/PLATON program was used in the structural refinement in cases where there were a large number of solvent molecules disordered within the structure.

UV/Vis absorption spectra were recorded on a Shimadzu UV-2450 UV/Vis recording spectrophotometer. Emission and excitation spectra were obtained on Horiba Scientific FluoroMax 4-P spectrofluorometer or a Horiba-Jobin-Yvon FluoroLog FL-3-11 spectrofluorometer with a double grating emission and excitation monochromators. Emission lifetime measurements were performed with a TBX-04-D picosecond photodetection module using NanoLED pulsed diode laser excitation sources of the appropriate wavelength. Results were analysed using the Horiba DAS software (version 6.3), and Datastation (version 2.4). Appropriate excitation repetition rates were chosen in order to ensure that no re-excitation of the sample occurred until the decay has reached the baseline. TAC (time to amplitude convertor) ranges were set at approximately twenty times the expected average decay time, and were less than the reciprocal of the source repetition rate. To prevent pile-up, the start-stop ratio (α) was maintained at less than 2 %. If the repetition rates required were > 100 kHz, the experiments were carried out in the reverse mode. Data was fit using monoexponential decays where possible, while attempting to maintain a χ^2 statistic of ~1, a Durbin-Watson statistic of ~2, a random spread of residuals with approximately 60 % of residuals within one standard deviation of the fitted parameter, and over 99 % of the residuals with three standard deviations. Emission quantum yields of solutions of **52** and **54** were measured using a Horiba Integrating Sphere, in the range of 350 nm – 850 nm, with data analysis performed using the Horiba PLQY Excel calculator (version 4). Further emission quantum yields of solutions were measured using the single-point relative method, using quinine sulfate or $[Ru(bpy)_2Cl_2][PF_6]$ as the reference, in CH_2Cl_2 or MeCN at RT. The single-point method was utilised through calculation of the integrated emission intensities of both the sample and the respective reference, measured on the same instrument, with identical entrance and exit slit values. Optically dilute samples (Abs = ~0.1) of both the sample and the reference were prepared.

All electrochemical experiments were performed with a CH Instruments potentiostat model 660B. Cyclic voltammograms were measured on 10 mmol solutions of the compounds in

acetonitrile, methylene chloride, or chloroform. Tetra-n-butylammonium hexafluorophosphate (Bu4NPF6, 0.1 M) was used as supporting electrolyte, a glassy carbon working electrode (Area = 0.0707 cm^2), a Pt wire counter electrode, and a Ag/AgCl reference electrode were used. All solutions were continuously degassed for ten minutes by nitrogen bubbling before the experiments were performed and a flow of nitrogen was maintained over the solution for the duration of the experiments. All electrodes were rinsed in distilled water and the chosen experiment solvent, and dried with tissue before being placed into the cyclic voltammogram vessel. The glassy carbon working electrode was further cleaned before use. First, some distilled water was added to an alumina pad, before firmly polishing the electrode surface on the pad in a figure-of-eight manner for two minutes, with regular twisting to prevent uneven cleaning of the exposed electrode surface. The electrode was further polished with a soft cloth in a similar manner for another two minutes, and then visually inspected.

Photocatalytic hydrogen production experiments were carried out using an air-cooling apparatus for maintaining the solutions at room temperature at 22 °C, during irradiation using LEDs (355 and 470 nm). MeCN used was dried over calcium hydride and the triethylamine dried over sodium before being freshly distilled under nitrogen. The samples were prepared in GC vials (4.9 ml volume, VWR) with a known headspace of 2.9 ml. Photosensitiser (**52** or **54**) and catalyst $K_2[PtCl_4]$ were taken in 1:1 ratio and dissolved in 4:1 MeCN/H_2O solution containing 1.2×10^{-4} M of PS. 1.9 ml of the PS/Pt solution and 90 µL of triethylamine were added to the GC vials in 2 ml sample under argon atmosphere. Subsequently, the GC vials were irradiated with 355(22×10^{-3} W m^{-2}) and 470 nm (0.4 W m^{-2}) wavelength LEDs for 18 hours. After irradiation, 100 µL samples were drawn from the headspace and injected into the GC.

5.2 Synthetic Preparations and Characterisation

12, **L46**, **L47**, **L48**, **L49**, **L50**, **L51**, **L52**, and **98** were purchased from commercial sources, and used without further purification.

99,[1] **100**,[2] **102**,[3] **105**,[4] and **106**[5] were prepared identically to literature preparations.

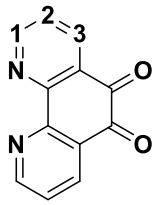

1,10-Phenanthroline-5,6-dione; 11

1,10-Phenanthroline-5,6-dione was prepared *via* a modified literature procedure.[6] 1,10-Phenanthroline (4.6 g, 25.52 mmol) and KBr (4.6 g, 38.65 mmol) were taken together and cooled to 0 °C. A cooled mixture of concentrated H_2SO_4 (35 mL) and HNO_3 (30 mL) was added dropwise while maintaining the reaction mixture at 0 °C. The reaction mixture was then heated to 130 °C for 3 h. The mixture was allowed to cool and was poured over ice (500 g). The resulting slurry was carefully neutralised with NaOH. The product was extracted into CH_2Cl_2 (100 mL x 2) and the combined organic phases were washed with water. The organic phases were dried over $MgSO_4$ and the solvent removed in vacuo yielding a yellow-orange solid. The product was recrystallised from hot EtOH, yielding a yellow solid (4.06g, 75 %).

^{1}H NMR (400 MHz, $CDCl_3$): δ 9.15 (ψd, 2H, $^3J_{HH}$ = 3.7 Hz, H1), 8.53 (d, 2H, $^3J_{HH}$ = 7.7 Hz, H3), 7.62 (dd, 2H, $^3J_{HH}$ = 7.9, $^4J_{HH}$ = 4.8 H2) ppm

HRMS (*m/z*): [M+H] ($C_{12}H_7N_2O_2$) Calc.: 211.0508, Found: 211.0511

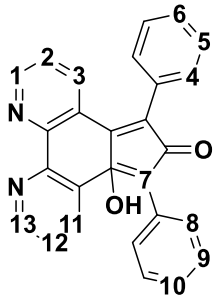

4b-hydroxy-5,7-diphenyl-4b,5-dihydro-6H-cyclopenta[f][1,10]phenanthrolin-6-one; 1

A solution containing 1,3-diphenyl-2-propanone (1.6011 g, 7.6 mmol) and 1,10-phenanthroline-5,6-dione (1.011 g, 4.8 mmol) in anhydrous MeOH (20 mL) was degassed by bubbling with nitrogen for 10 minutes. A solution of piperidine (1 mL) was added dropwise. The colour of the solution changed from yellow to dark brown and a yellow precipitate began to form. The reaction mixture was stirred for 16 h in the dark, and the resulting yellow precipitate was isolated by filtration. The precipitate was washed with cold MeOH, and cold hexane, yielding a pale off-white solid on drying (1.716 g, 56 %).

^{1}H NMR (600 MHz, $CDCl_3$): δ 8.82 (ψd, 1H, J = 3.7 Hz, H1), 8.79 (ψd, 1H, $^{3}J_{HH}$ = 3.5 Hz, H13), 8.06 (dd, 1H, $^{3}J_{HH}$ = 7.8 Hz, $^{4}J_{HH}$ = 1.2 Hz, H3), 7.62 (dd, 1H, $^{3}J_{HH}$ = 8.0 Hz, $^{4}J_{HH}$ = 1.3 Hz, H11), 7.55 (d, 2H, $^{3}J_{HH}$ = 7.2, H4), 7.51 (t, 2H, $^{3}J_{HH}$ = 7.6, H5), 7.46-7.41 (m, 4H, H6/H9/H10), 7.40-7.35 (m, 3H, H8/H2), 7.15 (dd, 1H, $^{3}J_{HH}$ = 8.0 Hz, $^{4}J_{HH}$ = 4.5 Hz, H12), 4.52 (s, 1H, H7), 2.56 (br s, 1H, OH) ppm.

^{13}C NMR (151 MHz, $CDCl_3$): δ 202.6 (C=O), 158.8 (C_Q), 152.4 (CH, C13), 150.8 (CH, C1), 150.2 (C_Q), 150.0 (C_Q), 140.2 (C_Q), 136.6 (CH, C11), 136.4 (C_Q), 134.8 (C_Q), 133.9 (CH, C3), 131.9 (CH, C4), 129.8 (C_Q), 129.1 (CH, C10), 129.0 (CH, C8), 128.9 (2C, CH, C5/C9), 128.2 (CH, C6), 125.2 (C_Q), 124.6 (CH, C2), 123.6 (CH, C12), 74.6 (C-OH), 60.9 (CH, C7) ppm.

IR (neat, νbar/cm^{-1}): 3662 (O-H, H-bonded), 3214 (O-H, broad, free), 1704 (C=O), 1415 (C=C, arom), 1341, 1150, 1089 (C-O), 816, 763, 739, 717, 694, 662, 624, 590, 567, 557, 549, 511, 482.

HRMS (*m/z*): [M+H] ($C_{27}H_{19}N_2O_2$) Calc.: 403.1447, Found: 403.1447

m.p.: 226 – 228 °C

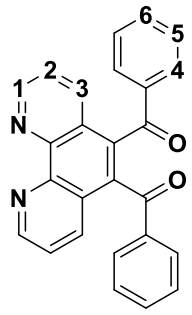

(1,10-phenanthroline-5,6-diyl)bis(phenylmethanone); 13

4b-hydroxy-5,7-diphenyl-4b,5-dihydro-6H-cyclopenta[f][1,10]phenanthrolin-6-one (0.5 g, 1.16 mmol) and Al_2O_3 (2.5 g) were combined in Chlorobenzene (30 mL) and refluxed for 16 h in air. The colour of the solution changed from yellow to blue to orange over the course of

the reaction time, before turning yellow. The solvent was removed *in vacuo*. The pale yellow solid was dissolved in the minimum amount of acetone and precipitated with hexanes, yielding a pale white solid (0.130 g, 29 %).

^{1}H NMR (400 MHz, $CDCl_3$): δ 9.30 (*ψ*d, 2H, $^{3}J_{HH}$ = 4.4 Hz, H1), 8.10 (*ψ*d, 2H, $^{3}J_{HH}$ = 8.6 Hz, H3), 7.73 (d, 4H, $^{3}J_{HH}$ = 7.5 Hz, H4), 7.65-7.55 (m, 4H, H2/H6), 7.39 (t, 4H, $^{3}J_{HH}$ = 7.7 Hz, H5) ppm.

^{13}C NMR (101 MHz, $CDCl_3$): δ 196.1 (1C, C=O), 151.2 (CH, C1), 145.5 (C_Q), 136.7 (C_Q), 134.8 (CH, C3), 134.2 (CH, C6), 133.9 (C_Q), 129.7 (CH, C4), 128.3 (CH, C5), 125.2 (C_Q), 123.2 (C_Q) ppm.

IR (neat, νbar/cm^{-1}): 1766, 1705, 1650 (C=O), 1290, 1237, 1177, 875, 794, 736, 724, 697, 667, 615.

HRMS (*m/z*): [M+H] ($C_{26}H_{17}N_2O_2$) Calc.: 389.1290, Found: 389.1298

m.p.: 280 – 286 °C

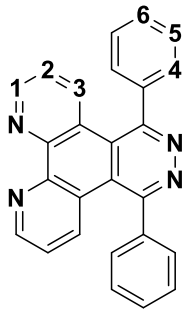

5,8-diphenylpyridazino[4,5-f][1,10]phenanthroline; 4

To a solution containing (1,10-phenanthroline-5,6-diyl)bis(phenylmethanone) (0.130 g, 0.33 mmol) in EtOH (10 mL) was added an aqueous solution of hydrazine monohydrate (50-60 %, 0.140 g, 1.32 mmol). A solution of KOH (0.093 mg, 1.66 mmol) in EtOH (5 mL) was added dropwise. The red reaction mixture was heated under reflux for 2 h. The solution was allowed to cool and the solvent removed *in vacuo*. The yellow solid was dissolved in the minimum amount of acetone and precipitated with hexanes, yielding a pale yellow solid (0.117 g, 93 %).

^{1}H NMR (400 MHz, $CDCl_3$): δ 9.19 (*ψ*d, 2H, $^{3}J_{HH}$ = 3.0 Hz, H1), 8.20 (d, 2H, $^{3}J_{HH}$ = 8.6 Hz, H3), 7.70 (d, 4h, $^{3}J_{HH}$ = 6.7 Hz, H4), 7.62-7.52 (m, 6H, H5/H6), 7.35 (dd, 2H, $^{3}J_{HH}$ = 7.9 Hz, $^{4}J_{HH}$ = 3.8 Hz, H2) ppm.

^{13}C NMR (101 MHz, $CDCl_3$): δ 156.3 (C_Q), 151.8 (CH, C1), 147.9 (C_Q), 138.9 (C_Q), 135.7 (CH, C3), 129.4 (CH, C4), 129.3 (CH, C6), 128.9 (CH, C5), 125.2 (C_Q), 123.6 (C_Q), 121.9 (C_Q) ppm.

IR (neat, νbar/cm^{-1}): 3052 (C-H, arom), 1490 (C=C, arom), 1442 (C=C, arom), 1369, 874, 823, 808, 757, 774, 744, 700, 681, 665, 651, 620, 559, 502.

HRMS (*m/z*): [M+H] ($C_{26}H_{17}N_4$) Calc.: 385.1453, Found: 385.1452

m.p.: > 350 °C

X-ray Crystals suitable for single crystal X-ray diffraction studies were obtained from the slow evaporation of a CH_2Cl_2/MeOH solution of the compound. Data collection and refinement was conducted by Dr. Brendan Twamley in Trinity College Dublin. A specimen of $C_{26}H_{16}N_4$, approximate dimensions 0.130 mm x 0.150 mm x 0.160 mm, was used for the X-ray crystallographic analysis. The X-ray intensity data were measured at 100(2)K using an Oxford Cryosystems Cobra low temperature device using a MiTeGen micromount.

A total of 1206 frames were collected. The total exposure time was 12.06 hours. The integration of the data using a monoclinic unit cell yielded a total of 88828 reflections to a maximum θ angle of 31.14° (0.69 Å resolution), of which 6124 were independent (average redundancy 14.505, completeness = 99.9%, R_{int} = 6.38%, R_{sig} = 3.22%) and 4446 (72.60%) were greater than 2σ(F^2). The final cell constants of $\underline{a}$ = 15.8865(7) Å, $\underline{b}$ = 14.9806(6) Å, $\underline{c}$ = 17.3527(7) Å, β = 113.229(2)°, volume = 3795.0(3) $Å^3$, are based upon the refinement of the XYZ-centroids of reflections above 20 σ(I). Data were corrected for absorption effects using the numerical method (SADABS). The calculated minimum and maximum transmission coefficients (based on crystal size) are 0.9842 and 1.0000.

The structure was solved and refined using the Bruker SHELXTL Software Package, using the space group C2/c, with Z = 8 for the formula unit, $C_{26}H_{16}N_4$. The final anisotropic full-matrix least-squares refinement on F^2 with 271 variables converged at R1 = 4.79%, for the observed data and wR2 = 12.18% for all data. The goodness-of-fit was 1.022. The largest peak in the final difference electron density synthesis was 0.403 $e^-/Å^3$ and the largest hole was -0.273 $e^-/Å^3$ with an RMS deviation of 0.056 $e^-/Å^3$. On the basis of the final model, the calculated density was 1.346 g/cm^3 and F(000), 1600 e^-.

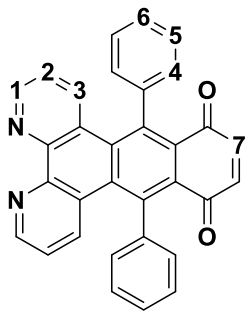

9,14-diphenylnaphtho[2,3-f][1,10]phenanthroline-10,13-dione; 14

4b-hydroxy-5,7-diphenyl-4b,5-dihydro-6H-cyclopenta[f][1,10]phenanthrolin-6-one (0.5 g, 1.16 mmol) and Al_2O_3 (2.5 g) were refluxed in degassed Chlorobenzene (30 mL) for 4 h under Ar. The colour of the solution changed from yellow to blue to orange over the course of the reaction time. A solution of benzoquinone (0.27 g, 2.5 mmol) in Chlorobenzene (mL) was added rapidly under Ar, and allowed to reflux for 1 h. The solvent was removed *in vacuo*. The orange solid was redissolved in xylenes, and refluxed for 16 h in air. The solvent was removed *in vacuo*. Column chromatography (alumina), CH_2Cl_2 → $CHCl_3$ → acetone (single column; no gradient solvent process used), yielded a dark orange solid (0.24 g, 84 %).

^{1}H NMR (400 MHz, $CDCl_3$): δ 8.95 (*ψ*d, 2H, $^3J_{HH}$ = 4.2 Hz, H1), 7.69 (dd, 2H, $^3J_{HH}$ = 8.4 Hz, H3), 7.53 – 7.49 (m, 2H, H4), 7.46 (t, 4H, $^3J_{HH}$ = 7.2 Hz, H6), 7.28 (d, 4H, $^3J_{HH}$ = 6.7 Hz, H5), 7.06 (dd, 2H, $^3J_{HH}$ = 4.4, $^4J_{HH}$ = 8.8, H2), 6.87 (s, 2H, H7) ppm.

^{13}C NMR (101 MHz, $CDCl_3$): δ 186.5 (C=O), 150.6 (C1), 147.9 (C_Q), 140.6 (C_Q), 140.4 (C_Q), 139.0 (C7), 136.8 (C3), 134.8 (C_Q), 130.8 (C_Q), 130.4 (C5), 129.5 (C6), 128.4 (C4), 126.9 (C_Q), 121.6 (C2).

IR (neat, νbar/cm^{-1}): 3044, 2921, 1660, 1620, 1327, 1228, 1087, 1019, 812, 745, 705.

HRMS (*m/z*): [M+H] ($C_{32}H_{18}N_2O_2$) Calc.: 463.1447, Found: 463.1447

X-ray Crystals suitable for single crystal X-ray diffraction studies were obtained from the slow evaporation of a toluene/hexanes solution of the compound. Data collection and refinement was conducted by Dr. Brendan Twamley in Trinity College Dublin. A clear orange block-like specimen of $C_{32}H_{18}N_2O_2$, approximate dimensions 0.120 mm x 0.170 mm x 0.180 mm, was used for the X-ray crystallographic analysis. The X-ray intensity data were measured at 100(2)K with an Oxford Cryosystems low temperature device using a MiTeGen micromount.

A total of 969 frames were collected. The total exposure time was 7.51 hours. The frames were integrated with the Bruker SAINT software package using a narrow-frame algorithm. The integration of the data using a monoclinic unit cell yielded a total of 47660 reflections to a maximum θ angle of 28.01° (0.76 Å resolution), of which 5299 were independent (average

redundancy 8.994, completeness = 99.8%, R_{int} = 6.30%, R_{sig} = 3.22%) and 4037 (76.18%) were greater than $2\sigma(F^2)$. The final cell constants of a = 15.1713(4) Å, b = 8.1437(2) Å, c = 17.8028(5) Å, β = 92.4755(14)°, volume = 2197.49(10) $Å^3$, are based upon the refinement of the XYZ-centroids of 9924 reflections above 20 σ(I) with 5.502° < 2θ < 55.99°. Data were corrected for absorption effects using the Multi-Scan method (SADABS). The ratio of minimum to maximum apparent transmission was 0.967. The calculated minimum and maximum transmission coefficients (based on crystal size) are 0.7210 and 0.7456.

The structure was solved with the XT structure solution program using Intrinsic Phasing and refined with the XL refinement package using Least Squares minimisation with Olex2, using the space group $P2_1/n$, with Z = 4 for the formula unit, $C_{32}H_{18}N_2O_2$. The final anisotropic full-matrix least-squares refinement on F^2 with 325 variables converged at R1 = 4.39%, for the observed data and wR2 = 14.62% for all data. The goodness-of-fit was 1.049. The largest peak in the final difference electron density synthesis was 0.290 $e^-/Å^3$ and the largest hole was -0.257 $e^-/Å^3$ with an RMS deviation of 0.054 $e^-/Å^3$. On the basis of the final model, the calculated density was 1.398 g/cm^3 and F(000), 960 e^-.

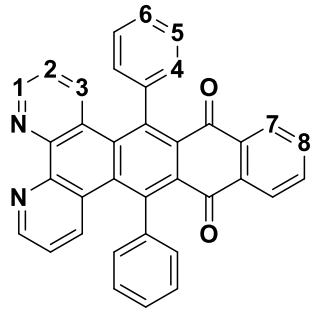

9,16-diphenylanthra[2,3-f][1,10]phenanthroline-10,15-dione; 15

4b-hydroxy-5,7-diphenyl-4b,5-dihydro-6H-cyclopenta[f][1,10]phenanthrolin-6-one (0.5 g, 1.16 mmol) and Al_2O_3 (2.5 g) were refluxed in degassed Chlorobenzene (30 mL) for 4 h under Ar. The colour of the solution changed from yellow to blue to orange over the course of the reaction time. A solution of naphthalene-1,4-dione (0.515 g, 43.25 mmol) in Chlorobenzene (mL) was added rapidly under Ar, and allowed to reflux for 1 h. The solvent was removed *in vacuo*. The orange/red solid was redissolved in xylenes, and refluxed for 16 h in air. The solvent was removed *in vacuo*. Column chromatography (alumina), CH_2Cl_2 → $CHCl_3$ → acetone, yielded a bright yellow solid (0.14 g, 22 %).

^{1}H NMR (400 MHz, $CDCl_3$): δ 8.97 (*ψ*d, 2H, $^3J_{HH}$ = 4.4 Hz, H1), 8.11 (dd, 2H, $^3J_{HH}$ = 3.3 Hz, $^4J_{HH}$ = 6.2 Hz, H8), 7.77 (dd, 2H, $^3J_{HH}$ = 3.5 Hz, $^4J_{HH}$ = 5.7c Hz, H7), 7.7 (d, 2H, $^3J_{HH}$ =

3.5 Hz, H3), 7.57 – 7.54 (m, 2H, H6), 7.5 (t, 4H, $^{3}J_{HH}$ = 7.7 Hz, H5), 7.35 (d, 4H, $^{3}J_{HH}$ = 7.0 Hz, H4), 7.09 (dd, 2H, $^{3}J_{HH}$ = 4.2 Hz, $^{4}J_{HH}$ = 8.4 Hz, H2) ppm.

^{13}C NMR (101 MHz, $CDCl_3$): δ 184.7 (C=O), 150.6 (C1), 148.0 (C_Q), 140.1 (C_Q), 141.0 (C_Q), 137.0 (C3), 135.1 (C_Q), 134.7 (C_Q), 134.0 (C7), 132.9 (C_Q), 130.6 (C4), 129.5 (C5), 128.3 (C6), 127.0 (C_Q), 126.9 (C8), 121.6 (C2) ppm.

IR (neat, νbar/cm^{-1}): 3041, 1975, 1738, 1660, 1619, 1328, 1229 1087, 765, 745, 704.

HRMS (*m/z*): [M+H] ($C_{36}H_{20}N_2O_2$) Calc.: 513.1603, Found: 513.1606

X-ray Crystals suitable for single crystal X-ray diffraction studies were obtained from the slow evaporation of a $CDCl_3$ solution of the compound. Data collection and refinement was conducted by Dr. Brendan Twamley in Trinity College Dublin. A specimen of $C_{39}H_{20}D_4Cl_{10}N_2O_2$, approximate dimensions 0.070 mm x 0.080 mm x 0.430 mm, was used for the X-ray crystallographic analysis. The X-ray intensity data were measured at 100(2)K using an Oxford Cryosystems low temperature device using a MiTeGen micromount.

A total of 513 frames were collected. The total exposure time was 5.80 hours. The integration of the data using a triclinic unit cell yielded a total of 24554 reflections to a maximum θ angle of 26.13° (0.81 Å resolution), of which 7691 were independent (average redundancy 3.193, completeness = 99.2%, R_{int} = 3.57%, R_{sig} = 4.25%) and 6045 (78.60%) were greater than 2σ(F^2). The final cell constants of a = 8.8542(4) Å, b = 15.6631(7) Å, c = 16.3565(7) Å, α = 115.7025(15)°, β = 92.7686(17)°, γ = 104.6925(16)°, volume =1944.23(15) Å^3, are based upon the refinement of the XYZ-centroids of reflections above 20 σ(I). Data were corrected for absorption effects using the Multi-Scan method (SADABS). The ratio of minimum to maximum apparent transmission was 0.886. The calculated minimum and maximum transmission coefficients (based on crystal size) are0.6601 and 0.7453.

The structure was solved using the Bruker APEX Software Package and refined with XL in Olex2, using the space group $P\bar{1}$, with Z = 2 for the formula unit, $C_{39}H_{20}D_4Cl_{10}N_2O_2$. The final anisotropic full-matrix least-squares refinement on F^2 with 490 variables converged at R1 = 3.97%, for the observed data and wR2 = 9.55% for all data. The goodness-of-fit was1.037. The largest peak in the final difference electron density synthesis was 0.562 e$^-$/Å^3 and the largest hole was -0.878 e$^-$/Å^3 with an RMS deviation of 0.071 e$^-$/Å^3. On the basis of the final model, the calculated density was 1.556 g/cm^3 and F(000), 916 e$^-$.

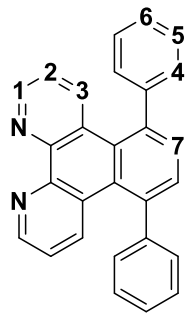

5,8-diphenylbenzo[f][1,10]phenanthroline; 3

4b-hydroxy-5,7-diphenyl-4b,5-dihydro-6H-cyclopenta[f][1,10]phenanthrolin-6-one (0.5 g, 1.16 mmol) and Al_2O_3 (2.5 g) were refluxed in degassed Chlorobenzene (30 mL) for 4 h under Ar. The colour of the solution changed from yellow to blue to orange over the course of the reaction time. A solution of bicyclo[2.2.1]hepta-2,5-diene (0.9 g, 9.83 mmol) in Chlorobenzene (mL) was added rapidly under Ar, and allowed to reflux for 1 h. The solvent was removed *in vacuo*. The yellow solid was redissolved in 1,2-dichlorobenzene, and refluxed for 16 h under Ar. The solvent was removed *in vacuo*. Column chromatography (silica), 5:95 MeOH:CH_2Cl_2, yielded an off-white solid (0.11 g, 23 %).

^{1}H NMR (400 MHz, $CDCl_3$): δ 8.97 (*ψ*d, 2H, $^3J_{HH}$ = 4.4 Hz, H1), 8.0 (d, 2H, $^3J_{HH}$ = 8.8 Hz, H3), 7.62 (s, 2H, H7), 7.47 (s, 10H, H4/H5/H6), 7.12 (dd, 2H, $^3J_{HH}$ = 4.6 Hz, $^4J_{HH}$ = 8.2 Hz, H2) ppm.

^{13}C NMR (101 MHz, $CDCl_3$): δ 149.5 (C2), 147.1 (C_Q), 143.6 (C_Q), 139.9 (C_Q), 136.7 (C4), 130.8 (C8), 129.5 (C5), 129.4 (C7), 129.3 (C_Q), 127.7 (C6), 127.2 (C_Q), 121.3 (C_Q) ppm.

IR (neat, νbar/cm^{-1}): 3378, 3051, 1185, 1537, 1394, 771, 739, 700.

HRMS (*m/z*): [M+H] ($C_{28}H_{18}N_2$) Calc.: 383.1548, Found: 383.1553

X-ray Crystals suitable for single crystal X-ray diffraction studies were obtained from the slow evaporation of a toluene/hexane solution of the compound. Data collection and refinement was conducted by Dr. Brendan Twamley in Trinity College Dublin. A specimen of $C_{28}H_{20}N_2O$, approximate dimensions 0.080 mm x 0.080 mm x 0.230 mm, was used for the X-ray crystallographic analysis. The X-ray intensity data were measured. The X-ray intensity data were measured at 100(2)K on a Bruker Apex Kappa Duo with an Oxford Cobra low temperature device using a MiTeGen micromount. Bruker APEX software was used to correct for Lorentz and polarization effects.

A total of 2808 frames were collected. The total exposure time was 21.32 hours. The frames were integrated with the Bruker SAINT software package using a narrow-frame algorithm. The integration of the data using a monoclinic unit cell yielded a total of 14036 reflections to a maximum θ angle of 69.97° (0.82 Å resolution), of which 3672 were independent (average

redundancy 3.822, completeness = 98.7%, R_{int} = 3.00%, R_{sig} = 2.36%) and 3475 (94.64%) were greater than $2\sigma(F^2)$. The final cell constants of a = 15.8802(5) Å, b = 5.03040(10) Å, c = 24.7689(7) Å, β = 96.6131(12)°, volume = 1965.47(9) $Å^3$, are based upon the refinement of the XYZ-centroids of 9974 reflections above 20 σ(I) with 5.602° < 2θ < 139.3°. Data were corrected for absorption effects using the Multi-Scan method (SADABS). The ratio of minimum to maximum apparent transmission was 0.884. The calculated minimum and maximum transmission coefficients (based on crystal size) are 0.6661 and 0.7533.

The structure was solved with the XT structure solution program using Intrinsic Phasing and refined with the XL refinement package using Least Squares minimisation with Olex2, using the space group $P2_1/c$, with Z = 4 for the formula unit, $C_{28}H_{20}N_2O$. The final anisotropic full-matrix least-squares refinement on F^2 with 288 variables converged at R1 = 3.88%, for the observed data and wR2 = 10.62% for all data. The goodness-of-fit was 1.024. The largest peak in the final difference electron density synthesis was 0.219 $e^-/Å^3$ and the largest hole was -0.201 $e^-/Å^3$ with an RMS deviation of 0.046 $e^-/Å^3$. On the basis of the final model, the calculated density was 1.353 g/cm^3 and F(000), 840 e^-.

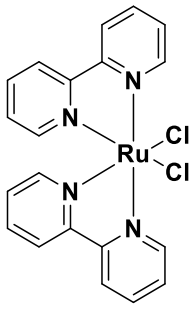

[Ru(2,2'-bipyridine)$_2$Cl$_2$]; 55

[Ru(2,2'-bipyridine)$_2$Cl$_2$] was prepared *via* a modified literature procedure.[7] $RuCl_3.3H_2O$ (0.78 g, 2.98 mmol), 2,2'-bipyridine (0.936 g, 5.99 mmol), and LiCl (0.085 g, 2.0 mmol) were combined in dimethylformamide (10 mL), and refluxed for 6 h under Ar. Upon cooling, HPLC grade acetone (20 mL) was added, and the resultant solution cooled to – 20 °C for 16 hr. A black precipitate was filtered from the solution. The precipitate was washed with cold H_2O (3 x 50 mL), and diethyl ether (4 x 50 mL), yielding a black solid on drying (0.9 g, 62 %).

^{1}H NMR (400 MHz, DMSO-d_6): δ 9.97 (d, 2H, $^3J_{HH}$ = 4.8 Hz), 8.64, (d, 2H, $^3J_{HH}$ = 7.5 Hz), 8.48 (d, 2H, $^3J_{HH}$ = 7.3 Hz), 8.07 (t, 2H, $^3J_{HH}$ = 6.4 Hz), 7.77 (t, 2H, $^3J_{HH}$ = 8.0 Hz), 7.68 (t, 2H, $^3J_{HH}$ = 8.0 Hz), 7.51 (d, 2H, $^3J_{HH}$ = 5.3 Hz), 7.10 (t, 2H, $^3J_{HH}$ = 6.4 Hz) ppm.

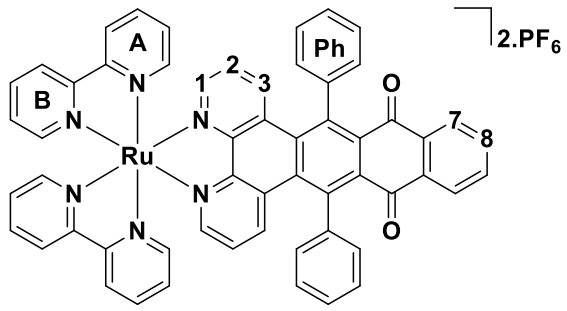

[Ru(2,2'-bipyridine)$_2$(9,16-diphenylanthra[2,3-f][1,10]phenanthroline-10,15-dione)][(PF_6)$_2$]; 48

[Ru(2,2'-bipyridine)$_2$Cl$_2$] (0.033 g, 0.07 mmol) and 9,16-diphenylanthra[2,3-f][1,10]phenanthroline-10,15-dione (0.03 g, 0.06 mmol) were combined in H_2O (3 mL) and 2-ethoxyethanol (3 mL), and refluxed under Ar for 24 h. Upon cooling, a saturated aqueous solution of KPF_6 was added dropwise, precipitating a light orange solid. The solid was collected *via* filtration, and washed with H_2O (1 x 25 mL), and diethyl ether (1 x 20 mL), yielding an orange solid on drying (0.02 g, 27 %).

^{1}H NMR (400 MHz, acetone-d_6): δ 8.52 (d, 4H, $^3J_{HH}$ = 7.6 Hz, A/B), 8.08 (t, 3H, $^3J_{HH}$ = 8.2 Hz, A/B), 8.05 (dd, 2H, $^3J_{HH}$ = 3.0 Hz, $^4J_{HH}$ = 5.0 Hz, H8), 7.88 (t, 4H, $^3J_{HH}$ = 6.1 Hz, H7/H3), 7.78 (d, 2H, $^3J_{HH}$ = 5.4 Hz, A), 7.70 (d, 2H, $^3J_{HH}$ = 8.2 Hz, H1), 7.68 (d, 2H, $^3J_{HH}$ = 5.8 Hz, B), 7.60 – 7.55 (m, 6H, Ph), 7.44 – 7.40 (m, 4H, A/Ph), 7.37 (t, 2H, $^3J_{HH}$ = 6.2 Hz, B), 7.25 (d, 2H, $^3J_{HH}$ = 7.8 Hz, Ph), 7.11 (dd, $^3J_{HH}$ = 4.9 Hz, $^4J_{HH}$ = 8.2 Hz, H2) ppm.

^{13}C NMR (101 MHz, acetone-d_6): δ 184.5 (C=O), 157.1 (C_Q), 156.9 (C_Q), 152.0 (B), 151.8 (A), 151.7 (C7), 149.8 (C_Q), 141.6 (C_Q), 140.6 (C_Q), 137.8 (A/B), 136.9 (C1), 134.7 (C3), 134.5 (C_Q), 134.4 (C_Q), 133.4 (C_Q), 130.7 (Ph), 130.5 (C_Q), 130.2 (Ph), 129.7 (Ph), 129.5 (Ph), 128.5 (Ph), 127.5 (A), 127.5 (B), 126.5 (C8), 124.3 (A/B), 124.2 (), 124.0 (C2) ppm.

IR (neat, νbar/cm^{-1}): 1675, 1599, 1445, 1326, 1237, 970, 834, 761, 725, 701.

HRMS (*m/z*): [M] ($C_{56}H_{36}F_{12}N_6O_2P_2Ru$) Calc.: 1216.1227, Found: 1071.1636 [M-PF_6]

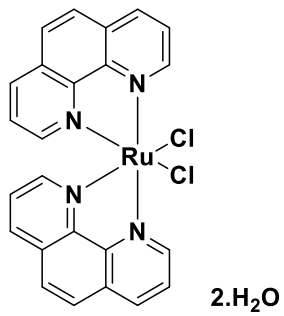

[(Ru(1,10-phenanthroline)$_2$Cl$_2$).2H_2O]; 56

[(Ru(1,10-phenanthroline)$_2$Cl$_2$).2H$_2$O] was prepared *via* a modified literature procedure.[8] RuCl$_3$.3H$_2$O (0.52 g, 1.07 mmol), 1,10-phenanthroline (0.716 g, 3.97 mmol), and LiCl (0.56 g, 13.2 mmol) were combined in dimethylformamide (10 mL), and refluxed for 16 h under N$_2$. Upon cooling, HPLC grade acetone (20 mL) was added, and the resultant solution cooled to – 20 °C for 16 hr. A black precipitate was filtered from the solution. The precipitate was washed with cold H$_2$O (3 x 50 mL), and diethyl ether (4 x 50 mL), yielding a black solid on drying (0.45 g, 74 %).

^{1}H NMR (400 MHz, DMSO-d$_6$): δ 10.30 (d, 2H, $^3J_{HH}$ = 6.5 Hz), 8.72 (d, 2H, $^3J_{HH}$ = 7.0 Hz), 8.29 (d, 2H, $^3J_{HH}$ = 8.2 Hz), 8.26 – 8.29 (m, 4H), 8.14 (d, 2H, $^3J_{HH}$ = 6.3 Hz), 7.34 (dd, 2H, $^3J_{HH}$ = 4.8 Hz, $^4J_{HH}$ = 7.4 Hz) ppm.

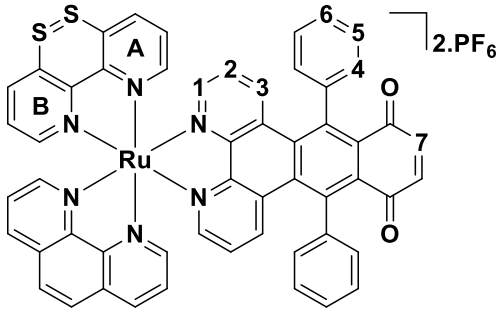

[Ru(1,10-phenanthroline)$_2$(9,14-diphenylnaphtho[2,3-f][1,10]phenanthroline-10,13-dione)][(PF$_6$)$_2$]; 49

[Ru(1,10-phenanthroline)$_2$Cl$_2$] (0.0575 g, 0.1 mmol) and 9,14-diphenylnaphtho[2,3-f][1,10]phenanthroline-10,13-dione (0.05 g, 0.1 mmol) were combined in ethylene glycol (6 mL) in a specialised sealed "snap-cap" vial. The vial was placed in a CEM Discover S-Class Single Mode Microwave reactor, and heated to 160 °C for 1 hr (150 W) under pressure. Upon cooling, the ethylene glycol solution was added to a saturated aqueous solution of KPF$_6$ (20 mL). CH$_2$Cl2 (50 mL) was added to the solution, and an aqueous work up performed. The solvent was removed *in vacuo*. Column chromatography (silica), 2:98 MeOH:CH$_2$Cl$_2$, yielded a dark orange solid (0.034 g, 28 %).

^{1}H NMR (600 MHz, acetone-d$_6$): δ 8.67 (d, 2H, $^3J_{HH}$ = 9.0 Hz, A), 8.57 (d, 2H, $^3J_{HH}$ = 8.7 Hz, B),8.26 (dd, 2H, $^3J_{HH}$ = 9.0 Hz, $^4J_{HH}$ = 19.0, Hz, S), 8.14 (d, 2H, $^3J_{HH}$ = 5.7 Hz, A),7.93 (d, 2H, $^3J_{HH}$ = 5.7 Hz, B), 7.82 (d, 2H, $^3J_{HH}$ =4.86 Hz, H3), 7.76 (dd, 2H, $^3J_{HH}$ = 4.8 Hz, $^4J_{HH}$ = 7.8, A), 7.71 -7.65 (m, 2H, H1), 7.60 – 7.48 (m, 8H, B/Ph), 7.39 (t, 2H, $^3J_{HH}$ = 6.9 Hz, Ph), 7.25 – 7.20 (m, 2H, Ph), 6.98 (dd, 2H, $^3J_{HH}$ = 5.7 Hz, $^4J_{HH}$ = 9.6, H2), 6.96 (s, 2H, H7) ppm.

^{13}C NMR (151 MHz, acetone-d$_6$): δ 186.4 (C=O), 153.1 (A), 152.7 (B), 152.3, (C3), 150.1 (C$_Q$), 150.0 (C$_Q$), 147.8 (C$_Q$), 147.6 C$_Q$ (C$_Q$), 140.1 (C$_Q$), 139.2 (C7), 136.9 (A), 136.7 (B),

136.6 (C1), 133.2 (C_Q), 132.5 (C_Q), 131.0 (C_Q), 131.0 (C_Q), 130.6 (Ph), 130.4 (Ph), 129.6 (Ph), 129.4 (Ph), 129.3 (C_Q), 128.6 (C_Q), 128.5 (Ph), 128.0 (S) 125.9 (A), 125.8 (B), 123.8 (C2) ppm.

HRMS (*m/z*): [M] ($C_{56}H_{34}F_{12}N_6O_2P_2Ru$) Calc.: 1214.1070, Found: 924.1822 [M-2PF_6]

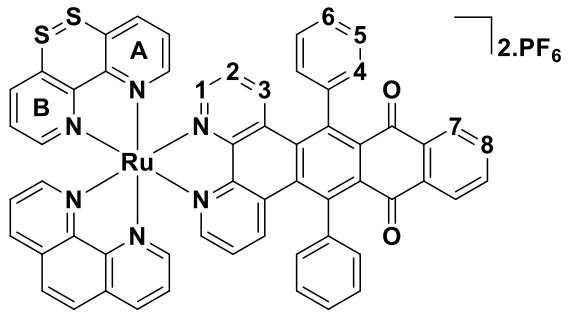

[Ru(1,10-phenanthroline)$_2$(9,16-diphenylanthra[2,3-f][1,10]phenanthroline-10,15-dione)][(PF_6)$_2$]; 50

[Ru(1,10-phenanthroline)$_2$$Cl_2$] (0.052 g, 0.091 mmol) and 9,16-diphenylanthra[2,3-f][1,10]phenanthroline-10,15-dione (0.05 g, 0.097 mmol) were combined in ethylene glycol (6 mL) in a specialised sealed "snap-cap" vial. The vial was placed in a CEM Discover S-Class Single Mode Microwave reactor, and heated to 160 °C for 1 hr (150 W) under pressure. Upon cooling, the ethylene glycol solution was added to a saturated aqueous solution of KPF_6 (20 mL). CH_2Cl2 (50 mL) was added to the solution, and an aqueous work up performed. The solvent was removed *in vacuo*. Column chromatography (silica), 2:98 MeOH:CH_2Cl_2, yielded a dark orange solid (0.049 g, 43 %).

^{1}H NMR (600 MHz, acetone-d_6): δ 8.68 (d, 2H, $^3J_{HH}$ = 8.8 Hz, A), 8.58 (d, 2H, $^3J_{HH}$ = 8.3 Hz, B), 8.27 (dd, 4H, $^3J_{HH}$ = 9.5 Hz, $^4J_{HH}$ = 20.0 Hz, S), 8.16 (d, 2H, $^3J_{HH}$ = 5.0, B), 8.04 (dd, 2H, $^3J_{HH}$ = 2.7 Hz, $^4J_{HH}$ = 6 Hz, H7), 7.93 (d, 2H, $^3J_{HH}$ = 5.5 Hz, A), 7.88 (dd, 2H, $^3J_{HH}$ = 2.7 Hz, $^4J_{HH}$ = 5.5 Hz, H8), 7.82 (d, 2H, $^3J_{HH}$ = 5.5 Hz, H3), 7.77 (dd, 2H, $^3J_{HH}$ = 5.5 Hz, $^4J_{HH}$ = 9.0 Hz, A), 7.68 (d, 2H, $^3J_{HH}$ = 8.3 Hz, H1), 7.61 – 7.58 (m, 8H, B/Ph), 7.40 (t, 2H, $^3J_{HH}$ = 7.2 Hz, Ph), 7.28 (d, 2H, $^3J_{HH}$ = 7.8 Hz, Ph), 6.99 (dd, 2H, $^3J_{HH}$ = 4.5 Hz, $^4J_{HH}$ = 8.5 Hz, H2) ppm.

^{13}C NMR (151 MHz, acetone-d_6): δ 184.6 (C=O), 153.3 (B), 152.7 (A), 152.2 (C3), 150.2 (C_Q), 147.8 (C_Q), 147.7 (C_Q), 141.7 (C_Q), 140.7 (C_Q), 136.9 (A), 136.8 (C1), 136.7 (B), 134.7 (C_Q), 134.5 (C_Q), 134.4 (C8), 133.4 (C_Q), 131.0 (C_Q), 131.0 (C_Q), 130.7 (Ph), 130.4 (C_Q), 130.3 (Ph), 129.7 (Ph), 129.5 (C_Q), 128.5 (Ph), 128.07 (Ph), 126.5 (S), 126.4 (C7), 125.9 (A), 125.8 (B), 123.8 (C2) ppm.

IR (neat, νbar/cm^{-1}): 3059, 1968, 1673, 1594, 1428, 1381, 1324, 1253, 1062, 970, 829, 719, 700.

HRMS (*m/z*): [M] ($C_{60}H_{36}F_{12}N_6O_2P_2Ru$) Calc.: 1264.1227, Found: 1119.1609 [M-PF_6]

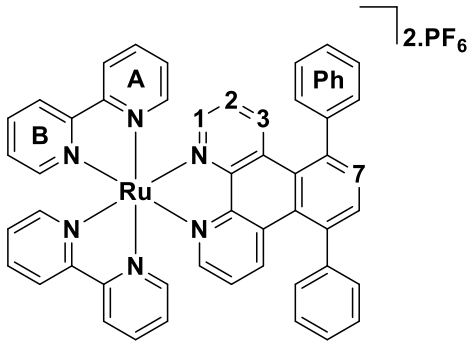

[Ru(2,2'-bipyridine)$_2$(5,8-diphenylbenzo[f][1,10]phenanthroline)][(PF_6)$_2$]; 51

[Ru(2,2'-bipyridine)$_2$$Cl_2$] (0.038 g, 0.078 mmol) and 5,8-diphenylbenzo[f][1,10]phenanthroline (0.03 g, 0.078 mmol) were combined in ethylene glycol (6 mL) in a specialised sealed "snap-cap" vial. The vial was placed in a CEM Discover S-Class Single Mode Microwave reactor, and heated to 160 °C for 1 hr (150 W) under pressure. Upon cooling, the ethylene glycol solution was added to a saturated aqueous solution of KPF_6 (20 mL). CH_2Cl2 (50 mL) was added to the solution, and an aqueous work up performed. The solvent was removed *in vacuo*. Column chromatography (silica), 2:98 MeOH:CH_2Cl_2, yielded an orange solid (0.061 g, 72 %).

^{1}H NMR (600 MHz, acetone-d_6): δ 8.84 (t, 4H, $^3J_{HH}$ = 6.2 Hz, A/B), 8.26 – 8.22 (m, 4H, A/H4), 8.20 (d, 4H, $^3J_{HH}$ = 7.6 Hz, B/H2), 8.12 (d, 2H, $^3J_{HH}$ = 6.1 Hz, A), 8.03 (d, 2H, $^3J_{HH}$ = 4.1 Hz, B), 7.88 (s, 2H, H7), 7.71 (br s, 2H, Ph), 7.66 – 7.59 (br t, 4H, Ph/A), 7.54 (t, 2H, $^3J_{HH}$ = 8.0 Hz, Ph), 7.51 – 7.43 (br t, 4H, B/Ph), 7.41 (dd, 2H, $^3J_{HH}$ = 5.5 Hz, $^4J_{HH}$ = 8.9 Hz, H2), 7.35 (br s, 2H, Ph) ppm.

^{13}C NMR (151 MHz, acetone-d_6): δ 157.4 (C_Q), 157.3 (C_Q), 152.0 (B), 151.9 (A), 151.2 (C3), 149.1 (C_Q), 142.8 (C_Q), 141.2 (C_Q), 138.0 (A), 137. 9 (B), 136.6 (C1), 132.8 (C7), 130.7 (C_Q), 130.0 (C_Q), 129.7 (C_Q), 129.0 (Ph), 128.4 (Ph), 128.3 (C_Q), 127.9 (Ph), 127.7 (Ph), 124.4 (C2), 124.4 (A), 124.4 (B) ppm.

IR (neat, νbar/cm^{-1}): 3040, 1708, 1603, 1445, 1221, 1011, 832, 760, 728, 707, 661, 613.

HRMS (*m/z*): [M] ($C_{48}H_{34}F_{12}N_6P_2Ru$) Calc.: 1086.1172, Found: 398.0963 [M/2; -2PF_6]

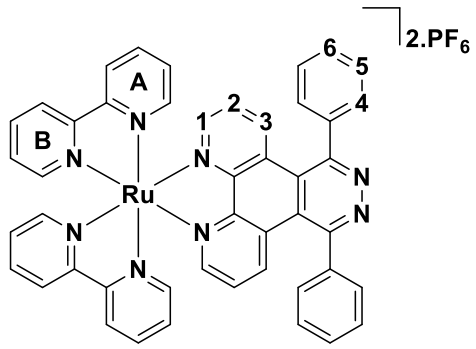

[Ru(2,2'-bipyridine)$_2$(5,8-diphenylpyridazino[4,5-f][1,10]phenanthroline)][(PF_6)$_2$]; 52

[Ru(2,2'-bipyridine)$_2$Cl$_2$] (0.035 g, 0.072 mmol) and 5,8-diphenylpyridazino[4,5-f][1,10]phenanthroline (0.034 g, 0.09 mmol) were combined in H_2O (2.5 mL) and 2-ethoxyethanol (2.5 mL), and heated to 145 °C under N_2 for 24 h. Upon cooling, a saturated aqueous solution of KPF_6 was added dropwise, precipitating a light orange solid. The solid was collected *via* filtration, and washed with H_2O (1 x 25 mL), and diethyl ether (1 x 20 mL). The complex was dissolved in a minimum amount of acetone, and precipitated with hexane. The solid was collected *via* filtration, yielding an orange solid on drying (0.03 g, 39 %).

^{1}H NMR (600 MHz, MeCN-d_3): δ 8.54 (t, 4H, $^3J_{HH}$ =8.4 Hz, A/B), 8.23 (dd, 2H, $_3J_{HH}$ = 8.78 Hz, $^4J_{HH}$ = 1.2 Hz, H3), 8.14-8.05 (m, 6H, A/B, H1), 7.80 (ψd, 2H, $^3J_{HH}$ = 5.6 Hz, B), 7.74 (br s, 4H, H4), 7.71-7.66 (m, 4H, A/H6), 7.66-7.61 (m, 4H, H5), 7.46 (ψtd, 2H, $^3J_{HH}$ = 7.2 Hz, $^4J_{HH}$ = 1.3 Hz, B), 7.39 (dd, 2H, $^3J_{HH}$ = 8.7 Hz, $^4J_{HH}$ = 5.4 Hz, H2), 7.35 (ψtd, 2H, $^3J_{HH}$ = 7.2 Hz, $^4J_{HH}$ = 1.3 Hz, A) ppm.

^{13}C NMR (151 MHz, acetonitrile-d_3): δ 158.4 (C_Q), 158.1 (C_Q), 157.8 (C_Q), 154.7 (C1), 153.2 (A), 152.7 (B), 151.4 (C_Q), 140.2 (C_Q), 139.0 (A), 138.9 (B), 137.1 (C3), 131.1 (C6), 130.6 (C4), 130.4 (C5), 128.8 (C_Q), 128.5 (B), 128.4 (A), 126.1 (C2), 126.0 (C_Q), 125.3 (B), 125.2 (A) ppm.

IR (neat, νbar/cm^{-1}): 3081, 1604, 1465, 1446, 1379, 1022, 833, 762, 730, 701, 628.

HRMS (m/z): [M-PF6] ($C_{46}H_{32}F_6N_8PRu$) Calc.: 798.1793, Found: 798.1794

X-ray Crystals suitable for single crystal X-ray diffraction studies were obtained from the slow evaporation of a small sample of the crude reaction solution of the compound. For that reason, the unit cell contains a mixture of solvents (2-ethoxyethanol, acetone, and MeOH) which have been treated as a diffuse contribution to the overall scattering without specific atom positions by SQUEEZE/PLATON. Data collection and refinement was conducted by Dr. Brendan Twamley in Trinity College Dublin. A specimen of $C_{46}H_{32}F_{12}N_8P_2Ru$, approximate dimensions 0.040 mm x 0.060 mm x 0.190 mm, was used for the X-ray crystallographic analysis. The X-ray intensity data were measured at 100(2)K using an

Oxford Cryosystems Cobra low temperature device using a MiTeGen micromount. Bruker APEX software was used to correct for Lorentz and polarization effects.

A total of 2823 frames were collected. The total exposure time was 16.47 hours. The integration of the data using a monoclinic unit cell yielded a total of 124078 reflections to a maximum θ angle of 25.40° (0.83 Å resolution), of which 8868 were independent (average redundancy 13.992, completeness = 99.7%, R_{int} = 12.12%, R_{sig} = 7.13%) and 6065 (68.39%) were greater than $2\sigma(F^2)$. The final cell constants of a = 13.8299(4) Å, b = 22.9240(7) Å, c = 15.9228(4) Å, β = 106.9810(12)°, volume = 4828.0(2) $Å^3$, are based upon the refinement of the XYZ-centroids of reflections above 20 σ(I). Data were corrected for absorption effects using the multi-scan method (SADABS). The calculated minimum and maximum transmission coefficients (based on crystal size) are 0.6991 and 0.7452.

The structure was solved and refined using the Bruker SHELXTL Software Package, using the space group $P2_1/c$, with Z = 4 for the formula unit, $C_{46}H_{32}F_{12}N_8P_2Ru$. The final anisotropic full-matrix least-squares refinement on F^2 with 622 variables converged at R1 = 5.22%, for the observed data and wR2 = 12.51% for all data. The goodness-of-fit was 1.036. The largest peak in the final difference electron density synthesis was 1.019 $e^-/Å^3$ and the largest hole was -0.661 $e^-/Å^3$ with an RMS deviation of 0.095 $e^-/Å^3$. On the basis of the final model, the calculated density was 1.497 g/cm^3 and F(000), 2184 e^-.

The unit cell contains a mixture of solvents (ethoxy ethanol, MeOH) which have been treated as a diffuse contribution to the overall scattering without specific atom positions by SQUEEZE/PLATON.

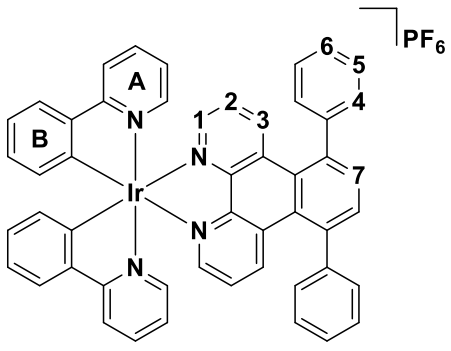

[Ir(2-phenylpyridine)$_2$(5,8-diphenylbenzo[f][1,10]phenanthroline)][PF_6]; 53

[Ir(2-phenylpyridine)$_2$Cl]$_2$ (0.041 g, 0.038 mmol) and 5,8-diphenylbenzo[f][1,10]phenanthroline (0.03 g, 0.078 mmol) were combined in $CHCl_3$ (4 mL), and refluxed in air for 16 h. Upon cooling, a saturated aqueous solution of KPF_6 was added dropwise, precipitating a light yellow solid. The solid was collected *via* filtration, and

washed with H_2O (1 x 25 mL), and diethyl ether (1 x 20 mL). The complex was dissolved in a minimum amount of acetone, and precipitated with hexane. The solid was collected *via* filtration, yielding a yellow solid on drying (0.025 g, 56 %).

^{1}H NMR (600 MHz, acetone-d_6): δ 8.30 (d, 2H, $^3J_{HH}$ = 8.0 Hz, H3), 8.25 (ψt, 4H, B/H1), 7.96 (t, 2H, $^3J_{HH}$ =8.4 Hz, B), 7.92 (d, 2H, $^3J_{HH}$ = 7.1 Hz, A), 7.88 (s, 2H, H7), 7.80 (d, 2H, $^3J_{HH}$ = 5.4 Hz, B), 7.73 (br s, 2H, Ph), 7.64 (br s, 2H, Ph), 7.56 – 7.51 (m, 4H, H2/Ph), 7.46 (br s, 2H, Ph), 7.35 (br s, 2H, Ph), 7.10 – 7.04 (m, 4H, B/A), 6.94 (t, 2H, $^3J_{HH}$ = 9.0 Hz, A), 6.41 (d, 2H, $^3J_{HH}$ = 7.4 Hz, A) ppm.

^{13}C NMR (151 MHz, acetone-d_6): δ 167.8 (C_Q), 150.4 (C_Q), 149.9 (C1), 149.5 (B), 148.3 (C_Q), 144.2 (C_Q), 142.7 (C_Q), 141.1 (B), 138.6 (C3), 138.1 (C7), 132.8 (A), 131.6 (C_Q), 131.1 (A), 130.3 (Ph), 130.1 (Ph), 129.7 (Ph), 129.2 (C_Q), 128.4 (Ph), 125.0 (C2), 125.0 (A), 123.5 (B), 122.5 (A), 120.0 (B) ppm.

IR (neat, νbar/cm^{-1}): 2920, 1606, 1582, 1477, 1063, 832, 756, 730, 703, 629.

HRMS (*m/z*): [M] ($C_{50}H_{34}F_6IrN_4P$) Calc.: 1028.2055, Found: 883.2445 [M-PF_6]

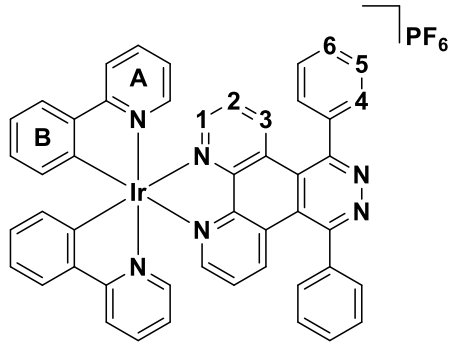

[Ir(2-phenylpyridine)$_2$(5,8-diphenylpyridazino[4,5-f][1,10]phenanthroline)][PF_6]; 54

[Ir(2-phenylpyridine)$_2$Cl]$_2$ (0.031 g, 0.029 mmol) and 5,8-diphenylpyridazino[4,5-f][1,10]phenanthroline (0.034 g, 0.062 mmol) were combined in $CHCl_3$ (4 mL), and refluxed in air for 16 h. Upon cooling, a saturated aqueous solution of KPF_6 was added dropwise, precipitating a light yellow solid. The solid was collected *via* filtration, and washed with H_2O (1 x 25 mL), and diethyl ether (1 x 20 mL). The complex was dissolved in a minimum amount of acetone, and precipitated with hexane. The solid was collected *via* filtration, yielding a yellow solid on drying (0.03 g, 88 %).

^{1}H NMR (600 MHz, acetone-d_6): δ 8.35 – 8.30 (m, 4H, H3/H1), 8.10 (d, 2H, B), 7.86 (ψt, 4H, B/A), 7.74 (br s, H4), 7.68 (ψt, 2H, H6), 7.65 – 7.60 (m, 2H, H5), 7.58 (d, 2H, $^3J_{HH}$ = 9.0 Hz, B), 7.49 (dd, 2H, $^3J_{HH}$ = 4.9 Hz, $^4J_{HH}$ = 9.5 Hz, H2), 7.10 (t, 2H, $^3J_{HH}$ = 4.9 Hz, A), 7.01 – 6.96 (m, 2H, B/A), 6.46 (d, 2H, $^3J_{HH}$ = 7.4 Hz, A) ppm.

^{13}C NMR (151 MHz, acetone-d_6): δ 168.3 (C_Q), 158.3 (C_Q), 153.5 (C1), 150.7 (B), 150.7 (C_Q), 150.5 (C_Q), 145.1 (C_Q), 140.1 (C_Q), 139.6 (B), 138.8 (C3), 132.5 (A) 131.3 (A), 131.0 (C6), 130.6 (C4), 130.5 (C5), 129.2 (), 126.9 (C2), 126.2 (), 125.9 (A), 124.4 (B), 123.7 (A), 120.8 (B) ppm.

IR (neat, νbar/cm^{-1}): 2970, 1739, 1607, 1477, 1373, 1227, 832, 756, 730, 700, 627.

HRMS (*m/z*): [M] ($C_{48}H_{32}F_6IrN_6P$) Calc.: 1030.1959, Found: 885.2328 [M-PF_6]

X-ray Crystals suitable for single crystal X-ray diffraction studies were obtained from the slow evaporation of a THF/diethyl ether solution of the compound. Data collection and refinement was conducted by Dr. Brendan Twamley in Trinity College Dublin. The two phenylpyridine ligands coordinated to Ir3 are disordered and this was modelled with both restraints and constraints. The disordered moiety occupancy for each phenylpyridine was refined at 61% and 57%. Several solvent molecules were disordered and modelled with both restraints and constraints. The less occupied part of a disordered THF (55:45% occupied) was modelled (only the oxygen atom) to maintain the molecule in a reasonable H-bonding position. A specimen of $C_{164}H_{138}F_{18}Ir_3N_{18}O_5P_3$, approximate dimensions 0.040 mm x 0.140 mm x 0.320 mm, was used for the X-ray crystallographic analysis. The X-ray intensity data were measured at 100(2)K using an Oxford Cryosystems Cobra low temperature device using a MiTeGen micromount. Bruker APEX software was used to correct for Lorentz and polarization effects.

A total of 5901 frames were collected. The total exposure time was 13.11 hours. The integration of the data using a monoclinic unit cell yielded a total of 552424 reflections to a maximum θ angle of 26.39° (0.80 Å resolution), of which 29189 were independent (average redundancy 18.926, completeness = 100.0%, R_{int} = 4.20%, R_{sig} = 1.62%) and 26194 (89.74%) were greater than 2σ(F^2).The final cell constants of a = 16.0857(5) Å, b = 38.3546(11) Å, c = 23.1955(6) Å, β = 94.9016(12)°, volume = 14258.4(7) Å^3, are based upon the refinement of the XYZ-centroids of reflections above 20 σ(I).Data were corrected for absorption effects using the multi-scan method (SADABS). The ratio of minimum to maximum apparent transmission was 0.792. The calculated minimum and maximum transmission coefficients (based on crystal size) are 0.5707 and 0.7454.

The structure was solved and refined using the Bruker SHELXTL Software Package, using the space group $P2_1/c$, with Z = 4 for the formula unit, $C_{164}H_{138}F_{18}Ir_3N_{18}O_5P_3$.The final anisotropic full-matrix least-squares refinement on F^2 with 1813 variables converged at R1 = 4.03%, for the observed data and wR2 = 10.09% for all data. The goodness-of-fit was 1.102. The largest peak in the final difference electron density synthesis was 2.518 e$^-$/Å^3 and the

largest hole was -1.936 $e^-/Å^3$ with an RMS deviation of 0.108 $e^-/Å^3$. On the basis of the final model, the calculated density was 1.608 g/cm^3 and F(000), 6904 e^-.

The two phenylpyridine ligands coordinated to Ir3 are disordered and this was modelled with restraints (SADI, ISOR) and constraints (EADP). The disordered moiety occupancy for each phenylpyridine was refined at 61% and 57%. Several solvent molecules were disordered and modelled with restraints (ISOR, DFIX) and constraints (EADP). The less occupied part of a disordered THF (55:45% occupied) was modelled with AFIX 1 (only the oxygen atom) to maintain the molecule in a reasonable H-bonding position.

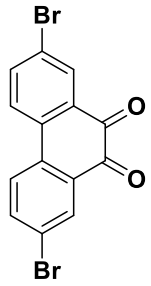

2,7-dibromophenanthrene-9,10-dione; 81

2,7-dibromophenanthrene-9,10-dione was prepared *via* a modified literature procedure.[9] phenanthrene-9,10-dione (1.75 g, 8.4 mmol) was dissolved in pre-cooled conc. H_2SO_4 (48 mL). N-Bromosuccinimide (3.2 g, 18 mmol) was added carefully, and the mixture was stirred in air for 16 h. The mixture was then added to ice-water, with the red precipitate collected by filtration (1.4 g, 47 %).

^{1}H NMR (400 MHz, DMSO-d_6): δ 8.25 (br s, 2H), 8.09 (br s, 2H), 7.96 (br s, 2H) ppm.

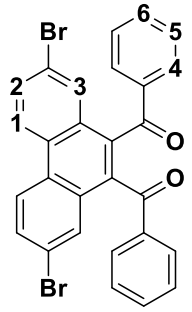

(2,7-dibromophenanthrene-9,10-diyl)bis(phenylmethanone); 79

A mixture of 5,10-dibromo-1,3-diphenyl-2H-cyclopenta[l]phenanthren-2-one and 5,10-dibromo-11b-hydroxy-1,3-diphenyl-1,11b-dihydro-2H-cyclopenta[l]phenanthren-2-one (0.5 g, total), and Al_2O_3 (2.5 g) were combined in Chlorobenzene (30 mL) and refluxed for 16 h

in air. The colour of the solution changed from orange-green to opaque green over the course of the reaction time, before turning yellow. The solvent was removed *in vacuo*. The pale yellow solid was dissolved in the minimum amount of acetone and precipitated with hexanes, yielding a pale white solid (0.174 g, 29 %).

^{1}H NMR (400 MHz, $CDCl_3$): δ 8.63 (d, 2H, $^{3}J_{HH}$ = 8.5 Hz, H1), 7.89 – 7.83 (m, 4H, H2/H3), 7.71 (d, 2H, $^{3}J_{HH}$ = 7.7 Hz, 43), 7.58 (t, 2H, $^{3}J_{HH}$ = 7.0 Hz, H6), 7.39 (t, 4H, $^{3}J_{HH}$ = 6.9 Hz, H5) ppm.

^{13}C NMR (101 MHz, $CDCl_3$): δ 197.1 (C=O), 137.0 (C_Q), 135.0 (C_Q), 134.4 (C6), 131.7 (C2), 130.3 (C4), 129.7 (C_Q), 129.4 (C3), 129.0 (C_Q), 128.7 (C5) 124.6 (C1), 122.3 (C_Q) ppm

HRMS (*m/z*): [M+H] ($C_{28}H_{16}Br_2O_2$) Calc.: 542.9589, Found: 542.9585

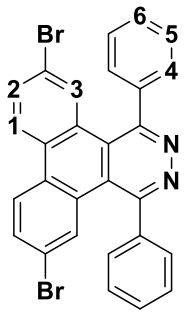

6,11-dibromo-1,4-diphenyldibenzo[f,h]phthalazine; 78

To a solution containing (2,7-dibromophenanthrene-9,10-diyl)bis(phenylmethanone) (0.1 g, 0.183 mmol) in EtOH (5 mL) was added an aqueous solution of hydrazine monohydrate (50-60 %, 0.2 g, 2 mmol). A solution of KOH (0.09 mg, 1.60 mmol) in EtOH (5 mL) was added dropwise. The red reaction mixture was heated under reflux for 16 h. The solution was allowed to cool and the solvent removed *in vacuo*. The yellow solid was dissolved in the minimum amount of acetone and precipitated with hexanes, yielding a pale yellow solid (0.84 g, 86 %).

^{1}H NMR (400 MHz, $CDCl_3$): δ 8.41 (d, 2H, $^{3}J_{HH}$ = 8.1 Hz, H1), 7.98 (d, 2H, $^{3}J_{HH}$ = 1.9 Hz, H3), 7.78 (dd, 2H, $^{3}J_{HH}$ = 8.9 Hz, $^{4}J_{HH}$ = 4.8, H2), 7.74 – 7.69 (m, 4H, H4), 7.60 – 7.53 (m, 6H, H5/H6) ppm.

^{13}C NMR (101 MHz, $CDCl_3$): δ 156.3 (C_Q), 133.0 (C2), 132.9 (C_Q), 132.0 (C3) 131.8 (C_Q), 131.1 (C_Q), 129.9 (C4/C6), 129.3 (C5), 129.2 (C_Q), 127.9 (C_Q), 124.9 (C1), 121.2 (C_Q) ppm.

IR (neat, νbar/cm^{-1}): 2918, 1593, 1460, 1368, 1218, 1088, 1000, 877, 808, 770, 694, 637.

HRMS (*m/z*): [M+H] ($C_{28}H_{17}Br_2N_2$) Calc.: 538.9753, Found: 538.9767

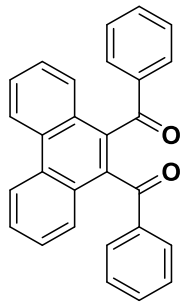

phenanthrene-9,10-diylbis(phenylmethanone); 101

phenanthrene-9,10-diylbis(phenylmethanone) was prepared *via* a modified literature procedure.[10] 1,3-diphenyl-2H-cyclopenta[l]phenanthren-2-one (0.35 g, 0.92 mmol) and Chloramine T hydrate (4.0 g, 17.6 mmol) were combined in CH_2Cl_2 (10 mL) and MeOH (10 mL). Without stirring, H_2O_2 (2 mL, 35 % in H_2O) was added very slowly dropwise. The solution was heated briefly with a heat gun. The colour of the solution changed from opaque green to yellow on addition of heat. The solvent was removed *in vacuo*. The solid was redissolved in CH_2Cl_2, and washed with an aqueous KOH solution (1 M, 2 x 100 mL). The solvent was removed *in vacuo*. Column chromatography (silica), 1:1 CH_2Cl_2:hexane, yielded an off-white solid (0.096 g, 27 %).

^{1}H NMR (400 MHz, $CDCl_3$): δ 8.84 (d, 2H, $^3J_{HH}$ = 8.6 Hz), 7.82 – 7.77 (m, 6H), 7.69 (d, 2H, $^3J_{HH}$ = 7.5 Hz), 7.55 (t, 4H, $^3J_{HH}$ = 8.6 Hz), 7.37 (t, 4H, $^3J_{HH}$ = 8.6 Hz) ppm.

HRMS (*m/z*): [M+H] ($C_{28}H_{18}O_2$) Calc.: 387.1385, Found: 387.1380

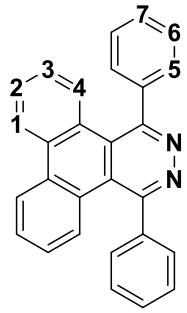

1,4-diphenyldibenzo[f,h]phthalazine; 94

To a solution containing phenanthrene-9,10-diylbis(phenylmethanone) (0.095 g, 0.25 mmol) in EtOH (5 mL) was added an aqueous solution of hydrazine monohydrate (50-60 %, 0.2 g, 2 mmol). A solution of KOH (0.09 mg, 1.60 mmol) in EtOH (5 mL) was added dropwise. The red reaction mixture was heated under reflux for 16 h. The solution was allowed to cool and the solvent removed *in vacuo*. The yellow solid was dissolved in the minimum amount of acetone and precipitated with hexanes, yielding a pale yellow solid (0.6 g, 63 %).

^{1}H NMR (400 MHz, $CDCl_3$): δ 8.61 (d, 2H, $^{3}J_{HH}$ = 7.6 Hz, H1), 7.93 (d, 2H, $^{3}J_{HH}$ = 9.2 Hz, H4), 7.77 – 7.72 (m, 4H, H5), 7.70 (t, 2H, $^{3}J_{HH}$ = 7.6 Hz, H3), 7.56 – 7.47 (m, 6H, H6/H7), 7.32 – 7.27 (m, 2H, H2) ppm.

^{13}C NMR (101 MHz, $CDCl_3$): δ 156.1 (C_Q), 140.4 (C_Q), 132.9 (C_Q), 130.0 (C5), 129.5 (C3), 129.2 (C4), 129.2 (C6), 128.9 (C7), 127.1 (C_Q), 126.6 (C_Q), 126.4 (C2), 123.5 (C1) ppm.

IR (neat, νbar/cm^{-1}): 3057, 1603, 1441, 1379, 1229, 1176, 1014, 821, 761, 727, 696, 635.

HRMS (*m/z*): [M+H] ($C_{28}H_{18}N_2$) Calc.: 383.1548, Found: 383.1538

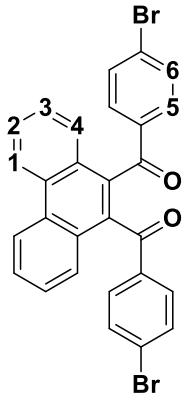

phenanthrene-9,10-diylbis((4-bromophenyl)methanone); 103

1,3-bis(4-bromophenyl)-2H-cyclopenta[l]phenanthren-2-one (0.35 g, 0.65 mmol) and Al_2O_3 (2.5 g) were combined in Chlorobenzene (30 mL) and refluxed for 16 h in air. The colour of the solution changed from green to orange over the course of the reaction time, before turning yellow. The solvent was removed *in vacuo*. The pale yellow solid was dissolved in diethyl ether, with an immediate precipitation of a white solid observed. The precipitate was collected by filtration (0.215 g, 61 %).

^{1}H NMR (400 MHz, $CDCl_3$): δ 8.84 (d, 2H, $^{3}J_{HH}$ = 7.6 Hz, H1), 7.78 (t, 2H, $^{3}J_{HH}$ = 7.5 Hz, H2), 7.64 (t, 6H, $^{3}J_{HH}$ = 9.3 Hz, H5/H4), 7.58 (d, 2H, $^{3}J_{HH}$ = 7.3 Hz, H3), 7.54 (d, 4H, $^{3}J_{HH}$ = 7.5 Hz, H6) ppm.

^{13}C NMR (101 MHz, $CDCl_3$): δ 197.4 (C=O), 136.4 (C_Q), 135.0 (C_Q), 132.0 (C6), 131.5 (C5), 130.6 (C_Q), 129.5 (C_Q), 128.3 (C2), 128.1 (C_Q) 127.7 (C3), 127.0 (C4), 123.2 (C1) ppm.

IR (neat, νbar/cm^{-1}): 1669, 1581, 1449, 1398, 1241, 1175, 1068, 1007, 937, 849, 810, 757, 716, 646.

HRMS (*m/z*): [M+Na] ($C_{28}H_{16}Br_2O_2$) Calc.: 542.9595, Found: 564.9757

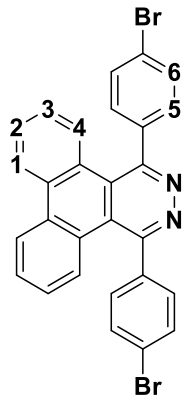

1,4-bis(4-bromophenyl)dibenzo[f,h]phthalazine; 95

To a solution containing phenanthrene-9,10-diylbis((4-bromophenyl)methanone) (0.215 g, 0.4 mmol) in EtOH (5 mL) was added an aqueous solution of hydrazine monohydrate (50-60 %, 0.2 g, 2 mmol). A solution of KOH (0.09 mg, 1.60 mmol) in EtOH (5 mL) was added dropwise. The red reaction mixture was heated under reflux for 16 h. The solution was allowed to cool and the solvent removed *in vacuo*. The yellow solid was dissolved in the minimum amount of acetone and precipitated with hexanes, yielding a pale yellow solid (0.2 g, 93 %).

^{1}H NMR (400 MHz, $CDCl_3$): δ 8.62 (d, 2H, $^{3}J_{HH}$ = 8.8 Hz, H1), 7.93 (d, 2H, $^{3}J_{HH}$ = 8.5 Hz, H4), 7.74 (t, 2H, $^{3}J_{HH}$ = 7.7 Hz, H3), 7.64 (s, 4H, H5/H6), 7.37 (t, 2H, $^{3}J_{HH}$ = 8.8 Hz, H2) ppm.

^{13}C NMR (101 MHz, $CDCl_3$): δ 155.2 (C_Q), 139.2 (C_Q), 133.0 (C_Q), 132.2 (C5), 131.6 (C6), 129.9 (C3), 129.0 (C4), 127.1 (C_Q), 126.7 (C_Q), 126.1 (C_Q), 123.9 (C_Q), 123.6 (C1) ppm.

IR (neat, νbar/cm^{-1}): 2922, 1371, 1101, 1009, 831, 763, 729.

HRMS (*m/z*): [M+H] ($C_{28}H_{16}Br_2N_2$) Calc.: 538.9758, Found: 538.9757

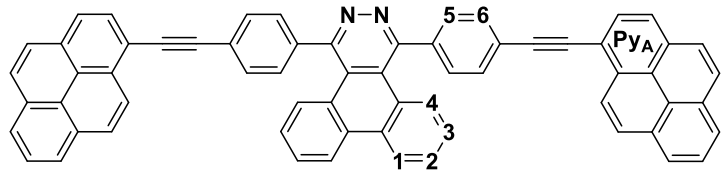

1,4-bis(4-(pyren-1-ylethynyl)phenyl)dibenzo[f,h]phthalazine; 97

1,4-bis(4-bromophenyl)dibenzo[f,h]phthalazine (0.1 g, 0.185 mmol), 1-ethynylpyrene (0.168 g, 0.74 mmol), CuI (0.0035 g, 0.0185 mmol), and PPh3 (0.0049 g, 0.0185 mmol) were combined in dimethylformamide (10 mL) and Et3N (10 mL), and degassed with Ar for 15 minutes. $Pd(PPh3)_4$ (0.011 mg, 0.0093 mmol) was degassed separately. The solution was transferred to the Pd catalyst *via* the cannula method under an Ar atmosphere. The reaction

mixture was heated to 80 °C for 16 h under Ar. Upon cooling, the solvent was removed *in vacuo*. Column chromatography (silica), CHCl3 → 1:1 CHCl3:EtOAc, yielded a yellow solid. The yellow solid was dissolved in diethyl ether, with an immediate precipitation of a yellow solid observed. The precipitate was collected by filtration (0.011 g, 7 %).

^{1}H NMR (400 MHz, $CDCl_3$): δ 8.75 (d, 2H, $^{3}J_{HH}$ = 8.7 Hz, Py), 8.67 (d, 2H, $^{3}J_{HH}$ = 7.6 Hz, H1), 8.28 (d, 4H, $^{3}J_{HH}$ = 8.2 Hz, Py_A/Py), 8.25 (d, 4H, $^{3}J_{HH}$ = 9.2 Hz, Py/Py), 8.20 (d, 2H, $^{3}J_{HH}$ = 7.6 Hz, Py_A), 8.15 (d, 2H, $^{3}J_{HH}$ = 9.2 Hz, Py), 8.11 (d, 2H, $^{3}J_{HH}$ = 9.4 Hz, Py), 8.10 – 8.05 (m, 4H, Py/H4), 7.88 (s, 8H, H5/H6), 7.77 (d, 2H, $^{3}J_{HH}$ = 6.6 Hz, H3), 7.41 (d, 2H, $^{3}J_{HH}$ = 7.1 Hz, H3) ppm.

^{13}C NMR (101 MHz, $CDCl_3$): δ 155.6 (C_Q), 140.3 (C_Q), 133.0 (C_Q), 132.3 (C6), 132.0 (C_Q), 131.5 (C_Q), 131.3 (C_Q), 131.1 (C_Q), 130.3 (C5), 130.0 (Py), 129.7 (C3), 129.3 (C4), 128.5 (Py), 128.3 (Py), 127.3 (Py), 126.7 (C2), 126.4 (C_Q), 126.3 (Py), 125.8 (Py_A), 125.7 (Py), 125.6 (Py), 124.6 (Py_A), 124.6 (C_Q) 124.5 (C_Q), 124.4 (C_Q) 123.7 (C1), 117.6 (C_Q), 94.9 (-CC-), 90.3 (-CC-) ppm.

IR (neat, νbar/cm^{-1}): 3037, 2343, 1602, 1371, 1178, 1011, 954, 837, 761, 728, 712, 678, 648, 610.

HRMS (*m/z*): [M+H] ($C_{64}H_{34}N_2$) Calc.: 831.2800, Found: 831.2769

5.3 References

1 S. Varughese and S. M. Draper, *Cryst. Growth Des.*, 2010, **10**, 2298–2305.

2 G. Y. Wooi and J. M. White, *Org. Biomol. Chem.*, 2005, **3**, 972–974.

3 B. Alameddine, R. S. Anju, F. Al-Sagheer and T. A. Jenny, *New J. Chem.*, 2016, **40**, 10363–10370.

4 X. Wang, S.-L. Gong, D. Song, Z.-H. Lu and S. Wang, *Adv. Funct. Mater.*, 2014, **24**, 7257–7271.

5 Y. Wang, X. Li, F. Li, W.-Y. Sun, C. Zhu and Y. Cheng, *Chem. Commun.*, 2017, **53**, 7505–7508.

6 J. Ettedgui and R. Neumann, *J. Am. Chem. Soc.*, 2009, **131**, 4–5.

7 E. A. Karlsson, B.-L. Lee, R.-Z. Liao, T. Åkermark, M. D. Kärkäs, V. S. Becerril, P. E. M. Siegbahn, X. Zou, M. Abrahamsson and B. Åkermark, *Chempluschem*, 2014, **79**, 936–950.

8 L.-Y. Zhang, Y.-J. Hou, M. Pan, L. Chen, Y.-X. Zhu, S.-Y. Yin, G. Shao and C.-Y. Su,

Dalton Trans., 2015, **44**, 15212–15219.

9 T. H. Vo, M. Shekhirev, D. A. Kunkel, F. Orange, M. J.-F. Guinel, A. Enders and A. Sinitskii, *Chem. Commun.*, 2014, **50**, 4172–4174.

10 D. F. Evans and M. W. Upton, *J. Chem. Soc., Dalt. Trans.*, 1985, 1141–1145.

General Thesis Conclusions

Conclusions

As per the general introduction to this thesis, addressing the shortage of synthetic methods to access readily modifiable core ring PAH systems is the core focus of this thesis, connecting all of the four chapters, despite their individual primarily applications.

Chapter 1 details a significant amount of synthetic work undertaken towards the development, and optimisation, of a novel room temperature Knoevenagel reaction using an unreported 1,10-phenanthroline cyclopentadienone system. From this work, four ligand architectures were developed and characterised, two incorporating a quinone moiety. The first 1,10-phenanthroline, pyridazine PAH-type compound was also successfully generated. During the course of the work, many other synthetic strategies were developed. Many of these attempts were very nearly successful, and with further time could yield significant advances in the library of accessible PAH-type ligands. Due to very recent literature optimised preparations of 5,6-dibromo-1,10-phenanthroline,[1] this work may be realised in the near future. These "gateway" systems may also be applicable to a number of other research areas when 1,10-phenanthroline has remained underutilised.

Chapter 2 is closely related to the work of Chapter 1, and may be considered as a two-part volume. Chapter 2 attempted to investigate the effect of metal complexation on those ligands developed through the synthetic work of Chapter 1, using the literature common metal centres of Ru(II) and Ir(III). Detailed and methodologically chosen multinuclear NMR studies were carried out to determine if a ring slowing or "locking" of the free phenyl rings was occurring for the majority of the systems generated. Variable temperature studies and 2D EXSY spectra were collected which conclusively showed that the free phenyl rings were behaving as rotamers, with a slowed rotation generating two extra signals in the ^{1}H NMR. Electrochemical measures determined exceptionally stable quinone reduction processes over a large potential window, postulated due to the quinones "internal" construction to the PAH *versus* the typical appended nature of literature systems. Photocatalytic proton reduction studies were also carried out, as well as a detailed account of future synthetic work. Work is ongoing towards the optimised development the PAH-type ligands for further photocatalytic proton reduction, using DFT methods to determine the position of the "trapped" electron in the photosensitiser, before its transfer to the proton reduction catalyst.

Chapter 3 details work towards the generation of novel pyridazine-containing compound for use in the generation of graphene nanoribbons (GNRs). Due to the benefits of synthetic control in the "bottom-up" strategy, a novel pyridazine-containing feedstock was identified and synthesised.

Successful on-surface polymerisation was observed on Au(111), but the necessary cyclodehydrogenation step does not appear to have worked correctly. A suggested decomposition route is put forward, detailing a loss of N_2 from the collapse of the pyridazine ring. Further work is needed to confirm this. Work is ongoing to explore this reaction on Ag(111) and Cu(111) which both require lower activation temperatures, but may generate multiple species due to their increased reactivity. A retrosynthetic analysis is also given towards the modification of the current compound, which may allow lower thermal annealing temperatures on Au(111) – this work is currently being explored. This work will inform the design of future pyridazine-substituted PAH molecules, and the design of on-surface cyclodehydrogenation steps for these systems in the future.

Chapter 4 details work undertaken towards novel donor-acceptor-donor compounds for their use as thermally assisted delayed fluorescence (TADF) emissive layers in organic light emitting diodes (OLEDs). The work features the development of a novel pyridazine-phenanthrene acceptor component, with attempts to use ethynylpyrene and ethynyl tri-phenylamine as the respective donor components. TADF behaviour is investigated by solvatochromic and degassing studies, with the presence of the pyrene-pyrene excimer also investigated by dilution studies. The pyrene excimer was found to play a significant roles in the solution-based emission profile of the compound, with this effect assumed to be even more pronounced in the solid state (thin film). However, this may prove to be a useful addition to the literature, as it has been recently shown that pyrene excimers in the solid state dramatically increase in the electron and hole mobility values of TADF materials.[2] The chapter also details a very large collection of novel compounds which may find use as TADF materials, utilising the pyridazine-phenanthrene acceptor component, which it itself may be further modified through the addition of electron withdrawing or donating groups.

Each chapter offers a small but meaningful contribution to the evolving role of PAH systems in a number of active research areas. Each chapter of this thesis is working towards a different application, but the fundamental synthetic work is common to all. These proprietary synthetic advances will shortly be investigated as patents or peer reviewed publications, with a hope that they will be fuel further work in nitrogen-containing PAH systems in diverse research fields.

References

1 S. Anne, P. T. David, S. Markus, G. Helmar, S. Dieter, P. Katrin, G. Dirk and R. Sven, *Eur. J. Inorg. Chem.*, 2017, **32**, 3799–3810.

2 G. Mallesham, C. Swetha, S. Niveditha, M. E. Mohanty, N. J. Babu, A. Kumar, K. Bhanuprakash and V. J. Rao, *J. Mater. Chem. C*, 2015, **3**, 1208–1224.

Annex

Table 1. Crystal data and structure refinement for **14**.

Empirical formula	$C_{32}H_{18}N_2O_2$	
Formula weight	462.48	
Temperature	100(2) K	
Wavelength	0.71073 Å	
Crystal system	Monoclinic	
Space group	$P2_1/n$	
Unit cell dimensions	a = 15.1713(4) Å	α= 90°.
	b = 8.1437(2) Å	β= 92.4755(14)°.
	c = 17.8028(5) Å	γ = 90°.
Volume	2197.49(10) $Å^3$	
Z	4	
Density (calculated)	1.398 Mg/m^3	
Absorption coefficient	0.088 mm^{-1}	
F(000)	960	
Crystal size	0.18 x 0.17 x 0.12 mm^3	
Theta range for data collection	2.290 to 28.009°.	
Index ranges	$-20\leq h\leq 20$, $-10\leq k\leq 10$, $-23\leq l\leq 23$	
Reflections collected	47660	
Independent reflections	5299 [R(int) = 0.0630]	
Completeness to theta = 25.242°	99.9 %	
Absorption correction	Semi-empirical from equivalents	
Max. and min. transmission	0.7456 and 0.7210	
Refinement method	Full-matrix least-squares on F^2	
Data / restraints / parameters	5299 / 0 / 325	
Goodness-of-fit on F^2	1.049	
Final R indices [$I>2\sigma(I)$]	R1 = 0.0439, wR2 = 0.1266	
R indices (all data)	R1 = 0.0685, wR2 = 0.1462	
Largest diff. peak and hole	0.290 and -0.257 $e.Å^{-3}$	

Table 2. Crystal data and structure refinement for **15**.

Empirical formula	$C_{39}H_{20}D_4Cl_{10}N_2O_2$	
Formula weight	911.13	
Temperature	100 K	
Wavelength	0.71073 Å	
Crystal system	Triclinic	
Space group	$P\bar{1}$	
Unit cell dimensions	a = 8.8542(4) Å	α=115.7025(15)°.
	b = 15.6631(7) Å	β= 92.7686(17)°.
	c = 16.3565(7) Å	γ= 104.6925(16)°.
Volume	1944.23(15) $Å^3$	
Z	2	
Density (calculated)	1.556 Mg/m^3	
Absorption coefficient	0.756 mm^{-1}	
F(000)	916	
Crystal size	0.43 x 0.08 x 0.07 mm^3	
Theta range for data collection	2.567 to 26.131°.	
Index ranges	$-10\leq h\leq 9$, $-19\leq k\leq 19$, $-20\leq l\leq 20$	
Reflections collected	24554	
Independent reflections	7691 [R(int) = 0.0357]	
Completeness to theta = 26.000°	99.8 %	
Absorption correction	Semi-empirical from equivalents	
Max. and min. transmission	0.7453 and 0.6601	
Refinement method	Full-matrix least-squares on F^2	
Data / restraints / parameters	7691 / 4 / 490	
Goodness-of-fit on F^2	1.037	
Final R indices [$I>2\sigma(I)$]	R1 = 0.0397, wR2 = 0.0877	
R indices (all data)	R1 = 0.0595, wR2 = 0.0955	
Largest diff. peak and hole	0.562 and -0.878 $e.Å^{-3}$	

Table 3. Crystal data and structure refinement for **3**.

Empirical formula	$C_{28}H_{20}N_2O$	
Formula weight	400.46	
Temperature	100.0 K	
Wavelength	1.54178 Å	
Crystal system	Monoclinic	
Space group	$P2_1/c$	
Unit cell dimensions	a = 15.8802(5) Å	α= 90°.
	b = 5.03040(10) Å	β= 96.6131(12)°.
	c = 24.7689(7) Å	γ= 90°.
Volume	1965.47(9) $Å^3$	
Z	4	
Density (calculated)	1.353 Mg/m^3	
Absorption coefficient	0.647 mm^{-1}	
F(000)	840	
Crystal size	0.23 x 0.08 x 0.08 mm^3	
Theta range for data collection	2.801 to 69.974°.	
Index ranges	$-18\leq h\leq 19$, $-6\leq k\leq 6$, $-24\leq l\leq 29$	
Reflections collected	14036	
Independent reflections	3672 [R(int) = 0.0300]	
Completeness to theta = 67.679°	99.9 %	
Absorption correction	Semi-empirical from equivalents	
Max. and min. transmission	0.7533 and 0.6661	
Refinement method	Full-matrix least-squares on F^2	
Data / restraints / parameters	3672 / 0 / 288	
Goodness-of-fit on F^2	1.024	
Final R indices [$I>2\sigma(I)$]	R1 = 0.0388, wR2 = 0.1040	
R indices (all data)	R1 = 0.0405, wR2 = 0.1062	
Largest diff. peak and hole	0.219 and -0.201 $e.Å^{-3}$	

Table 4. Crystal data and structure refinement for **4**.

Empirical formula	$C_{26}H_{16}N_4$	
Formula weight	384.43	
Temperature	100(2) K	
Wavelength	0.71073 Å	
Crystal system	Monoclinic	
Space group	C2/c	
Unit cell dimensions	a = 15.8865(7) Å	α= 90°.
	b = 14.9806(6) Å	β= 113.229(2)°.
	c = 17.3527(7) Å	γ= 90°.
Volume	3795.0(3) $Å^3$	
Z	8	
Density (calculated)	1.346 Mg/m^3	
Absorption coefficient	0.082 mm^{-1}	
F(000)	1600	
Crystal size	0.160 x 0.150 x 0.130 mm^3	
Theta range for data collection	1.948 to 31.135°.	
Index ranges	$-22\leq h\leq 23$, $-21\leq k\leq 21$, $-25\leq l\leq 25$	
Reflections collected	88828	
Independent reflections	6124 [R(int) = 0.0638]	
Completeness to theta = 25.242°	100.0 %	
Absorption correction	Numerical	
Max. and min. transmission	1.0000 and 0.9842	
Refinement method	Full-matrix least-squares on F^2	
Data / restraints / parameters	6124 / 0 / 271	
Goodness-of-fit on F^2	1.022	
Final R indices [$I>2\sigma(I)$]	R1 = 0.0479, wR2 = 0.1085	
R indices (all data)	R1 = 0.0772, wR2 = 0.1218	
Largest diff. peak and hole	0.403 and -0.273 $e.Å^{-3}$	

Table 5. Crystal data and structure refinement for **52**.

Empirical formula	$C_{46}H_{32}F_{12}N_8P_2Ru$	
Formula weight	1087.80	
Temperature	100(2) K	
Wavelength	0.71073 Å	
Crystal system	Monoclinic	
Space group	$P2_1/c$	
Unit cell dimensions	a = 13.8299(4) Å	α= 90°.
	b = 22.9240(7) Å	β= 106.9810(12)°.
	c = 15.9228(4) Å	γ= 90°.
Volume	4828.0(2) $Å^3$	
Z	4	
Density (calculated)	1.497 Mg/m^3	
Absorption coefficient	0.479 mm^{-1}	
F(000)	2184	
Crystal size	0.190 x 0.060 x 0.040 mm^3	
Theta range for data collection	1.540 to 25.403°.	
Index ranges	$-16\leq h\leq 16$, $-27\leq k\leq 27$, $-19\leq l\leq 19$	
Reflections collected	124078	
Independent reflections	8868 [R(int) = 0.1212]	
Completeness to theta = 25.242°	100.0 %	
Absorption correction	Semi-empirical from equivalents	
Max. and min. transmission	0.7452 and 0.6991	
Refinement method	Full-matrix least-squares on F^2	
Data / restraints / parameters	8868 / 0 / 622	
Goodness-of-fit on F^2	1.036	
Final R indices [$I>2\sigma(I)$]	R1 = 0.0522, wR2 = 0.1114	
R indices (all data)	R1 = 0.0928, wR2 = 0.1251	
Largest diff. peak and hole	1.019 and -0.661 $e.Å^{-3}$	

Table 6. Crystal data and structure refinement for **54**.

Empirical formula	$C_{164}H_{138}F_{18}Ir_3N_{18}O_5P_3$	
Formula weight	3452.43	
Temperature	100(2) K	
Wavelength	0.71073 Å	
Crystal system	Monoclinic	
Space group	$P2_1/c$	
Unit cell dimensions	a = 16.0857(5) Å	α= 90°.
	b = 38.3546(11) Å	β= 94.9016(12)°.
	c = 23.1955(6) Å	γ= 90°.
Volume	14258.4(7) $Å^3$	
Z	4	
Density (calculated)	1.608 Mg/m^3	
Absorption coefficient	2.916 mm^{-1}	
F(000)	6904	
Crystal size	0.320 x 0.140 x 0.040 mm^3	
Theta range for data collection	1.377 to 26.395°.	
Index ranges	$-20\leq h\leq 20$, $-47\leq k\leq 47$, $-29\leq l\leq 28$	
Reflections collected	552424	
Independent reflections	29189 [R(int) = 0.0420]	
Completeness to theta = 25.242°	100.0 %	
Absorption correction	Semi-empirical from equivalents	
Max. and min. transmission	0.7454 and 0.5707	
Refinement method	Full-matrix least-squares on F^2	
Data / restraints / parameters	29189 / 123 / 1813	
Goodness-of-fit on F^2	1.102	
Final R indices [$I>2\sigma(I)$]	R1 = 0.0403, wR2 = 0.0970	
R indices (all data)	R1 = 0.0472, wR2 = 0.1009	
Largest diff. peak and hole	2.518 and -1.936 $e.Å^{-3}$	

"Phencyclone is even harder to work with."

R. Conway-Kenny, PhD Thesis, University of Dublin, 2017.